Organo and Amino Phosphonium Cation Derived Ferro and Piezoelectric Materials and their Utility in Mechanical Energy Harvesting Applications

A Thesis
Submitted in Partial Fulfillment of the Requirements
for the Degree of

Doctor of Philosophy

by

T. Vijayakanth

ID: 20143306

Department of Chemistry
Indian Institute of Science Education and Research, Pune
January 2020

Dedicated to

My loved one who is no more in this world but lives in my heart...

भारतीय विज्ञान शिक्षा एवं अनुसंधान संस्थान, पुणे
INDIAN INSTITUTE OF SCIENCE EDUCATION AND RESEARCH (IISER), PUNE
(An Autonomous Institution, Ministry of Human Resource Development, Govt. of India)
Dr. Homi Bhabha Road, Pune 411008.

Dr. R. Boomi Shankar
Professor
Department of Chemistry,
IISER Pune

CERTIFICATE

Certified that the work incorporated in the thesis entitled "***Organo and Amino Phosphonium Cation Derived Ferro and Piezoelectric Materials and their Utility in Mechanical Energy Harvesting Applications"*** submitted by **Mr. T. Vijayakanth** was carried out by the candidate, under my supervision. The work presented here or any part of it has not been included in any other thesis submitted previously for the award of any degree or diploma from any other university or institution.

R. Boomi Sankar.

Date: 15th January-2020
Place: Pune

Dr. R. Boomi Shankar
(Research Supervisor)

boomi@iiserpune.ac.in •Ph: +91-20-25908208

भारतीय विज्ञान शिक्षा एवं अनुसंधान संस्थान, पुणे
INDIAN INSTITUTE OF SCIENCE EDUCATION AND RESEARCH (IISER), PUNE
(An Autonomous Institution, Ministry of Human Resource Development, Govt. of India)
Dr. Homi Bhabha Road, Pune 411008.

DECLARATION

I declare that, this written submission represents my ideas in my own words and where other's ideas have been included; I have adequately cited and referenced the original sources. I also declare that I have adhered to all principles of academic honesty and integrity and have not misrepresented or fabricated or falsified any idea/data/fact/ source in my submission. I understand that violation of the above will be cause for disciplinary action by the Institute and can also evoke penal action from the sources which have thus not been properly cited or from whom proper permission has not been taken when needed.

Date: 15th January-2020
Place: Pune

Mr. T. Vijayakanth
ID: 20143306

Acknowledgement

I want to express my sincere gratitude to everyone who travelled along with me at every moment of my life in the past few years. In this journey, so many special people made me feel like I am one of the family members to them, which helped me immeasurably to stay healthy and live in a happy life.

First and foremost, I would like to express my immense gratitude to my research supervisor, mentor and advisor, Prof. Dr. R. Boomi Shankar, for his continuous support, motivation, valuable suggestion and constant guidance and most importantly for his patience and faith in me during this entire Ph.D. journey. Sir, you have given me an opportunity to pursue the research work with the fascinating topic of my interest, which helped me to complete the research project on the course of planned time. Also, I would like to thank you once again for letting me go through initial difficulties that everyone faces in their Ph.D. life, which helped me and finds out the taste of success in the later stage of this research program. Thank you for your encouragement and help in finding new scientific ideas during the entire Ph.D. I could not have imagined a better supervisor than you to complete my research work with the enormous freedom provided by you. I always think and firmly believe that motivated me to take everything in a positive note.

I am also thankful to Prof. K. N. Ganesh (Former Director) and the present director Prof. Jayant B. Udgaonkar, IISER Pune, for providing outstanding research facilities and the beautiful campus environments. I would also like to extend my sincere thanks to Dr. B. Praveenkumar (PZT centre, ADRE-Pune, DRDO) and his students Mrs. Pillutla Divya, Mrs. Priyangi Kulkarni and Mr. Prashanth for providing the piezoelectric and dielectric measurements data for all my samples. Indeed, their kind-hearted help and valuable scientific discussions are encouraged me to understand these concepts even further. My sincerest thanks go to Dr. Kadhiravan Shanmuganathan (National Chemical Laboratory, CSIR-NCL) and his student Mr. Farsa Ram for providing the piezoelectric energy harvesting data. Again, I am grateful to say thank you to them for allowing me to work in their lab and learn a new scientific skill, which enhanced the understanding of my work more profoundly.

My sincere appreciations go to the members of my Research Advisory Committee (RAC), Dr. B. Praveenkumar (ARDE, DRDO) and Dr. R. Vaidyanathan (IISER-Pune) for providing their encouragements and valuable suggestions during the scientific meetings to improve my research work. My gratitude also extends to all the chemistry faculty members and mainly, Prof. H. N. Gopi, chair Chemistry, Department of Chemistry, IISER-Pune, for his support as well as conducting the various scientific activities in the department in every year. I also had great working experience with our collaborators starting from Dr. B. Praveenkumar (ARDE, DRDO), Dr. Kadhiravan Shanmuganathan (National Chemical Laboratory, CSIR-NCL), Dr. Anukul Jana (Tata Institute of Fundamental Research, TIFR, Hyderabad) and Dr. Dinesh Kabra (Indian Institute of Technology, IIT Bombay), thank them for their support and providing me an opportunity to contribute in a different type of collaborative research projects.

I am extremely grateful to say thanks to all the technical staff members for their support and allowing me to access various instruments: Ms. Archana (SCXRD), Mr. Ravinder (TGA and SCXRD), Mr. Parven Nasa (SCXRD and PXRD), Mr. Prashant Kale (PXRD), Mr. Nilesh Dumbre (PXRD and SEM), Mr. Anil & Mr. Yatish (SEM), Ms. Megha (Raman spectra), Ms. Swati M. Dixit (MALDI-TOF and CHN analysis), Ms. Sandeep (HRMS), Mrs. Deepali &Mr. N. Dalvi (NMR), Mr. Mahesh Jadhav (TGA), Mr. Suresh Prajapati (UG Chemistry Lab), Mr. Ganesh Dimbar (IR). I would also like to acknowledge the whole IT department members and particularly Mr. Suresh anna for his support and help to solve all the laptop problem. I extend my sincere thanks to the entire administrative department members of IISER-Pune for their support, especially Col. (Retd.) G. Raja Sekhar (Registrar, IISER-Pune), Dr. V. S. Rao, Mr. Prabhash and Mr. Mayuresh. I genuinely pay my acknowledgement for the support from the office staff of Dean Doctoral Studies, especially Ms. Dipali Dalvi and Mr. Tushar. I wish to thank Dr. Umeshareddy Kacherki (Librarian) for support through the library services.

Most important of all, I would like to pay my sincere gratitude to all my lab members for their unconditional support and guidance, which allowed me to complete my Ph.D. work in a happy note. I thank each one of them, particularly my seniors, starting from Dr. Arvind, Dr. Anant, Dr. Ashok ji, Dr. Mahesh, without them, it won't be possible to complete my Ph.D. A special thanks to Anant, Ashok ji and Mahesh for their great support and beautiful moments throughout these all the years. It is always a great pleasure to work with you all. I would also like to extend my sincere thanks to all the other lab members starting from Rajasekar, Santhosh, Rishabh, Sachin, Neetu, Meghamala, Swati, Anupriya, Supriya, Rishu and Cavya for their support as well as maintaining the healthy environment in the lab. Also, I would like to thank many BSMS students, Arun, Indra, Saubrah, Atul, Sravan, Rani and Hrithik. My deepest appreciations also go to Atul (IISER, Pune), Navya Sree (University of Hyderabad) and Uddipana Kakati (Institute of Chemical Technology, Mumbai), for contributing needful support and helpful discussions to my research work.

I want to express my sincere gratitude to some of the seniors from other labs, especially Dr. Gopalakrishna, Dr. Santosh Gadekar, Dr. Kiran Reddy, Dr. Dharma, Dr. Anantharaj, Dr. Ganesh, Mrs. Kavitha and Dr. Kundan, I thank them all for their support and help. I would like to pay my gratitude to all my dear teachers and friends from various institutions, specifically to Dr. D. Saravanan (National College, Trichy), for his constant support and help throughout my master's degree program. I would like to extend my sincere thanks to all my dear friends from IISER, Pune, for the support and happier moments that I can always remember and enjoy every day of my life. I am also thankful for the organizing committee of IISER, Premier League, Pune, for conducting every year's cricket match on our campus. I will take the opportunity to say thanks to all the cricket teams in IISER, Pune, for giving me a chance to play cricket and enjoy every bit of happy moments on the field. Notably, a special thanks to all my teammates (*Alchemist*) for giving me the immense support and more blissful moments in every year. It's very tough to think of better team players than you people. I feel words not adequate to say thank you to everyone and I am always happy to be part of our team.

My sincere gratitude also goes to all the friends from 2014 batchmates of IISER, Pune and even all the Tamil friends starting from Dharma anna, Anantharaj anna, Mani anna, Mano anna, Shankar anna, Ravi anna, Nandha, Alagar, Siva, Bala and Thamarai for their support and help throughout the entire Ph.D. life. It is a great pleasure and I am fortunate to have all of you as a part of my life. Once again, I am thanking you all for providing such beautiful and happier moments every time.

I am also thankful to the various people present on the campus and providing excellent services to keep the campus safe, clean (Security and House-keeping Staffs) and healthier (V-square, Shivsagar and MDP) working environments.

I would like to pay my heartfelt appreciation to my parents, who are supportive and always allowed me to express myself all the time. The faith they showed on me every time is impressive and it gives immense pleasure for me to be part of such a small and happier family. I have to mention here, without my uncle's support, I can't imagine any higher studies in my life. He is the main reason and inspiration for me to reach every small step of my life.

I am very much thankful to IISER-Pune and University of Grants Commission (UGC) for providing the research fellowships for pursuing the Ph.D. My appreciations also extends to John Wiley & Sons, American Chemical Society (ACS), Royal Society of Chemistry (RSC), Elsevier Science Ltd., Springer, etc. for accepting and publishing my research articles and also their permission to reprint the materials under copyright.

My Ph.D. thesis would not have been possible without the contributions of my dear friend; she is no more in this world and lives my soul. I have learned a lot from you and you are always an inspiration and special to me. It's very tough to explain with words whenever I think about you, but life goes on this way. We will meet more in the future somewhere in this world, which was the last word used by you. I am hoping to see you somewhere on the earth again. The inveterate happiness you have given always stays with me. Once again, I thank you for each and everything that you have provided to me.

Finally, I thank nature for giving every bit of opportunities to learn and treat failure and success in the same fashion throughout the entire life. Always, I accepted with both the hands and, once again, immense thanks to you.

Vijayakanth

Contents

Contents

Contents

Synopsis

*The thesis entitled "**Organo and Amino Phosphonium Cation Derived Ferro and Piezoelectric Materials and their Utility in Mechanical Energy Harvesting Applications**" focused on the synthesis of non-centrosymmetric polar organic and organic-inorganic hybrid organo phosphonium salts, study their structures, ferroelectric, piezoelectric and dielectric behaviour and utilize them for mechanical energy harvesting and storage applications.*

Chapter 1: Introduction

This introduction chapter 1 discusses the fundamental concepts about the non-linear dielectric materials such as piezoelectric, pyroelectric and ferroelectric properties. Notably, a comprehensive literature survey on diverse type of ferroelectric materials based on organic and organic-inorganic hybrid polar systems have been described. The later part of this chapter briefly illustrates the key examples on the use of piezo and ferroelectric substances and their polymeric composite materials for mechanical energy harvesting applications. It also provides an outline of the present thesis.

Chapter 2: Hydrogen-bonded Organo-amino Phosphonium Halides: Dielectric, Piezoelectric and Possible Ferroelectric Properties

Molecular ferroelectric materials are an exciting class of materials for potential applications in energy and electronics. In recent years, enormous attention has been given to the area of metal-organic ferroelectrics and small molecule-based ferroelectric organic materials. These molecules possess advantages such as simple synthesis, lightweight, structural tunability, high flexibility, high thermal stability, reasonable Curie temperature and the potential for low-temperature fabrication procedures. In this effort, we synthesized examples of hydrogen-bonded binary salts of diphenyl diisopropylamino phosphonium halides $[Ph_2(^iPrNH)_2P]\cdot X$ [abbreviated as DPDP·X where X = Cl, Br, I] which show dielectric, piezoelectric and NLO properties and some potentially ferroelectric attributes at room temperature. The single-crystal X-ray analysis of all these assemblies was shown to exhibit 1D H-bonded chain structures along the crystallographic b-axis. The *P–E* loop measurements of these salts gave curves similar to those of nonlinear leaky dielectric materials. However, the vertical piezoresponse force microscopy (V-PFM) analyses showed the existence of polarizable domain inversions, indicating the possibility of ferroelectric behavior in these materials. Also, bias-dependent PFM studies reveal their piezoelectric nature as the obtained converse piezoelectric coefficients are consistent with the d_{33} values obtained by the direct quasi-static methods (Figure 2).

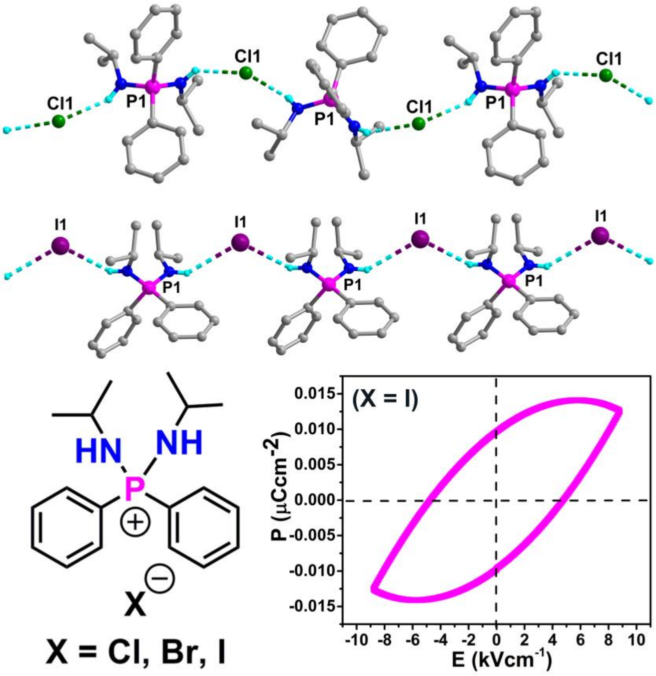

Figure 1: *1D-hydrogen bonded chain structure of polar organic salts and a representative polarization vs. electric field (P-E) loop at room temperature.*

Chapter 3: A Flexible Composite Mechanical Energy Harvester from a Ferroelectric Organoamino Phosphonium Salt

Ferroelectric materials derived from organic and organic-inorganic hybrid assemblies have been the topic of intense research for high-technological applications. Apart from their traditional utility, they have recently been found to exhibit applications in the domains of photovoltaics and piezoelectric energy harvesters. Converting mechanical energy into electrical energy is of tremendous interest because of the simplicity of its generation via the forces derived from pressure, bending, folding and stretching motions. Thus, ferroelectric materials with intrinsic dipole moment and spontaneous polarization are expected to give a good power generation response. In this context, a new binary organic salt diphenyl diisopropylamino phosphonium hexafluorophosphate (DPDP·PF_6) was shown to exhibit a good ferroelectric response and employed as a mechanical energy harvester. Ferroelectric measurements on the single crystals of DPDP·PF_6 gave a well saturated rectangular hysteresis loop with a remnant (P_r) polarization value ~6 μC cm^{-2}. Further, composite devices based on polydimethylsiloxane (PDMS) films for various weight percentages (3, 5, 7, 10 and 20 wt %) of DPDP·PF_6 were prepared and examined for power generation by using a force-measurement setup. A maximum output peak to peak voltage (V_{PP}) of 8.5 V and an output peak to peak current (I_{PP}) of 0.5 μA was obtained for the non-poled composite film with 10 wt % of DPDP·PF_6. These results promise the efficacy of organic ferroelectric substances as potential mechanical energy harvesters (Figure 3).

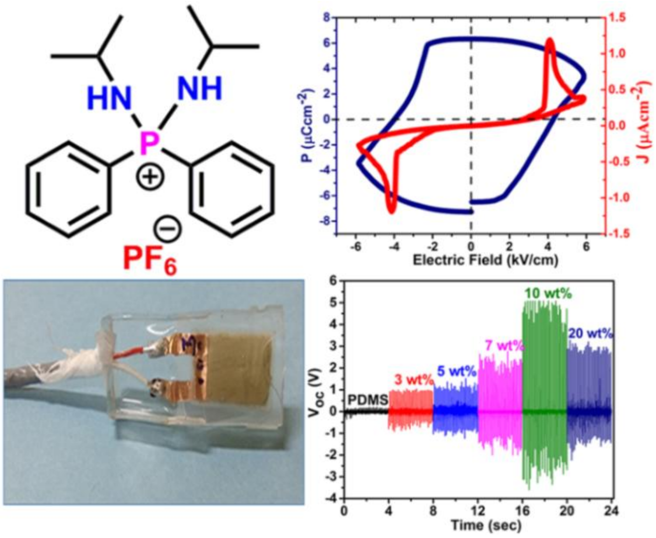

Figure 3: *View of molecular structure and its ferroelectric nature of DPDP·PF_6 at room temperature. Photograph of the as-made composite device of DPDP·PF_6 with PDMS and the output voltage data for the composite devices with various loading amounts of DPDP·PF_6.*

Chapter 4: All-organic Composites of Ferro- and Piezoelectric Phosphonium Salts for Mechanical Energy Harvesting Application

Organic molecular ferroelectrics owing to their lightweight, flexibility, phase stability and mechanical robustness are drawing attention in the fields of flexible electronics, optical systems and energy harvesting applications. In this chapter, we synthesized a series of binary organoamino phosphonium salts containing triphenyl isopropylaminophosphonium (TPAP), diphenyl diisopropylaminophosphonium (DPDP), phenyl triisopropylaminophosphonium (PTAP) and tetraisopropylaminophosphonium (TIAP) cations supported by lower symmetric tetrahedral BF_4^-, ClO_4^- and IO_4^- anions. The *P-E* hysteresis loop measurements on these polar organic salts gave high remnant polarization (P_r) values of 35.36, 21.83 and 21.12 μC cm^{-2} for the DPDP·BF_4, DPDP·ClO_4 and DPDP·IO_4 salts having 1D-hydrogen bonded chain structures built from strong N-H···X (X = F or O) interactions. For the first time, highly flexible composite devices have been prepared for the piezoelectric salts of TPAP·BF_4, DPDP·BF_4 and TIAP·BF_4 using thermoplastic polyurethane (TPU) as the matrix. The observed maximum peak to peak output voltages (V_{PP}) for the 10 wt % composite devices of TPAP·BF_4/TPU, DPDP·BF_4/TPU and TIAP·BF_4/TPU are found to be 7.37, 8.95 and 4.75 V, respectively. These composite devices exhibit excellent durability, cycling stability and viscoelastic properties. They also show the capacitor charging capabilities reaching their maximum charging points within 60 seconds (Figure 4).

Figure 4: *Organoamino phosphonium salts and their polymeric composite materials for mechanical energy harvesting applications.*

Chapter 5: Piezoelectric Energy Harvesting from a Ferroelectric Hybrid Salt $[Ph_3MeP]_4[Ni(NCS)_6]$ Embedded in a Polymer Matrix

Organic-inorganic hybrid ferroelectrics are an exciting class of molecular materials with promising applications in the area of energy and electronics. Herein, we report the synthesis, ferroelectric and piezoelectric energy harvesting behavior of a 3d metal ion-containing A_4BX_6 type organic-inorganic hybrid salt $[Ph_3MeP]_4[Ni(NCS)_6]$ (**1**) that crystallizes in the polar monoclinic space group *Cc*. The *P*-*E* hysteresis loop studies on **1** show a remnant ferroelectric polarization value of 18.71 μC cm^{-2}, at room temperature. Composite thermoplastic polyurethane (TPU) films with 5, 10, 15 and 20 weight percent (wt %) compositions of **1** were prepared and employed for piezoelectric energy harvesting applications. A maximum output voltage and current of 19.29 V and 14 μA have been observed for the 15 wt % **1**-TPU film. The output power- and current density values were computed to be 2.51 mW cm^{-3} and 3.59 μA cm^{-2}, respectively, for the 15 wt % **1**-TPU device, which is the highest known so far for any organic and organic-inorganic hybrid composite piezoelectric energy harvester fabricated from a non-piezoelectric polymer matrix. Further, the capacitor charging experiments on the 15 wt % **1**-TPU composite device shows an excellent energy storage performance with the highest stored energies and measured charges of 198.8 μJ and 600 μC, respectively (Figure 5).

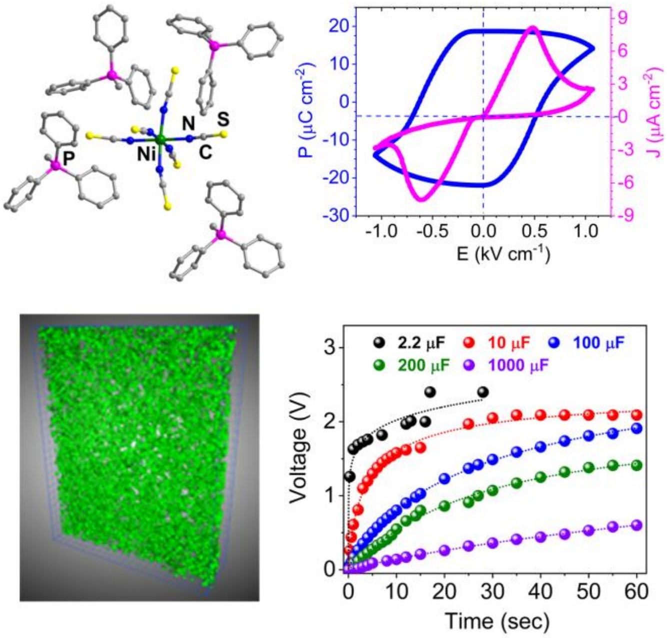

Figure 5: *View of the molecular structure, P-E hysteresis loop and its polymeric composites of **1** embedded in the TPU matrix.*

****

Abbreviations

Anal.	Analysis
Br_2	Liquid Bromine
Calcd.	Calculated
CIF	Crystallographic Information File
DSC	Differential Scanning Calorimetry
DTA	Differential Thermal Analysis
d_{33}	Piezoelectric Coefficient
E_c	Coercive Field
g_{33}	Piezoelectric Voltage Coefficient
ESI	Electron Spray Ionization
$FASnI_3$	Formamidinium Tin Iodide
FeRAM	Ferroelectric Random Access Memory
FT-IR	Fourier Transform Infrared Spectroscopy
Hz	Hertz
KDP	Potassium Dihydrogen Phosphate
LPG	Liquefied Petroleum Gas
MALDI-TOF	Matrix-Assisted Laser Desorption/Ionization – Time of Flight
MeCN	Acetonitrie
MEMS	Micro-electromechanical System
MeOH	Methanol
mg	Milligram
min	Minutes
ml	Milliliter
mm	Millimeter
mmol	Millimoles
M.P.	Melting Point
$NaNO_2$	Sodium Nitrite
NEMS	Nano-electromechanical System
NMR	Nuclear Magnetic Resonance
PDMS	Polydimethylsiloxane
PFM	Piezoresponse Force Microscopy
P_r	Remnant Polarization
P_s	Saturation Polarization
PVDF	Polyvinylidene difluoride
PXRD	Powder X-ray Diffraction
RAM	Random Access Memory
RT	Room Temperature
SCXRD	Single Crystal X-ray Diffraction
SEM	Scanning Electron Microscopy
T_c	Curie Temperature
TGA	Thermogravimetric Analysis
TGS	Triglycine Sulphate
TPU	Thermoplastic Polyurethane
ZnO	Zinc Oxide

Rights & Permissions

Chapter 2

Reprinted (adapted) with permission from “*Dalton. Trans.* **2019**, *48*, 7331-7336” © 2019 The Royal Society of Chemistry.

Chapter 3

Reprinted (adapted) with permission from “*Angew. Chem. Int. Ed.* **2018**, *57*, 9054–9058.” © 2018 Wiley-VCH Verlag GmbH & Co. KGaA, Weinheim.

Chapter 4

Reproduced with permission from “*Chem. Mater.* **2019**, *31*, 5864-5972” © 2019 American Chemical Society.

Chapter 5

Reprinted (adapted) with permission from “*Angew. Chem. Int. Ed.* **2020**, DOI: 10.1002/anie.202001250.” © 2020 Wiley-VCH Verlag GmbH & Co. KGaA, Weinheim.

Publications

Contributions Included in the Thesis:

1. A Flexible Composite Mechanical Energy Harvester from a Ferroelectric Organoamino Phosphonium Salt

   Thangavel Vijayakanth, Anant Kumar Srivastava, Farsa Ram, Priyangi Kulkarni, Kadhiravan Shanmuganathan, Balu Praveenkumar and Ramamoorthy Boomishankar

   Angew. Chem. Int. Ed. **2018**, *57*, 9054-9058.

2. Hydrogen-bonded Organo-amino Phosphonium Halides: Dielectric, Piezoelectric and Possible Ferroelectric Properties

   Thangavel Vijayakanth, Richa Pandey, Priyangi Kulkarni, Balu Praveenkumar, Dinesh Kabra and Ramamoorthy Boomishankar

   Dalton. Trans. **2019**, *48*, 7331-7336.

3. All-organic Composites of Ferro- and Piezoelectric Phosphonium Salts for Mechanical Energy Harvesting Application

   Thangavel Vijayakanth, Farsa Ram, Balu Praveenkumar, Kadhiravan Shanmuganathan and Ramamoorthy Boomishankar

   Chem. Mater. **2019**, *31*, 5964−5972.

4. Piezoelectric Energy Harvesting from a Ferroelectric Hybrid Salt $[Ph_3MeP]_4[Ni(NCS)_6]$ Embedded in a Polymer Matrix

   Thangavel Vijayakanth, Farsa Ram, Balu Praveenkumar, Kadhiravan Shanmuganathan and Ramamoorthy Boomishankar

   Angew. Chem. Int. Ed. **2020**, DOI: 10.1002/anie.202001250.

Contributions not included in the Thesis:

5. NHC-stabilized 1-hydrosilaimine: Synthesis, Structure and Reactivity

   Debabrata Dhara, **Thangavel Vijayakanth**, Milan Kr. Barman, Khevath Praveen Kumar Naik, Nicolas Chrysochos, Cem B. Yildiz, Ramamoorthy Boomishankar, Carola Schulzke, Vadapalli Chandrasekhar and Anukul Jana

   Chem. Comm. **2017**, *53,* 8592−8595.

6. Altering Polarization Attributes in Ferroelectric Metallo-Cavitands by Varying Hydrated Alkali-Metal Guest Cations

   Anant Kumar Srivastava, **Thangavel Vijayakanth**, Pillutla Divya, B. Praveenkumar, Alexander Steiner and Ramamoorthy Boomishankar

   J. Mater. Chem. C **2017**, *5*, 7352–7359.

7. Contrasting Reactivity of (boryl)(aryl)lithium-amide With Electrophiles: N- vs. p-aryl-C-nucleophilic Substitution

Debabrata Dhara, **Thangavel Vijayakanth**, Mithilesh Kumar Nayak, Pankaj Kalita, Ramamoorthy Boomishankar, Cem Burak Yildiz, Vadapalli Chandrasekhar and Anukul Jana

Dalton. Trans. **2018**, *47,* 14411-14415.

8. Stereochemically Distinct Cyclotetrasiloxanes Containing 3-Pyridyl Moieties and Their Functional Coordination Polymers

   Mahesh S. Deshmukh, **Thangavel Vijayakanth** and Ramamoorthy Boomishankar

   Inorg. Chem. **2016**, *55,* 3098−3104.

9. Tetraanilino Phosphonium Dihydrogen Phosphate: A Hydrogen-bonded Ferroelectric Organic Salt Exhibiting High Polarization at Room Temperature

   Anant Kumar Srivastava, **Thangavel Vijayakanth**, Pillutla Divya, B. Praveenkumar and Ramamoorthy Boomishankar

   (*Manuscript under preparation)*

10. Investigation of the Ultra-Low Dielectric Constant in a Hydrogen-bonded Tetraanilino Phosphonium Trimesate Salt

    Anant Kumar Srivastava, **Thangavel Vijayakanth**, Pillutla Divya, B. Praveenkumar and Ramamoorthy Boomishankar

    (*Manuscript under preparation*)

11. Nanocellulose Reinforced Flexible Composite Nanogenerators with Enhanced Vibrational Energy Harvesting and Sensing Properties
    Farsa Ram, Aniket Gudadhe, **Thangavel Vijayakanth**, Swapnil Aherrao, Vivek Borkar, Ramamoorthy Boomishankar and Kadhiravan Shanmuganathan
    (*Manuscript submitted*)

12. Hybrid Organic-Inorganic Pseudohalogenometallate Polymer Composites for Piezoelectric Energy Harvesting Application
    Thangavel Vijayakanth, Farsa Ram, Balu Praveenkumar, Kadhiravan Shanmuganathan and Ramamoorthy Boomishankar
    (*Manuscript under preparation*)

Chapter 1

Introduction

1.1 Introduction to piezo and ferroelectric materials for mechanical energy harvesting applications

The multifunctional behavior of organic and organic-inorganic hybrid materials has spread out into various interdisciplinary fields of covering chemistry, physics and materials science.[1-3] Recently, materials exhibiting piezoelectric, ferroelectric, and multiferroic properties are of great interest due to their utility in molecular electronics, non-linear optical devices, biomaterials, photovoltaics and energy harvesting applications.[4-7] The structure-property relationships play a vital role in determining pyroelectric and the ferroelectric nature of these materials. Ferroelectrics are the special class of dielectric substances in which the spontaneous electrical polarization can be reversed or re-aligned by the application of an external electric field.[8] The first examples of ferroelectric materials are derived from the hydrogen-bonded systems such as sodium potassium tartrate tetrahydrate (Rochelle salt, $NaKC_4H_4O_6 \cdot 4H_2O$) and potassium dihydrogen phosphate (KDP, KH_2PO_4). After that, numerous families of non-hydrogen bonded inorganic ceramic oxide materials have been investigated for their excellent ferroelectric polarization properties.[9-11] Supramolecular ferroelectric materials derived from small molecule-based organic and organic-inorganic hybrid ferroelectrics have been attracted and given much attention because of their facile solution-phase synthesis, lightweight, flexibility, high thermal stability, high remnant polarization and reasonable Curie temperature.[12-15] In addition to their extensive applications in high-tech devices for ferroelectric random access memory, ultrasound imaging, capacitor, actuator, transistor, sensor, photovoltaics, more recently, they have lately been explored as potential thermoelectric and piezoelectric energy harvesters.[16-21] Nature endows an abundant supply of sustainable and renewable energy resources such as wind, wave, biomass, thermal and mechanical energies to meet the increasing global demands of modern-day life.[22-26] Among various energy harvesting approaches, the high abundance of mechanical energy is quite natural and can be accessed when a suitable material is subjected to external pressure, bending, folding and stretching motions of human body activities.[27-31] The electromechanical response (conversion of mechanical energy into electrical energy) is normally generated via the triboelectric, piezoelectric, pyroelectric, or ferroelectric properties of materials.[32-36] The first exciting development of a nanogenerator was discovered by Wang and co-workers based on zinc oxide nanowires (ZnO) in 2006.[37] Inspired with this discovery, several materials such as perovskite-type inorganic ceramic oxides, polyvinylidene difluoride (PVDF) and its copolymers and composites of various types encompassing these materials have been examined for piezoelectric energy harvesting applications.[38-40] However, the use of traditional inorganic ceramic oxide materials possesses certain limitations such as high-temperature fabrication techniques, longer processing times, high molecular weight, tedious poling procedures and importantly, the presence of toxic heavy-metal contents pose serious environmental hazards that preclude their use in wearable electronics.[41-43] Moreover, the active piezo- and ferroelectric form of PVDF based materials require additional processes such as melt quenching, mechanical stretching, the addition of external binders, ultra-high cooling, high-temperature annealing and high-voltage poling procedures.[44-46] In this context, it is desirable to prepare polar ferroelectric materials containing heavy metal-free and non-ceramic energy harvester for mechanical energy harvesting applications.

The outline of this thesis demonstrates the synthesis and characterization of low-symmetric piezo and ferroelectric materials derived from organic and organic-inorganic hybrid salts embedded in polymeric composite materials for piezoelectric energy harvesting applications. This introductory chapter provides an insight into the concept and background of various types of dielectric materials with para, piezo, pyro and ferroelectric properties. It provides a key literature on some new examples of piezo and ferroelectric materials made up of organic and organic-inorganic hybrid compounds and literatures pertaining to the important examples of composite mechanical energy harvesters based on ferro- and piezoelectric materials.

1.2 Dielectric materials

Dielectric substances are electrically insulating or an inferior conductor of electric currents. When dielectric materials are subjected to the electric field, generally, no electric current flows inside the materials, unlike conducting metals. The electric polarization occurs when positive and negative electric charges move towards and opposite directions of the applied electric field. From the macroscopic point of view, the induced amount of positive and negative charges on either side of the plates is the same.[47]

Nevertheless, microscopically, these induced electric charges such as atom nuclei, electrons and ions cannot move freely because of the Coulombic force of attraction when they are displaced from their equilibrium positions. This charge separation process is known as polarization. These materials are generally classified into two types a) linear and b) non-linear dielectrics. In linear dielectric materials, the dielectric polarization of the system is directly related to the applied electric field, whereas, in the case of non-linear dielectrics, the relationship is exactly opposite to each other. Even in the absence of electric field, a non-linear dielectric material can retain their electric polarization which allows them to be utilized in various components such as dielectric capacitors, dielectric resonators, transducers, transformers, radiofrequency transmission lines, power cables, and gate dielectrics.[48]

The Neumann’s principle provides the insightful information about the relationship between the molecules and their physical properties, in which the non-linear dielectric properties of the materials depends on their symmetry elements and the crystal symmetries of the molecular systems.[10] The space group of any system in three dimensions can be constructed with the combinations of 32 crystallographic point groups and 14 Bravais lattice which belong to the 7 crystal lattice systems. Among 32 crystallographic point groups, 21 (except *432*) of them correspond to non-centrosymmetric (no spatial inversion) classes and 11 belong to centrosymmetric (inversion center) classes.[13] The piezoelectric polarization (in which the mechanical force induces the polarization) of the non-linear dielectric material were found themselves within the 20 point groups. Of these 20 point groups, 10 of them displays a unique polar axis and are the subgroup classes of piezoelectric materials that exhibit both pyroelectricity (in which thermal changes induces the polarization) and ferroelectricity (in which polarization is reversed by the application of an electric field). In general, primarily being a dielectric, all the subgroups of ferroelectric is pyroelectric as well as piezoelectric, but the reverse is not true. Thus the non-linear nature of certain dielectrics is crystallographically classified into three main types such as a) Piezoelectric, b) Pyroelectric and c) Ferroelectric materials (Figure 1.1).

1.2.1 Piezo, pyro and ferroelectricity

Piezoelectricity is the generation of electric charges when a suitable material is subjected to an applied stress or mechanical force, which results in electric polarization. The first piezoelectricity effect was demonstrated more than 100 years ago on a single crystal of Rochelle salt by Curie brothers (Pierre and Jacques Curie). This electromechanical effect arises from the linear relationship between the mechanical force and the applied electric field of a crystalline material with a lack of inversion centrosymmetry.[49]

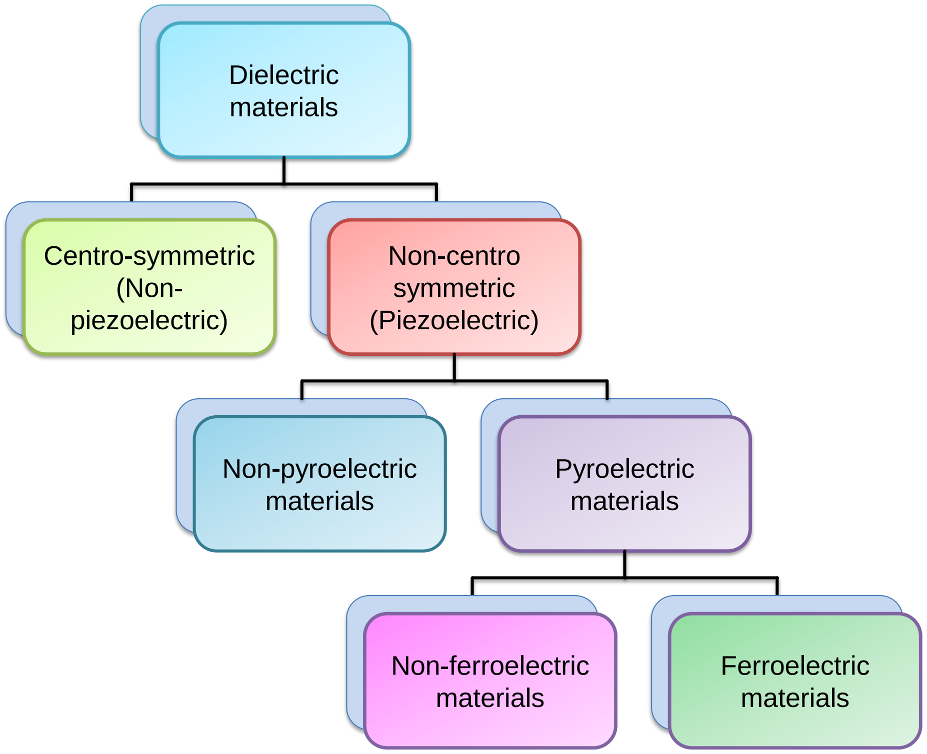

Figure 1.1: *Classifications of dielectric materials.*

The electromechanical effect of materials is majorly classified into two types a) direct piezoelectric effect and b) converse or reverse piezoelectric effect. The piezoelectric charge constant or coefficient (d) is the polarization changes per unit of applied mechanical stress (direct piezoelectric effect) or the mechanical strain experienced by the nonlinear material per unit of an applied electric field (converse piezoelectric effect). These materials can be characterized by various piezoelectric coefficients such as d_{31}, d_{32} and d_{33}, respectively.[49,50] The double subscripts are used to describe the direction of different quantities, such as applied force and the generation of electrical charges on the piezoelectric material. The first and second subscript adjacent to (d) denotes the electric polarization and applied electric field, respectively. The magnitude of the piezoelectric coefficients are denoted by the units pC N^{-1} (direct piezoelectric effect) and pm N^{-1} (converse piezoelectric effect), respectively. The generated direct piezoelectric charges are measured by employing the Berlin court method with a dynamical mechanical force setup made up of commercial piezo-meter. The utility of these materials can be realized in numerous real-life applications such as piezoelectric sensors and actuators, piezo-motor, LPG stove lighter, transformer, detection of sonar waves and most importantly they have been used in energy conversions as piezoelectric energy harvesters.[50-52]

Pyroelectricity is the phenomenon of crystalline polar point group substances (1, 2, m, mm2, 3, 3m, 4, 4mm, 6, 6mm) which generates the electric polarization under certain thermal conditions either by heating or cooling. The change in temperature modifies their atomic spatial position (polarization) and produces a transient voltage across the crystal lattice. Pyroelectricity mostly occurs in every piezoelectric material and hence they are found to be useful in thermal and gas sensing devices, infrared sensors, pyroelectric sensors, thermistors, detectors, pyrometers and pyroelectric energy harvesters.[53-55]

Ferroelectrics are the distinct class of dielectric substances, in which the spontaneous electrical polarization can be reversed or reoriented by the external applied electric field. Ferroelectrics are a subgroup of piezo and pyroelectric materials and are shown by the substances with the 10 polar point group (C_1, C_S, C_2, C_{2v}, C_3, C_{3v}, C_4, C_{4v}, C_6, *and* C_6v) symmetries. These polar substances can switch their polarization direction when they are subjected to an applied electric field which forms a typical curve known as a *P-E* hysteresis loop. In the *P-E* hysteresis loop, at the initial point (O), the numbers of positive and negative domains are distributed equally so that the net polarization will be zero (Figure 1.2). When the intensity of electric field increases in the positive directions (OAB), the maximum number of dipoles get aligned in the direction of an applied electric field (C), which is otherwise known as saturation polarization ($P_{s,}$ OI). The reversal of the electric field in the opposite directions at zero points (I) still shows some quantity of polarization known as remnant polarization ($P_{r,}$ OD or OG). The amount of electric field required to bring back remnant polarization zero is known as a coercive field ($E_{c,}$ OE or OH) of any non-linear materials. Further, extension of the electric field strength in the opposite direction can bring all the switchable negative domains into aligning in the negative polarity of an electric field (FE). In this way, the hysteresis loop is formed for the polar acentric materials that exhibit ferroelectricity.[4,8]

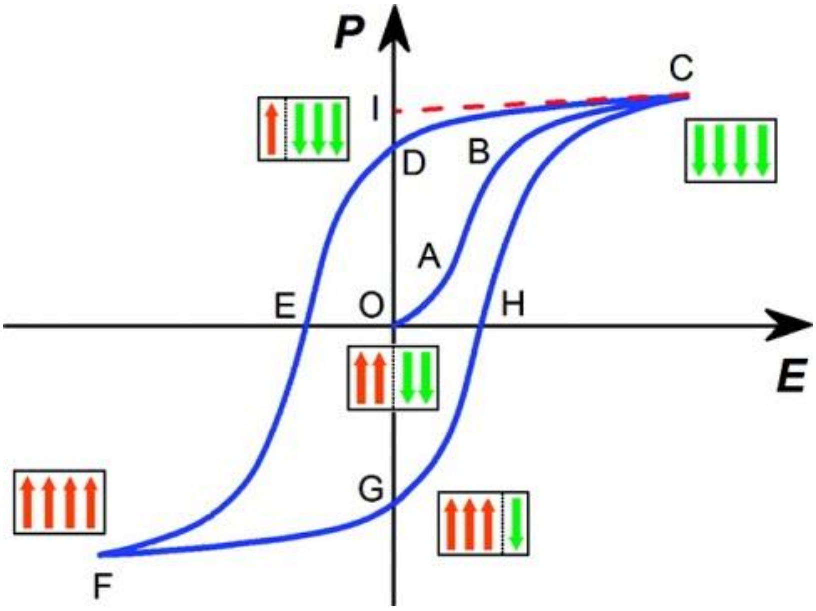

Figure 1.2: *The relationship between polarization (P) and electric field (E) hysteresis loop.* (Adapted with permission from ref. 4. Copyright © 2012 American Chemical Society.

The degree of polar arrangements present in ferroelectric materials can be disturbed with the increasing amount of temperature gradients. The non-linear dielectric (ferroelectric) becomes linear dielectric (paraelectric) material, above a specific temperature known as Curie temperature (T_c). These structural phase changes can be mainly classified into two types, such as first-order and second-order transition depending on several factors such as Gibbs free energy, temperature and pressure. The distortion in a polar arrangement leads to the occurrence of structural phase transitions from a high symmetry, high-temperature (paraelectric phase) to the ordered arrangement of low symmetry, low-temperature (ferroelectric phase).[56] These phase changes can alter diverse characteristics such as crystal structure symmetry, thermal behavior and electrical properties. In general, these structural fluctuations in the phase transitions can be identified by performing various characterization techniques, for instance, thermal analysis, single crystal and powder diffraction analysis, *P-E* hysteresis loop, temperature and field-dependent dielectric constant measurements and spectroscopic measurements such as second harmonic generation.[57]

1.3 Earlier history and broad classifications of ferroelectric materials

The earlier discovery of ferroelectric materials has been focused to the hydrogen-bonded assemblies of Rochelle salt (sodium potassium tartrate tetrahydrate, $NaKC_4H_4O_6{\cdot}4H_2O$), potassium dihydrogen phosphate (KH_2PO_4, KDP) and Triglycine sulfate $[(NH_2CH_2COOH)_3{\cdot}H_2SO_4]$ (TGS).[9,58-59] However, all these salts have many disadvantages, such as instability, poor mechanical strength, the complexity of structural factors, low ferroelectric polarization and below room-temperature Curie temperature, etc. After that, numerous families of perovskite structured inorganic ceramic oxides having the general formula of ABX_3 type (where A is monovalent cation, B is divalent transition metal ion and X = oxygen anion) have been noticed for their Ferroelectricity and structural stability in a wide range of temperatures. The perovskite materials of barium titanate ($BaTiO_3$), lead titanate ($PbTiO_3$), lithium niobate ($LiNbO_3$), potassium niobate ($KNbO_3$) and lead zirconate titanate ($PbZrTiO_3$), etc., were shown to exhibit excellent properties such as air-stable, water-insoluble, high spontaneous polarization, fatigue-free, high piezoelectric coefficient value and high Curie temperature.[60-61] Thus, these ferroelectric materials are employed as non-volatile memory devices, magnetic field detectors, storage devices, capacitors, piezoelectric sensors, photovoltaic devices, field-effect transistors and recently in the domain of mechanical energy harvesters.[62-63] Despite having excellent physical and chemical properties, obtaining these materials require high-temperature synthesis, high-temperature sintering and high-voltage poling. Moreover, the presence of rigid and toxic heavier metal contents poses a serious environmental hazard which further hampers them to be used in wearable and flexible electronics.[64-65]

In search of new ferroelectric materials, enormous attention has been given to several non-ceramic and heavy metal-free ferroelectric compounds. In this regard, polyvinylidene difluoride and its copolymers were shown to display excellent piezo and ferroelectric polarization among all the known polymers.[4,66-68] However, these materials require higher coercive field and mechanical deformations to obtain a ferroelectric β phase to align its polymeric chains along the direction of the applied electric field. Alternatively, low molecular weight based organic and organic-inorganic hybrids ferroelectric materials have been attracted dramatically due to their facile solution synthesis, lightweight, flexibility, thermal stability, low coercive field, notable ferroelectric polarization and Curie temperature. Recently, these ferroelectric materials embedded polymeric composites have been witnessed for excellent energy harvesting applications in the domain of flexible molecular electronics.[20, 69]

Ferroelectrics are generally categorized into three main types, such as inorganic, organic and organic-inorganic hybrid materials, respectively. The current section provides some vision into each type of ferroelectric material and its sub-classifications.

1.4 Inorganic ferroelectric materials

Inorganic ceramic oxides [$BaTiO_3$, ($Pb(Zr, Ti)O_3$) and $LiNbO_3$] are the first examples known for the non-hydrogen bonded ferroelectrics after the earlier discovery of hydrogen-bonded ferroelectric material such as KDP.[4,9] These compounds do not have any polar ions in their crystal structures. However, the reason for the formation of polar arrangement in these solids might be attributed to the relative displacement of ions from their atomic positions. It should be noted that these ceramic materials show high remnant polarization and Curie temperatures in a wide range of temperatures. However, the presence of heavy metal and/or toxic element contents precludes their use in wearable electronics. Another example of inorganic ferroelectric material is sodium nitrite ($NaNO_2$), in which the intrinsic permanent dipoles or the reorientation of dipolar NO_2^- ions create the ferroelectric polarization.[4,70] The other well-known hydrogen-bonded inorganic ferroelectric material was discovered in KDP (KH_2PO_4), which shows the spontaneous polarization at very low Curie temperature (P_s = 4.8 μC cm^{-2}, T_c = 123 K). Hence, the search for alternate choice of ferroelectric materials for high technological applications has been intensified over the past two decades.[4,9]

1.5 Organic ferroelectric materials

Organic ferroelectric materials display many additional advantages than inorganic ferroelectric materials in many ways, such as facile synthesis, lightweight, mechanical flexibility, non-toxic elements, etc. Notably, these materials are fascinating to be used as a flexible substrate for molecular organic electronics and electro-optic applications.[11,71-72] They are mainly subdivided into two categories such as single component and organic binary salts ferroelectric materials. In this regard, the current section is mainly focused on ferroelectric materials derived from single-component organic, organic binary salt and charge-transfer materials.

1.5.1 Single component organic ferroelectric materials

The first example of a single component, low molecular mass ferroelectric material to be discovered is Thiourea by A. L. Solomon, in 1956.[73] The multifunctional behavior (piezo, pyro and ferroelectric) of thiourea was observed below room temperature. It shows an excellent ferroelectric polarization (P_s ~ 3.2 μC cm^{-2}) at low Curie temperature (T_c ~ 120 K). Later on, several of *SCOFM* were reported based on TEMPO, (2,2,6,6-tetramethyl-1-piperidinyloxy), Benzil, DNP (diacetylene-1,6-bis(2,4-dinitrophenoxy)-2,4-hexadiyne), CDA (cyclohexane-1,1-diacetic acid), TCAA (trichloro acetamide), etc. which were shown to exhibit ferroelectric behavior near room temperature or above.[11,74-78] However, reports on a single component organic ferroelectric materials with high spontaneous polarization and Curie temperature are rare in the literature.

In 2010, Yoshinori Tokura et al. reported the above room temperature ferroelectric behavior on croconic acid (4,5-dihydroxy-4-cyclopentene-1,2,3-trione, $H_2C_5O_5$) molecular crystals.[75,78] A derivative of other families of cyclic oxocarbon acid systems (except for croconic acid) was shown to crystallize in centrosymmetric space groups.[75,79-80] In croconic acid, each pentagonal ring of the carbon atoms was connected through the oxygen and hydroxyl groups which involve in cooperative proton tautomerism mechanism (Figure 1.3a). The ferroelectricity of this molecule is created via proton migration through a polarizable pi-conjugated bond. The observed spontaneous polarization for the 2D hydrogen-bonded polar sheet was found to be high at ~ 21 μC cm^{-2} as compared to other known single-component molecular ferroelectric materials. Most interestingly, this compound does not show any Curie temperature up to 400 K, which is unusual in most of the reported molecular ferroelectric materials.[75,78]

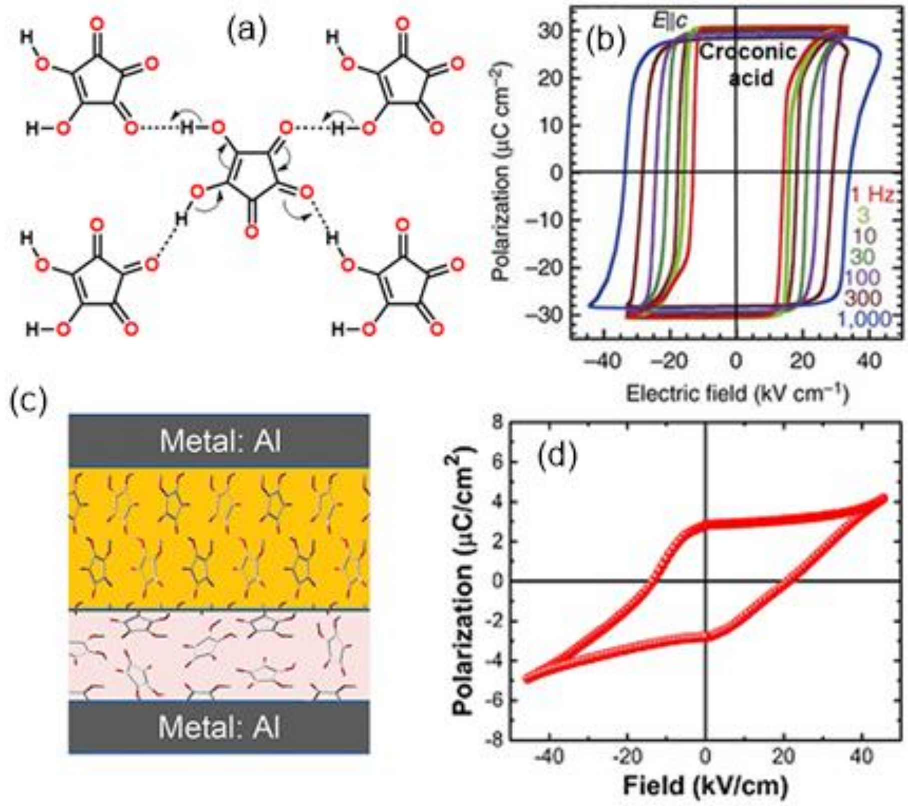

Figure 1.3: *(a) Proton tautomerism in croconic acid. (b) Ferroelectric hysteresis loop for a single crystal of croconic acid. (c) The schematic view of the uniaxial croconic acid devices (500 < d < 2100 nm) with Al electrodes depicting a double-layer system with different crystalline orientations. (d) The polarization-voltage hysteresis loop of the device based on the thin film of croconic acid (with thickness ~ 2 mm) after applying a bias of 20 V.* (Adapted with permission from ref. 78. Copyright © 2017 The Author(s) of Publication and ref. 81. Copyright © 2018 WILEY-VCH Verlag GmbH & Co. KGaA, Weinheim.

Recently, the same research group has been demonstrated the improved ferroelectric polarization (P_S ~ 30 μC cm^{-2}) based on a single crystal of croconic acid (Figure 1.3b).[78] Despite showing excellent ferroelectric performances over other single component organic ferroelectric materials, it shows instability and corrosive nature even at ambient conditions which further limits its utility in organic electronics applications. However, owing to the uniaxial nature of croconic acid ferroelectric polarization (with only two opposite polarization directions along the polar c-axis), thin-films of croconic acid are expected to yield a reduced or zero effective remnant polarization for its randomly-oriented crystallites.

In this effort, Hu et al. have demonstrated ferroelectricity in croconic acid films deposited on various substrates by thermal evaporation and showed its potential to function as a memory device.[81] The as-grown thick films (>500 nm) adopt the preferred crystalline orientation (Figure 1.3c), required for the polarization, as the cross-sectional scanning electron microscope (SEM) images of the film show the rod-like crystallites that lie perpendicular to the substrate. Further, the piezoresponse force microscopy (PFM), current density-voltage (J-V) and polarization-voltage (P-V) measurements on the devices, under air (with some moderate relative humidity) gave a higher polarization in comparison with the measurements performed under vacuum. This observation suggests that the space charges, induced by moisture and the charge injection/trapping near the electrodes, are seemingly responsible for achieving stable ferroelectric polarization. The devices made up of croconic acid films exhibit the polarization values ranging from 3-30 μC cm^{-2} and coercive fields of 13-30 kV cm^{-1}, depending on the thickness of the film which is comparable with the values obtained for its single crystals (Figure 1.3d). Also, the obtained devices can operate at low operational voltages (<5 V) as well.[81]

The trisubstituted haloimodazoles and halogenated 2-methylimidazoles also exhibit ferroelectricity which is further mediated by the formation of N-H···N linear chains involved in a hydrogen-bonded structure.[82] They are naturally distorted crystals which crystallize in non-centrosymmetric lattices, where weak halogen bonding imposes imbalanced packing forces in the lattice that are responsible for the curved morphology of their crystals. The detailed crystallographic analysis revealed that these systems possess highly anisotropic intermolecular interactions and signs of plastic crystal phases. Further, the piezoresponse hysteresis loop measurements indicated switchable polarization characteristics at room temperature, which supports piezoelectricity & ferroelectricity in some of these systems. Individually, the trisubstituted haloimidazoles and halogenated 2-methylimidazoles exhibit weak ferroelectric/piezoelectric response. However, mixed crystals grown from a combination of halogenated 2-methylimidazoles and trisubstituted haloimidazoles results in a disrupted halogen bond network, which in turn improves the ferroelectric and piezoelectric properties. The coupled electrical and mechanical properties of such systems can be employed further for the development of flexible devices.

1.5.2 Binary organic ferroelectric materials

This section typically deals with the recent exciting reports pertaining to the binary organic ferroelectric salts. There have been several research activities based on organic binary salts that are explored for piezo and ferroelectric properties.

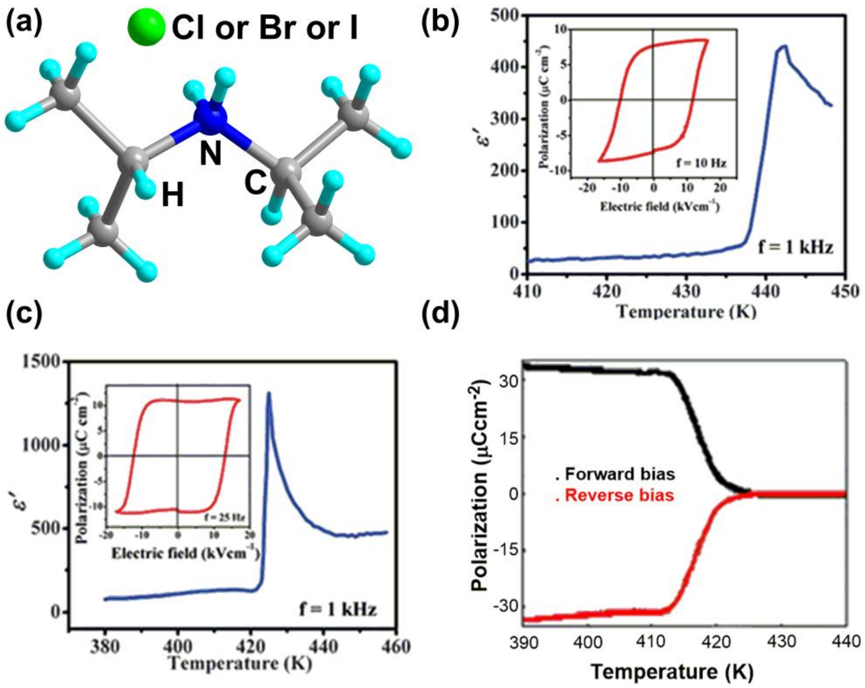

Figure 1.4: *(a) The molecular structure of the halide salts of DIPA cation. Temperature-dependence of the dielectric constant for DIPAC (b) and DIPAB (c) crystals along b-axis. Insets: The respective P-E hysteresis loops. (d) The temperature-dependent pyroelectric measurement of DIPAI.* Adapted with permission from ref. 13. Copyright © 2016 The Royal Society of Chemistry and ref. 85. Copyright © 2017 AIP Publishing.

Recently, the systematic investigation of new molecular ferroelectric materials has been discovered in simple molecular crystals of diisopropyl ammonium halides (DIPAH, here H = Cl, Br, I).[83-85] All these three derivatives, such as diisopropyl ammonium chloride (DIPAC), diisopropyl ammonium bromide (DIPAB) and diisopropyl ammonium iodide (DIPAI) show the ordered and disordered structure of ammonium cations at the respective low and high-temperature phases which are responsible for the observation of ferroelectric behavior in these systems. Among all, the increasing trend of ferroelectric polarization DIPAC, DIPAB and DIPAI are found to be $P_S \sim 8.9, 23, 33\ \mu\mathrm{C\ cm^{-2}}$, respectively (Figure 1.4). The increasing trend of ferroelectric polarization DIPAC< DIPAB <DIPAI, indicates the larger atomic size and higher dipole moment strength of DIPAI salt. These results are comparable to that of many traditional inorganic ceramic oxides and ferroelectric polymers.[4,11]

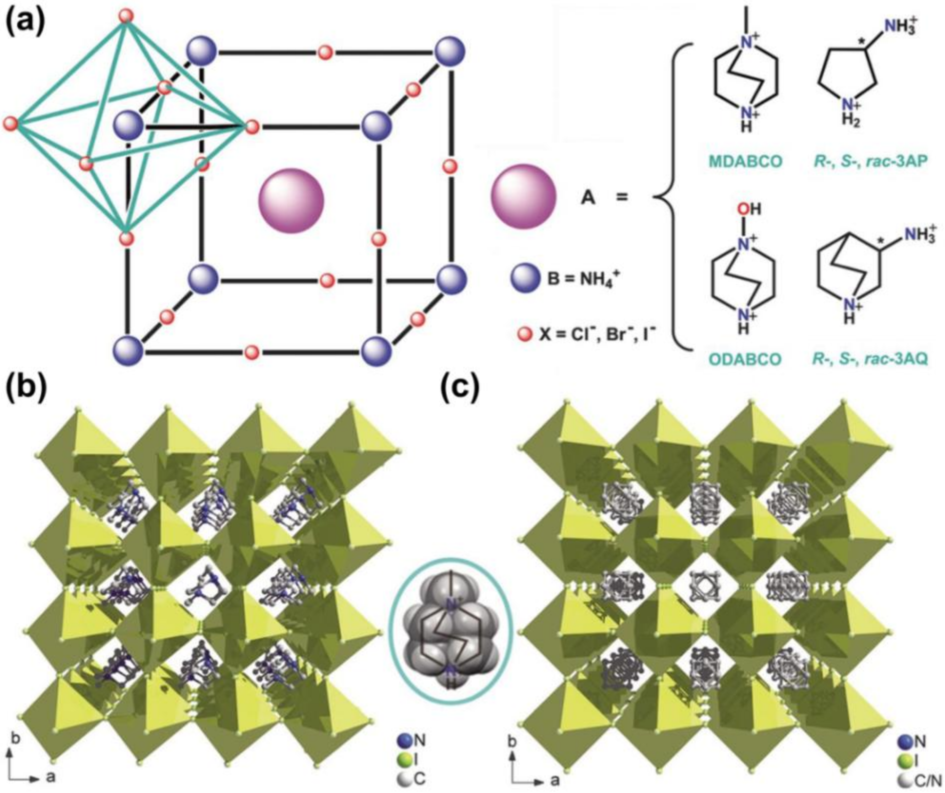

Figure 1.5: *(a) The chemical structures of 3D-metal free ferroelectric perovskite. (b) and (c) crystal packing diagrams of MDABCO-NH_4I_3 in the ferroelectric (293 K) and paraelectric phase (463 K).* Adapted with permission from ref. 86. Copyright © 2018 The American Association for the Advancement of Science.

More recently (in 2018), for the first time, metal-free three dimensional perovskite structured organic ferroelectric materials have been reported by Xiong and co-workers (Figure 1.5).[86] These organic metal-free perovskites have the general formula of ABX_3 (A = organic divalent cation, B = organic monovalent cation and X = halide anions) were synthesized by the use of MDABCO (N-methyl-N'-diazabicyclo[2.2.2]octonium)–ammonium triiodide salt at room temperature. The 3D-perovskite structures were formed by the corner-sharing of $(NH_4)X_6$ (X is Cl, Br, or I) octahedra which enclose the overall framework and the organic ammonium cations are positioned in the middle of the cavities. The forces of attraction between the host and guest frameworks are held together by the ionic and hydrogen-bonded interactions. The X-ray single crystal analysis of MDABCO-NH_4I_3 was shown to crystallize at ferroelectric (293 K) and paraelectric (463 K) phases in the space groups of trigonal $R3$ and cubic $P432$, respectively. The single crystals of MDABCO-NH_4I_3 show an excellent piezo and ferroelectric polarization. Further, the observed ferroelectric polarization can be validated from performing the pyroelectric current measurements which gave the P_S value of ~ 22 μC cm^{-2} along the crystallographic [111] plane. These results are relatively comparable to that of inorganic ceramic perovskite materials and promise the potential of these compounds as an alternative choice of materials for flexible electronic device applications.

1.6 Organic-inorganic hybrid ferroelectric materials

The design innovative of materials based on crystal engineering of distinct organic and inorganic counterparts together has led to the development of novel ferroelectric systems.[2,10,87-88] These hybrid classes of compounds can impart close proximity between the organic and inorganic components via various covalent, non-covalent and ionic interactions. Known examples of hybrid organic-inorganic materials are shown to exist in several compositions such as ABX_3, A_2BX_4, A_3BX_6 and A_4BX_6 (where A is the monovalent organic cation, B is the transition metal ion and X = Cl^-, Br^-, I^-, $HCOO^-$, CN^-, SCN^-, NCS^-, N_3^- and $N(CN)_2^-$, etc.).[89-90] However, most of them, barring a few examples of metal-formates and metallohalogenates, tend to crystallize in the centrosymmetric space groups that are incompatible for piezoelectric, pyroelectric, or ferroelectric properties.[91] Depending on the nature of organic and inorganic counterparts, these hybrid materials can tend to form various types of frameworks starting form 1D, 2D and 3D or 0D discrete type of structure. This section provides some key examples of the recent reports pertaining to organic-inorganic hybrid ferroelectric materials supported by organic (especially those of ammonium or phosphonium) cations.

1.6.1 Metallohalide ferroelectric materials

Perovskite metallohalides, belonging to the organo-halogenometallate family are well known for their application as light-harvesting layers in solar cells; however, recent research is focused on their ferroelectric behavior as well. Ferroelectricity in many organo-halogenometallates has been discovered.[10,56,91]

Recently, Junhua Luo and co-workers reported an unusual two-dimensional multi-layered ferroelectric perovskite framework $[(C_4H_9NH_3)_2(CH_3NH_3)_2][PbBr_{10}]$ (Figure 1.6).[92] This compound has an evident phase change from ferroelectric to paraelectric polarization at T_C = 315 K. Further, the appearance of ferroelectricity was validated from *P-E* hysteresis loop measurement which shows a P_S value of 2.9 μC cm^{-2} and a coercive field of 16 kV cm^{-1}. The crystal wafer of this 2D perovskite was employed to fabricate stable photodetectors with extremely low dark current with a high response rate and large on/off current ratio on a single functional layer. These results signify their use in various applications such as photoferroelectric properties, multiferroics, and high-performance optoelectronic devices.

However, it is still challenging to find an alternate source for lead-free perovskite frameworks. Recent reports based on lead-free hybrid ferroelectric materials such as (N-methylpyrrolidinium)$_3$Sb$_2$Br$_9$ shows a large P_s and P_r values of 7.6 μCcm^{-2}, 7.3 μCcm^{-2}, respectively. The discrete nature of this perovskite-like compound was due to the distorted nature of its $SbBr_6$ octahedra. Also, a band-gap value of 2.76 eV has been observed for this compound, demonstrating its semiconducting behaviour.[93]

In an exciting finding, Xiong and co-workers have revealed above-room-temperature ferroelectricity in the semiconducting organic-inorganic hybrid material (2-(ammoniomethyl)pyridinium)SbI$_5$.[94] This compound shows a Curie temperature (T_c) of 360 K. The ferroelectric phase exhibits a sizeable spontaneous polarization (P_s ~ 4 μC cm^{-2}) and low coercive field (E_c ~ 9 kV cm^{-1}). Also, it displays a small bandgap of 2.03 eV with a strong absorption ability that is much smaller than that for $BiFeO_3$ (2.7 eV) and lead-halide perovskite ferroelectrics (2.7-3.65 eV). These properties promise its applications in high-performance ferroelectric optoelectronic and photovoltaic devices.

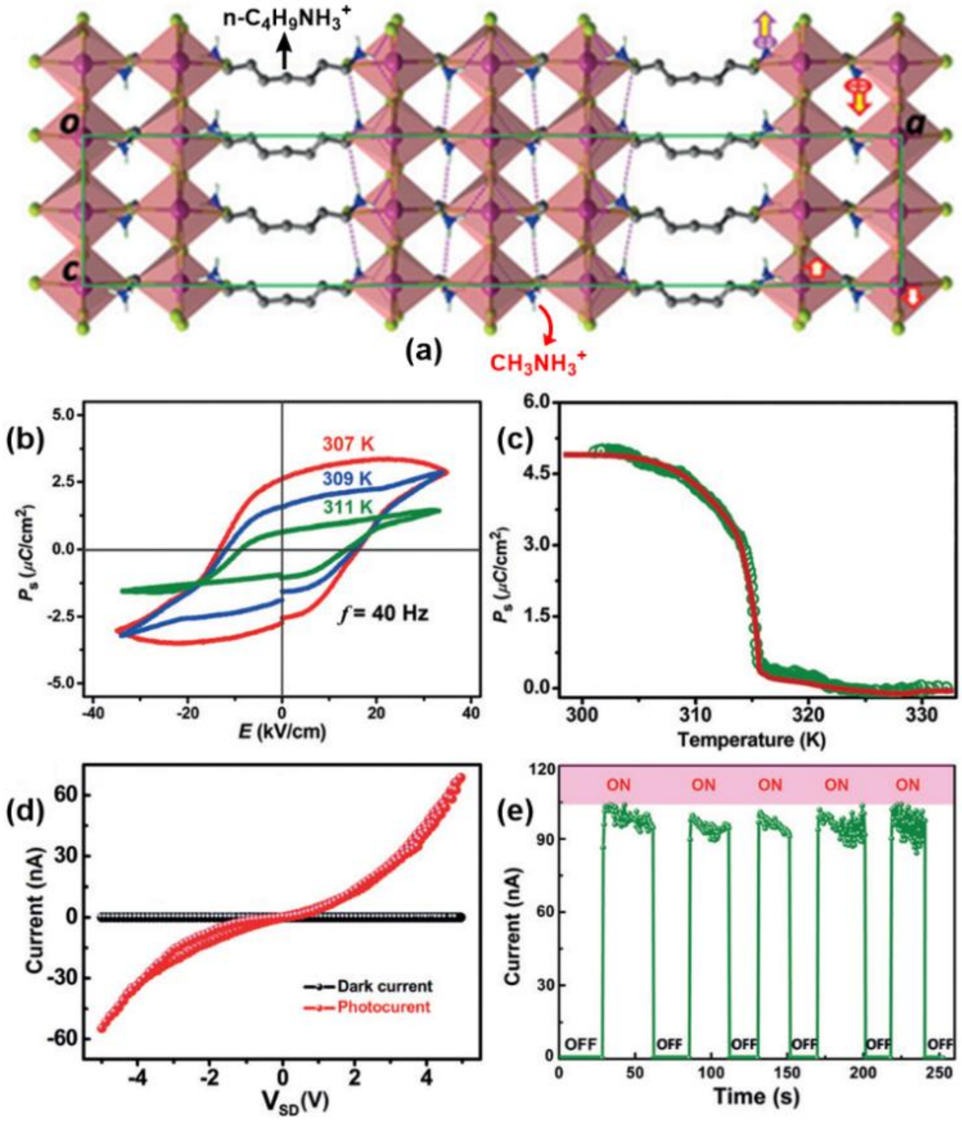

Figure 1.6: *(a) Packing structure of $[(C_4H_9NH_3)_2(CH_3NH_3)_2][PbBr_{10}]$ along b-axis at 293 K, (b) its ferroelectric hysteresis loops at various temperatures and (c) the temperature dependence of its spontaneous polarization obtained by the pyroelectric measurements. (d) The on/off ratio of photocurrent to dark current (λ=420 nm). (e) The recyclable switching operation of photocurrent response, showing no obvious reduction in long-time illumination.* Adapted with permission from ref. 92. Copyright © 2017 WILEY-VCH Verlag GmbH & Co. KGaA, Weinheim.

New examples of lead-free ferroelectric organic-inorganic hybrid materials based on *Trimethylchloromethylammonium (TMCM)* and *Trimethylbromomethylammonium (TMBM)* cations such as [TMCM][$MnCl_3$], [TMCM][$CdCl_3$] and [TMBM][$MnBr_3$] have been synthesized by the same group (Figure 1.7)[95-97] All three compounds exhibit high T_C values (more than 400K). These perovskite hybrids are isostructural and exhibit multiaxial polarization (twelve-fold polarization directions) derived from the transition from LT monoclinic (*Cc*) phase to HT paraelectric phase with hexagonal (*P6₃/mmc*) symmetry.

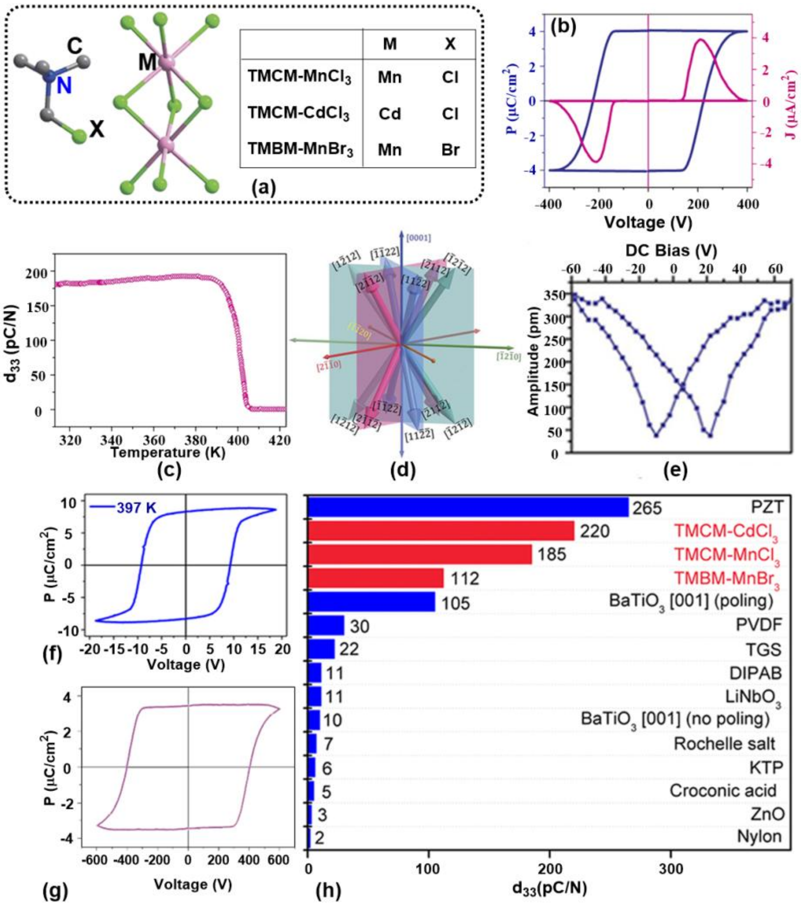

Figure 1.7: *(a) A family halogenometallate perovskites derived from [TMCM]+ and [TMBM]+ cations. (b) Ferroelectric hysteresis loop and the corresponding leakage current density plot for [TMCM][$MnCl_3$]. The ferroelectric hysteresis loops for (c) [TMCM][$CdCl_3$] and (d) [TMBM][$MnBr_3$]. (e) A comparison chart of measured d_{33} values for these new halogenometallates and certain well-known piezoelectric materials.* Adapted with permission from ref. 95. Copyright © 2017 The American Association for the Advancement of Science and ref. 96. Copyright © 2017 American Chemical Society.

Interestingly, the in-plane and out-of-plane high-resolution piezo-response force microscopy (HR-PFM) investigations on [(TMCM)MnCl$_3$] established the presence of twelve unique polarization vectors by averaging of its phase and amplitude images.[95] More importantly, along with ferroelectricity, large piezoelectric response (d$_{33}$) values have been observed for these hybrid salts; 185 pC N^{-1} for [(TMCM)MnCl$_3$], 220 pC N^{-1} for [(TMCM)CdCl$_3$] and 112 pC N^{-1} for [(TMBM)MnBr$_3$].[95-97] The multiple polarization directions explain the origin of excellent electromechanical conversion and strong spontaneous polarization in all three compounds. The observed d$_{33}$ values are comparable with the best performing piezoceramics, much higher than that of BTO and slightly lower than that of PZT, promising their utility in future piezo-devices. In another attempt, the same group has developed another molecular ferroelectric salt [(TMCM)CdBr$_3$] that shows uniaxial polarization and competitive halogen bonds. The [(TMCM)CdBr$_3$] retains the ferroelectric behaviour and exhibits a high d$_{33}$ value of 139 pC N^{-1} which is greater than that obtained for most of the uniaxial ferroelectrics, BaTiO$_3$ and [(TMBM)MnBr$_3$].[98] Apart from this, a significant extent of two-dimensional metal-halides based ferroelectric materials have been shown to exhibit high piezo and pyroelectricity, low voltage operation, record fast switching polarization, excellent white light emission, self-powered photodetection and thermochromic behaviour.[99-103]

Till today, the A-site cations of the majority of perovskite ferroelectric materials are limited to organo ammonium cations, whereas ammonium analog of other cations is very rare in literature. Recently, an interesting finding has been investigated based on above room temperature luminescent phosphonium perovskite ferroelectrics, [(CH$_3$)$_4$P]CdCl$_3$ with a moderate remnant polarization of (P_r ~ 0.43 μC cm^{-2}) and high curie temperature (T_c ~ 348 K) (Figure 1.8).[104] They also showed the structural influence of the phosphorus atom and the presence of longer P-C bond length in [(CH$_3$)$_4$P]CdCl$_3$ through by performing the electrical and thermal measurements. The variable temperature single-crystal X-ray diffraction analysis indicates that this compound crystallizes in the non-centrosymmetric space group at room temperature phase (RTP, $P6_3$) and centrosymmetric space group in intermediate and high-temperatures (ITP and HTP, $P6_3/m$). The main difference between RTP and ITP phases is the orientation of the [(CH$_3$)$_4$P]$^+$ cations, the ITP and RTP phases are isostructural with a disordered structure for the $[(CH_3)_4P]^+$ cations without changing the higher crystal symmetry of $[(CH_3)_4P]CdCl_3$. Further, the existence of stripe-like ferroelectric domains of $[(CH_3)_4P]CdCl_3$ was identified by using piezoresponse force microscopy (PFM) analysis.

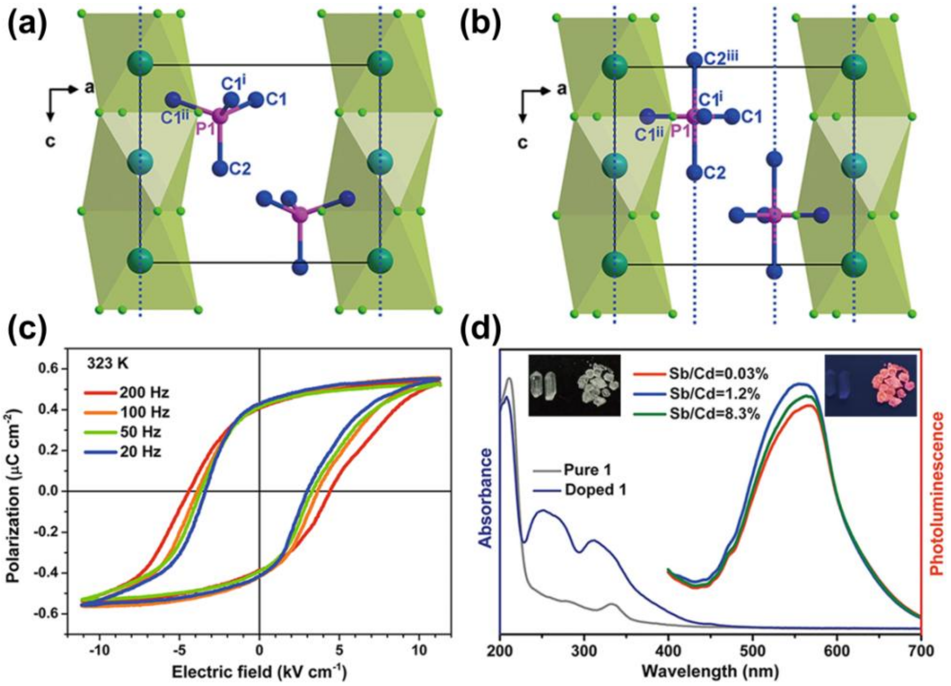

Figure 1.8: *(a) and (b) Packing views of $[(CH_3)_4P]CdCl_3$ along b-axis at 293 and 373 K. (c) its ferroelectric hysteresis loops at various frequencies and (d) absorption spectra of $[(CH_3)_4P]CdCl_3$ and Sb^{3+} doped $[(CH_3)_4P]CdCl_3$ and the emission spectra of Sb^{3+} doped $[(CH_3)_4P]CdCl_3$ (inset images are showing crystals of $[(CH_3)_4P]CdCl_3$ (left) and Sb^{3+} doped $[(CH_3)_4P]CdCl_3$ (right) under ambient and UV light).* Adapted with permission from ref. 104. Copyright © 2019, Springer Nature.

Interestingly, an orange coloured emission was observed by the doping different concentrations of Sb^{3+} ions into this compound at room temperature. The introduction of Sb^{3+} ions did not disturb the hexagonal polar structure of this compound and was shown to display ferroelectric polarization at different frequencies. This new strategy of doping phosphor components into organic-inorganic hybrid ferroelectric materials can allow the designing of various luminescent ferroelectric materials for photovoltaic and electro-optical applications.

1.6.2 Metallocyanates ferroelectric materials

Metallocyanates are one of the essential classes of organic-inorganic hybrid materials which are found to exhibit interesting magnetic, electric and optical properties.[91,105-107] Well-known examples for cyanide ion connected metal coordination compounds (metallocyanates or cyanometallates) are ($Fe^{III}_4[Fe^{II}(CN)_6]_3$), $K_3[Fe(CN)_6]$, $K_4[Fe(CN)_6]$, $K_3[Co(CN)_6]$ and $K_3[Cr(CN)_6]$. These hybrid compounds can form single and double perovskite structures with the formula of ABX_3 and $A_2[B’’B”’’(X)_6]$, (where A is the monovalent organic cation, B’’ is monovalent alkali cation, B”” is the transition metal ion and X = CN^{-}), respectively.

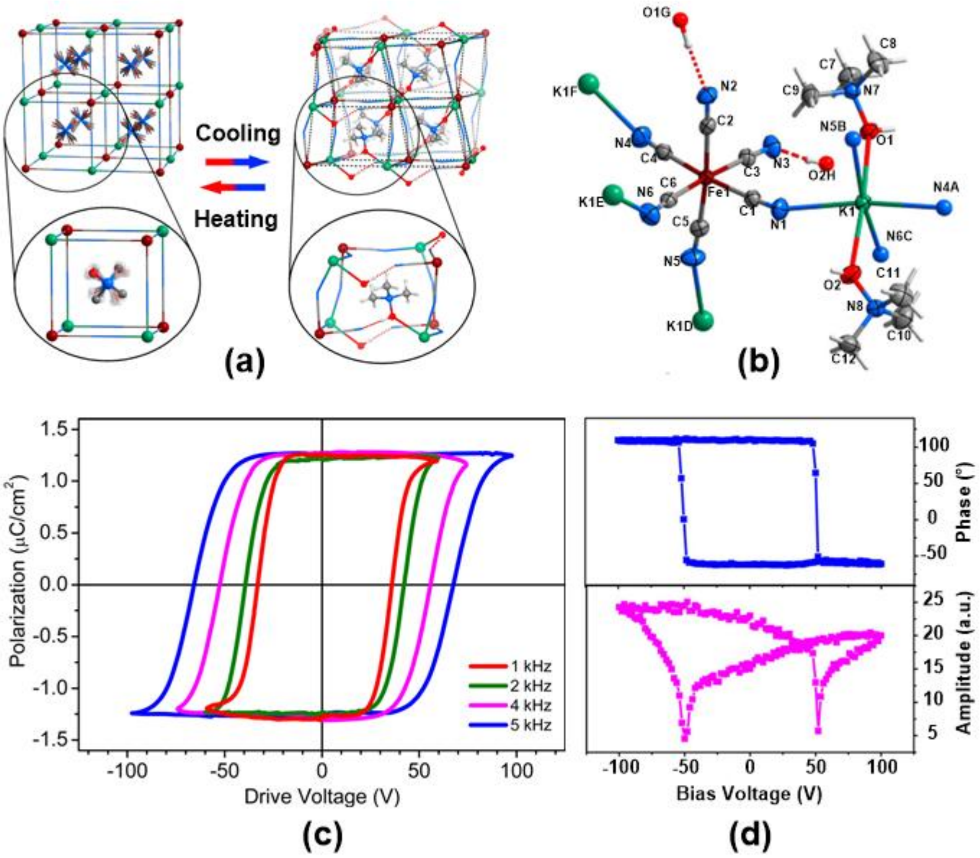

Figure 1.9: *(a) Temperature-dependent bond switching in $[(CH_3)_3NOH]_2[KFe(CN)_6]$ due to the disordered and ordered nature of $[(CH_3)_3NOH]^+$ cation at HTP and LTP, respectively. (b) The asymmetric unit of $[(CH_3)_3NOH]_2[KFe(CN)_6]$ in the LTP and (c) its room temperature ferroelectric hysteresis loops. (d) The phase and amplitude hysteresis loops obtained during the PFM measurements at selected points on the thin film of $[(CH_3)_3NOH]_2[KFe(CN)_6]$.* Adapted with permission from ref. 108. Copyright © 2017 American Chemical Society.

In this heterometallic perovskite structure, the bond between B’’–CN is weak and ionic, while the B””–CN bond is stronger and covalent. The A-site cations (ammonium or phosphonium cation) can act as a guest molecule and the rest of the structure behave as a host framework. The interactions of the host and guest frameworks and the size of the guest ions often dictate the topology of overall structure from higher dimension 3D to lower dimension 0D of discrete assemblies. Most of these hybrid frameworks were crystallized in centrosymmetric space groups and shown to exhibit multiple-step dielectric phase transitions that were supplemented by the order-disorder nature of the ions. Results pertaining to the nonlinear dielectric materials based metallocyanates are rare in literature.[90-91]

Recently, for the first time, Xiong and co-workers demonstrated the ferroelectric to paraelectric phase transition in $[(CH_3)_3NOH]_2[KFe(CN)_6]$ (TMC-1) salt (Figure 1.9).[108] The cyanometallate TMC-1 were prepared by the mixing of equivalent quantities of trimethylamine N-oxide hydrochloride and $K_3[Fe(CN)_6]$ at room temperature. The X-ray single crystal analysis shows TMC-1 was crystallized in the monoclinic *Cc* (polar at low temperature) and cubic $Fm\bar{3}m$ (non-polar at high temperature) space groups at 298 K and 408 K, respectively. The crystal structure of TMC-1 shows the Fe^{3+} ion is bound by six CN^{-} ions. Out of the six cyanide ions, four of them are bridged between the alkali K^{+} and Fe^{3+} ions. The hydroxy group of the $(CH_3)_3NOH^{+}$ cation transforms from an uncoordinated state to a coordinated state on going from an HT phase to the LT phase. Bond-rearrangement triggered order-disorder mechanism is unprecedented among organic and organic-inorganic hybrid ferroelectrics.

1.7 Application of ferroelectric materials

The multifaceted properties of ferroelectric materials have been broadly studied and utilized into various electroactive component systems such as microsensor, dielectric capacitors, ferroelectric field-effect transistors (*FeFET*), ferroelectric random access memory (*FeRAM*), photovoltaics, energy storage and conversion devices, electro-optical systems, micro and nanoelectromechanical systems (*MEMS* and *NEMS*) and as an energy harvester for mechanical energy harvesting applications (Figure 1.10).[7,109-113]

The existence of piezoelectric property in ferroelectric materials has been utilized for many other commercial applications, including electronic devices (television remote controller, microphones, fire alarms, igniter and micro-robotics), transducers, piezo actuators, piezo sensors, etc. Besides, the hybrid ABX_3 type piezo and ferroelectric perovskite materials with excellent light-harvesting properties are utilized in photovoltaics containing solar cell devices with very high power conversion efficiencies.[114-116] The superior performance of these materials for optoelectronic applications is driven by their easy solution synthesis, high charge mobility, strong optical absorption, photoconductivity and tunable bandgap properties.[117-121]

Figure 1.10: *(a) Diverse applications of non-linear dielectric materials (piezo, pyro and ferroelectric materials).* Adapted with permission from ref. 113. Copyright © 2013 The Royal Society Chemistry.

Most importantly, in recent times, piezo and ferroelectric materials were further commercialized as flexible electronic materials along with various polymers in the form of composite materials to harvest the electromechanical response from highly abundant natural energy sources. In addition to their other extensive studies, this section mainly focuses on the use of piezo and ferroelectric materials for mechanical energy harvesting applications.

1.8 Piezo and ferroelectric materials for mechanical energy harvesting applications

In modern-day life, energy prerequisites are increased drastically with the significant growth of civilization and industrialization in every part of the world. These energy demands are mostly fulfilled by non-renewable energy sources such as fossil fuels (coal, petroleum and natural gas), metal ores and earth minerals. However, the use of these energy sources is going to be available only for a limited time. The alternative sustainable and highly abundant energy sources such as solar, thermal, wind, wave, biomass, and mechanical energy have been demonstrated to solve the above problem to certain extend.[122-125]

Among all, converting mechanical energy into electrical energy is attractive because of their easy accessibility via human body activities such as blood flow, heart beating, oscillation, breathing, stretching and bending of body movements (Figure 1.11). These electromechanical responses can be harvested from these activities and used in many electronic devices like laptops, cell phones, music players, MEMS, nano and wireless sensors, nanorobots and implantable devices.[126,109-113]

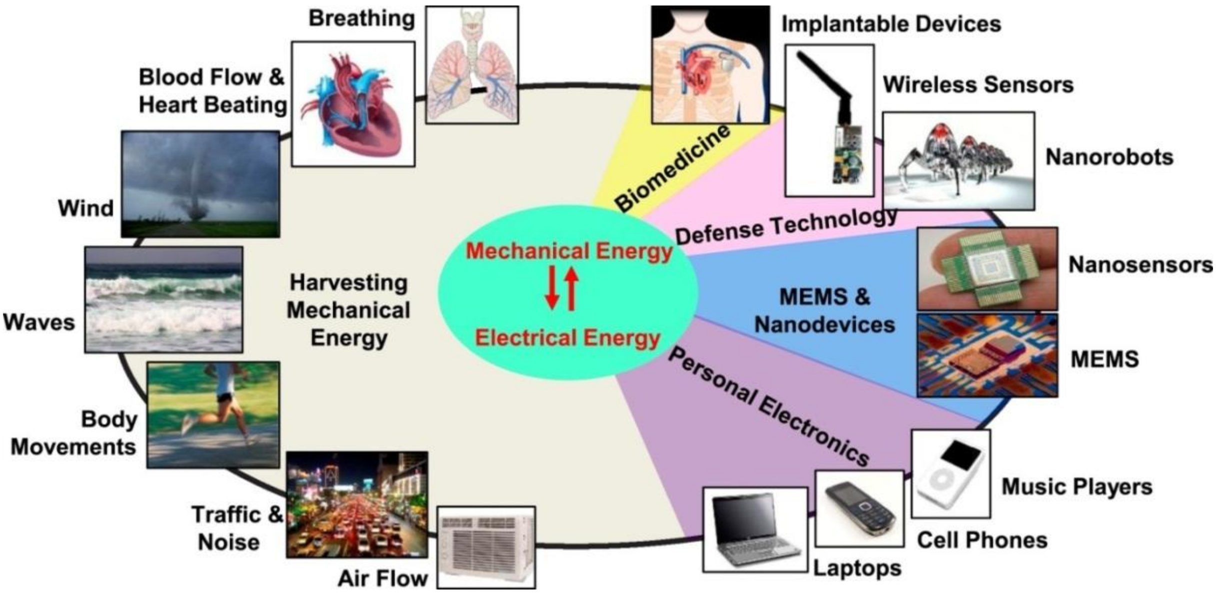

Figure 1.11: *Perspectives of various energy sources for harvesting mechanical energy and converting into electrical energy (left) and their potential utility for future electronic devices (right).* Adapted with permission from ref. 126. Copyright © 2016 Elsevier Ltd.

The first piezoelectric nanogenerator (mechanical energy harvester) was discovered by Zhang et al. based on semiconducting zinc oxide (ZnO) nanowire (Figure 1.12).[127] The array of vertical ZnO nanowires was synthesized by using the vapor-liquid-solid method and shown to exhibit column like wires with the top side face viewing like hexagonal face. The length of the nanowires and diameters were found to be 1-3 microns and 30-100 nm, respectively.

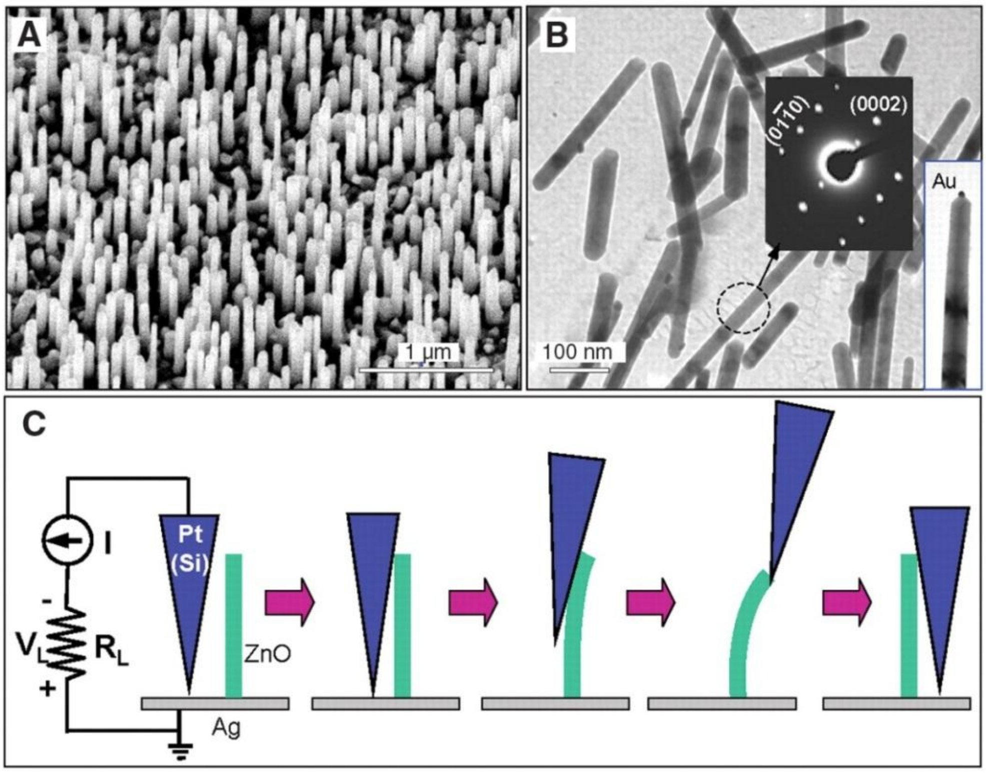

Figure 1.12: *(a) and (b) Scanning electron and Transmission electron microscopes of ZnO nanowires. (c) Experimental setup and procedures for deforming the ZnO nanowires with conductive AFM tip to harvest the electromechanical response.* Adapted with permission from ref. 127. Copyright © 2006 American Association for the Advancement of Science.

The electromechanical response for ZnO nanowires has been demonstrated via the bending operations by using contact mode of atomic force microscopy (AFM) analysis. The observed output voltage and output power for the ZnO nanowire were found to be 8 mV and 0.5 pW, at an applied frequency of 1 MHz with an active area 10 µm x 10 µm. However, the performances of the ZnO energy harvester are very low to utilize them for any commercial applications. It might be due to the low piezo and ferroelectric polarization of ZnO nanowire which causes the output device performance. It is important to note that the piezoelectric coefficient (d_{33}) is directly proportional to the remnant polarization (d_{33} α $\mathcal{E}P_r$) of the materials. In general, it is expected that the use of materials with high piezo and ferroelectric polarization can enhance the piezoelectric energy harvesting performances of the device.

Inspired from the earlier discovery of ZnO nanowire nanogenerator, several piezo and ferroelectric materials made up of inorganic perovskite ceramic metal oxides (barium titanate, lead titanate, lithium niobate, sodium niobate and lead zirconate titanate) have been employed for the mechanical energy harvesting applications (Figure 1.13). However, the utility of traditional inorganic ceramic oxides requires high-temperature fabrication techniques, the longevity of processing time, tedious poling procedure and the presence of heavy density elements and toxic metal content which imparts severe environmental hazardous for their use in wearable electronics.[38-43,128]

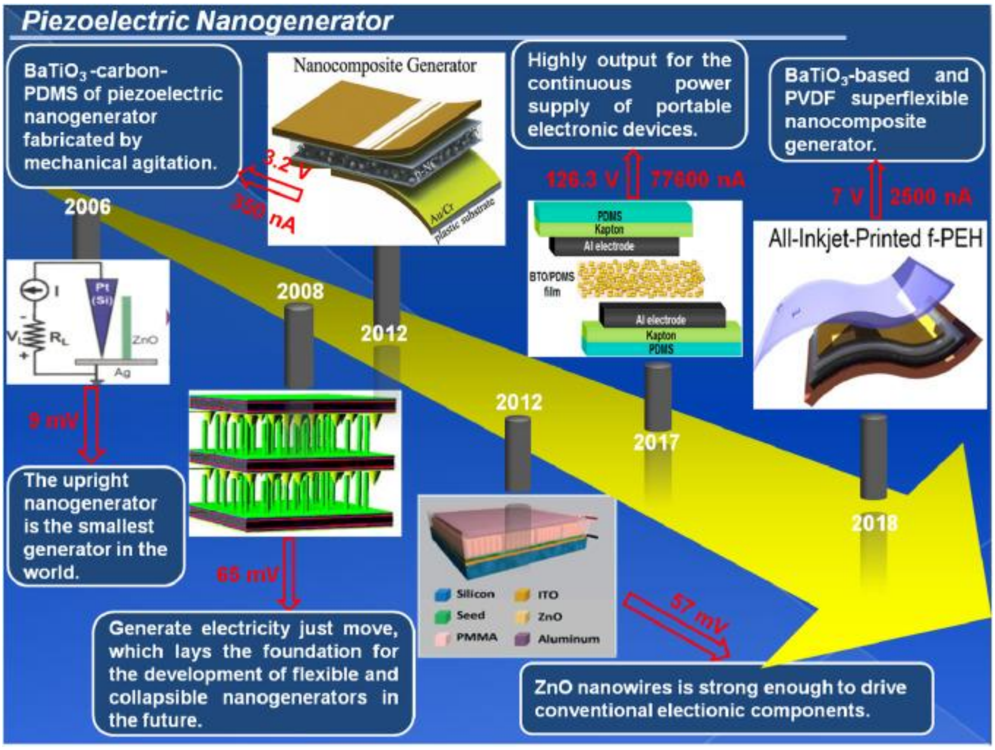

$BaTiO_3$-carbon-PDMS of piezoelectric nanogenerator fabricated by mechanical agitation.

Highly output for the continuous power supply of portable electronic devices.

$BaTiO_3$-based and PVDF superflexible nanocomposite generator.

The upright nanogenerator is the smallest generator in the world.

Generate electricity just move, which lays the foundation for the development of flexible and collapsible nanogenerators in the future.

ZnO nanowires is strong enough to drive conventional electionic components.

Figure 1.13: *Developments in the piezoelectric energy harvesters since the first discovery of ZnO nanowire in 2006.* Adapted with permission from ref. 128. Copyright © 2018 Elsevier Ltd.

Alternately, it is desirable to prepare heavy metal-free and non-ceramic materials for piezoelectric energy harvesting applications. For this purpose, organic polymer composite materials made of polyvinylidene fluoride (PVDF) and its copolymers have been widely utilized as mechanical energy harvester. However, difficulties pertaining to the enhancement of the piezo and ferroelectric polarizable domains (β phase) of PVDF, it still remains a very challenging material.[44-46]

Interestingly, piezo and ferroelectric materials derived from organic and organic-inorganic hybrid materials offer alternate materials because of their facial synthesis, lightweight, simple fabrication techniques, low cost and mechanical flexibility. Recently, polymeric composites of these materials have been widely attracted to address and resolved some of the issues mentioned above pertaining to the ceramic materials and PVDF.[20,69] The first organic-inorganic hybrid piezoelectric energy harvester based on perovskite methylammonium lead iodide ($MAPbI_3$) as its polydimethylsiloxane (PDMS) composite films were reported by Kim and co-workers in 2016 (Figure 1.14a and b).

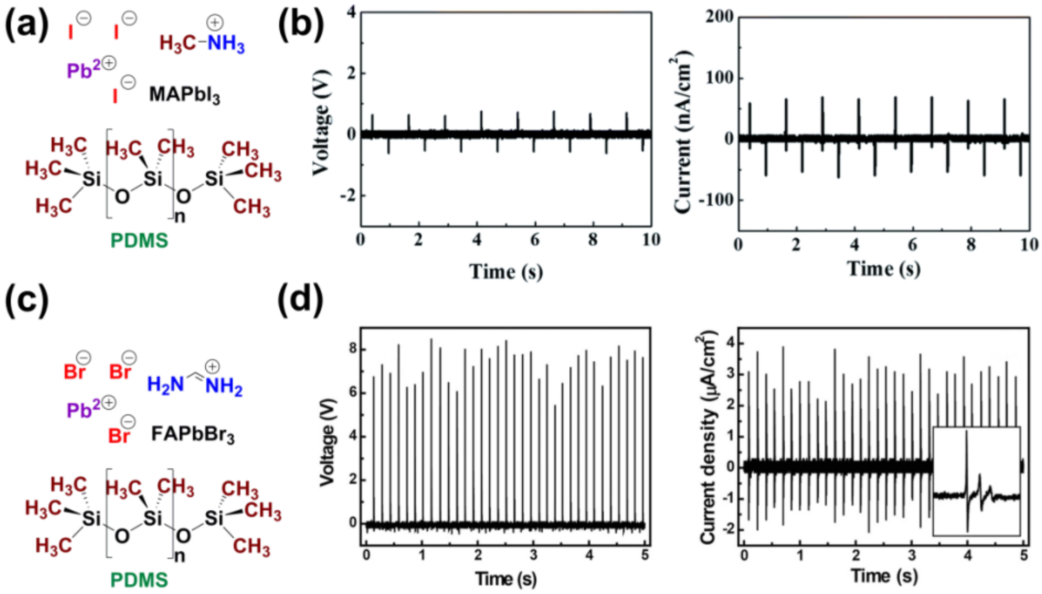

Figure 1.14: *(a) and (c) Schematic view of the chemical structures of $MAPbI_3$-PDMS and $FAPbBr_3$-PDMS. (b) and (d) Piezoelectric energy harvesting performance of $MAPbI_3$-PDMS and $FAPbBr_3$-PDMS composite devices.* Adapted with permission from ref. 129. Copyright © 2016 The Royal Society of Chemistry and ref. 130. Copyright © 2016 WILEY-VCH Verlag GmbH & Co. KGaA, Weinheim.

The piezoelectric energy harvesting performance of the non-poled devices of these composites gave an of the output voltage of 1 V and current density of 50 nA cm^{-2}.[129] When these $MAPbI_3$-PDMS composite devices were subjected to a very high electric field (80 kV cm^{-1}) poling process, they showed an enhanced device performance with an output voltage 2.7 V and current density of 140 nA cm^{-2}. However, the overall output performance of these devices is poor that limits their utility for any commercial applications.

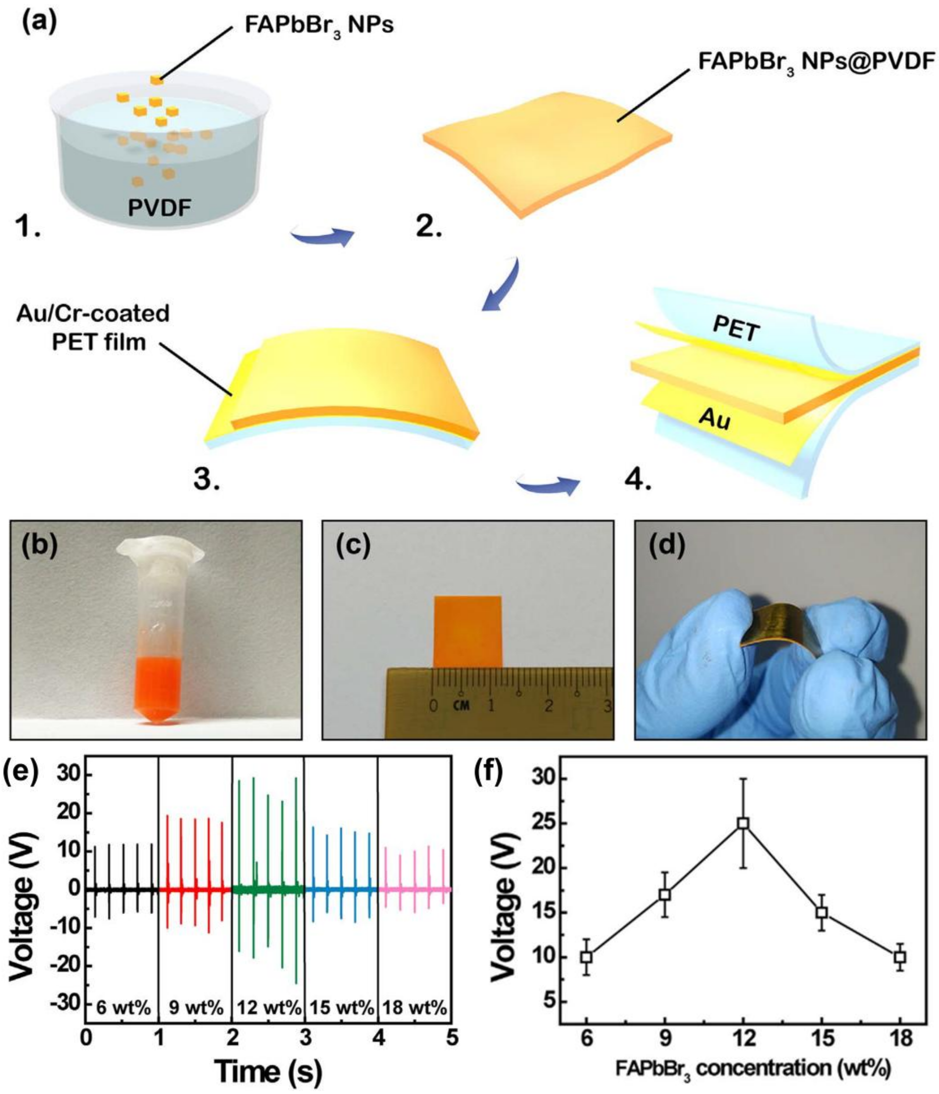

Figure 1.15: *(a) Detailed procedure for preparing composite films of $FAPbBr_3$ NPs @PVDF. (b), (c) and (d) Photograph of a mixed solution, selective area (1.2 x 1.4 cm^2) and a flexible composite device of $FAPbBr_3$ NPs @PVDF nanogenerator. (e) and (d) Output device performance of $FAPbBr_3$ NPs @PVDF nanogenerator.* Adapted with permission from ref. 131. Copyright © 2017 Elsevier Ltd.

Later on, a high performance of flexible piezoelectric energy harvester composed of formamidinium lead bromide ($FAPbBr_3$) with PDMS polymer composite was designed and shown to exhibit the maximum output voltage of 8.5 V and current density of 3.8 μA cm^{-2}, respectively (Figure 1.14c and d).[130] Further, the generated output voltages from this device was utilized for charging a capacitor (47 nF) that can subsequently light up the LEDs (light-emitting diodes) via a full-wave bridge rectifier circuit.

Recently, Zheng and coworkers have fabricated another piezoelectric composite energy harvester based on formamidinium lead bromide ($FAPbBr_3$) nanoparticles (NPs) embedded on polyvinylidene difluoride (PVDF) polymer matrix (Figure 1.15).[131] The composite film preparation process involves the dissolution of $FAPbBr_3$ NPs into the PVDF solution by adopting the solution casting method. After the thermal annealing process, these films were peeled off from the glass substrate which shows a uniform distribution of $FAPbBr_3$ NPs in the composite films. Subsequently, these films were sandwiched between gold (Au) and chromium (Cr) coated polyethylene terephthalate (PET) substrates which act as the top and bottom of electrodes of the device. These flexible and poled devices display a high enhancement in the energy harvesting performance with the maximum output voltage and current density of 30 V and 6.2 μA cm^{-2}, respectively, for an optimized ratio of 12 wt % $FAPbBr_3$ NPs @PVDF composite devices (Figure 1.15e and f). The multifold enhancement in the performance of these composite devices can be attributed to the use of piezoelectric PVDF polymer and the homogeneous distribution of $FAPbBr_3$ nanoparticles in the composite films.

Recently, a lead-free formamidinium tin iodide ($FASnI_3$) embedded PVDF polymeric hybrid composite nanogenerator has been shown to display an excellent output voltage and power density of 23 V and 35.05 mW cm^{-2}, respectively, for (0.5:0.5) wt % of $FASnI_3$:PVDF composite device (Figure 1.16).[132] Further, these devices were utilized for the practical application of charging a capacitor and lighting up of the LEDs. Few more examples of piezoelectric energy harvesters such as encapsulated ZnO nanowires into a parylene C polymer matrix,[133] Electrospun Nanofiber Mat of $MAPbI_3$-PVDF nanogenerator,[134] $MAPbI_3$-PVDF nanogenerator,[135-136] $MASnI_3$-PVDF nanogenerator,[137] PVDF-PLLA-SnO_2 NF-$MAPbI_3$,[138] SnO_2 NF-$MAPbI_3$,[138] etc., were fabricated and shown to exhibit low to moderate piezoelectric energy harvesting output device performance. Despite of these advances, several of these composite materials suffer from air and moisture stability due to reactive metal-halide bonds and pose environmental concerns due to the presence of toxic heavy metal ions.[41-43,64-65]

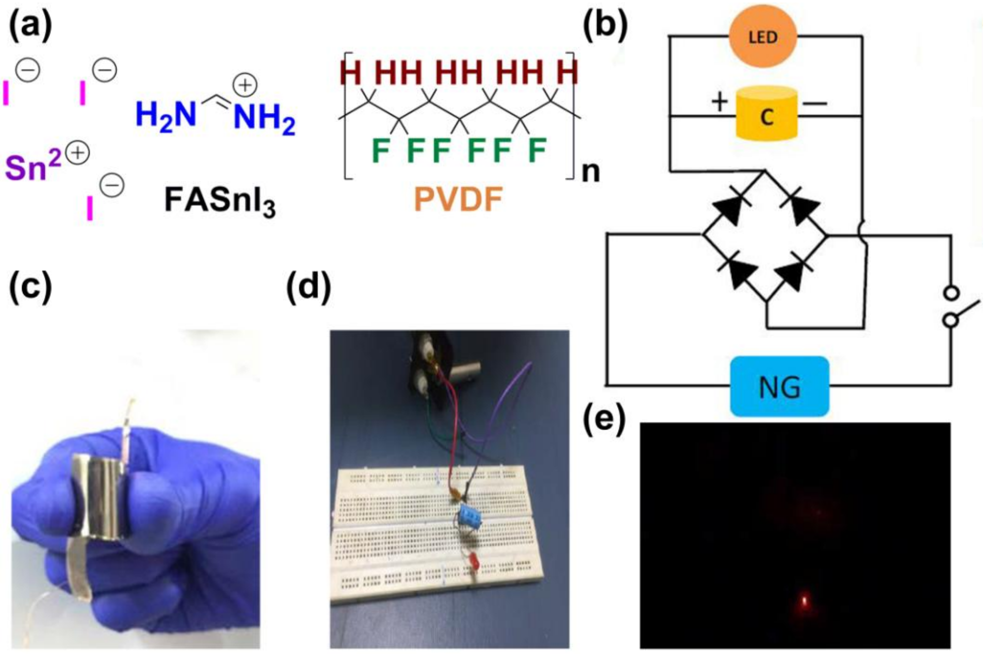

Figure 1.16: *(a) Chemical structure of $FASnI_3$-PVDF. (b) Schematic circuit diagram for capacitor charging experiment. (c) A view of the flexible composite film of $FASnI_3$-PVDF . (d) Capacitor charging and LED driving set up and (e) glowing LED.* Adapted with permission from ref. 132. Copyright © 2019, American Chemical Society.

One of the viable solutions to tackle this problem is to employ light-weight 3d metal ions in combination with pseudo-halogenometallate counter-anions within the framework of organic-inorganic hybrid structures. Thus, the polymeric composites made up of organic-inorganic hybrid materials containing piezo and ferroelectric active phase at ambient conditions are a more favorable and attractive approach to harvest the electromechanical response and can be utilized for future wearable electronics and micropower generator applications.

1.9 Scope of the present thesis

This thesis demonstrates the synthesis of acentric polar P(V) based organic and organic-inorganic hybrid piezo and ferroelectric materials for mechanical energy harvesting applications. Chapter 2 will discuss the synthesis of organoamino phosphonium salts supported by monoatomic halide anions and their possible ferroelectric properties analyzed by Sawyer-Tower circuit studies and piezoresponse force microscopy analysis. Chapter 3 will describe the synthesis of aminophosphonium salts containing multiatomic octahedral hexafluoro phosphate ion which shows excellent ferroelectric polarization. For the first time, polymeric composites of this organic salt were shown for mechanical energy harvesting applications with polydimethylsiloxane (PDMS) polymer matrix. Chapter 4 will discuss the synthesis of heteroleptic organoamino phosphonium salts stabilized multiatomic lower symmetric tetrahedral anions (BF_4^-, ClO_4^- and IO_4^-) which are shown to display excellent piezo and ferroelectric polarization. Further, flexible composite devices for these salts were prepared with the combination of non-piezoelectric thermoplastic polyurethane (TPU) polymer for piezoelectric energy harvesting applications. The last chapter (Chapter 5) will discuss the synthesis of organic-inorganic hybrid piezo and ferroelectric materials supported by pseudometallohalogenate frameworks. This hybrid ferroelectric material shows a frequency-dependent ferroelectric polarization at room temperature. Finally, the mechanical energy harvesting performance this hybrid material with TPU polymer was shown to display excellent output device performance (output voltage, output current, current and power densities) as compared to known piezoelectric energy harvesters made up of organic and organic-inorganic hybrid ferroelectric materials.

Thus the present thesis aims:

- To synthesize the low symmetric organo and aminophosphonium salts supported mono and multiatomic anions containing P(V) scaffolds.
- To study the non-centrosymmetric nature of organic and organic-inorganic hybrid salts containing piezo and ferroelectric properties.
- To develop them for potential piezo and ferroelectric energy harvesting applications embedded in a non-piezoelectric polymer matrix.

In this regard, a new synthetic design to obtain lower symmetric molecular ferroelectric materials with their enhanced ferroelectric and composite device performance was briefly addressed. These outcomes demonstrate the effectiveness of organic and organic-inorganic hybrid ferroelectric materials for energy harvesting applications and promise their potential utility in future wearable electronics.

1.10 REFERENCES

(1) Li, W.; Wang, Z.; Deschler, F.; Gao, S.; Friend, R. H.; Cheetham, A. K. *Nat. Rev. Mater*. **2017**, *2*, 16099.

(2) Hu, W. J.; Kopyl, S.; Kholkin, A.; Rocha, J. *Coord. Chem. Rev.* **2019**, *387*, 398–414.

(3) Chakraborty, P.; Nag, A.; Chakraborty, A.; Pradeep, T. *Acc. Chem. Res.* **2019**, *52*, 2–11.

(4) Zhang, W.; Xiong, R. G. *Chem. Rev.* **2012**, *112*, 1163–1195.

(5) Eerenstein, W.; Mathur, N. D.; Scott, J. F. *Nature* **2006**, *442*, 759–765.

(6) Yang, S. Y.; Seidel, J.; Byrnes, S. J.; Shafer, P.; Yang, C. H.; Rossell, M. D.; Yu, P.; Chu, Y. H.; Scott, J. F.; Ager, J. W.; Martin, L. W.; Ramesh, R. *Nat. Nanotechnol.* **2010**, *5*, 143–147.

(7) Bowen, C. R.; Kim, H. A.; Weaver, P. M.; Dunn, S. *Energy Environ. Sci.* **2014**, *7*, 25–44.

(8) Lines, M. E.; Glass, A. M. *Principles and Applications of Ferroelectrics and Related Materials*; Oxford University Press: New York, 1977.

(9) Valasek, J. *Phys. Rev.* **1921**, *17*, 475–481.

(10) Hang, T.; Zhang, W.; Ye, H.Y.; R. G. Xiong. *Chem. Soc. Rev.* **2011**, *40*, 3577–3598.

(11) Horiuchi, S.; Tokura, Y. *Nat. Mater.* **2008**, *7*, 357–366.

(12) Asadi, K.; van der Veen, M. A. *Eur. J. Inorg. Chem.* **2016**, *27*, 4332–4344.

(13) Shi, P. P.; Tang, Y. Y.; Li, P. F.; Liao, W. Q.; Wang, Z. X.; Ye, Q.; Xiong, R. G. *Chem. Soc. Rev.* **2016**, *45*, 3811–3827.

(14) Zhang, W.; Ye, H. Y.; Xiong, R. G. *Coord. Chem. Rev.* **2009**, *253*, 2980–2997.

(15) Guo, M.; Cai, H. L.; Xiong, R. G. *Inorg. Chem. Commun.* **2010**, *13*, 1590–1598.

(16) Scott, J. F. *Ferroelectric memories*, Springer Science & Business Media, 2013.

(17) Han, S.T.; Zhou, Y.; Roy, V. A. L. *Adv. Mater.* **2013**, *25*, 5425–5449.

(18) Jin, H.; Li, J.; Iocozzia, J.; Zeng, X.; Wei, P. C.; Yang, C.; Li, N.; Liu, Z.; He, J. H.; Zhu, T.; Wang, J.; Lin, Z.; Wang, S. *Angew. Chem. Int. Ed.* **2019**, *58*, 15206–15226.

(19) Narita, F.; Fox, M. *Adv. Eng. Mater.* **2018**, *20*, 1700743.

(20) Jella, V.; Ippili, S.; Eom, J. H.; Pammi, S. V. N.; Jung, J. S.; Tran, V. D.; Nguyen, V. H.; Kirakosyan, A.; Yun, S.; Kim, D.; Sihn, M. R.; Choi, J.; Kim, Y. J.; Kim, H. J.; Yoon, S. G. *Nano Energy* **2019**, *57*, 74–93.

(21) Zhang, D.; Wang, Y.; Yang, Y. *Small* **2019**, *15*, 1805241.

(22) Ellabban, O.; Abu-Rub, H.; Blaabjerg, F. *Renewable Sustainable Energy Rev.* **2014**, *39*, 748–764.

(23) Tao, P.; Ni, G.; Song, C.; Shang, W.; Wu, J.; Zhu, J.; Chen, G.; Deng, T. *Nat. Energy* **2018**, *3*, 1031–1041.

(24) Chen, J.; Huang, Y.; Zhang, N.; Zou, H.; Liu, R.; Tao, C.; Fan, X.; Wang, Z. L. *Nat. Energy* **2016**, *1*, 16138.

(25) Tu, Y.; Wang, R.; Zhang, Y.; Wang, J. *Joule* **2018**, *2*, 1452–1475.

(26) Invernizzi, F.; Dulio, S.; Patrini, M.; Guizzetti, G.; Mustarelli, P. *Chem. Soc. Rev.* **2016**, *45*, 5455–5473.

(27) Tian, R.; Liu, Y.; Koumoto, K.; Chen, J. *Joule* **2019**, *3*, 1399-1403.

(28) Maharjan, P.; Cho, H.; Rasel, M. S.; Salauddin, M.; Park, J. Y. *Nano Energy* **2018**, *53*, 213–224.

(29) Wang, Z. L.; Chen, J.; Lin, L. *Energy Environ. Sci.* **2015**, *8*, 2250–2282.

(30) Zhang, Y.; Xie, M.; Adamaki, V.; Khanbareh, H.; Bowen, C. R. *Chem. Soc. Rev.* **2017**, *46*, 7757–7786.

(31) Hu, F.; Cai, Q.; Liao, F.; Shao, M.; Lee, S. T. *Small* **2015**, *11*, 5611–5628.

(32) Chen, J.; Wang, Z. L. *Joule* **2017**, *1*, 480–521.

(33) Shepelin, N. A.; Glushenkov, A. M.; Lussini, V. C.; Fox, P. J.; Dicinoski, G. W.; Shapter, J. G.; Ellis, A. V. *Energy Environ. Sci.* **2019**, 1143–1176.

(34) Yang, Z.; Zhou, S.; Zu, J.; Daniel, I. *Joule* **2018**, *2*, 642–697.

(35) Li, M.; Porter, A. L.; Wang, Z. L. *Nano Energy* **2017**, *34*, 93–102.

(36) Briscoe, J.; Dunn, S. *Nano Energy* **2015**, *14*, 15–29.

(37) Wang, Z. L.; Song, J. *Science* **2006**, *312*, 242–246.

(38) Park, K. I.; Jeong, C. K.; Kim, N. K.; Lee, K. J. *Nano Convergence.* **2016**, *3*, 12.

(39) Persano, L.; Dagdeviren, C.; Su, Y.; Zhang, Y.; Girardo, S.; Pisignano, D.; Huang, Y.; Rogers, J. A. *Nat. Commun.* **2013**, *4*, 1610–1633.

(40) Lu, X.; Qu, H.; Skorobogatiy, M. *ACS Nano* **2017**, *11*, 2103–2114.

(41) Bai, Y.; Jantunen, H.; Juuti, *J. Adv. Mater.* **2018**, *30,* 1707271.

(42) Safaei, M.; Sodano, H. A.; Anton, S. R. *Smart Mater. Struct.* **2019**, *28*, 113001.

(43) Liu, H.; Zhong, J.; Lee, C.; Lee, S. W.; Lin, L. *Applied Physics Reviews* **2018**, *5,* 041306.

(44) Park, S. H.; Lee, H. B.; Yeon, S. M.; Park, J.; Lee, N. K. *ACS Appl. Mater. Interfaces* **2016**, *8*, 24773–24781.

(45) Alluri, N. R.; Chandrasekhar, A.; Jeong, J. H.; Kim, S.J. *J. Mater. Chem. C* **2017**, *5*, 4833–4844.

(46) Park, J. H.; Kurra, N.; AlMadhoun, M. N.; Odeh, I. N.; Alshareef, H. N. *J. Mater. Chem. C* **2015**, *3*, 2366–2370.

(47) Rosenberg, H. M. *The solid state*. Oxford University Press: 1988.

(48) Sebastian, M. T. *Dielectric Materials for Wireless Communication*; Elsevier, Science and Technology Publishers: Oxford, U.K., 2008.

(49) Uchino, K. *In Advanced Piezoelectric Materials*; Woodhead Publishing Ltd.: Cambridge, UK, 2010.

(50) Manjon-Sanz, A. M.; Dolgos, M. R. *Chem. Mater.* **2018**, *30*, 8718–8726.

(51) Vijaya, M. S. *Piezoelectric Materials and Devices: Applications in Engineering and Medical Sciences*; CRC Press: Boca Raton, 2012.

(52) Mason, W. P. *J. Acoust. Soc. Am.* **1981**, *70*, 1561–1566.

(53) Richerson, D. W. *Modern ceramic engineering: properties, processing, and use in design*. CRC press: 2005.

(54) Rogalski, A. *Infrared Physics & Technology*. **2002**, *43*, 187–210.

(55) Dereniak, E. L.; Boreman, G. D. *Infrared detectors and systems*; Wiley: New York, 1996.

(56) Tang, Y. Y.; Li, P. F.; Liao, W. Q.; Shi, P. P.; You, Y. M.; Xiong, R. G. *J. Am. Chem. Soc.* **2018**,*140*, 8051–8059.

(57) Zhang, H. Y.; Tang, Y. Y.; Shi, P. P.; Xiong, R. G. *Acc. Chem. Res.* **2019**, *52*, 1928–1938.

(58) Busch, G.; Scherrer, P. *Naturwissenschaften* **1935**, *23*, 737.

(59) Eerenstein, W.; Mathur, N. D.; Scott, J. F. *Nature* **2006**, *442*, 759–765.

(60) Cross, L. E. *Ferroelectric Ceramics: Tailoring Properties for Specific Applications*. In: Ferroelectric Ceramics. Monte Verità (Proceedings of the Centro Stefano Franscini, Ascona). Birkhäuser Basel: 1993.

(61) Uchino, K. *Ferroelectric Devices* 2nd Edition. CRC press: 2009.

(62) Scott, J. F. *Science* **2007**, *315*, 954–959.

(63) Scott, J. F. *Ferroelectric memories* Vol. 3. Springer Science & Business Media: 2000.

(64) Damjanovic D. *Lead-Based Piezoelectric Materials*. In: Safari A., Akdoğan E.K. (eds) *Piezoelectric and Acoustic Materials for Transducer Applications*. Springer, Boston, MA, 2008.

(65) Wei, H.; Wang, H.; Xia, Y.; Cui, D.; Shi, Y.; Dong, M.; Liu, C.; Ding, T.; Zhang, J.; Ma,Y.; Wang, N.; Wang, Z.; Sun, Y.; Wei, R.; Guo, Z. *J. Mater. Chem. C,* **2018**, *6*, 12446–12467.

(66) García-Iglesias, M.; de Waal, B. F. M.; Gorbunov, A. V.; Palmans, A. R. A.; Kemerink, M.; Meijer, E. W. *J. Am. Chem. Soc.* **2016**, *138*, 6217–6223.

(67) Hu, Z.; Tian, M.; Nysten, B.; Jonas, A. M. *Nat. Mater.* **2009**, *8*, 62–67.

(68) Naber, R. C. G.; Asadi, K.; Blom, P. W. M.; de Leeuw, D. M.; de Boer, B. *Adv. Mater.* **2010**, 22, 933–945.

(69) Ippili, S.; Jella, V.; Kim, J.; Hong, S.; Yoon, S. G. *Nano Energy* **2018**, *49*, 247–256.

(70) Hoshino, S.; Shibuya, I. *J. Phys. Soc. Japan.* **1961**, *16*, 1254–1255.

(71) Hirai, M.; Tanaka, N.; Sakai, M.; Yamaguchi, S. *Chem. Rev.* **2019**, *119*, 8291–8331.

(72) Baumgartner. T. *Acc. Chem. Res.* **2014**, *47*, 1613–1622.

(73) Solomon, A. L. *Phys. Rev.* **1956**, *104*, 1191.

(74) Horiuchi, S.; Ishii, F.; Kumai, R.; Okimoto, Y.; Tachibana, H.; Nagaosa, N.; Tokura, Y. *Nat. Mater.* **2005**, *4*, 163–166.

(75) Horiuchi, S.; Tokunaga, Y.; Giovannetti, G.; Picozzi, S.; Itoh, H.; Shimano, R.; Kumai, R.; Tokura, Y. *Nature* **2010**, *463*, 789–792.

(76) Horiuchi, S.; Kumai, R.; Tokura, Y. *Angew. Chem. Int. Ed.* **2007**, *46*, 3497–3501.

(77) Horiuchi, S.; Kagawa, F.; Hatahara, K.; Kobayashi, K.; Kumai, R.; Murakami, Y.; Tokura, Y. *Nat. Commun.* **2012**, *3*, 1308.

(78) Horiuchi, S.; Kobayashi, K.; Kumai, R.; Ishibashi, S. *Nat. Commun.* **2017**, *8*, 14426.

(79) Semmingsen, D.; Groth, P. *J. Am. Chem. Soc.* **1987**, *109*, 7238–7239.

(80) Semmingsen, D.; Hollander, F. J.; Koetzle, T. F. *J. Chem. Phys.* **1977**, *66*, 4405–4412.

(81) Hu, L.; Feng, R.; Wang, J.; Bai, Z.; Jin, W.; Zhang, L.; Nie, Q. M.; Qiu, Z. J.; Tian, P.; Cong, C.; Zheng, L.; Liu, R. *Adv. Funct. Mater.* **2018**, *28*, 1705463.

(82) Owczarek, M.; Hujsak, K. A.; Ferris, D. P.; Prokofjevs, A.; Majerz, I.; Szklarz, P. A.; Zhang, H.; Sarjeant, A. A.; Stern, C. L.; Jakubas, R.; Hong, S.; Dravid, V. P.; Stoddart, J. F. *Nat. Commun*., **2016**, *7*, 13108.

(83) Fu, D. W.; Zhang, W.; Cai, H. L.; Ge, J. Z.; Zhang, Y.; Xiong, R. G. *Adv. Mater.* **2011**, *23*, 5658–5662.

(84) Fu, D. W.; Cai, H. L.; Liu, Y.; Ye, Q.; Zhang, W.; Zhang, Y.; Chen, X. Y.; Giovannetti, G.; Capone, M.; Li, J.; Xiong, R. G. *Science* **2013**, *339*, 425–428.

(85) Saripalli, R. K.; Swain, D.; Prasad, S.; Nhalil, H.; Bhat, H. L.; Guru Row, T. N.; Elizabeth, S. *J. Appl. Phys.*, **2017**, *121*, 114101.

(86) Ye, H. Y.; Tang, Y. Y.; Li, P. F.; Liao, W. Q.; Gao, J. X.; Hua, X. N.; Cai, H.; Shi, P. P.; You, Y. M.; Xiong, R. G. *Science* **2018**, *361*, 151–155.

(87) Li, W.; Wang, Z.; Deschler, F.; Gao, S.; Friend, R. H.; Cheetham, A. K. *Nat. Rev. Mater*., **2017**, *2*, 16099.

(88) Asadi, K.; van der Veen, M. A. *Eur. J. Inorg. Chem.* **2016**, *27*, 4332–4344.

(89) Zhang, X.; Li, L.; Sun, Z.; Luo, J. *Chem. Soc. Rev.,* **2019**, *48*, 517–539.

(90) Xu, W. J.; Du, Z. Y.; Zhang, W. X.; Chen, X. M. *CrystEngComm* **2016**, *18*, 7915–7928.

(91) Shi, C.; Bin Han, X.; Zhang, W. *Coord. Chem. Rev.* **2019**, *378*, 561–576.

(92) Li, L.; Sun, Z.; Wang, P.; Hu, W.; Wang, S.; Ji, C.; Hong, M.; Luo, J. *Angew. Chem. Int. Ed.*, **2017**, *56*, 12150–12154.

(93) Sun, Z.; Zeb, A.; Liu, S.; Ji, C.; Khan, T.; Li, L.; Hong, M.; Luo, J. *Angew. Chem. Int. Ed.*, **2016**, *55*, 11854–11858.

(94) Li, P. F.; Tang, Y. Y.; Liao, W. Q.; Ye, H. Y.; Zhang, Y.; Fu, D. W.; You, Y. M.; Xiong, R. G. *NPG Asia Mater.*, **2017**, *9*, e342.

(95) You, Y. M.; Liao, W. Q.; Zhao, D.; Ye, H. Y.; Zhang, Y.; Zhou, Q.; Niu, X.; Wang, J.; Li, P. F.; Fu, D. W.; Wang, Z.; Gao, S.; Yang, K.; Liu, J. M.; Li, J.; Yan, Y.; Xiong, R. G. *Science*, **2017**, *357*, 306–309.

(96) Liao, W. Q.; Tang, Y. Y.; Li, P. F.; You, Y. M.; Xiong, R. G. *J. Am. Chem. Soc.*, **2017**, *139*, 18071–18077.

(97) Liao, W. Q.; Zhao, D.; Tang, Y. Y.; Zhang, Y.; Li, P. F.; Shi, P. P.; Chen, X. G.; You, Y. M.; Xiong, R. G. *Science* **2019**, *363*, 1206–1210.

(98) Liao, W. Q.; Tang, Y. Y.; Li, P. F.; You, Y. M.; Xiong, R. G. *J. Am. Chem. Soc.*, **2018**, *140*, 3975–3980.

(99) Harada, J.; Kawamura, Y.; Takahashi,Y.; Uemura,Y.; Hasegawa,T.; Taniguchi, H.; Maruyama, K. *J. Am. Chem. Soc.* **2019**, *141*, 9349–9357.

(100) Sun, Z.; Yi, X.; Tao, K.; Ji, C.; Liu, X.; Li, L.; Han, S.; Zheng, A.; Hong, M.; Luo, J. A *Angew. Chem., Int. Ed.* **2018**, *57*, 9833–9837.

(101) Ji, C.; Wang, S.; Li, L.; Sun, Z.; Hong, M.; Luo, J. *Adv. Funct. Mater.* **2019**, *29*, 1805038.

(102) Liu, X.; Wang, S.; Long, P.; Li, L.; Peng, Y.; Xu, Z.; Han, S.; Sun, Z.; Hong, M.; Luo, J. *Angew. Chem. Int. Ed.* **2019**, *58*, 14504–14508.

(103) Liu, J. C.; Liao, W. Q.; Li, P. F.; Tang, Y. Y.; Chen, X. G.; Song, X. J.; Zhang, H. Y.; Zhang, Y.; You, Y. M.; Xiong, R. G. **2019**, *59*, 3495–3499.

(104) Zhou, L.; Shi, P. P.; Liu, X. M.; Feng, J. C.; Ye, Q.; Yao, Y. F.; Fu, D. W.; Li, P. F.; You, Y. M.; Zhang, Y.; Xiong, R. G. *NPG Asia Mater.* **2019**, *11*, 1.

(105) Hill, J. A.; Thompson, A. L.; Goodwin, A. L. *J. Am. Chem. Soc.* **2016**, *138*, 5886–5896.

(106) Alexandrov, E. V.; Virovets, A. V.; Blatov, V. A.; Peresypkina, E. V. *Chem. Rev.* **2015**, *115*, 12286–12319.

(107) Nai, J.; Zhang, J.; Lou, X. W. *Chem.* **2018**, *4*, 1967–1982.

(108) Xu, W. J.; Li, P. F.; Tang, Y. Y.; Zhang, W. X.; Xiong, R. G.; Chen, X. M. *J. Am. Chem. Soc.*, **2017**, *139*, 6369–6375.

(109) Muralt, P. *Integr. Ferroelectr.* **1997**, *17*, 297–307.

(110) Kanno, I. *Jpn. J. Appl. Phys.* **2018**, *57*, 040101.

(111) Ma. J.; Hu, J.; Li, Z.; Nan, C. W. *Adv. Mater.* **2011**, *23*, 1062–1087.

(112) Jena, A. K.; Kulkarni, A.; Miyasaka, T. *Chem. Rev.* **2019**, *119*, 3036–3103.

(113) Varghese, J.; Whatmore, R. W.; Holmes, J. D. *J. Mater. Chem. C,* **2013**, *1*, 2618–2638.

(114) Quan, L. N.; Rand, B. P.; Friend, R. H.; Mhaisalkar, S. G.; Lee, T. W.; Sargent, E. H. *Chem. Rev.* **2019**, *119*, 7444–7477.

(115) Qiu, L.; He, S.; Ono, L. K.; Qi, Y. *Adv. Energy Mater.* **2019**, *9*, 1902726.

(116) Stoumpos, C. C.; Kanatzidis, M. G. *Acc. Chem. Res.* **2015**, *48*, 2791–2802.

(117) Gao, S.; Yi, X.; Shang, J.; Liu, G.; Li, R. W. *Chem. Soc. Rev.* **2019**, *48*, 1531–1565.

(118) Manser, J. S.; Christians, J. A.; Kamat, P. V. *Chem. Rev.* **2016**, *116*, 12956–13008.

(119) Kojima, A.; Teshima, K.; Shirai, Y.; Miyasaka, T. *J. Am. Chem. Soc.* **2009**, *131*, 6050–6051.

(120) Kulkarni, S. A.; Mhaisalkar, S. G.; Mathews, N.; Boix, P. P. *Small Methods* **2019**, *3*, 1800231.

(121) Jung, M.; Ji, S. G.; Kim, G. ; Il Seok, S. *Chem. Soc. Rev.* **2019**, *48*, 2011–2038.

(122) Ryu, H.; Yoon, H. J.; Kim, S. W. *Adv. Mater.* **2019**, *31*, 1802898.

(123) Cheng, T.; Gao, Q.; Wang, Z. L. *Adv. Mater. Technol.* **2019**, *4*, 1800588.

(124) X. Huang, Wang, L.; Wang, H.; Zhang, b.; Wang, X.; Stening, R. Y. Z.; Sheng, X.; Yin, L. *Small* **2019**, 1902827.

(125) Ryu, H.; Kim, S. W. *Small* **2019**, 1903469.

(126) Dagdeviren, C.; Joe, P.; Tuzman, O. L.; Park, K.; Lee, K. J.; Shi, Y.; Huang, Y.; Rogers, J. A. *Extreme Mech. Lett.* **2016**, *9,* 269–281.

(127) Wang, Z. L.; Song, J. *Science* **2006**, *312*, 242–246.

(128) Hu, D.; Yao, M.; Fan, Y.; Ma, C.; Fan, M.; Liu, M. *Nano Energy* **2019**, *55*, 288–304.

(129) Kim, Y. J.; Dang, T. V.; Choi, H. J.; Park, B. J.; Eom, J. H.; Song, H. A.; Seol, D.; Kim, Y.; Shin, S. H.; Nah, J.; Yoon, S. G. *J. Mater. Chem. A*, **2016**, *4*, 756–763.

(130) Ding, R.; Liu, H.; Zhang, X.; Xiao, J.; Kishor, R.; Sun, H.; Zhu, B.; Chen, G.; Gao, F.; Feng, X.; Chen, J.; Chen, X.; Sun, X.; Zheng, Y. *Adv. Funct. Mater.* **2016**, *26*, 7708–7716.

(131) Ding, R.; Zhang, X.; Chen, G.; Wang, H.; Kishor, R.; Xiao, J.; Gao, F.; Zeng, K.; Chen, X.; Sun, X. W.; Zheng, Y. *Nano Energy* **2017**, *37*, 126–135.

(132) Pandey, R.; Gangadhar, S. B.; Grover, S.; Singh, S. K.; Kadam, A.; Ogale, S.; Waghmare, U. V.; Rao, V. R.; Kabra, D. *ACS Energy Lett*. **2019**, *4*, 1004–1011.

(133) Dahiya, A. S.; Morini, F.; Boubenia, S.; Nadaud, K.; Alquier, D.; Poulin-Vittrant, G. *Adv. Mater. Technol.* **2017**, *3*, 1700249.

(134) Sultana, A.; Alam, M. M.; Sadhukhan, P.; Ghorai, U. K.; Das, S.; Middya, T. R.; Mandal, D. *Nano Energy* **2018**, *49*, 380–392.

(135) Jella, V.; Ippili, S.; Eom, J. H.; Choi, J.; Yoon, S. G. *Nano Energy* **2018**, *53*, 46–56.

(136) Sultana, A.; Sadhukhan, P.; Alam, M.; Das, S.; Middya, T. R.; Mandal, D. *ACS Appl. Mater. Interfaces* **2018**, *10*, 4121–4130.

(137) Ippili, S.; Jella, V.; Eom, J. H.; Kim, J.; Hong, S.; Choi, J. S.; Tran, V. D.; Hieu, N. V.; Kim, Y. J.; Kim, H. J.; Yoon, S. G. *Nano Energy* **2019**, 57, 911–923.

(138) Tusiime, R.; Zabihi, F.; Tebyetekerwa, M.; Yousry, Y. M.; Wu, Y.; Eslamian, M.; Yang, S.; Ramakrishna, S.; Yua, M.; Zhang, H. *J. Mater. Chem. C*, **2019**, *8*, 2643 –2658.

End of Chapter 1

Chapter 2

Hydrogen-bonded Organo-amino Phosphonium Halides: Dielectric, Piezoelectric and Possible Ferroelectric Properties

2.1 Introduction

Multifunctional substances that show dielectric, ferroelectric and piezoelectric properties are an exciting class of materials for high-technique device applications. Ferroelectrics are a distinct class among the general group of dielectric materials in which electrically polarizable domains can be reversed or reoriented under the external electric field.[1] The existence of intrinsic permanent dipoles and the spontaneous electric polarization enhances the utility of these materials in various multifunctional components such as ferroelectric random access memories (FeRAM), high dielectric constant capacitors, infrared detectors, micro-sensors and actuators, field-effect transistors, photovoltaic devices, electromechanical transducers and switchable NLO devices.[2-13] Over the decades, a great number of ferroelectric compounds derived from inorganic perovskite oxides such as barium titanate ($BaTiO_3$), lead titanate ($PbTiO_3$), lithium niobate ($LiNbO_3$) and lead zirconate titanate ($PbZrTiO_3$) were employed for these applications.[14-16] Inspired from the first examples of H-bonded ferroelectric materials such as Rochelle salt and potassium dihydrogen phosphate (KDP), enormous attention has been given in recent years to the area of metal-organic ferroelectrics,[17-22] organic-inorganic hybrid ferroelectrics[23-27] and small molecule-based ferroelectric organic materials. These molecules possess advantages such as easy synthesis, lightweight, high flexibility, high thermal stability and reasonable Curie temperature.[28-29] However, several of these materials exhibit ferroelectric to paraelectric phase transition temperatures well below or slightly closer to the room temperature and hence will be of limited utility to practical applications. In fact, ferroelectric materials whose electrically polarizable domains in the direction of the applied field do not show any notable curie behaviour (T_c) before the melting point temperature are rare in the literature.[30-32] Recently, we have reported phosphorus (V) based organic salt, diphenyl diisopropylamino phosphonium hexafluorophosphate ($DPDP{\cdot}PF_6$), which shows an excellent ferroelectric response, very high phase stability, good dielectric and piezoelectric response. Further, its composites with poly(dimethyl)siloxane were utilized for mechanical energy harvesting application.[33] Inspired by these findings, we set out to look at the various salts of DPDP cation and investigate their structural, thermal and polarization attributes. Herein, we report the synthesis, structure and potential ferroelectric properties for the halide salts of diphenyl diisopropylamino phosphonium cation, DPDP·X (X = Cl, Br and I). Further, these polar ionic salts were shown to exhibit dielectric, piezoelectric and second harmonic generation (SHG) activity at room temperature.

2.2 Experimental section

2.2.1 General remarks

All the manipulations involving phosphorus halides were carried out under dry nitrogen conditions in standard Schlenk glassware. The dichloromethane (CH_2Cl_2) solvent was dried over phosphorus pentaoxide (P_2O_5). Diphenylchlorophosphine (Ph_2PCl), isopropylamine, liquid bromine (Br_2) Sodium chloride (NaCl) and Sodium iodide (NaI) were purchased from Sigma Aldrich and used as received. The NMR spectra were recorded in deuterated chloroform ($CDCl_3$) on a Bruker 400 MHz spectrometer (^{1}H NMR, 400.13 MHz; ^{13}C {^{1}H} NMR, 100.62 MHz; ^{31}P {^{1}H} NMR, 161.97 MHz, at room temperature using $SiMe_4$ (^{1}H, ^{13}C) and 85% H_3PO_4 (^{31}P) as standards. The ESI and MALDI-TOF spectra were obtained by using Waters Synapt G2 and the Applied Biosystem MALDI-TOF/TOF spectrometers, respectively. FT-IR spectrum was performed on a Perkin-Elmer spectrometer with samples prepared as KBr pellets. The variable temperature powder X-ray diffraction data were measured in the 2-theta range of 5° to 50° on a Bruker-D8 Advance X-ray diffractometer. The thermogravimetric analysis was performed by using the PerkinElmer STA-6000 analyzer with a heating rate of 10 °C/min in a nitrogen atmosphere. Melting point analyses were performed by using the Electrothermal melting point apparatus and were uncorrected.

2.2.2 Synthesis

2.2.2.1 Synthesis of diphenyl diisopropylaminophosphonium bromide (DPDP·Br): The starting compound of DPDP·Br was synthesized by our earlier reported procedure.[33]

2.2.2.2 Synthesis of diphenyl diisopropylaminophosphonium chloride (DPDP·Cl): To a stirred solution of DPDP·Br (1 g, 0.0026 mol) in methanol (20 mL), NaCl (0.46 g, 0.0078 mol) in water (10 mL) was slowly added with the formation of

NaBr precipitate. The reaction mixture was stirred at room temperature for a further period of 10-15 min. and filtered through celite. The obtained clear solution was left out for the crystallization. Colorless plate-like crystals of DPDP·Cl were obtained after one week. Yield: 0.85 g (97%). M.P. 224-229°C. ^{1}H NMR (400 MHz, $CDCl_3$) δ 8.05 – 7.97 (m, 4H), 7.62 – 7.55 (m, 2H), 7.50 – 7.45 (m, 4H), 6.75 – 6.69 (m, 2H), 3.37 – 3.25 (m, 2H), 1.20 (d, *J* = 6.5 Hz, 12H). ^{13}C NMR (100 MHz, $CDCl_3$) δ 133.87, 133.15, 129.35, 125.34, 44.65, 24.80. ^{31}P NMR (162 MHz, $CDCl_3$): δ 34.74 ppm. FT-IR data in KBr pellet (cm^{-1}): 3141, 2967, 2882, 2729, 1591, 1426, 1312, 1161, 1075, 1020, 919, 892, 832, 751, 726, 699 and 615. MALDI-TOF = 301.1828 [M$^+$]. Anal. Calcd. For $C_{18}H_{26}ClN_2P$: C 64.18; H 7.78; N 8.32. Found: C 64.11; H 7.71; N 8.30.

2.2.2.3 Synthesis of diphenyl diisopropylaminophosphonium iodide (DPDP·I): To a stirred solution of DPDP·Br (1 g, 0.0026 mol) in any one of the solvent systems such as MeOH, MeOH/H_2O, MeCN, MeCN/H_2O, MeCN/MeOH, (20 mL), NaI (1.17 g, 0.0078 mol) in water (10 mL) was slowly added with the formation of NaBr precipitate. The reaction mixture was stirred at room temperature for a further period of 10-15 min. And filtered through celite. The obtained clear solution was left out for the crystallization. Colourless crystals of any one of the two polymorphic phase of DPDP·I (PM1) or DPDP·I (PM2) were obtained after seven days.

Synthesis of Polymorph DPDP·I (PM1): M.P. 203-207 °C. ^{1}H NMR (400 MHz, $CDCl_3$) δ 7.99 – 7.93 (m, 4H), 7.70 – 7.65 (m, 2H), 7.59 – 7.54 (m, 4H), 5.39 – 5.33 (m, 2H), 3.50 – 3.38 (m, 2H), 1.28 (d, *J* = 6.5 Hz, 12H). ^{13}C NMR (100 MHz, $CDCl_3$) δ 134.52, 133.18, 129.69, 124.05, 45.25, 25.06. ^{31}P NMR (162 MHz, $CDCl_3$): δ 35.40 ppm. FT-IR data in KBr pellet (cm^{-1}): 3142, 2973, 2935, 1584, 1422, 1315, 1165, 1056, 1020, 915, 899, 832, 754, 725, 693, and 624. MALDI-TOF = 301.1828 [M$^+$]. Anal. Calcd. For $C_{18}H_{26}IN_2P$: C 50.48; H 6.12; N 6.54. Found: C 50.45; H 6.10; N 6.53.

Synthesis of Polymorph DPDP·I (PM2): M.P. 203-205 °C. ^{1}H NMR (400 MHz, $CDCl_3$) δ 8.01 – 7.94 (m, 4H), 7.67 – 7.63 (m, 2H), 7.57 – 7.52 (m, 4H), 5.52 – 5.47 (m, 2H), 3.52 – 3.41 (m, 2H), 1.28 (d, *J* = 6.5 Hz, 12H). ^{13}C NMR (100 MHz, $CDCl_3$) δ 134.43, 133.25, 129.62, 124.13, 45.21, 25.06. ^{31}P NMR (162 MHz, $CDCl_3$): δ 35.12 ppm. FT-IR data in KBr pellet (cm^{-1}): 3127, 2967, 2929, 1590, 1436, 1308, 1161, 1053, 1019, 916, 890, 830, 754, 726, 690, and 624. MALDI-TOF = 301.1828 [M^+]. Anal. Calcd. For $C_{18}H_{26}IN_2P$: C 50.48; H 6.12; N 6.54. Found: C 50.45; H 6.10; N 6.53.

2.2.3 Crystallography

Single crystal X-ray diffraction data for DPDP·Br, DPDP·Cl, and DPDP·I (PM1 & PM2), at various temperatures were obtained on a Bruker Smart Apex Duo diffractometer by using Mo Kα radiation (λ= 0.71073Å). The structures were solved by intrinsic or direct methods and then refined by full-matrix least-squares against F^2 using all data by using SHELXL-2014/7 built in the Apex 3 program.[34] Crystallographic refinement data for these compounds are listed in Table S1. All the non-hydrogen atoms were refined anisotropically. Hydrogen atoms were constructed in geometric positions to their parent atoms.[35] The bond distances and angles and structural illustrations were obtained by using the DIAMOND-3.1 software package.

Table 2.1: Details of crystallographic data collection and structure refinements for DPDP·Cl, DPDP·Br, DPDP·I (PM1) and DPDP·I (PM2).

Compound	**DPDP·Cl**	**DPDP·Cl**	**DPDP·Br**	**DPDP·Br**
Chemical formula	$C_{18}H_{26}ClN_2P$	$C_{18}H_{26}ClN_2P$	$C_{18}H_{26}BrN_2P$	$C_{18}H_{26}BrN_2P$
Formula weight	336.83	336.83	381.29	381.29
Temperature	100(2)K	373(2)K	100(2)K	373(2)K
Crystal system	Orthorhombic	Orthorhombic	Orthorhombic	Orthorhombic
Space group	$Pna2_1$	$Pna2_1$	$Pna2_1$	$Pna2_1$
a (Å); α (°)	14.820(3): 90	14.976(8): 90	14.851(4): 90	14.966(6): 90
b (Å); β(°)	13.479(3): 90	13.602(6): 90	13.856(3): 90	13.906(6): 90
c (Å); γ (°)	9.4805(17): 90	9.504(5): 90	9.599(2): 90	9.583(4): 90
V ($Å^3$); Z	1893.8(6): 4	1936.0(17): 4	1975.3(8): 4	1994.4(15): 4
ρ (calc.) g cm^{-3}	1.181	1.156	1.282	1.270
μ(Mo K_α) mm^{-1}	0.285	0.279	2.161	2.141
$2\theta_{max}$ (°)	55.76	55.74	55.75	54.96
R(int)	0.0630	0.0560	0.0324	0.0767
Completeness to θ	100	100	100	100
Data / param.	4521/ 175	3856/ 175	4082/ 175	4102/ 175
GOF	1.041	1.021	1.071	1.029
R1 [F>4σ(F)]	0.0414	0.0414	0.0198	0.0461
wR2 (all data)	0.1175	0.1177	0.0513	0.1303
max. peak/hole (e.$Å^{-3}$)	0.706/-0.382	0.354/-0.156	0.321/-0.438	0.448/-0.479

Compound	DPDP·I(PM1)	DPDP·I(PM1)	DPDP·I(PM2)	DPDP·I(PM2)
Chemical formula	$C_{18}H_{26}IN_2P$	$C_{18}H_{26}IN_2P$	$C_{18}H_{26}IN_2P$	$C_{18}H_{26}IN_2P$
Formula weight	428.28	428.28	428.28	428.28
Temperature	100(2)K	373(2)K	100(2)K	373(2)K
Crystal system	Monoclinic	Monoclinic	Monoclinic	Monoclinic
Space group	*Cc*	*Cc*	$P2_1$	$P2_1$
a (Å); α (°)	15.2497(15): 90	15.3375(17): 90	9.602(10): 90	9.6471(13): 90
b (Å); β(°)	9.0129(9): 102.343(2)	9.1435(10): 102.476(3)	15.137(15): 92.026(19)	15.345(2): 92.161(3)
c (Å); γ (°)	14.6473(15): 90	14.7606(17): 90	13.562(15): 90	13.770(2): 90
V (Å^3); Z	1966.6(3): 4	2021.1(4): 4	1970.(4): 4	2037.0(5): 4
ρ (calc.) g cm^{-3}	1.446	1.407	1.444	1.396
μ(Mo K_α) mm^{-1}	1.709	1.663	1.706	1.650
$2\theta_{max}$ (°)	56.58	55.74	53.46	54.96
R(int)	0.0330	0.0532	0.0600	0.0701
Completeness to θ	100	100	100	100
Data / param.	4451/ 175	3927/ 175	8349/349	8293/357
GOF	1.068	1.042	1.011	1.020
R1 [F>4σ(F)]	0.0194	0.0385	0.0279	0.0432
wR2 (all data)	0.0426	0.1000	0.0595	0.1063
max. peak/hole (e.Å^{-3})	0.370/-0.579	0.861/-0.721	0.304/-0.398	0.525/-0.638

2.2.4 Ferroelectric and dielectric measurements

The temperature dependent ferroelectric measurements were performed on the single crystals of DPDP·Br, DPDP·Cl and DPDP·I (PM1 & PM2) using a Sawyer-Tower circuit at an operating frequency of 20 to 50 Hz. The single crystal of these organo amino phosphonium salts was deposited with a conducting silver paste prior to the measurements. The polarization (*P*) vs. Electric Field (*E*) measurements were performed on an aixACCT TF-2000E model hysteresis loop analyzer. Further, the electric field dependent dielectric polarization of these samples was performed on their single crystals of DPDP·Br, DPDP·Cl and DPDP·I (PM1 & PM2) by keeping the frequency constant at different voltages. The temperature and frequency dependent dielectric constants were measured in a Novocontrol Dielectric Spectrometer. The frequency dependent dielectric polarization of all the phosphonium halides was performed on their single crystals between 100 Hz and 1 MHz by using LCR meter. The observed capacitance value of these salts further converted into dielectric constant. The d_{33} measurements were performed on a Piezotest meter model PM300 on the single crystals of DPDP·Br, DPDP·Cl and DPDP·I (PM1 & PM2).[36] The theoretical dipole moment of the all the phosphonium salts was calculated by using the Gaussian 09 program. The phosphonium cation assigned as a lower layer and anionic part as a selected high layer to perform the ONIOM calculation. The dipole moment calculations were performed by using the DFT methods.[37]

2.2.5 Second harmonic generation measurements

The second harmonic generation (SHG) analysis of all the synthesized phosphonium salts was measured by using Kurtz and Perry method. The irradiation frequency of 1064 nm was generated by using Q-switched Nd:YAG laser. For the SHG measurements, the unsieved powders of the sample obtained from the ground single crystals were filled into a capillary tube, and a powdered KDP sample was used as a reference. The intensities of the output emitted from the samples were detected by a photomultiplier tube.

2.2.6 Piezoresponse force microscopy (PFM) measurements

In the PFM study, the alternating current (AC) voltage is kept constant at 2.5 V and the applied external electric field from the metal (Pt-Ir) coated conductive tip is perpendicular to the as-prepared thin film of samples. For this study, the thin films of DPDP·Br, DPDP·Cl and DPDP·I (PM1 & PM2) samples were spin-coated on the ITO/Glass substrate and annealed at 120°C. The polarization switching and local piezoelectric responses of all the thin film samples were studied at room temperature with an Asylum Research MFP-3D atomic force microscope working in contact mode. An ASYLEC-01 cantilever made of a tetrahedral silicon tip coated with titanium / Iridium (5/20) was used to apply a small A.C. voltage with an amplitude of 2.5 V. Measurements were performed by applying two oscillating voltages with frequencies below and above resonance (320 kHz), operating the cantilever in the dual a.c. Resonance tracking mode.

2.3 Results and discussion

2.3.1 Synthesis, characterization and crystal structures: The bromo-salt $[Ph_2(^iPrNH)_2P]\cdot Br$ (DPDP·Br) was synthesized starting from Ph_2PCl via bromination reaction followed by the addition of $^iPrNH_2$. The corresponding $[Ph_2(^iPrNH)_2P]\cdot Cl$ and $[Ph_2(^iPrNH)_2P]\cdot I$ salts (DPDP·Cl and DPDP·I) were synthesized via halogen exchange reactions of DPDP·Br with excess equivalents of sodium chloride and sodium iodide, respectively. The DPDP·Cl and DPDP·I salts was directly isolated as single crystals from their aqueous methanolic reaction mixtures (Scheme 2.1 and Figures 2A.1-2A.3, Appendix 2).

Scheme 2.1: Synthesis of organoamino phosphonium salts DPDP·Cl, DPDP·Br, DPDP·I (PM1) and DPDP·I (PM2).

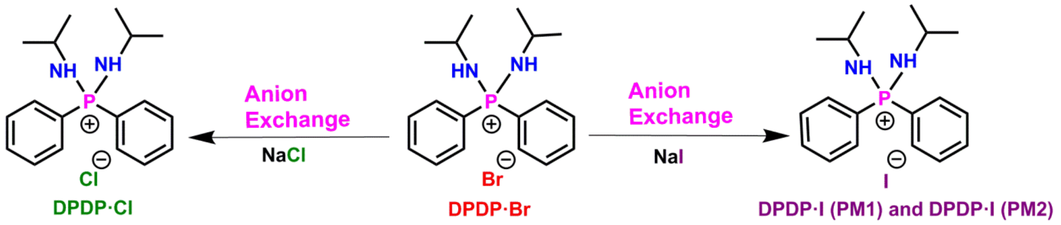

The single crystal X-ray diffraction analysis confirmed the formation of all these three binary salts. The structural analysis of DPDP·Cl and DPDP·Br reveals the presence of non-centrosymmetric polar symmetry as both of them were crystallized in the orthorhombic space group $Pna2_1$ (Figure 2A.4, Appendix 2). Surprisingly the iodide salt, DPDP·I, was found to randomly crystallize in two polymorphic phases of monoclinic *Cc* (PM1) and monoclinic $P2_1$ (PM2) space groups (Figure 2A.5, Appendix 2). While the most prevalent polymorphic phase was observed to be PM1, the number of instances of isolating the PM2 phase was also not too low. Altering the solvent systems with MeOH, MeOH/H_2O, MeCN, MeCN/H_2O, MeCN/MeOH, however, did not consistently yield any one of the single polymorphic phase. The phase purity of each of the polymorphic phase in every batch of crystallization was confirmed by a careful powder X-ray diffraction (PXRD) analysis. The X-ray analysis of all these salts shows the presence of one unit of phosphonium salt in the asymmetric unit, except DPDP·I (PM2) which contains two phosphonium cations and two iodide anions in the asymmetric unit. The phosphonium centres in them exhibit a distorted tetrahedral geometry (Figures 2.1a,c and 2.2a,c). The N-P-N angles in all these assemblies range from 108.2(2) to 120.554(132)^o signifying the involvement of the N-H protons in the H-bonding sites. The crystal structure revealed the presence of 1D-hydrogen bonding chain structures assisted by the N-H…X interactions (Figures 2.1b-2.1d and 2.2b-2.2d). In both DPDP·Cl and DPDP·Br, the adjacent phosphonium halides are arranged anti-parallel (trans-oriented) to each other giving rise to zigzag H-bonded chains (Type 1) along the b-axis. Whereas in the *c*-centred polymorph of DPDP·I (PM1), a parallel (cis-oriented) arrangement of the adjacent phosphonium iodides along the b-axis was observed resulting in a corrugated H-bonded 1D-chains (Type 2).

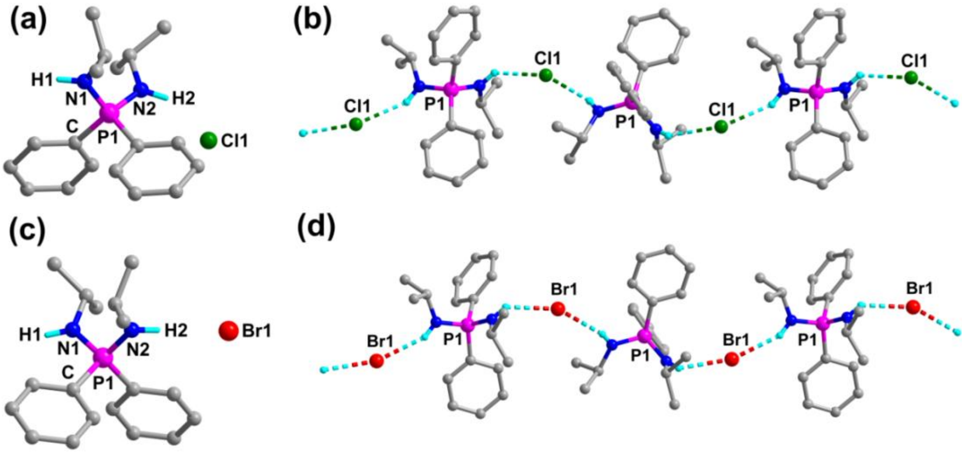

Figure 2.1: *Molecular structure of DPDP·Cl (a) and DPDP·Br (c) and their 1-D hydrogen-bonded structures (b and d).*

Interestingly, in the *P*-centred polymorph PM2, with two molecules in the asymmetric unit, both types of H-bonds exist. Thus, the binary fragment containing P1 and I1 moieties exhibit Type 2 like interactions (along a-axis) and the H-bonded chains of P2…I2 fragments exhibit Type 1 like interactions (along b-axis). The observed hydrogen bond distance and angles were found to be comparable with those observed for the other amino-phosphonium salts (Tables 2.1, 2A.1 and 2A.2, Appendix 2).[38-39] The N…X…N angles in the present instance were measured to be flexible and range from 114.35 (83) to 153.95 (81)°. The P-N-H…X torsion angles found in the Type 2 chains of DPDP·I (polymorphs PM1 and PM2) are in the range between 114.77(354) and 120.67(282)°. In contrast, these torsion angles were found to be acute (ranging from 95.88(20) to 97.26(461)°) in one side and obtuse (from 134.66(442) to 137.39(25)°) in the other side, in all the zigzag chains derived from Type 1 H-bonding (Table 2A.3, Appendix 2). Besides, the ortho H-atoms of one of the phenyl rings were involved in a C-H…X type interactions in all these assemblies along the 1D-chain.

The other derivatives of aminophosphonium salts supported monoatomic halide ions were shown to crystallize in centro and non-centrosymmetric space groups (Table 2A.4, Appendix 2).

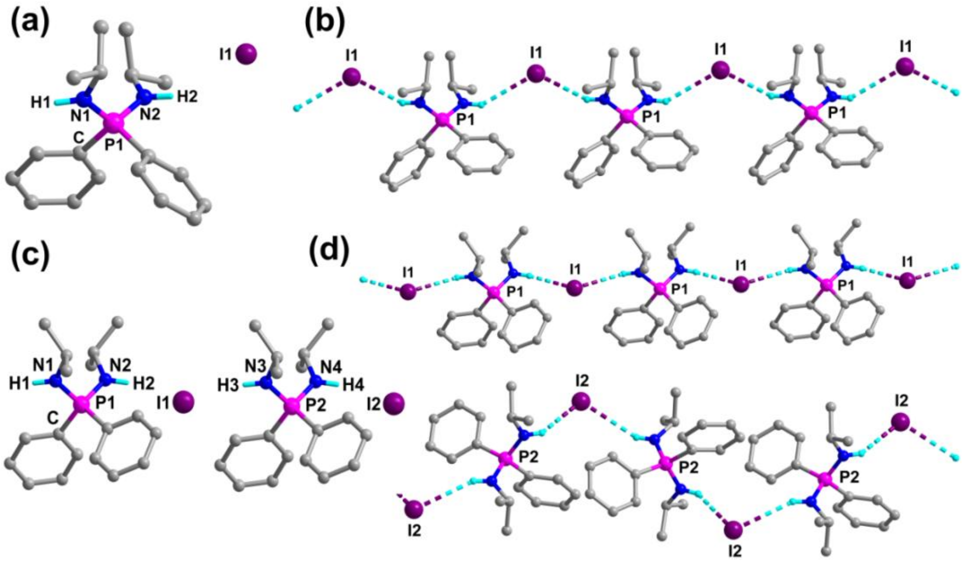

Figure 2.2: *Molecular structures of DPDP·I (PM1) (a) and DPDP·I (PM2) (c) their 1-D hydrogen-bonded structures (b and d).*

Further to identify any curie symmetry in these polycrystalline solids, we performed variable temperature single-crystal X-ray diffraction analysis (VT-SCXRD) between 100 and 473 K (close their melting points). These investigations showed the absence of phase transitions in the entire range of temperatures for these phosphonium salts, albeit with some marginal changes in the lattice parameters at higher temperatures. Particularly, inter-conversion between the polymorphs of DPDP·I (PM1 to PM2 and vice versa) was observed to absent (Figures 2A.6-2A.9, Appendix 2). However, there are marked volume changes observed around 375 K in all these salts, which might be due to the thermal motion of atoms at higher temperatures leading to a volume expansion of the unit cells.

The variable temperature PXRD analysis also supports these observations as the experimental PXRD patterns match exactly to the simulated patterns at any given temperature. Examination of the thermogravimetric analysis (TGA) coupled with differential thermal studies (DTA) reveals two heat anomalies for each of these halide salts above 473 K. While the first ones are associated with their melting point, the second ones (above 550 K) are corresponding to their decomposition (Figures 2A.10-2A.12, Appendix 2).

2.3.2 Ferroelectric, piezoelectric and dielectric studies

The point group symmetries of DPDP·Cl (C_{2v}), DPDP·Br (C_{2v}) and DPDP·I [polymorph PM1 (C_S) and polymorph PM2 (C_2)] are compatible with one of the 10 polar point groups associated with ferroelectricity.[40] The polarization versus electric field (*P*-*E*) loops of all these phosphonium salts were performed on their single crystals with an operating frequency of 30 Hz at room temperature. The observed spontaneous polarization (P_S) values of DPDP·Cl, DPDP·Br, DPDP·I (PM1) and DPDP·I (PM2) were found to be 0.0089, 0.0108, 0.0095 and 0.0127 μC cm^{-2}, respectively (Figure 2.3a-d). The coercive field (E_c) values of DPDP·Cl, DPDP·Br, DPDP·I (P1) and DPDP·I (P2) were relatively smaller and found to be 3.73, 3.39, 3.70 and 4.75 kV cm^{-1}, respectively.

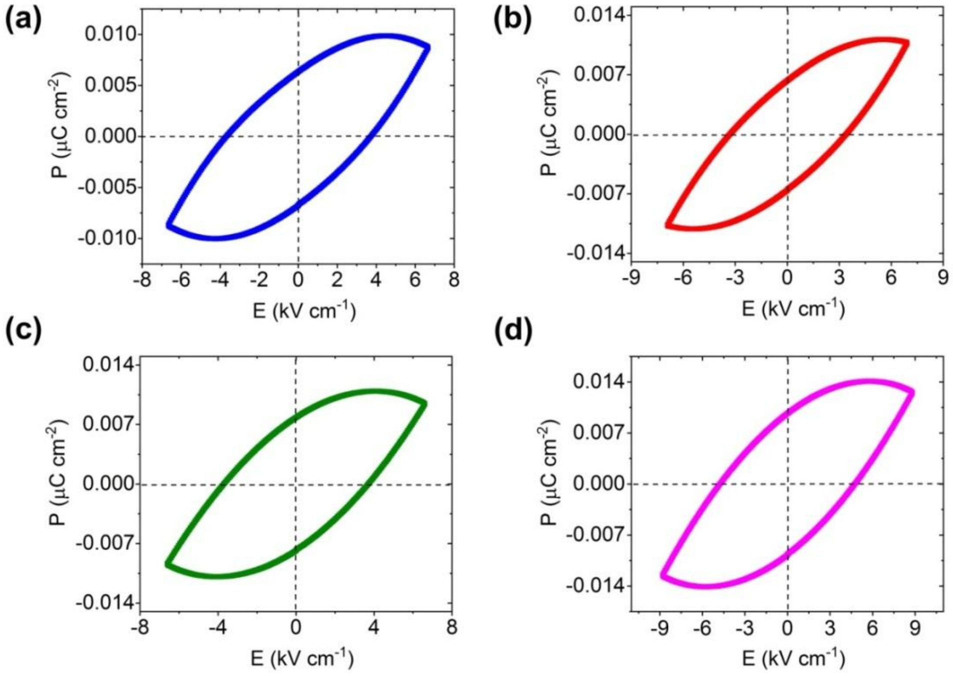

Figure 2.3: *Room temperature P-E loops for (a) DPDP·Cl, (b) DPDP·Br, (c) DPDP·I (PM1) and (d) DPDP·I (PM2) at an operating frequency of 30 Hz.*

Similar *P-E* loop characteristics have been observed for these salts in the frequency range between 20 and 50 Hz as well. Further, we performed the temperature-dependent *P-E* loop measurements for all these phosphonium compounds between 296 and 373 K. These experiments indicate a small decrease in E_c values for all these compounds, as observed for certain molecular ferroelectric materials. A concomitant minor increase in the P_s values has also been observed for all these materials signifying an improved alignment of dipoles at higher temperatures (Figures 2A.13-2A.15, Appendix 2). Since the shapes of the observed *P-E* loops are reminiscent of non-linear leaky dielectric material[1] we attempted to investigate the ferroelectric nature of these materials by electric-field dependent dielectric measurements. These results did not show any characteristic butterfly-shaped loops typical for ferroelectric materials (Figures 2A.16-2A.19, Appendix 2). However, it is to be mentioned that these field-dependant measurements have also been hampered by longer measurement times at lower frequencies.

To check the presence of electrically active polarizable ferroelectric domains, the vertical piezoresponse force microscopy (V-PFM) measurements were performed. In order to reduce the effect of electrostatic interactions, the measurements were done at the "*OFF*" state. The piezoresponse hysteresis loop can be derived and plotted using the equation PR(E) = A(E)cos[φ(E)].[41] The out of plane V-PFM analysis was performed at room temperature for the salts of DPDP·Cl, DPDP·Br, DPDP·I (PM1) and DPDP·I (PM2) in the form of polycrystalline films. Figure 2.4a is the topography image of the thin film sample of DPDP·Cl showing the lamellar shaped domains in it. Figure 2.4c and 2.4d are the corresponding amplitude image and loop obtained under the bias field of ±10 V. The Figure. 2.4e and 2.4f shows the phase response obtained upon switching the external electric field. Similar domain characteristics have been observed as well for the salts of the other halide ions (Figure 2A.20, Appendix 2). These polarizable domains were shown to exhibit field dependant orientations and can be switched in the upward or downward directions under the external field depicting the possibility of ferroelectric behaviour in these materials.

The magnitude of piezoelectric polarizations for the films of these phosphonium salts was extracted from the piezoresponse loops presented in the Figures 2.4b and 2A.20 (Figures 2A.20f and 2A.20i, Appendix 2). The converse piezoelectric coefficient values of 8, 7 and 14 pm V^{-1} were obtained for the salts of DPDP·Cl, DPDP·I (PM1) and DPDP·I (PM2), respectively.

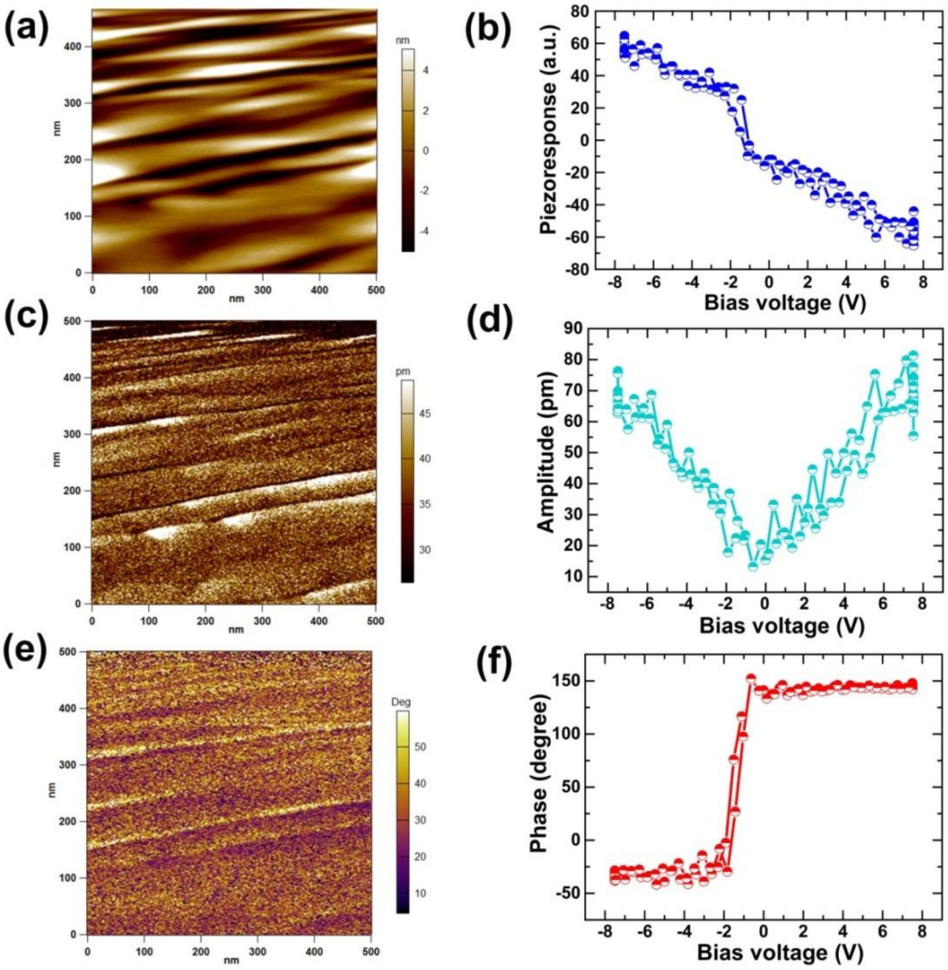

Figure 2.4: *The room temperature V-PFM analysis of DPDP·Cl showing (a) the topography of lamellar shaped domains, (b) piezoresponse loop, (c) amplitude and (e) phase images and the corresponding (d) amplitude-voltage (f) phase-voltage loops.*

Further, the direct piezoelectric response of these phosphonium halides on their as-grown single crystals was derived from the quasi-static method by using a d_{33} piezometer at an operating frequency of 110 Hz and with an applied mechanical stress of 0.25 N.[42] The observed d_{33} values of 3, 4, 7 and 8 pC N^{-1} for DPDP·Cl, DPDP·Br, DPDP·I (PM1) and DPDP·I (PM2) illustrate the existence of thermally stable preferential orientation of electric domains in all of them. The Figure. 2.5a shows the trends in the piezoelectric coefficient (d_{33}) values which correlate well with the increasing polarizability of these halide ions as well as with their corresponding computed dipole moments. The d_{33} coefficients obtained for these phosphonium salts compares well with those observed for the known molecular ferro- and piezoelectric materials.[43-44]

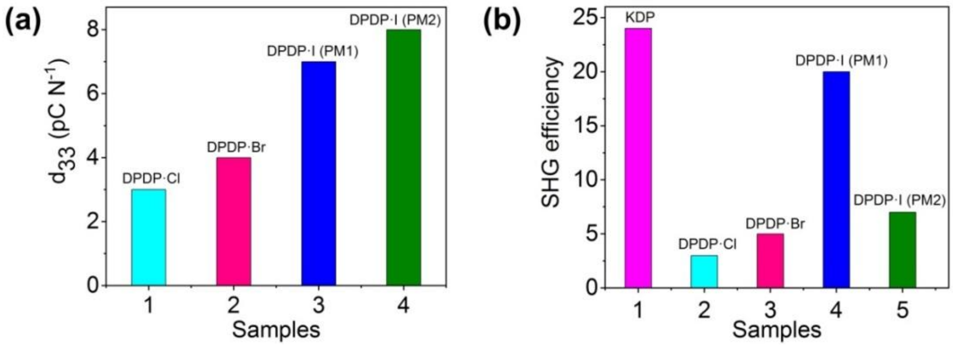

Figure 2.5: *(a) Direct piezoelectric coefficient* (d_{33}) *and (b) SHG efficiencies of the phosphonium halides at room temperature.*

Furthermore, the existence of acentric crystal structures for all these phosphonium salts is authenticated by preliminary non-linear optical measurements. The second harmonic generation (SHG) activity on the unsieved polycrystalline samples of these salts was investigated by using Kurtz and Perry method.[45] These measurements indicated that these organo amino phosphonium salts are SHG active at room temperature. The SHG efficiencies of 0.13, 0.21, 0.83, and 0.29 with respect to KH_2PO_4 (KDP: 1.00) were obtained for the respective DPDP·Cl, DPDP·Br, DPDP·I (PM1) and DPDP·I (PM2) salts (Figure 2.5b). Further, the SEM images of the unsieved particles that are utilized for the SHG measurements show that the majority of the particles were in the range between 1 to 10 μm (Figure 2A.21, Appendix 2).

The existence of polarization on the bulk samples of these phosphonium salts was determined by dielectric permittivity studies on their compacted pellets. The temperature dependence of dielectric permittivity (ε_r) and loss (tan δ) of all these compounds were examined at different frequencies in the range between 1 kHz and 10 MHz (Figure 2.6a-d). The real part of dielectric constant (ε') values of DPDP·Cl, DPDP·Br, DPDP·I (PM1) and DPDP·I (PM2) at room temperature were observed to be similar and measures at 6.69, 6.95, 6.99 and 7.07, respectively, at the operating frequency 10 MHz. However, at higher temperatures, the polymorph PM2 of DPDP·I shows a higher dielectric constant value than that of its polymorph PM1. This can be attributed to two unique types of H-bonding present in their unit cell packing. Also, a slight increase in the ε' values of DPDP·Cl, DPDP·Br, DPDP·I (PM1) and DPDP·I (PM2) can be attributed to increasing in the polarizability of the anions upon moving from Cl to I anions that would contribute to their overall electric polarization. The values of dielectric constant and loss for each of these salts were found to increase with the increase in temperature. This suggests the dominance of ionic mobilities and non-conductive charge carriers near their respective melting points.

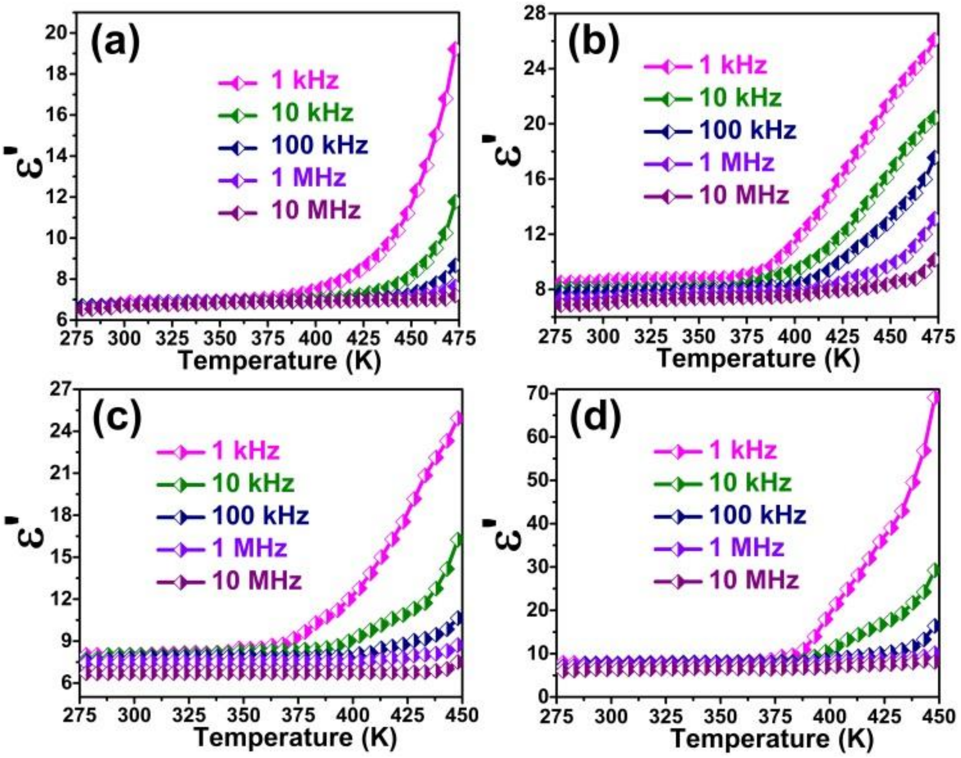

Figure 2.6: *Temperature dependence of ε' for (a) DPDP·Cl, (b) DPDP·Br, (c) DPDP·I (PM1) and (d) DPDP·I (PM2).*

The theoretical dipole moments of these phosphonium salts were extracted by performing the ONIUM calculations built in the Gaussian software. The calculated dipole moment values of 17.33, 17.97, 21.29 and 69.14 D for DPDP·Cl, DPDP·Br, DPDP·I (PM1) and DPDP·I (PM2), respectively, support the observed trends in their polarization and permittivity values (Table 2A.5, Appendix 2). The absence of curie symmetry or structural phase transition in these organic salts is due to the presence of robust hydrogen bonding between the cations and the anions in their crystal lattice.[46-49] Furthermore, we performed the frequency dependent dielectric constant measurements with the change in temperatures (Figures 2A.22-2A.29, Appendix 2).

A similar set frequency dependent data has been obtained at room temperature for the single crystal samples as well (Table 2A.6, Appendix 2). The evaluation of dielectric constants at lower frequencies indicates the contribution of all the polarization (Interface, dipolar, ionic and atomic) mechanisms to the overall macroscopic polarization.[50-51]

2.4 Conclusion

In summary, we have synthesized and structurally characterized a series of organoamino phosphonium halide salts which show dielectric, piezoelectric and NLO properties. The possible ferroelectric nature of these salts has also been investigated by the *P-E* loop and piezoresponse force microscopy measurements. The robust nature of these binary polar salts is exemplified by their thermal stability and phase purity for a wide range of temperatures. While the *P-E* loop results are inconclusive and reminiscent of a leaky non-linear dielectric material, the PFM studies show the promise of these materials as potential ferroelectric substances. Since the 1D-hydrogen bonded chain structures of these asymmetric salts facilitate the long-range alignment of dipoles that are responsible for their permanent polarization, a careful choice of the counter anions along with the DPDP cation would lead to a material with improved ferroelectric characteristics. Currently, we are focussed on employing several heteroleptic phosphonium cations towards the syntheses of a family of ferroelectric organic salts and their utility in piezoelectric energy harvesting applications.

2.5 References

(1) Lines, M. E.; Glass, A. M. *Principles and Applications of Ferroelectrics and Related Materials*; Oxford University Press: New York, 1977.

(2) Scott, J. F. *Ferroelectric memories*, Springer Science & Business Media, 2013.

(3) De Araujo, C. A. P.; Cuchiaro, J. D.; Mc Millan, D. L.; Scott, M. C.; Scott, J. F. *Nature* **1995**, *374*, 627–629.

(4) Han, S.T.; Zhou, Y.; Roy, V. A. L. *Adv. Mater.* **2013**, *25*, 5425–5449.

(5) Scott, J. F. *Science* **2007**, *315*, 954–959.

(6) Fan, Z.; Sun, K.; Wang, J. *J. Mater. Chem. A*, **2015**, *3*, 18809–18828.

(7) Yu, H.; Chung, C. C.; Shewmon, N.; Ho, S.; Carpenter, J. H.; Larrabee, R.; Sun, T.; Jones, J. L.; Ade, H.; O'Connor, B. T.; So, F. *Adv. Funct. Mater*., **2017**, *27*, 1700461.

(8) Uchino, K. *Ferroelectric Devices*, CRC Press, 2nd edn, 2009.

(9) Scott, J. F. *Ferroelectric memories*, Springer Science & Business Media, 2013.

(10) Xu, Y. *Ferroelectric materials and their applications*, Elsevier, 2013.

(11) Yuan, Y.; Xiao, Z.; Yang, B.; Huang, J. *J. Mater. Chem. A* **2014**, *2*, 6027–6041.

(12) Butler, K. T.; Frost, J. M.; Walsh, A. *Energy Environ. Sci*., **2015**, *8*, 838–848.

(13) Mingabudinova, L. R.; Vinogradov, V. V.; Milichko, V. A.; Hawkins, E. H.; Vinogradov, A. V. *Chem. Soc. Rev*., **2016**, *45*, 5408–5431.

(14) Haertling, G. H. *J. Am. Ceram. Soc*. **1999**, *82*, 797-818.

(15) Saito, Y.; Takao, H.; Tani, T.; Nanoama, T.; Takatori, K.; Homma, T.; Nagaya, T.; Nakamura, M. *Nature*, **2014**, *432*, 84–87.

(16) Tayi, A. S.; Kaeser, A.; Matsumoto, M.; Aida, T.; Stupp, S. I. *Nat. Chem*., **2015**, *7*, 281–294.

(17) Srivastava, A. K.; Praveenkumar, B.; Mahawar, I. K.; Divya, P.; Shalini, S.; Boomishankar, R. *Chem. Mater*. **2014**, *26*, 3811–3817.

(18) Srivastava, A. K.; Divya, P.; Praveenkumar, B.; Boomishankar, R. *Chem. Mater.* **2015**, *27*, 5222–5229.

(19) Srivastava, A. K.; Vijayakanth, T.; Divya, P.; Praveenkumar, B.; Steiner, A.; Boomishankar, R. *J. Mater. Chem. C* **2017**, *5*, 7352–7359.

(20) Yadav, A.; Srivastava, A. K.; Kulkarni, P.; Divya, P.; Steiner, A.; Praveenkumar, B.; Boomishankar, R. *J. Mater. Chem. C* **2017**, *5*, 10624–10629.

(21) Yadav, A.; Kulkarni, P.; Steiner, A.; Praveenkumar, B.; Boomishankar, R. *Chem. Eur. J.* **2018**, *24*, 14639–14643.

(22) Stroppa, A.; Barone, P.; Jain, P.; Perez-Mato, J. M.; Picozzi, S. *Adv. Mater*., **2013**, *25*, 2284–2290.

(23) Li, W.; Wang, Z.; Deschler, F.; Gao, S.; Friend, R. H.; Cheetham, A. K. *Nat. Rev. Mater*., **2017**, *2*, 16099.

(24) Tammam, A. K.; El-Dean, T. S.; Mostafa, M. F. *Ferroelectrics* **2015**, *481*, 34–40.

(25) Zhao, W. P.; Shi, C.; Stroppa, A.; Di Sante, D.; Cimpoesu, F.; Zhang, W. *Inorg. Chem*., **2016**, *55*, 10337–10342.

(26) Li, L.; Sun, Z.; Wang, P.; Hu, W.; Wang, S.; Ji, C.; Hong, M.; Luo, J. *Angew. Chem. Int. Ed*., **2017**, *56*, 12150–12154.

(27) Sun, Z.; Zeb, A.; Liu, S.; Ji, C.; Khan, T.; Li, L.; Hong, M.; Luo, J. *Angew. Chem. Int. Ed.*, **2016**, *55*, 11854–11858.

(28) Tang, Y. Y.; Li, P. F.; Liao, W. Q.; Shi, P. P.; You, Y. M.; Xiong, R. G. *J. Am. Chem. Soc.* **2018**, *140*, 8051–8059.

(29) Asadi, K.; van der Veen, M. A. *Eur. J. Inorg. Chem.* **2016**, *27*, 4332–4344.

(30) Horiuchi, S.; Tokura, Y. *Nat.Mater*, **2008**, *7*, 357–366.

(31) Horiuchi, S.; Kobayashi, K.; Kumai, R.; Ishibashi, S. *Nat. Commun*, **2017**, *8*, 14426.

(32) Hu, L.; Feng, R.; Wang, J.; Bai, Z.; Jin, W.; Zhang, L.; Nie, Q. M.; Qiu, Z. J.; Tian, P.; Cong, C.; Zheng, L.; Liu, R. *Adv. Funct. Mater.* **2018**, *28*, 1705463.

(33) Vijayakanth, T.; Srivastava, A. K.; Ram, F.; Kulkarni, P.; Shanmuganathan, K.; Praveenkumar, B.; Boomishankar, R. *Angew. Chem. Int. Ed.* **2018**, *57*, 9054–9058.

(34) Sheldrick, G. M. Crystal Structure Refinement with SHELXL, *Acta Crystallogr. Sect. C.* **2015**, *71*, 3–8.

(35) Spek, A. L. *Acta Crystallogr., Sect. D* **2009**, *D65*, 148–155.

(36) Li, X.; Chen, C.; Deng, H.; Zhang, H.; Lin, D.; Zhao, X.; Luo, H. *Crystals* **2015**, *5*, 172–192.

(37) Frisch, M.; Trucks, G.; Schlegel, H. *Gaussian 03, Revision B. 05, Gaussian, Inc., Wallingford*, CT, **2004**.

(38) Gupta, A. K.; Nicholls, J.; Debnath, S.; Rosbottom, I.; Steiner, A.; Boomishankar, R. *Cryst. Growth Des.* **2011**, *11*, 555–564.

(39) De la Fuente, G. F.; Huheey, J. E. *Phosphorus, Sulfur, Silicon Relat. Elem.*, **1993**, *78*, 23–36.

(40) Li, J.; Liu, Y.; Zhang, Y.; Cai, H. L.; Xiong, R. G. *Phys. Chem. Chem. Phys.*, **2013**, *15*, 20786–20796.

(41) Xiao, X.; Ong, W. L.; Guo, Z. M.; Ho, G. W.; Zeng, K. Y. *ACS Appl. Mater. Interfaces*, **2015**, *7*, 11412–11422.

(42) Cain, M. G. *Characterization of ferroelectric bulk materials and thin films*. Springer, 2014.

(43) Horiuchi, S.; Tsutsumi, J.; Kobayashi, K.; Kumai, R.; Ishibashi, S. *J. Mater. Chem. C*, **2018**, *6*, 4714–4719.

(44) You, Y. M.; Liao, W. Q.; Zhao, D.; Ye, H. Y.; Zhang, Y.; Zhou, Q.; Niu, X.; Wang, J.; Li, P. F.; Fu, D. W.; Wang, Z.; Gao, S.; Yang, K.; Liu, J.; Li, J.; Yan, Y.; Xiong, R. G. *Science* **2017**, *357*, 306–309.

(45) Kurtz, S. K.; Perry, T. T. *J. Appl. Phys.*, **1968**, *39*, 3798–3813.

(46) Kobayashi, K.; Horiuchi, S.; Ishibashi, S.; Murakami, Y.; Kumai, R. *J. Am. Chem. Soc.* **2018**, *140*, 3842–3845.

(47) Narayanan, A.; Cao, D.; Frazer, L.; Tayi, A. S.; Blackburn, A. K.; Sue, A. C. H.; Ketterson, J. B.; Stoddart, J. F.; Stupp, S. I. *J. Am. Chem. Soc.* **2017**, *139*, 9186–9191.

(48) Tayi, A. S.; Shveyd, A. K.; Sue, A. C. H.; Szarko, J. M.; Rolczynski, B. S.; Cao, D.; Kennedy, T. J.; Sarjeant, A. A.; Stern, C. L.; Paxton, W. F.; Wu, W.; Dey, S. K.; Fahrenbach, A. C.; Guest, J. R.; Mohseni, H.; Chen, L. X.; Wang, K. L.; Fraser Stoddart, J.; Stupp, S. I. *Nature*, **2012**, *488*, 485–489.

(49) Horiuchi, S.; Kumai, R.; Tokura, Y. *J. Am. Chem. Soc.*, **2013**, *135*, 4492–4500.

(50) Stassen, I.; Burtch, N.; Talin, A.; Falcaro, P.; Allendorf, M.; Ameloot, R. *Chem. Soc. Rev.*, **2017**, *46*, 3185–3241.

(51) Volksen, W.; Miller, R. D.; Dubois, G. *Chem. Rev.*, **2010**, *110*, 56–110.

End of Chapter 2

Chapter 3

A Flexible Composite Mechanical Energy Harvester from a Ferroelectric Organoamino Phosphonium Salt

3.1 Introduction

Ferroelectric materials derived from organic and organic-inorganic hybrid assemblies have been the topic of intense research in the past decade as the alternate choice of materials for high-technique applications in the areas of energy and electronics.[1-3] In addition to their traditional utility as ferroelectric random access memories, capacitors, sensors, actuators and electromechanical transducers, they exhibit applications in the domains of photovoltaics and mechanical energy harvesters.[4-11] Harvesting energy from sustainable and renewable sources such as solar, thermal, vibrational and mechanical energy have attracted immense attention to meet the global demands of energy consumption in everyday life.[12-14] Among various approaches, converting mechanical energy into electrical energy is of tremendous interest because of the simplicity of its generation via the forces derived from pressure, bending, folding and stretching motions.[15-22] Inspired from the earlier discovery of nanogenerators based on ZnO nanowires, several piezoelectric and ferroelectric materials including inorganic perovskite ceramic materials such as barium titanate, lead titanate, lithium niobate, sodium niobate and lead zirconate titanate have been employed for energy harvesting applications.[23-26] Ferroelectrics are the subgroup of piezoelectric materials in which the electric dipoles can be reoriented or flipped by the application of an external electric field.[27-28] Since the piezoelectric coefficient is directly proportional to the electric polarization (d_{33} α εP_r), ferroelectric materials with intrinsic permanent dipole moment, high spontaneous polarization, and piezoelectric response is expected to increase the performance of the nanogenerator.[29-31]

In this context, it is desirable to prepare non-ceramic and heavy-metal free power generators for addressing certain issues pertaining to heavier elements such as high-temperature processing, high-voltage poling, toxicity and to impart improved flexibility for the devices.[32-33] Although polyvinylidene fluoride (PVDF) and its copolymers based composite materials have attracted greatly as energy harvesters due to their high piezoelectric response, achieving polar ferroelectric and piezoelectric order in these materials are still challenging.[34-35] Moreover, PVDF requires mechanical stretching, high-temperature annealing or poling and requires external additives to obtain polar ferroelectric β phase.[36-38] Alternatively, polymer composites made up of ferro- and piezoelectric organic compounds offer an attractive approach for this application. Herein, we report a flexible mechanical energy harvester derived from a simple ferroelectric phosphorus-based organic salt $Ph_2(^{i}PrNH)_2P]\cdot PF_6$ ($DPDP\cdot PF_6$) embedded in a PDMS matrix. The organo-aminophosphonium salt $DPDP\cdot PF_6$ retains its polar symmetry for a wide range of temperatures from 100 to 463 K. The ferroelectric measurements on the single crystals of this compound gave a remnant polarization (P_r) of 6.32 μC cm^{-2}. The fabricated composites with polymeric PDMS films were shown to harvest electrical energy with a maximum output voltage of 8.5 V and an output current of 0.5 μA (at 15 N impact force and 10 Hz frequency) for the composite with 10 wt % of $DPDP\cdot PF_6$. To the best of our knowledge, this is the first report for a flexible energy harvester based on a binary organic ferroelectric salt.

3.2 Experimental section

3.2.1 General Remarks

All the manipulations involving phosphorus halides were carried out under dry nitrogen conditions in standard Schlenk glassware and the under glove box. The dichloromethane (CH_2Cl_2) solvent was dried over phosphorus pentaoxide (P_2O_5). Triphenylphosphine (PPh_3), diphenylchlorophosphine (Ph_2PCl) and dichlorophenylphosphine ($PhPCl_2$) were purchased from Sigma Aldrich and used as received. Potassium hexafluorophosphate (KPF_6), polydimethylsiloxane (PDMS) and liquid bromine (Br_2) were purchased from Alfa Aesar and used as received. NMR spectra were recorded on a Bruker 400 MHz spectrometer (^{1}H NMR, 400.13 MHz; $^{13}C\{^{1}H\}$ NMR, 100.62 MHz; $^{31}P\{^{1}H\}$ NMR, 161.97 MHz, ^{19}F NMR, 377 MHz) at room temperature using $SiMe_4$ (^{1}H, ^{13}C), 85% H_3PO_4 (^{31}P) and $CFCl_3$ (^{19}F). All the NMR data were recorded in deuterated chloroform ($CDCl_3$) containing tetramethylsilane (TMS) and deuterated methanol containing trichloro fluoro methane as an internal standard. The ESI and MALDI-TOF spectra were obtained by using Waters Synapt G2 and the Applied Biosystem MALDI-TOF/TOF spectrometer, respectively. The variable temperature powder X-ray diffraction data were measured in the 2-theta range of 5° to 50° on a Bruker-D8 Advance X-ray diffractometer. The thermogravimetric analysis was performed by using the PerkinElmer STA-6000 analyzer with a heating rate of 10 °C/min in a nitrogen atmosphere. Melting point analyses were performed by using the Electrothermal melting point apparatus and were uncorrected. The second harmonic generation (SHG) effect of DPDP·PF_6 on the powdered sample was measured by using Kurtz and Perry method. The irradiation frequency 1064 nm was generated by using Q- switched Nd:YAG laser. As grown, single crystals was grinded in the form of unsieved powders, which filled into a capillary tube and powder KDP samples used as a reference for measurements.

3.2.2 Synthesis

3.2.2.1 Synthesis of DPDP·Br (diphenyl diisopropylaminophosphonium bromide): The compound DPDP·Br was synthesized by the modified literature procedure.[39] To a solution of chlorodiphenylphosphine (5.97 g, 0.0270 mol) in dry CH_2Cl_2 (20 mL) kept at -10°C under a nitrogen atmosphere, liquid Br_2 (4.32 g, 0.0270 mol) was added dropwise. The reaction mixture was stirred at -10°C under a nitrogen atmosphere for 30 minutes to yield a yellow suspension. Subsequently, freshly distilled isopropylamine (3.12 g, 0.0541 mol) and triethylamine (NEt_3) (5.47 g, 0.0541 mol) was added dropwise one by one at -10°C. The final reaction mixture was slowly warmed to the room temperature and stirred for a further period of 60 min to yield a yellow solid. Distilled water (50 mL) was added to this reaction mixture and the water-insoluble product was isolated. The crude product was purified by silica column chromatography by using 3% methanol in dichloromethane to give pure DPDP·Br as a white solid. Yield 10.15 g (98%). M.P. 221-223 °C. ^{1}H NMR (400 MHz, $CDCl_3$) δ 8.03 – 7.98 (m, 4H), 7.64 – 7.60 (m, 2H), 7.54 – 7.50 (m, 4H), 6.46 (dd, *J* = 13.5, 10.0 Hz, 2H), 3.39 – 3.28 (m, 2H), 1.23 (d, *J* = 6.5 Hz, 12H). ^{13}C NMR (100 MHz, $CDCl_3$) δ 133.92, 133.07, 129.35, 125.00, 76.71, 44.74, 24.77. ^{31}P NMR (162 MHz, $CDCl_3$): δ 34.55 ppm. MALDI-TOF = 301.1828 [M^+]. Anal. Calcd. For $C_{18}H_{26}BrN_2P$: C 56.70; H 6.87; N 7.35. Found: C 56.69; H 6.85; N 7.34.

3.2.2.2 Synthesis of DPDP·PF_6 (diphenyl diisopropylaminophosphonium hexaflurophosphate): To a stirred solution of DPDP·Br (3 g, 0.0079 mol) in methanol (20 mL), KPF_6 (2.17 g, 0.0118 mol) in water (10 mL) was slowly added with the formation of KBr precipitate. The reaction mixture was stirred at room temperature for a further period of 10-15 min. and filtered through celite.[40] The obtained clear solution was left for the crystallization process. Colorless block-shaped crystals of DPDP·PF_6 were obtained after one week. Yield: 3.45 g (98%). M.P. 195-197 °C. ^{1}H NMR (400 MHz, CD_3OD) δ 7.86 – 7.81 (m, 4H), 7.80 – 7.75 (m, 2H), 7.68 – 7.63 (m, 4H), 3.50 – 3.41 (m, 2H), 1.21 (d, *J* = 6.5 Hz, 12H). ^{13}C NMR (100 MHz, CD_3OD) δ 134.43, 132.48, 129.52, 124.63, 47.67, 43.96, 23.76. ^{31}P NMR (162 MHz, CD_3OD) δ 33.23 (s, 1P), [(-118.56 – (-162.41)] (m, 1P). ^{19}F NMR (377 MHz, CD_3OD) δ -73.78 (d, 1J (P-F) = 752 Hz , 6F). MALDI-TOF = 301.1828 [M^+]. Anal. Calcd. For $C_{18}H_{26}F_6N_2P_2$: C 48.44; H 5.87; N 6.28. Found: C 48.45; H 5.89; N 6.28.

3.2.2.3 Synthesis of TPAP·Br (triphenyl isopropylaminophosphonium bromide): The compound TPAP·Br was synthesized by the modified literature procedure.[41] To a solution of triphenylphosphine (5 g, 0.0191 mol) in dry CH_2Cl_2 (30 mL) kept at -10°C under a nitrogen atmosphere, liquid Br_2 (3.0464 g, 0.0191 mol) was added dropwise. The reaction mixture was stirred at -10°C under a nitrogen atmosphere for 30 minutes to yield a yellow suspension. Subsequently, freshly distilled isopropylamine (1.1268 g, 0.0191 mol) and triethylamine (NEt_3) (1.9289 g, 0.0191 mol) was added dropwise one by one at -10°C. The final reaction mixture was slowly warmed to the room temperature and stirred for a further period of 60 min to yield a yellow solid. Distilled water (50 mL) was added to this reaction mixture and the water-insoluble product was isolated. The crude product was purified by silica column chromatography by using 3% methanol in dichloromethane to give pure TPAP·Br as a white solid. Yield 7.50 g (98%). M.P. 250-255 °C. ^{1}H NMR (400 MHz, $CDCl_3$) δ 7.97 – 7.85 (m, 6H), 7.78 – 7.74 (m, 3H), 7.67 – 7.63 (m, 6H), 3.26 – 3.15 (m, 1H), 1.41 (d, *J* = 6.5 Hz, 6H). ^{13}C NMR (100 MHz, $CDCl_3$) δ 130.38, 129.51, 125.60, 118.48, 42.85, 20.54. ^{31}P NMR (162 MHz, $CDCl_3$): δ 35.72 ppm. MALDI-TOF = 320.1563 [M^+]. Anal. Calcd. For $C_{21}H_{23}BrNP$: C 63.01; H 5.79; N 3.50. Found: C 62.97; H 5.45; N 3.42.

3.2.2.4 Synthesis of TPAP·PF_6 (triphenyl isopropylaminophosphonium hexaflurophosphate): To a stirred solution of TPAP·Br (3 g, 0.0075 mol) in methanol (25 mL), KPF_6 (2.07 g, 0.0112 mol) in water (10 mL) was slowly added with the formation of KBr precipitate. The reaction mixture was stirred at room temperature for a further period of 10- 15 min. and filtered through celite. The obtained clear solution was left for the crystallization process. Colorless block-shaped crystals of TPAP·PF_6 were obtained after one week. Yield: 3.40 g (97%). M.P. 161-165 °C. ^{1}H NMR (400 MHz, CD_3OD) δ 7.89 – 7.80 (m, 6H), 7.79 – 7.77 (m, 3H), 7.75 – 7.70 (m, 6H), 3.38 – 3.30 (m, 1H), 1.19 (d, J = 6.5 Hz, 6H). ^{13}C NMR (100 MHz, CD_3OD) δ 135.00, 133.47, 129.93, 120.99, 47.67, 45.75, 23.87.^{31}P NMR (162 MHz, CD_3OD) δ 36.57 (s, 1P), [(-124.69 – (-160.95)] (m, 1P). ^{19}F NMR (377 MHz, CD_3OD) δ -73.84 (d, ^1J (P-F) = 752 Hz, 6F). MALDI-TOF = 320.1563 [M^+]. Anal. Calcd. For $C_{21}H_{23}F_6NP_2$: C 54.20; H 4.98; N 3.01. Found: C 54.10; H 5.01; N 3.03.

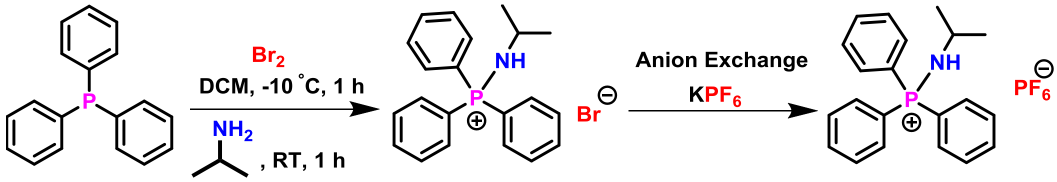

Scheme 3.1. Synthesis of TPAP·Br and TPAP·PF_6.

3.2.2.5 Synthesis of PTAP·Br (phenyl triisopropylaminophosphonium bromide): The compound PTAP·Br was synthesized by the modified literature procedure.[42] To a solution of dichlorophenylphosphine (6.56 g, 0.0368 mol) in dry CH_2Cl_2 (20 mL) kept at -10°C under a nitrogen atmosphere, liquid Br_2 (5.89 g, 0.0368 mol mol) was added dropwise. The reaction mixture was stirred at -10°C under a nitrogen atmosphere for 30 minutes to yield a yellow suspension. Subsequently, freshly distilled isopropylamine (6.53 g, 0.1105 mol) and triethylamine (NEt_3) (11.18 g, 0.1105 mol) was added dropwise one by one at -10°C. The final reaction mixture was slowly warmed to the room temperature and stirred for a further period of 60 min to yield a yellow solid. Distilled water (50 mL) was added to this reaction mixture and the water-insoluble product was isolated. The crude product was purified by silica column chromatography by using 3% methanol in dichloromethane to give pure PTAP·Br as a white solid. Yield 13.10 g (98%). M.P. 210-215 °C. MALDI-TOF = 282.2094 [M^+]. Anal. Calcd. For $C_{15}H_{29}BrN_3P$: C 49.73; H 8.07; N 11.60. Found: C 49.71; H 8.02; N 11.58.

3.2.2.6 Synthesis of PTAP·PF_6 (phenyl triisopropylaminophosphonium hexaflurophosphate): To a stirred solution of PTAP·Br (3 g, 0.0083 mol) in methanol (20 mL), KPF_6 (2.29 g, 0.0125 mol) in water (10 mL) was slowly added with the formation of KBr precipitate. The reaction mixture was stirred at room temperature for a further period of 10- 15 min. and filtered through celite. The obtained clear solution was left for the crystallization process. Colorless block-shaped crystals of PTAP·PF_6 were obtained after one week. Yield: 3.50 g (98%). M.P. 127-132 °C. MALDI-TOF = 282.2094 [M^+]. Anal. Calcd. For $C_{15}H_{29}F_6N_3P_2$: C 42.16; H 6.84; N 9.83. Found: C 42.13; H 6.78; N 9.79.

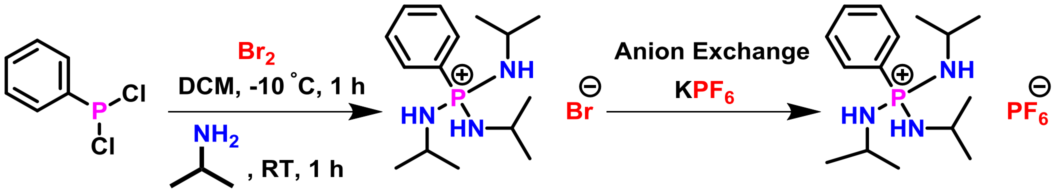

Scheme 3.2. Synthesis of TPAP·Br and TPAP·PF_6.

3.2.3 Crystallography: Single crystal reflections for DPDP·PF_6 at various temperatures were obtained on a Bruker Smart Apex Duo diffractometer by using Mo Kα radiation (λ= 0.71073Å). The structures were solved by intrinsic or direct methods and then refined by full-matrix least-squares against F^2 using all data by using SHELXL-2014/7 built in the Apex-3 program.[43] Crystallographic refinement data for DPDP·PF_6 at various temperatures is listed in (Table 3.1). All the non-hydrogen atoms were refined anisotropically if not stated otherwise. Hydrogen atoms were constructed in geometric positions to their parent atoms.[44] The bond distances and angles and structural illustrations were obtained by using the DIAMOND-3.1 software package.

Table 3.1: Details of crystallographic data collection at variable temperatures of DPDP·PF$_6$, PTAP·PF$_6$ and TPAP·PF$_6$.

Compound	**DPDP·PF$_6$**	**DPDP·PF$_6$**	**DPDP·PF$_6$**
Chemical formula	$C_{18}H_{26}F_6N_2P_2$	$C_{18}H_{26}F_6N_2P_2$	$C_{18}H_{26}F_6N_2P_2$
Formula weight	446.35	446.35	446.35
Temperature	100(2)K	296(2)K	463(2)K
Crystal system	Monoclinic	Monoclinic	Monoclinic
Space group	*Cc*	*Cc*	*Cc*
a (Å); α (°)	15.8469(8); 90	15.9829(19); 90	16.196(11); 90
b (Å); β(°)	9.2507(4); 104.210(2)	9.3035(12); 104.156(3)	9.417(7); 103.779(15)
c (Å); γ (°)	14.8370(7); 90	14.9620(17); 90	15.215(11); 90
V (Å^3); Z	2108.48(17); 4	2157.2(5); 4	2253.78(3); 4
ρ (calc.) g cm^{-3}	1.406	1.374	1.315
μ mm^{-1}	0.264	0.258	0.247
$2\theta_{max}$ (°)	56	56	56
R(int)	0.0278	0.0556	0.0577
Completeness to θ	99.9	99.9	99.6
Data / param.	5177/254	5117/253	4807/229
GOF	1.033	1.041	1.038
R1 [F>4σ(F)]	0.0271	0.0370	0.0509
wR2 (all data)	0.0639	0.0928	0.1565
max. peak/hole (e.Å^{-3})	0.272/-0.249	0.238/-0.218	0.202/-0.152

Compound	**TPAP·PF$_6$**	**PTAP·PF$_6$**
Chemical formula	$C_{21}H_{23}F_6NP_2$	$C_{15}H_{29}F_6N_3P_2$
Formula weight	465.34	427.35
Temperature	100(2)K	100(2)K
Crystal system	Monoclinic	Monoclinic
Space group	*C2/c*	$P2_1/n$
a (Å); α (°)	17.259(5); 90	10.315(3); 90
b (Å); β(°)	7.920(2); 100.346(7)	16.150(5); 96.152(7)
c (Å); γ (°)	32.458(10); 90	12.629(4); 90
V (Å^3); Z	4364.59(2); 4	2091.7(12); 4
ρ (calc.) g cm^{-3}	1.416	1.357
μ mm^{-1}	0.257	0.264
$2\theta_{max}$ (°)	56	56
R(int)	0.0928	0.1336
Completeness to θ	99.5	99.3
Data / param.	5413/270	5194/236
GOF	1.061	1.015
R1 [F>4σ(F)]	0.0599	0.0609
wR2 (all data)	0.1568	0.1589
max. peak/hole (e.Å^{-3})	0.978/-0.869	0.576/-0.465

3.2.4 Ferroelectric, dielectric and piezoelectric measurements: The ferroelectric measurements were performed on the single crystals of DPDP·PF_6 using a Sawyer-Tower circuit at room temperature. The single crystal of DPDP·PF_6 was deposited with a conducting silver paste was used for ferroelectric measurement. The polarization and fatigue measurements were performed on an aixACCT TF-2000E model hysteresis loop analyzer. Leakage currents were measured dynamically for various voltage steps during the hysteresis loop measurements. The dielectric measurements were performed on the pressed powder pellets of DPDP·PF_6 and on the DPDP·PF_6/PDMS composite films. The temperature and frequency dependent dielectric constants were measured in a Novocontrol Dielectric Spectrometer. The d_{33} measurements were performed on a Piezotest meter model PM300 on the single crystals of DPDP·PF_6 and the DPDP·PF_6/PDMS composite films.

3.2.5 Device fabrication process: DPDP·PF_6/PDMS composites were prepared by mixing the pre-calculated amount of DPDP·PF_6 and PDMS/curing agent so that the final composite contains approximately 3, 5, 7, 10 and wt % DPDP·PF_6 in PDMS. After degassing, the individual solutions were poured into separate Petri dishes and heated at 70°C for 4 h. The obtained homogeneous white-colored films were then peeled off from the petri dish. A thin layer of silver paste was applied on each side of the film and dried at 50°C for 4 h. Subsequently, copper electrodes were applied on both sides of the film and the leads were attached to copper electrodes by soldering. The entire composite and the contacts were secured by PDMS encapsulation to yield the final device.[45]

As fabricated devices were tested using an in-house fabricated impact machine, where the rotational movement of a motor shaft is converted into vertical motion using cam. Every rotation of the motor yields a vertical motion, which ultimately gives an impact to the device. The voltage and current were measured using the Tektronix oscilloscope (Model no. MSO2024 16CH MSO). For the current measurement, a 10 MΩ resistor was attached to devices in parallel mode and the voltage drop was measured across the device. The output current for the devices was calculated using Ohm's law (I = V/R). The current density was obtained by dividing the output current by an active area of the device.

3.3 Results and discussion

3.3.1 Synthesis, characterization and crystal structures: The organoamino-phosphonium salt $[Ph_2(^iPrNH)_2P]\cdot PF_6$, DPDP·$PF_6$, was synthesized from diphenylchlorophosphine (Ph_2PCl) as shown in Scheme 3.3 (Figures 3A.1-3A.4, Appendix 3). Crystals of DPDP·PF_6 were directly obtained by the anion exchange reaction of DPDP·Br with KPF_6 and were solved in the acentric monoclinic space group *Cc*.

Scheme 3.3: Synthesis of the phosphonium salts DPDP.Br and DPDP.PF$_6$.

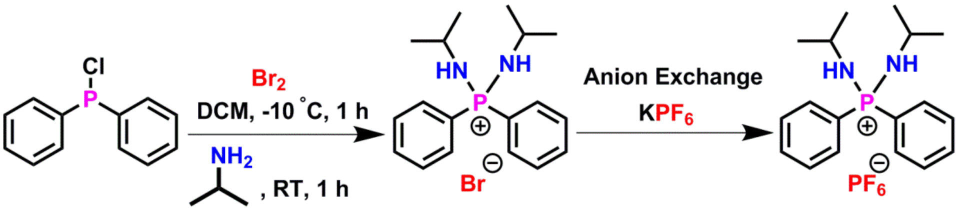

The asymmetric unit consists of a phosphonium cation and a non-coordinating hexafluorophosphate anion while the unit-cell contains four DPDP·PF_6 motifs (Figure 3.1a and b). The coordination environment around the cationic phosphorus center is distorted tetrahedral. The measured distances of 1.6210(18) and 1.6242(19) Å for P1-N1 and P1-N2, respectively, were in the expected range typically observed for amino-P(V) scaffolds. The N-H protons of the two amino groups are pointing opposite to each other and involved in an intermolecular H-bonding with the PF_6^- anions. As a result, the N1-P-N2 angle is wider (avg. 120.76 (10)°) than the ideal tetrahedral angle. Concomitantly, other angles were marginally distorted ranging from 104.93(10) to 108.34(10)° within the cationic segment (Tables 3A.1 and 3A.2, Appendix 3). Each amino proton is hydrogen-bonded to two F-atoms of PF_6^- anion in a chelating fashion (with one strong and one weak interaction) and resulting in the formation of a 1D-chain like structure (Figures 3.1c and 3A.5, Appendix 3).

A closer look at the structure of DPDP·PF_6 reveals that the organo- and amino groups around the central phosphonium cation presumably has played a key role in imparting asymmetry in the system.[46] To probe the presence of any centrosymmetric phase in the structure of DPDP·PF_6, single crystal X-ray diffraction analysis was performed in the temperature range between 100 and 463 K with an incremental step of 25 K between the measurements. A detailed structural analysis confirmed no change in symmetry and space group at all the measured temperatures albeit with a marginal increase in the lattice distances and cell volume (Figure 3A.8, Appendix 3).

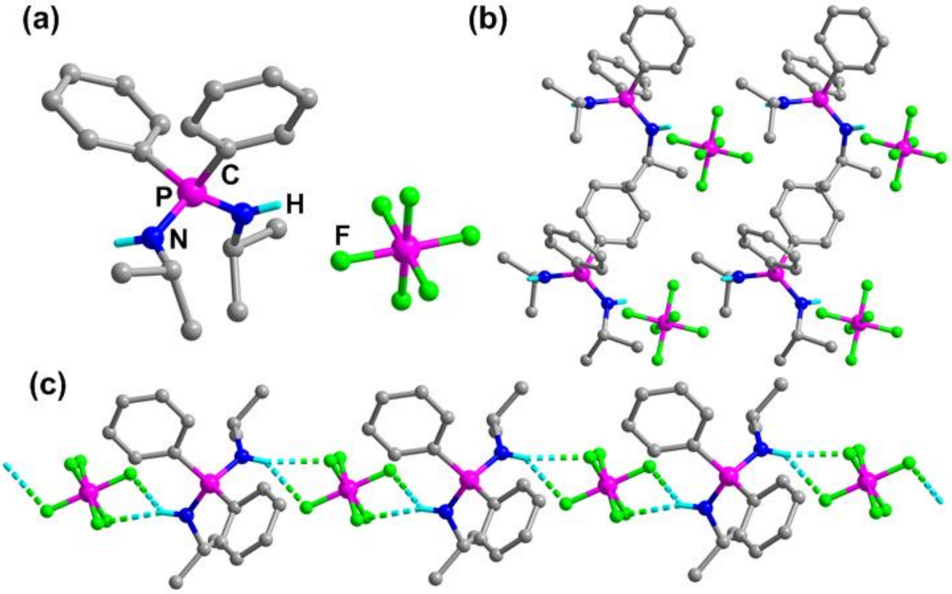

Figure 3.1: *(a) Molecular structure of DPDP·PF$_6$ and (b) its packing diagram along the b-axis. (c) The 1D-chain structure of DPDP·PF$_6$ mediated by N-H…F hydrogen bonding.*

The powdered unsieved sample of this salt shows a second harmonic generation (SHG) efficiency of 0.2, with respect to the reference KDP, which confirms the noncentrosymmetric nature of DPDP·PF$_6$ at room temperature. The variable-temperature powder X-ray diffraction (VT-PXRD) profile of DPDP·PF$_6$ did not exhibit any phase change or the systematic absence of peaks upon increasing the temperatures from 298 to 463 K (Figure 3A.9a, Appendix 3). The thermogravimetric analysis coupled with differential thermal studies indicated that there are two heat anomalies, one for the melting at 471 K and a subsequent one at 603 K for decomposition (Figure 3A.9b, Appendix 3).

3.3.2 Ferroelectric, piezoelectric and dielectric studies

The point group symmetry for the structure of DPDP·PF$_6$ is C_s which belongs to one of the ten polar point groups (C_1, C_s, C_2, C_{2v}, C_3, C_{3v}, C_4, C_{4v}, C_6, and C_{6v}) that are suitable for ferroelectric measurements.[47-49] The polarization (P) vs. electric field (E) measurements were performed on the single crystals of DPDP·PF_6 by using a Sawyer-Tower circuit at an operating frequency of 0.1 Hz (Figures 3.2 and 3A.10, Appendix 3). These crystals gave a remnant (P_r) and saturation (P_s) polarization values of 6.32 and 3.50 μC cm^{-2}, respectively (Figure 3.2a). The coercive fields (E_c) obtained in these studies were found to be 4.27 kV cm^{-1}.

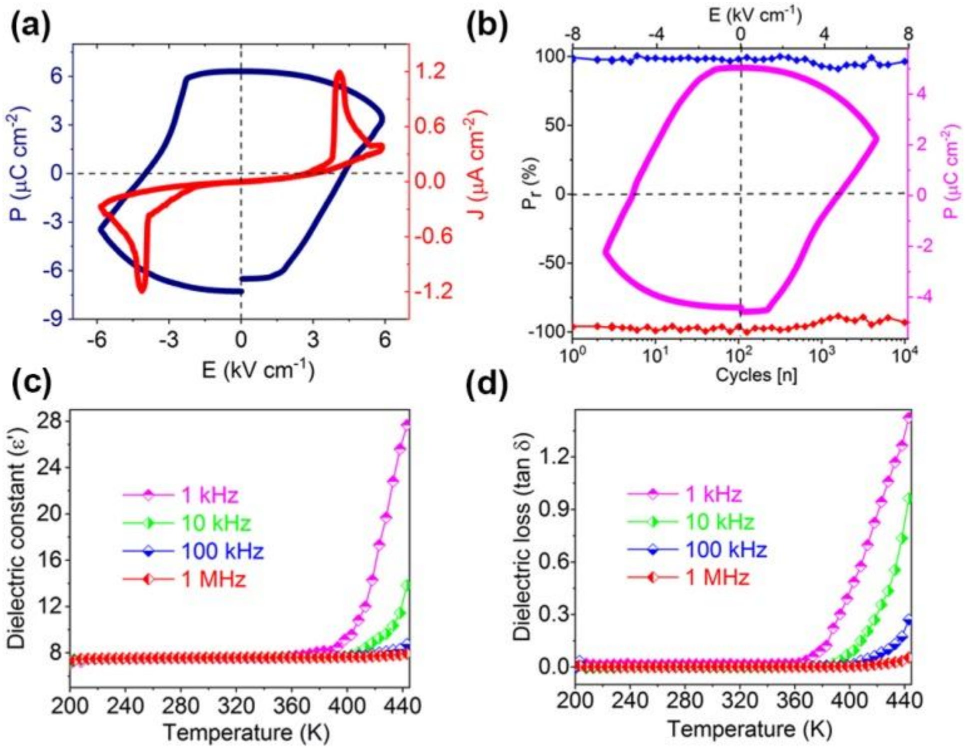

Figure 3.2: *P-E hysteresis loop and the corresponding leakage current plot of DPDP·PF_6 and (b) Ferroelectric fatigue measurements up to 10^4 cycles and P-E loop after the fatigue cycles. Temperature dependent (c) dielectric constant (ε') and (d) dielectric loss (tan δ) for various frequencies.*

While the P_r for DPDP·PF_6 is comparable with some of the well-known molecular ferroelectrics, the obtained E_c value is much lower than most of them.[50-54] The observed P_r values are much higher than certain other phosphonium stabilized ferroelectric materials.[55-57] Also, several metal-organic materials stabilized by related N-donor functionalized amido-P(V) ligands have shown to exhibit ferroelectric behavior.[58-60] The leakage current density measurements indicate low leakage behavior, which is of the order of 1.2 μA cm^{-2} along with peaks associated with domain switching typical for ferroelectric materials (Figure 3.2a). Further, fatigue measurements exemplified the retention of ferroelectric polarization for several switching cycles as 90% of its P_r as well as the rectangular shape of the hysteresis loop is retained even after 10^4 cycles (Figure 3.2b). The high and stable polarization in this species can be attributed to its asymmetric ionic nature coupled with its H-bond assisted 1D-chain like the alignment of bipolar phosphonium cations and PF_6^- anions along the b-axis (which is the direction of measurements) with a net long-range polar order. Further, we performed temperature dependent dielectric permittivity studies for DPDP·PF_6 on its compacted polycrystalline sample. The real part of the dielectric constant (ε') initially increases slowly with an onset of anomalous behaviour at 390 K (Figure 3.2c). However, no dielectric peak maxima were attained up to the temperature close to its melting point. These results are consistent with the crystallographic (both VT-SCXRD and VT-PXRD) data and with certain recent reports pertaining to molecular ferroelectrics.[61-62] The observed ε' values were found to vary between 7 and 27 upon sweeping the temperature from 200 to 463 K. The sharp rise in the ε' values can be attributed to its ionic structure that shows an increase in charge carriers and ion mobility at higher temperatures. A similar trend has also been observed in the corresponding dielectric loss (tan δ) plot as well (Figure 3.2d). The frequency dependent dielectric measurements gave higher ε' values at lower frequencies indicating the involvement of all the polarization (interface, dipolar, ionic and atomic) mechanisms (Figures 3A.11 and 3A.12, Appendix 3).[63-64] A preliminary piezo measurements on the single crystals of DPDP·PF_6 gave a piezoelectric coefficient (d_{33}) of 8 pC N^{-1} under the applied force of 0.20 N. The observed piezo-response may be attributed to the oriented domain configurations in the single crystals.[65] These values are consistent with some of the known molecular and polymeric ferro- and piezoelectric materials.[66]

3.3.3 Mechanical energy harvester

Owing to a greater attention for flexible mechanical energy harvesters and nanogenerators based on piezo- and ferroelectric materials, we examined the power generator response of DPDP·PF_6 in its composite form with the polydimethylsiloxane (PDMS) polymer (Figure 3.3a-c). The composite devices with 3, 5, 7, 10 and 20 wt % of DPDP·PF_6 in PDMS (DPDP·PF_6/PDMS) were prepared by the dispersion of appropriate quantities of DPDP·PF_6 into a homogeneous solution of PDMS precursors (Scheme 3A.1 and Table 3A.3, Appendix 3). All the obtained films unveiled exceptional flexibility as demonstrated by its ease for twisting, two-fold bending and rolling operations (Figure 3A.13, Appendix 3). The morphologies of all the DPDP·PF_6/PDMS composites were investigated by X-ray 3D-tomography analysis. The magnified cross-sectional views of 3D-Xray tomography images show a random distribution of the DPDP·PF_6 particles in the PDMS matrix (Figures 3.3d, 3A.14 and 3A.15, Appendix 3).

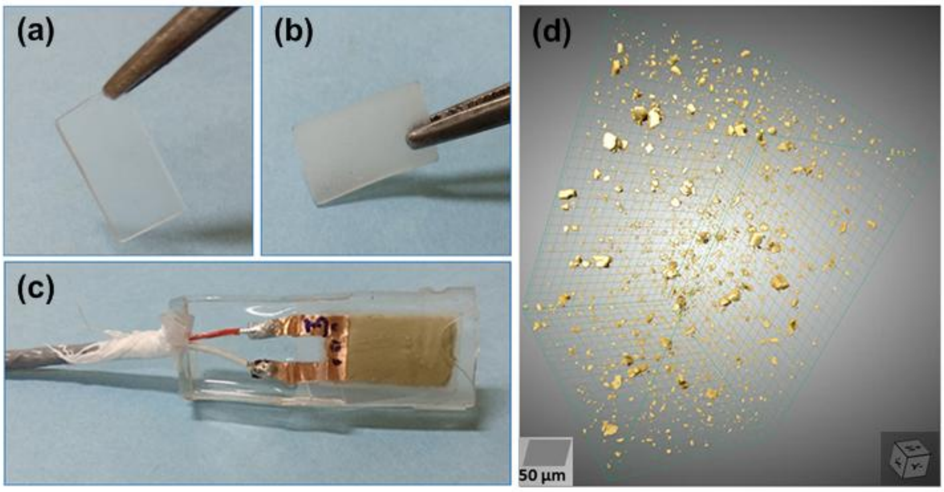

Figure 3.3: *Images of (a) neat PDMS, (b) DPDP·PF_6/PDMS (10 wt %) and (c) the corresponding device. (d) The 3D-Xray tomography images of DPDP·PF_6/PDMS (10 wt %; grid-scale: 50 µm).*

A comparative analysis revealed a much higher particle distribution and density for the 20 wt % composite than the 10 wt % composite. Furthermore, the presence of ferroelectric particles and the crystallite purity of DPDP·PF_6 in the composites were identified by using Raman spectroscopy. Pure PDMS matrix has characteristic peaks at 487 and 708 cm^{-1} for the symmetrical Si-O-Si and Si-C stretching modes, respectively.[67-68] For DPDP·PF_6, major peaks are found for aromatic and aliphatic Raman active modes at 1590, 1316, 1117, 998 cm^{-1}. These peaks were present in the DPDP·PF_6/PDMS (10 wt %) composite as well in addition to the peaks due to Si-O-Si and Si-C bonds in PDMS (Figure 3A.16, Appendix 3).

The performances of the devices (with electrodes) have been tested by using an in-house fabricated impact machine and an oscilloscope. The output voltage and output currents for non-poled DPDP·PF_6/PDMS materials with different ratios (3, 5, 7, 10 and 20 wt %) of ferroelectric DPDP·PF_6 fillers are generated from a periodically applied mechanical force. The performance of the DPDP·PF_6/PDMS devices improved with increase in concentration of DPDP·PF_6 upto 10 wt % and decreased for the 20 wt % composite. The obtained maximum output peak to peak voltage (V_{PP}) and output peak to peak current (I_{PP}) of DPDP·PF_6/PDMS were found to be 8.5 V and 0.5 μA, respectively, for the 10 wt % composite under an optimized 15 N compressive force and 10 Hz frequency (Figures 3.4a,c, 3A.17 and 3A.18, Appendix 3). These observations are consistent with a few ceramic oxide-polymer composite nanogenerators which show particle agglomeration at higher oxide concentrations with a net reduction in the dipole moments.[69-71]

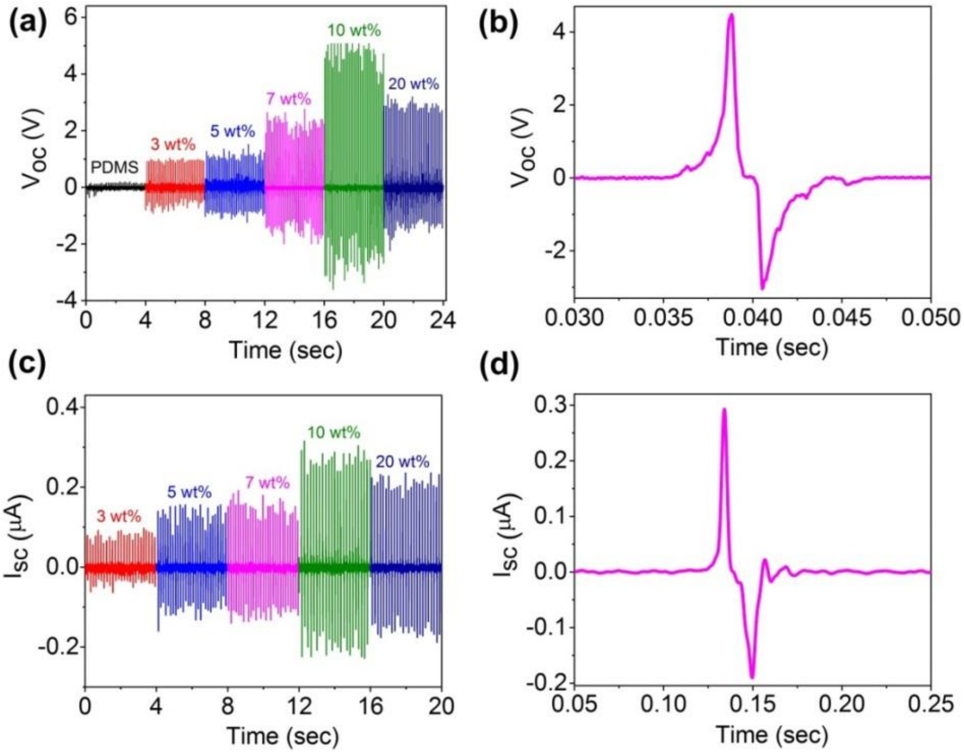

Figure 3.4: *The mechanical generator output voltages (a) and currents (c) for all the DPDP·PF_6/PDMS devices. The output voltage (b) and current (d) obtained in a one cycle of measurement for the 10 wt % device.*

The 3D-Xray tomography images support this claim, where the higher 20 wt % composite shows some aggregations (Figures 3A.14 and 3A.15, Appendix 3). A closer view of the output voltage and current plots confirm a single piezoelectric response generated from each press and release cycle of the composite film (Figure 3.4b,d). The maximum current density (CD) and power density (PD) values of 0.28 μA cm^{-2} and 1.74 μW cm^{-3}, respectively, were observed for the 10 % composite (Figure 3A.19, Appendix 3). The performance of the DPDP·PF_6/PDMS system is fairly comparable to several composites derived from ferroelectric (organic-inorganic and inorganic)-nonpiezoelectric polymer materials.[30, 71-73, 75]

The observed room temperature ε' values for the neat PDMS, 3, 5, 10 and 20 wt % DPDP·PF_6/PDMS were found to be 5.6, 5.8, 6.9, 7.3 and 7.5, respectively, at 1 kHz (Figure 3A.20, Appendix 3). A linear increase in ε' values from 3 to 20 wt % indicates the contribution from the ferroelectric particles for the overall dipole moment of the composite films.[74-75] Similarly, a marginal increase in the piezoelectric coefficient (d_{33}) values from 3 to 5 pC N^{-1} has been observed upon increasing the wt % of the ferroelectric component from 3 to 20 % (Figure 3A.21, Appendix 3). This clearly indicates that the organic-polymer matrix interface plays a vital role in determining the dielectric and piezoelectric properties of the DPDP·PF_6/PDMS composites. Furthermore, it is to be noted that the effective energy harvesting performance of these materials depends on the layer thickness, strength of the mechanical force applied, structural morphologies and the weight ratio between polymer and piezoelectric filler.[45]

3.4 Conclusion

In summary, we have reported the synthesis of a new ferroelectric polar organic binary salt of DPDP·PF_6 containing organo- and amino functionalities. Ferroelectric measurements on the single crystals of this salt gave a P_r value ~6 μC cm^{-2}. The 1D-arrangement of organo aminophosphonium cations and PF_6^- anions aided by the presence of N-H···F intermolecular hydrogen bond in its asymmetric lattice helps in the effective alignment of dipoles responsible for ferroelectric behaviour. Also, it exhibits high thermal and phase stability and sharp polarization response. In combination with polymeric PDMS films, device structures with excellent mechanical flexibility for various wt % (3, 5, 7, 10, 20) of DPDP·PF_6 were prepared. The mechanical energy harvesting performance of these devices show the current density of 0.28 μA cm^{-2}, and power density of 1.74 μW cm^{-3} for the 10 wt %

DPDP·PF_6/PDMS composite. These results demonstrate the effectiveness of organic ferroelectric materials for energy harvesting applications and promise their potential utility in future wearable electronics.

3.5 References

(1) Asadi, K.; Li, M. Y.; Blom, P. W. M.; Kemerink, M.; de Leeuw, D. M. *Mater. Today* **2011**, *14*, 592–599.

(2) Saparov, B.; Mitzi, D. B. *Chem. Rev.* **2016**, *116*, 4558–4596.

(3) Manser, J. S.; Christians, J. A.; Kamat, P. V. *Chem. Rev.* **2016**, *116*, 12956–13008.

(4) Das, S.; Appenzeller, J. *Nano Lett.* **2011**, *11*, 4003–4007.

(5) De Araujo, C. A. P.; Cuchiaro, J. D.; Mc Millan, D. L.; Scott, M. C.; Scott, J. F. *Nature* **1995**, *374*, 627–629.

(6) Han, S.T.; Zhou, Y.; Roy, V. A. L. *Adv. Mater.* **2013**, *25*, 5425–5449.

(7) Scott, J. F. *Science* **2007**, *315*, 954–959.

(8) Martin, L. W.; Rappe, A. M. *Nat. Rev. Mater.* **2016**, *2*, 16087.

(9) Yuan, Y.; Xiao, Z.; Yang, B.; Huang, J. *J. Mater. Chem. A* **2014**, *2*, 6027–6041.

(10) Paillard, C.; Bai, X.; Infante, I. C.; Guennou, M.; Geneste, G.; Alexe, M.; Kreisel, J.; Dkhil, B. *Adv. Mater.* **2016**, *28*, 5153–5168.

(11) Stroppa, A.; Di Sante, D.; Barone, P.; Bokdam, M.; Kresse, G.; Franchini, C.; Whangbo, M. H.; Picozzi, S. *Nat. Commun.* **2014**, *5*, 5900.

(12) Bowen, C. R.; Kim, H. A.; Weaver, P. M.; Dunn, S. *Energy Environ. Sci.* **2014**, *7*, 25–44.

(13) Ellabban, O.; Abu-Rub, H.; Blaabjerg, F. *Renewable and Sustainable Energy Rev.* **2014**, *39*, 748–764.

(14) Invernizzi, F.; Dulio, S.; Patrini, M.; Guizzetti, G.; Mustarelli, P. *Chem. Soc. Rev.* **2016**, *45*, 5455–5473.

(15) Lee, J.H.; Kim, J.; Kim, T. Y.; Al Hossain, M. S.; Kim, S.W.; Kim, J. H. *J. Mater. Chem. A* **2016**, *4*, 7983–7999.

(16) Siang, J.; Lim, M. H.; Salman Leong, M. *Int. J. Energy Res.* **2018**, *42*, 1866–1893.

(17) Yi, F.; Ren, H.; Shan, J.; Sun, X.; Wei, D.; Liu, Z. *Chem. Soc. Rev.* **2018**. *47*, 3152–3188.

(18) Zhang, Y.; Xie, M.; Adamaki, V.; Khanbareh, H.; Bowen, C. R. *Chem. Soc. Rev.* **2017**, *46*, 7757–7786.

(19) Hu, F.; Cai, Q.; Liao, F.; Shao, M.; Lee, S. T. *Small* **2015**, *11*, 5611–5628.

(20) Wang, Z. L.; Chen, J.; Lin, L. *Energy Environ. Sci.* **2015**, *8*, 2250–2282.

(21) Fan, F. R.; Tang, W.; Wang, Z. L. *Adv. Mater.* **2016**, *28*, 4283–4305.

(22) Wang, Z. L.; Zhu, G.; Yang, Y.; Wang, S.; Pan, C. *Mater. Today* **2012**, *15*, 532–543.

(23) Wang, Z. L.; Song, J. *Science* **2006**, *312*, 242–246.

(24) Lee, M.; Chen, C. Y.; Wang, S.; Cha, S. N.; Park, Y. J.; Kim, J. M.; Chou, L. J.; Wang, Z. L. *Adv. Mater.* **2012**, *24*, 1759–1764.

(25) Wang, Z. L.; Wu, W. *Angew. Chem. Int. Ed.* **2012**, *51*, 11700–11721.

(26) Weng, W.; Chen, P.; He, S.; Sun, X.; Peng, H. *Angew. Chem. Int. Ed.* **2016**, *55*, 6140–6169.

(27) Zhang, W.; Xiong, R. G. *Chem. Rev.* **2012**, *112*, 1163–1195.

(28) Hang, T.; Zhang, W.; Ye, H.Y.; Xiong, R. G. *Chem. Soc. Rev.* **2011**, *40*, 3577–3598.

(29) Ren, X.; Fan, H.; Zhao, Y.; Liu, Z. *ACS Appl. Mater. Interfaces* **2016**, *8*, 26190–26197.

(30) Ding, R.; Liu, H.; Zhang, X.; Xiao, J.; Kishor, R.; Sun, H.; Zhu, B.; Chen, G.; Gao, F.; Feng, X.; Chen, J.; Chen, X.; Sun, X.; Zheng, Y. *Adv. Funct. Mater.* **2016**, *26*, 7708–7716.

(31) Ding, R.; Zhang, X.; Chen, G.; Wang, H.; Kishor, R.; Xiao, J.; Gao, F.; Zeng, K.; Chen, X.; Sun, X. W.; Zheng, Y. *Nano Energy* **2017**, *37*, 126–135.

(32) Li, J.; Wang, X. *APL Mater.* **2017**, *5*, 073801.

(33) Persano, L.; Dagdeviren, C.; Su, Y.; Zhang, Y.; Girardo, S.; Pisignano, D.; Huang, Y.; Rogers, J. A. *Nat. Commun.* **2013**, *4*, 1610–1633.

(34) Park, S. H.; Lee, H. B.; Yeon, S. M.; Park, J.; Lee, N. K. *ACS Appl. Mater. Interfaces* **2016**, *8*, 24773–24781.

(35) Pi, Z.; Zhang, J.; Wen, C.; Zhang, Z. bin; Wu, D. *Nano Energy* **2014**, *7*, 33–41.

(36) Park, J. H.; Kurra, N.; AlMadhoun, M. N.; Odeh, I. N.; Alshareef, H. N. *J. Mater. Chem. C* **2015**, *3*, 2366–2370.

(37) Alluri, N. R.; Chandrasekhar, A.; Jeong, J. H.; Kim, S.J. *J. Mater. Chem. C* **2017**, *5*, 4833–4844.

(38) Ko, E. J.; Lee, E. J.; Choi, M. H.; Sung, T. H.; Moon, D. K. *Sensors Actuators, A Phys.* **2017**, *259*, 112–120.

(39) De la Fuente, G. F.; Huheey, J. E. *Phosphorus Sulfur Silicon Relat. Elem.* **1993**, *78*, 23–36.

(40) Gupta, A. K.; Nicholls, J.; Debnath, S.; Rosbottom, I.; Steiner, A.; Boomishankar, R. Organoamino Phosphonium Cations as Building Blocks for Hierarchical Supramolecular Assemblies. *Cryst. Growth Des.* **2011**, *11*, 555–564.

(41) Bailey, P. J.; Grant, K. J.; Parsons, S. *Organometallics* **1998**, *17*, 551–555.

(42) Martinez-Arripe, E.; Jean-Baptiste-Dit-Dominique, F.; Auffrant, A.; Le Goff, X. F.; Thuilliez, J.; Nief, F. *Organometallics* **2012**, *31*, 4854–4861.

(43) Sheldrick, G. M. *Acta Crystallogr., Sect. A* **2008,** *64*, 112–122.

(44) Spek, A. L. *Acta Crystallogr., Sect. D* **2009**, *65*, 148–155.

(45) Alluri, N. R.; Chandrasekhar, A.; Vivekananthan, V.; Purusothaman, Y.; Selvarajan, S.; Jeong, J. H.; Kim, S. J. *ACS Sustain. Chem. Eng.* **2017**, *5*, 4730–4738.

(46) The related $[Ph_3(^iPrNH)P]\cdot PF_6$ ($TPAP\cdot PF_6$), and $[Ph(^iPrNH)_3P]\cdot PF_6$ ($PTAP\cdot PF_6$) were found to crystallize in the centrosymmetric monoclinic space groups *C*2/*c* and $P2_1/n$, respectively (Figures 3A.6 and 3A.7, Appendix 3).

(47) Asadi, K.; van der Veen, M. A. *Eur. J. Inorg. Chem.* **2016**, 27, 4332–4344.

(48) Horiuchi, S.; Tokura, Y. *Nat. Mater.* **2008**, *7*, 357–366.

(49) Di Sante, D.; Stroppa, A.; Picozzi, S. *Phys. Chem. Chem. Phys.* **2012**, *14*, 14673–14681.

(50) Horiuchi, S.; Kobayashi, K.; Kumai, R.; Ishibashi, S. *Nat. Commun.* **2017**, *8*, 14426.

(51) Hu, L.; Feng, R.; Wang, J.; Bai, Z.; Jin, W.; Zhang, L.; Nie, Q. M.; Qiu, Z. J.; Tian, P.; Cong, C.; Zheng, L.; Liu, R. *Adv. Funct. Mater.* **2018**, *28*, 1705463.

(52) Shi, P. P.; Tang, Y. Y.; Li, P. F.; Ye, H. Y.; Xiong, R. G. *J. Am. Chem. Soc.* **2017**, *139*, 1319–1324.

(53) Harada, J.; Yoneyama, N.; Yokokura, S.; Takahashi, Y.; Miura, A.; Kitamura, N.; Inabe, T. *J. Am. Chem. Soc.* **2018**, *140*, 346–354.

(54) Zhang, W.; Tang, Y.; Li, P.; Shi, P.; Liao, W.; Ye, H.; Zhang, Y.; Xiong, R. G. *J. Am. Chem. Soc.* **2017**, 1*39,* 10897–10902.

(55) Di Sante, D.; Stroppa, A.; Jain, P.; Picozzi, S. *J. Am. Chem. Soc.* **2013**, *135*, 18126–18130.

(56) Tammam, A. K.; El-Dean, T. S.; Mostafa, M. F. *Ferroelectrics* **2015**, *481*, 34–40.

(57) Srivastava, A. K.; Praveenkumar, B.; Mahawar, I. K.; Divya, P.; Shalini, S.; Boomishankar, R. *Chem. Mater*. **2014**, *26*, 3811–3817.

(58) Srivastava, A. K.; Divya, P.; Praveenkumar, B.; Boomishankar, R. *Chem. Mater.* **2015**, *27*, 5222–5229.

(59) Srivastava, A. K.; Vijayakanth, T.; Divya, P.; Praveenkumar, B.; Steiner, A.; Boomishankar, R. *J. Mater. Chem. C* **2017**, *5*, 7352–7359.

(60) Yadav, A.; Srivastava, A. K.; Kulkarni, P.; Divya, P.; Steiner, A.; Praveenkumar, B.; Boomishankar, R. *J. Mater. Chem. C* **2017**, *5*, 10624–10629.

(61) Narayanan, A.; Cao, D.; Frazer, L.; Tayi, A. S.; Blackburn, A. K.; Sue, A. C. H.; Ketterson, J. B.; Stoddart, J. F.; Stupp, S. I. *J. Am. Chem. Soc.* **2017**, *139*, 9186–9191.

(62) Horiuchi, S.; Kumai, R.; Tokura, Y. *Adv. Mater.* **2011**, *23*, 2098–2103.

(63) Rob, S.; Stassen, I.; Burtch, N. *Chem. Soc. Rev.* **2017**, *46*, 3185–3241.

(64) Lines, M. E.; Glass, A. M. *Principles and Applications of Ferroelectrics and Related Materials*; Oxford University Press: New York, 1977.

(65) Li, X.; Chen, C.; Deng, H.; Zhang, H.; Lin, D.; Zhao, X.; Luo, H. *Crystals* **2015**, *5*, 172–192.

(66) You, Y. M.; Liao, W. Q.; Zhao, D.; Ye, H. Y.; Zhang, Y.; Zhou, Q.; Niu, X.; Wang, J.; Li, P. F.; Fu, D. W.; Wang, Z.; Gao, S.; Yang, K.; Liu, J.; Li, J.; Yan, Y.; Xiong, R. G. *Science* **2017**, *357*, 306–309.

(67) Alluri, N. R; Vivekananthan, V.; Chandrasekhar, A.; Kim, S. J. *Nanoscale* **2018**, *10*, 907–913.

(68) Romasanta, L. J.; Leret, P.; Casaban, L.; Hernández, M.; de la Rubia, M. A.; Fernández, J. F.; Kenny, J. M.; Lopez-Manchado, M. A.; Verdejo, R. *J. Mater. Chem.* **2012**, *22*, 24705–24712.

(69) Siddiqui, S.; Kim, D. Il; Roh, E.; Duy, L. T.; Trung, T. Q.; Nguyen, M. T.; Lee, N. E. *Nano Energy* **2016**, *30*, 434–442.

(70) Zhang, G.; Liao, Q.; Zhang, Z.; Liang, Q.; Zhao, Y.; Zheng, X.; Zhang, Y. *Adv. Sci.* **2015**, *3*, 1500257-1500263.

(71) Luo, C.; Hu, S.; Xia, M.; Li, P.; Hu, J.; Li, G.; Jiang. H.; Zhang. W. *Energy Technol*. **2018**, 6, 922–927.

(72) Gao, T.; Liao, J.; Wang, J.; Qiu, Y.; Yang, Q.; Zhang, M.; Zhao, Y.; Qin, L.; Xue, H.; Xiong, Z.; Chen, L.; Wang. Q. M. *J. Mater. Chem. A* **2015**, 9965–9971.

(73) Gupta, M. K.; Kim, S. W.; Kumar, B. *ACS Appl. Mater. Interfaces* **2016**, *8*, 1766–1773.

(74) Fang, Z.; Chan, K. H.; Lu, X.; Tan, C. F.; Ho, G. W. *J. Mater. Chem. A* **2018**, *6*, 52–57.

(75) Yan, J.; Jeong, Y. G. *ACS Appl. Mater. Interfaces* **2016**, *8*, 15700–15709.

End of Chapter 3

Chapter 4

All-organic Composites of Ferro- and Piezoelectric Phosphonium Salts for Mechanical Energy Harvesting Application

4.1 Introduction

The structure-property relationships of dielectric materials have spanned out into various classes of materials with piezoelectric, ferroelectric, paraelectric, pyroelectric and ferroelastic characteristics.[1-6] Ferroelectric materials are employed as memory devices, magnetic field detectors, storage devices, photovoltaic devices, field-effect transistors and recently in the domain of mechanical energy harvesters due to their switchable high polarization.[7-12] Nature endows an abundant supply of sustainable resources that can be channeled into various energies, such as wind, thermal, wave, biomass and mechanical energies, to meet the increasing demands of modern life.[13-14] Amongst these, harvesting mechanical energy offers a facile approach as it is easily accessible when a suitable material is subjected to pressure, vibrations and even by the simple movement of human body parts like bending, folding, oscillation and stretching motions.[15-17] The electromechanical responses are normally generated via the triboelectric, pyroelectric, piezoelectric or ferroelectric nature of the materials. [18-20] Wang and co-workers discovered the first exciting development of a nanogenerator by subjecting hexagonal zinc oxide (ZnO) nanowires to external forces.[21] Since then, several inorganic ceramic oxides, polyvinylidene fluoride (PVDF) and its copolymers and polymer composites of these materials have been demonstrated as potential electromechanical energy harvesters.[22] Nevertheless, the utility of such materials requires high-temperature or melt quenching techniques, longer processing times and other stimuli effects such as stretching and high-voltage poling. Moreover, several of these materials pose serious environmental hazards due to their toxic heavy-metal contents that preclude their use in wearable electronics.[23-25]

Thus, it is desirable to prepare all-organic mechanical energy generators by combining low molecular weight ferro-/piezoelectric substances with a non-piezoelectric polymer, which not only addresses the issues mentioned above but also can provide the desired device flexibility. Herein, we report the synthesis of series of compounds based on triphenyl isopropylaminophosphonium (TPAP), diphenyl diisopropylaminophosphonium (DPDP), phenyl triisopropylaminophosphonium (PTAP) and tetraisopropylaminophosphonium (TIAP) cations in the presence of lower symmetric tetrahedral BF_4^-, ClO_4^- and IO_4^- anions (Scheme 4.5) of which several of them exhibit non-centrosymmetric crystal symmetries compatible for piezo- and/or ferroelectric properties. Ferroelectric measurements on the salts of DPDP·BF_4, DPDP·ClO_4 and DPDP·IO_4, TPAP·BF_4 gave the remnant polarization values of 35.36, 21.83, 21.12 and 0.22 μC cm^{-2}. Polymer composites of the piezoelectric TPAP·BF_4, DPDP·BF_4 and TIAP·BF_4 salts with thermoplastic polyurethane (TPU) were subsequently prepared and subjected to mechanical energy harvesting studies which gave sizable output voltages along with notable current density (CD) and power density (PD) values. The voltages generated from these devices were further utilized for rapidly charging a capacitor. These findings offer an efficient protocol for developing all-organic flexible devices for the ferro and piezoelectric energy harvesting and storage applications.

4.2 Experimental section

4.2.1 General remarks

All the manipulations involving phosphorus halides were carried out under dry nitrogen conditions in standard Schlenk glassware. The solvent dichloromethane (CH_2Cl_2) was dried over phosphorus pentaoxide (P_2O_5). The starting precursors of triphenylphosphine (PPh_3), diphenylchlorophosphine (Ph_2PCl), dichlorophenylphosphine ($PhPCl_2$), phosphorus pentachloride (PCl_5) and liquid bromine (Br_2) were purchased from Sigma Aldrich and used as received. The other starting materials, such as sodium tetrafluoroborate ($NaBF_4$), sodium perchlorate ($NaClO_4$), sodium periodate ($NaIO_4$) and thermoplastic polyurethane (TPU) were purchased from Alfa Aesar and used as received. The NMR data for all the phosphonium compounds were recorded on a Bruker 400 and JEOL 400 MHz spectrometer of (^1H NMR, 400.13 MHz; ^{13}C {^1H} NMR, 100.62 MHz; ^{31}P {^1H} NMR, 161.97 MHz, ^{19}F NMR, 377 MHz, ^{11}B NMR (128 MHz) by using tetramethylsilane [($SiMe_4$) (^1H, ^{13}C)], 85% H_3PO_4 (^{31}P), trichloro fluoro methane $CFCl_3$ (^{19}F) and boron trifluoride etherate $BF_3{\cdot}OEt_2$ (^{11}B) as an internal standard reference sample for all the experiments. The ESI and MALDI-TOF spectra were obtained by using Waters Synapt G2 and the Applied Biosystem MALDI-TOF/TOF spectrometer, respectively. The thermogravimetric analysis was performed by using the PerkinElmer STA-6000 analyzer with a heating rate of 10 °C/min in a nitrogen atmosphere. Melting point analyses were performed by using a Buchi M-560 melting point apparatus and were uncorrected. FT-IR spectrum was performed on a Perkin-Elmer spectrometer with samples prepared as KBr pellets. The variable temperature powder X-ray diffraction data (VT-PXRD) were measured in the 2-theta range of 5° to 50° on a Bruker-D8 Advance X-ray diffractometer. The FE-SEM analysis of all the piezo and ferroelectric crystallites and their composites films (all different wt %) were performed by using Zeiss ultra plus FE-SEM instrument with a minimum spatial resolution of 1 µm. The 3D X-ray microtomography analyses were performed by using a Carl Zeiss Versa 510 microscope with an applied X-ray energy of 50 kV. The viscoelastic properties (energy storage and loss modulus) of pure TPU and all the 10 wt % (TPAP·BF_4/TPU, DPDP·BF_4/TPU, TIAP·BF_4/TPU and DPDP·PF_6/TPU) polymeric composite films were carried out on a TA Instruments RSA III model Dynamic Mechanical Analyzer using rectangular film strips.

4.2.2 Synthesis

The bromide and chloride precursors TPAP·Br, DPDP·Br, PTAP·Br and TIAP·Cl and the DPDP·PF_6 were prepared as per the earlier reported procedures.[26,27] To a stirred solution of bromide or chloride salts of the phosphonium precursors in methanol (25 mL), a slight excess of the sodium salt of tetrafluoroborate or perchlorate or periodate ion in water (10 mL) was slowly added with the precipitation of NaBr or NaCl salt. The reaction mixtures were stirred at room temperature for a further period of 10-15 min. and filtered through celite. The obtained clear solutions were left for crystallization at room temperature. Colorless crystals of the corresponding products were obtained in about 5 days. Details pertaining to the individual syntheses and analytical data can be found in the Supporting Information.

4.2.2.1 Binary salt 1: Triphenyl isopropylaminophosphonium tetrafluoroborate (TPAP·BF_4): To a stirred solution of TPAP·Br (3 g, 0.0075 mol) in methanol (25 mL), $NaBF_4$ (1.24 g, 0.0113 mol) in water (10 mL) was slowly added with the formation of NaBr precipitate. The reaction mixture was stirred at room temperature for a further period of 10-15 min. and filtered through celite. The obtained clear solution was left for the crystallization at room temperature. Colorless block-shaped crystals of

TPAP·BF_4 were obtained after 5 days. Yield: 2.97 g (97%). M.P. 153-155 °C. ^1H NMR (400 MHz, CD_3OD) δ 7.89 – 7.81 (m, 6H), 7.80 – 7.77 (m, 3H), 7.76 – 7.71 (m, 6H), 3.38 – 3.30 (m, 1H), 1.19 (d, J = 6.4 Hz, 6H). ^{13}C NMR (100 MHz, CD_3OD) δ 134.97, 133.40, 129.86, 120.94, 45.69, 23.85. ^{31}P NMR (162 MHz, CD_3OD) δ 36.55. ^{19}F NMR (377 MHz, CD_3OD) δ -154.70 (s), -154.76 (s), -155.66 (dd, J = 22.3, 11.1 Hz). ^{11}B NMR (128 MHz, CD_3OD) δ 0.43 – 0.17 (m), -1.14 (s). FT-IR data in KBr pellet (cm^{-1}): 3211, 2966, 2879, 2815, 2734, 1587, 1462, 1370, 1113, 1083, 996, 749, 724 and 691. MALDI-TOF = 320.1563 [M^+]. Anal. Calcd. For $C_{21}H_{23}BF_4NP$: C 61.94; H 5.69; N 3.44. Found: C 61.91; H 5.63; N 3.43.

4.2.2.2 Binary salt 2: Triphenyl isopropylaminophosphonium perchlorate (TPAP·ClO_4): To a stirred solution of TPAP·Br (3 g, 0.0075 mol) in methanol (25 mL), $NaClO_4$ (1.38 g, 0.0113 mol) in water (10 mL) was slowly added with the formation of NaBr precipitate. The reaction mixture was stirred at room temperature for a further period of 10- 15 min. and filtered through celite. The obtained clear solution was left for the crystallization at room temperature. Colorless block-shaped crystals of TPAP·ClO_4 were obtained after one week. Yield: 3.09 g (98%). M.P. 155-158 °C. ^1H NMR (400 MHz, CD_3OD) δ 7.89 – 7.81 (m, 6H), 7.80 – 7.77 (m, 3H), 7.76 – 7.71 (m, 6H), 3.37 – 3.31 (m, 1H), 1.19 (d, J = 6.4 Hz, 6H). ^{13}C NMR (100 MHz, CD_3OD) δ 135.03, 133.48, 129.94, 121.00, 45.76, 23.89. ^{31}P NMR (162 MHz, CD_3OD) δ 36.55. FT-IR data in KBr pellet (cm^{-1}): 3257, 2970, 2883, 2360, 1588, 1484, 1438, 1391, 1110, 1041, 997, 903, 751, 725, 692 and 624. MALDI-TOF = 320.1563 [M^+]. Anal. Calcd. For $C_{21}H_{23}ClNO_4P$: C 60.08; H 5.52; N 3.34. Found: C 60.02; H 5.53; N 3.31.

4.2.2.3 Binary salt 3: Triphenyl isopropylaminophosphonium periodate (TPAP·IO_4): To a stirred solution of TPAP·Br (1 g, 0.0025 mol) in methanol (25 mL), $NaIO_4$ (0.81 g, 0.0038 mol) in water (10 mL) was slowly added with the formation of NaBr precipitate. The reaction mixture was stirred at room temperature for a further period of 10-15 min. and filtered through celite. The obtained clear solution was left for the crystallization at room temperature. A colorless plate-like crystal of TPAP·IO_4 was obtained after one week. Yield: 1.25 g (97%). M.P. 150-156 °C. ^1H NMR (400 MHz, CD_3OD) δ 7.90 – 7.81 (m, 6H), 7.79 – 7.77 (m, 3H), 7.75 – 7.73 (m, 6H), 3.36 – 3.28 (m, 1H), 1.19 (d, J = 6.4 Hz, 6H). ^{13}C NMR (100 MHz, CD_3OD) δ 135.04, 133.49, 129.94, 121.01, 45.76, 23.90. ^{31}P NMR (162 MHz, CD_3OD) δ 36.56. FT-IR data in KBr pellet (cm^{-1}): 3169, 2967, 2878, 2815, 1586, 1484, 1388, 1176, 1042, 996, 846, 755, 726 and 691. MALDI-TOF = 320.1563 [M$^+$]. Anal. Calcd. For $C_{21}H_{23}INO_4P$: C 49.33; H 4.53; N 2.74. Found: C 49.31; H 4.51; N 2.75.

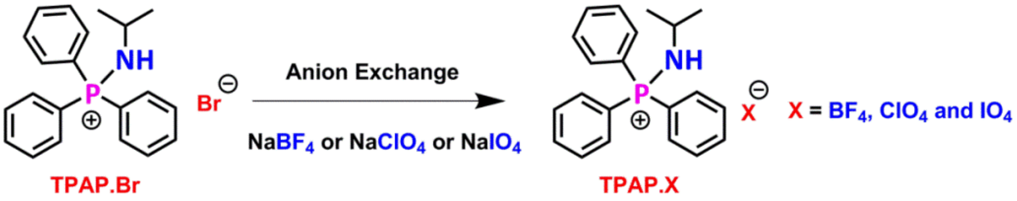

Scheme 4.1. Synthesis of organic binary salts TPAP·X (X = BF_4, ClO_4 and IO_4).

4.2.2.4 Binary salt 4: Diphenyl diisopropylaminophosphonium tetrafluoroborate (DPDP·BF_4): To a stirred solution of DPDP·Br (3 g, 0.0077 mol) in methanol (20 mL), $NaBF_4$ (1.27 g, 0.0116 mol) in water (10 mL) was slowly added with the formation of NaBr precipitate. The reaction mixture was stirred at room temperature for a further period of 10-15 min. and filtered through celite. The obtained clear solution was left for the crystallization at room temperature. Colorless block-shaped crystals of DPDP·BF_4 were obtained after one week. Yield: 2.95 g (98%). M.P. 173-178 °C. ^{1}H NMR (400 MHz, CD_3OD) δ 7.87 – 7.80 (m, 4H), 7.79 – 7.75 (m, 2H), 7.68 – 7.63 (m, 4H), 3.51 – 3.39 (m, 2H), 1.21 (d, J = 6.5 Hz, 12H). ^{13}C NMR (100 MHz, CD_3OD) δ 134.36, 132.41, 129.46, 124.58, 43.90, 23.65. ^{31}P NMR (162 MHz, CD_3OD) δ 33.20. ^{19}F NMR (377 MHz, CD_3OD) δ -154.55 (s, ^{10}B), -154.60 (s, ^{11}B), -155.53 (dd, J = 22.4, 11.2 Hz). ^{11}B NMR (128 MHz, CD_3OD) δ 0.41–0.15 (m), -1.16 (s). FT-IR data in KBr pellet (cm^{-1}): 3297, 3140, 2975, 2835, 1590, 1464, 1389, 1127, 1055, 916, 890, 753, 726 and 696. MALDI-TOF = 301.1828 [M$^+$]. Anal. Calcd. For $C_{18}H_{26}BF_4N_2P$: C 55.69; H 6.75; N 7.22. Found: C 55.61; H 6.71; N 7.20.

4.2.2.5 Binary salt 5: Diphenyl diisopropylaminophosphonium perchlorate (DPDP·ClO_4): To a stirred solution of DPDP·Br (3 g, 0.0077 mol) in methanol (20 mL), $NaClO_4$ (1.42 g, 0.0116 mol) in water (10 mL) was slowly added with the formation of NaBr precipitate. The reaction mixture was stirred at room temperature for a further period of 10-15 min. and filtered through celite. The obtained clear solution was left for the crystallization at room temperature. Colorless block-shaped crystals of DPDP·ClO_4 were obtained after one week. Yield: 3.03 g (98%). M.P. 190-

195 °C. ^{1}H NMR (400 MHz, CD_3OD) δ 7.88 – 7.81 (m, 4H), 7.80 – 7.75 (m, 2H), 7.68 – 7.63 (m, 4H), 3.50 – 3.41 (m, 2H), 1.21 (d, *J* = 6.5 Hz, 12H). ^{13}C NMR (100 MHz, CD_3OD) δ 134.42, 132.49, 129.52, 124.64, 43.97, 23.78. ^{31}P NMR (162 MHz, CD_3OD) δ 33.23. FT-IR data in KBr pellet (cm^{-1}): 3263, 2976, 2872, 1462, 1426, 1388, 1117, 1021, 997, 888, 832, 757, 725 and 695. MALDI-TOF = 301.1828 [M^{+}]. Anal. Calcd. For $C_{18}H_{26}ClN_2O_4P$: C 53.94; H 6.54; N 6.99. Found: C 53.91; H 6.52; N 6.95.

4.2.2.6 Binary salt 6: Diphenyl diisopropylaminophosphonium periodate (DPDP·IO_4): To a stirred solution of DPDP·Br (3 g, 0.0077 mol) in methanol (20 mL), $NaIO_4$ (2.48 g, 0.0116 mol) in water (10 mL) was slowly added with the formation of NaBr precipitate. The reaction mixture was stirred at room temperature for a further period of 10-15 min. and filtered through celite. The obtained clear solution was left for the crystallization at room temperature. Colorless block-shaped crystals of DPDP·IO_4 were obtained after one week. Yield: 3.65 g (96%). M.P. 142-145 °C. ^{1}H NMR (400 MHz, CD_3OD) δ 7.88 – 7.82 (m, 4H), 7.80 – 7.75 (m, 2H), 7.68 – 7.64 (m, 4H), 3.50 – 3.41 (m, 2H), 1.22 (d, *J* = 6.5 Hz, 12H). ^{13}C NMR (100 MHz, CD_3OD) δ 134.44, 132.49, 129.53, 124.65, 43.96, 23.80. ^{31}P NMR (162 MHz, CD_3OD) δ 33.23. FT-IR data in KBr pellet (cm^{-1}): 3141, 2968, 2931, 2834, 1426, 1368, 1161, 1075, 1020, 845, 750 and 699. MALDI-TOF = 301.1828 [M^{+}]. Anal. Calcd. For $C_{18}H_{26}IN_2O_4P$: C 43.92; H 5.32; N 5.69. Found: C 43.90; H 5.31; N 5.68.

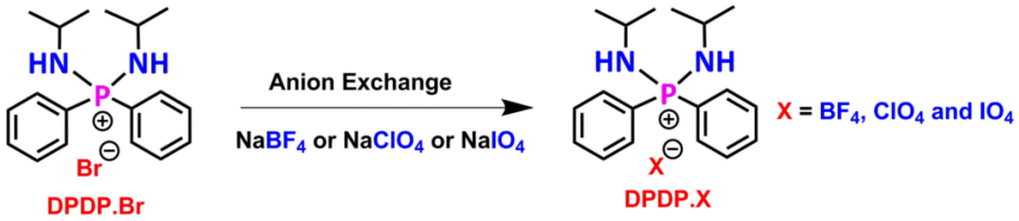

Scheme 4.2. Synthesis of organic binary salts DPDP·X (X = BF_4, ClO_4 and IO_4).

4.2.2.7 Binary salt 7: Phenyl triisopropylaminophosphonium tetrafluoroborate (PTAP·BF_4): To a stirred solution of PTAP·Br (1 g, 0.0028 mol) in methanol (20 mL), $NaBF_4$ (0.46 g, 0.0042 mol) in water (10 mL) was slowly added with the formation of NaBr precipitate. The reaction mixture was stirred at room temperature for a further period of 10-15 min. and filtered through celite. The obtained clear solution was left for the crystallization at room temperature. Colorless rod-shaped crystals of PTAP·BF_4 were obtained after one week. Yield: 0.98 g (98%). M.P. 146-149 °C. ^1H NMR (400 MHz, CD_3OD) δ 7.94 – 7.92 (m, 1H), 7.91 – 7.88 (m, 1H), 7.75 – 7.70 (m, 1H), 7.66 – 7.60 (m, 2H), 3.34 – 3.32 (m, 3H), 1.16 (d, *J* = 6.9 Hz, 18H). ^{13}C NMR (100 MHz, CD_3OD) δ 133.70, 131.91, 129.05, 126.83, 43.25, 23.84. ^{31}P NMR (162 MHz, CD_3OD) δ 29.89. ^{19}F NMR (377 MHz, CD_3OD) δ -154.72 (s, ^{10}B), -154.77 (s, ^{11}B), -155.67 (dd, *J* = 22.3, 11.1 Hz). ^{11}B NMR (128 MHz, CD_3OD) δ 0.45–0.19 (m), -1.13 (s). FT-IR data in KBr pellet (cm^{-1}): 3138, 2975, 2936, 2879, 1591, 1468, 1422, 1124, 1033, 927, 882, 844, 750, 713 and 692. MALDI-TOF = 282.2094 [M^+]. Anal. Calcd. For $C_{15}H_{29}BF_4N_3P$: C 48.80; H 7.92; N 11.38. Found: C 48.71; H 7.91; N 11.37.

4.2.2.8 Binary salt 8: Phenyl triisopropylaminophosphonium perchlorate (PTAP·ClO_4): To a stirred solution of PTAP·Br (3 g, 0.0083 mol) in methanol (20 mL), $NaClO_4$ (2.29 g, 0.0125 mol) in water (10 mL) was slowly added with the formation of NaBr precipitate. The reaction mixture was stirred at room temperature for a further period of 10-15 min. and filtered through celite. The obtained clear solution was left for the crystallization at room temperature. A mixture of crystals was identified and separated under the microscope. The plate-like crystals were used for X-ray diffraction analysis, which shows the presence of phosphonium cation and tetrafluoroborate anion, respectively. However, we were unable to separate more quantity of PTAP·ClO_4 is due to poor quality of crystals and hence for other characterizations.

4.2.2.9 Binary salt 9: Phenyl triisopropylaminophosphonium periodate (PTAP·IO_4): To a stirred solution of PTAP·Br (1 g, 0.0028 mol) in methanol (20 mL), $NaIO_4$ (0.90 g, 0.0042 mol) in water (10 mL) was slowly added with the formation of NaBr precipitate. The reaction mixture was stirred at room temperature for a further period of 10-15 min. and filtered through celite. The obtained clear solution was left for the crystallization at room temperature. Colorless rod-shaped crystals of PTAP·IO_4 were obtained after one week. Yield: 1.28 g (96%). M.P. 153-156 °C. ^1H NMR (400 MHz, CD_3OD) δ 7.93 – 7.91 (m, 1H), 7.91 – 7.88 (m, 1H), 7.73 – 7.68 (m, 1H), 7.65 – 7.60 (m, 2H), 3.33 – 3.32 (m, 3H), 1.14 (d, *J* = 6.9 Hz, 18H). ^{13}C NMR (100 MHz, CD_3OD) δ 133.71, 131.92, 129.03, 126.81, 43.27, 23.83. ^{31}P NMR (162 MHz, CD_3OD) δ

29.91. FT-IR data in KBr pellet (cm^{-1}): 3217, 2966, 2869, 1471, 1434, 1187, 1045, 1012, 908, 877, 805, 748, 726 and 693. MALDI-TOF = 282.2094 [M$^+$]. Anal. Calcd. For $C_{15}H_{29}IN_3O_4P$: C 38.07; H 6.18; N 8.88. Found: C 38.01; H 6.15; N 8.84.

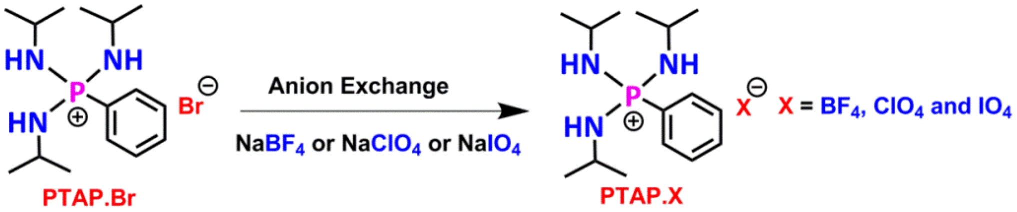

Scheme 4.3. Synthesis of organic binary salt PTAP·X (X = BF_4, ClO_4 and IO_4).

Tetraisopropylaminophosphonium chloride (TIAP·Cl): The compound TIAP·Cl was synthesized by the modified literature procedure.[27] To a solution of PCl_5 (5 g, 0.024 mol) in dry hexane (100 mL) kept at -10°C under a nitrogen atmosphere, a freshly distilled isopropylamine (11.35 g, 0.192 mol) was added dropwise at -10°C. Further, the resulting reaction mixture was stirred at -10°C under a nitrogen atmosphere for 30 minutes and then was slowly brought back to room temperature to yield a white colored solid. The final reaction mixture was then refluxed for a further period of 5 hours until the white precipitate formation is ceased. Distilled water (100 mL) was added to this reaction mixture and the water-insoluble product was isolated. Yield 6.86 g (95%). M.P. 190-195 °C. ^{1}H NMR (400 MHz, CD_3OD)) δ 3.44 – 3.35 (m, 4H), 1.22 (d, J = 6.4 Hz, 24H). ^{13}C NMR (100 MHz, CD_3OD)) δ 43.45, 24.01. ^{31}P NMR (162 MHz, $CDCl_3$): δ 20.01 ppm. MALDI-TOF = 263.2359 [M$^+$]. Anal. Calcd. For $C_{12}H_{32}ClN_4P$: C 48.23; H 10.79; N 18.75. Found: C 48.17; H 10.23; N 18.12.

4.2.2.10 Binary salt 10: Tetraisopropylaminophosphonium tetrafluoroborate (TIAP·BF_4): To a stirred solution of TIAP·Cl (3 g, 0.0100 mol) in methanol (20 mL), $NaBF_4$ (1.65 g, 0.015 mol) in water (10 mL) was slowly added with the formation of NaBr precipitate. The reaction mixture was stirred at room temperature for a further period of 10-15 min. and filtered through celite. The obtained clear solution was left for the crystallization at room temperature. Colorless needle-shaped crystals of TIAP·BF_4 were obtained after three days. Yield: 3.41 g (97%). M.P. 230-235 °C. ^{1}H NMR (400 MHz, CD_3OD)) δ 3.41 – 3.32 (m, 4H), 1.20 (d, J = 6.4 Hz, 24H). ^{13}C NMR (100 MHz, CD_3OD)) δ 43.48, 24.02. ^{31}P NMR (162 MHz, CD_3OD) δ 20.98 ppm. ^{19}F

NMR (377 MHz, CD_3OD) δ -154.36 (s, ^{10}B), -154.41 (s, ^{11}B), -155.35 (dd, J = 22.4, 11.1 Hz). ^{11}B NMR (128 MHz, CD_3OD) δ 0.43–0.17 (m), -1.15 (s). FT-IR data in KBr pellet (cm^{-1}): 3220, 2983, 2932, 2878, 1425, 1385, 1367, 1083, 1036, 919, 896, 731 and 691. MALDI-TOF = 263.2359 [M^+]. Anal. Calcd. For $C_{12}H_{32}BF_4N_4P$: C 41.16; H 9.21; N 16.00. Found: C 41.11; H 9.17; N 15.97.

4.2.2.11 Binary salt 11: Tetraisopropylaminophosphonium perchlorate (TIAP·ClO_4): To a stirred solution of TIAP·Cl (3 g, 0.0100 mol) in methanol (20 mL), $NaClO_4$ (1.84 g, 0.015 mol) in water (10 mL) was slowly added with the formation of NaBr precipitate. The reaction mixture was stirred at room temperature for a further period of 10-15 min. and filtered through celite. The obtained clear solution was left for the crystallization at room temperature. Colorless needle-shaped crystals of TIAP·ClO_4 were obtained after one week. Yield: 3.53 g (97%). M.P. 227-231 °C. ^1H NMR (400 MHz, CD_3OD) δ 3.42 – 3.32 (m, 4H), 1.20 (d, J = 6.4 Hz, 24H). ^{13}C NMR (100 MHz, CD_3OD) δ 43.56, 24.10. ^{31}P NMR (162 MHz, CD_3OD) δ 20.98 ppm. FT-IR data in KBr pellet (cm^{-1}): 3220, 2972, 2937, 2876, 1463 1423, 1385, 1120, 1094, 1037, 932, 897, 847, 726 and 626. MALDI-TOF = 263.2359 [M^+]. Anal. Calcd. For $C_{12}H_{32}ClN_4O_4P$: C 39.72; H 8.89; N 15.44. Found: C 39.73; H 8.87; N 15.41.

4.2.2.12 Binary salt 12: Tetraisopropylaminophosphonium periodate (TIAP·IO_4): To a stirred solution of TIAP·Cl (1 g, 0.0033 mol) in methanol (20 mL), $NaIO_4$ (1.05 g, 0.0049 mol) in water (10 mL) was slowly added with the formation of NaBr precipitate. The reaction mixture was stirred at room temperature for a further period of 10-15 min. and filtered through celite. The obtained clear solution was left for the crystallization process. Colorless block-shaped crystals of TIAP·IO_4 were obtained after one week.

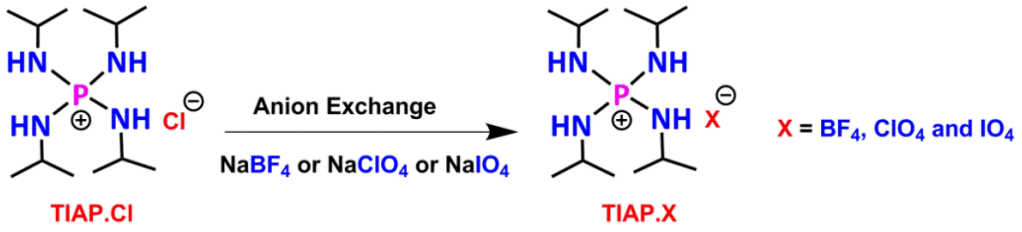

Scheme 4.4. Synthesis of organic binary salt TIAP·X (X = BF_4, ClO_4 and IO_4).

Yield: 1.45 g (96%). M.P. 160-166 °C. ^{1}H NMR (400 MHz, CD_3OD)) δ 3.41 – 3.32 (m, 4H), 1.21 (d, J = 6.4 Hz, 24H). ^{13}C NMR (100 MHz, CD_3OD) δ 43.56, 24.12. ^{31}P NMR (162 MHz, CD_3OD) δ 20.99 ppm. FT-IR data in KBr pellet (cm^{-1}): 3218, 2983, 2966, 1462, 1383, 1166, 1123, 1036, 919, 897, 757, 726 and 619. MALDI-TOF = 263.2359 [M$^+$]. Anal. Calcd. For $C_{12}H_{32}IN_4O_4P$: C 31.73; H 7.10; N 12.33. Found: C 31.67; H 7.11; N 12.35.

4.2.3 Crystallography: The single-crystal X-ray diffraction (SCXRD) analyses for all the phosphonium compounds were obtained on a Bruker Smart Apex Duo diffractometer by using Mo Kα radiation (λ= 0.71073Å). The structures were solved by intrinsic or direct methods and then refined by full-matrix least-squares against F^2 using all data by using SHELXL-2017 built in the Apex 3 suite.[28] Crystallographic refinement data for all the phosphonium salts at various temperature intervals are listed in (Table 4.1). All the non-hydrogen atoms were refined anisotropically if not stated otherwise. Hydrogen atoms were constructed in geometric positions to their parent atoms.[29] For the TPAP.IO_4 salt, the anionic IO_4 unit was disordered over four different positions. One of the phenyl rings in this salt was also disordered over two positions. Atom positions of all the disordered sites as well their occupancies were modeled using the same distance and similar U-restraints by applying SAME, SIMU and SUMP commands. The bond distances and angles and other structural illustrations were obtained by using the DIAMOND-3.1 software package.

Table 4.1: Crystallographic data for all newly synthesized phosphonium salts at various temperatures.

Compound	**TPAP·BF$_4$**	**DPDP·BF$_4$**	**DPDP·BF$_4$**	**PTAP·BF$_4$**
Chemical formula	$C_{21}H_{23}BF_4NP$	$C_{18}H_{26}BF_4N_2P$	$C_{18}H_{26}BF_4N_2P$	$C_{15}H_{29}BF_4N_3P$
Formula weight	407.18	388.19	388.19	369.19
Temperature	100(2)K	100(2)K	150(2)K	100(2)K
Crystal system	Monoclinic	Monoclinic	Monoclinic	Monoclinic
Space group	*Pn*	*Pn*	*Cc*	$P2_1/n$
a (Å); α (°)	9.248(3); 90	14.622(8); 90	15.5655(15); 90	9.7284(12); 90
b (Å); β(°)	8.694(3); 104.641(7)	9.048(5); 103.163(14)	9.0923(9); 103.175(2)	16.1549(19); 92.182(3)
c (Å); γ (°)	12.874(4); 90	15.561(8); 90	14.6950(14); 90	12.5433(14); 90
V (Å^3); Z	1001.5(6); 2	2004.6(18); 4	2025.0(3); 4	1969.9(4); 4
ρ (calc.) g cm^{-3}	1.350	1.286	1.273	1.245
μ(Mo K$_\alpha$) mm^{-1}	0.179	0.177	0.175	0.177
2θ_{max} (°)	54.66	52.74	56.54	55.76
R(int)	0.0494	0.0959	0.0357	0.0630
Completeness to θ	99.9	99.9	100	100
Data / param.	3958/217	7869/469	4449/211	4697/205
GOF	1.031	1.020	1.043	1.050
R1 [F>4σ(F)]	0.0403	0.0631	0.0559	0.0414
wR2 (all data)	0.0937	0.1668	0.1608	0.1109
max. peak/hole (e.Å^{-3})	0.328/-0.300	1.473/-0.513	1.141/-0.445	0.593/-0.622

Compound	**TIAP·BF$_4$**	**TPAP·ClO$_4$**	**TPAP·ClO$_4$**	**DPDP·ClO$_4$**
Chemical formula	$C_{12}H_{32}BF_4N_4P$	$C_{21}H_{23}ClNO_4P$	$C_{21}H_{22}ClNO_4P$	$C_{18}H_{26}ClN_2O_4P$
Formula weight	350.19	419.82	418.81	400.83
Temperature	100(2)K	150(2)K	200(2)K	100(2)K
Crystal system	Tetragonal	Monoclinic	Monoclinic	Monoclinic
Space group	*I-42m*	*Pc*	*Pn*	*Pn*
a (Å); α (°)	9.871(3); 90	13.953(5); 90	9.4106(19); 90	14.6743(9); 90
b (Å); β(°)	9.871(3); 90	8.682(3); 107.560(9)	8.751(19); 104.366(6)	9.0435(6); 102.926(2)
c (Å); γ (°)	9.547(3); 90	17.573(6); 90	12.871(3); 90	15.6533(10); 90
V (Å^3); Z	930.2(7); 2	2029.6(11); 4	1026.8(4); 2	2024.7(2); 4
ρ (calc.) g cm^{-3}	1.250	1.374	1.355	1.315
μ(Mo K$_\alpha$) mm^{-1}	0.185	0.294	0.291	0.292
2θ_{max} (°)	56.70	54.2	55.5	55.76
R(int)	0.0419	0.1178	0.0767	0.0733
Completeness to θ	100	99.9	100	100
Data / param.	631/32	7788/505	4218/253	9677/470
GOF	1.121	1.045	1.035	1.045
R1 [F>4σ(F)]	0.0221	0.0644	0.0570	0.0450
wR2 (all data)	0.0577	0.1124	0.1337	0.1067
max. peak/hole (e.Å^{-3})	0.200/-0.174	0.379/-0.361	0.331/-0.352	0.982/-0.740

Compound	**DPDP·ClO$_4$**	**PTAP·ClO$_4$**	**TIAP·ClO$_4$**	**TPAP·IO$_4$**
Chemical formula	$C_{18}H_{26}ClN_2O_4P$	$C_{15}H_{29}ClN_3O_4P$	$C_{12}H_{32}ClN_4O_4P$	$C_{21}H_{23}INO_{3.99}P$
Formula weight	400.83	381.83	362.83	510.84
Temperature	125(2)K	100(2)K	100(2)K	100(2)K
Crystal system	Monoclinic	Monoclinic	Tetragonal	Monoclinic
Space group	*Cc*	*P*2$_1$	*I*-42*m*	*P*2$_1$/*c*
a (Å); α (°)	15.5855(18); 90	9.368(2); 90	9.9290(12); 90	12.622(3); 90
b (Å); β(°)	9.0967(11);102.867(3)	15.391(3); 94.152(5)	9.9290(12); 90	7.5999(17); 90.525(5)
c (Å); γ (°)	14.7829(17); 90	27.587(6); 90	9.7163(12); 90	22.535(5); 90
V (Å^3); Z	2043.2(4); 4	3966.9(15) ; 8	957.9(3); 2	2161.6(8); 4
ρ (calc.) g cm^{-3}	1.303	1.279	1.258	1.570
μ(Mo K$_\alpha$) mm^{-1}	0.290	0.296	0.304	1.578
$2\theta_{max}$ (°)	56.54	52.74	56.58	50.06
R(int)	0.0568	0.1099	0.0493	0.0643
Completeness to θ	100	100	100	99.9
Data / param.	4506/211	16216/866	650/32	3814/288
GOF	1.030	1.005	1.116	1.464
R1 [F>4σ(F)]	0.0409	0.0515	0.0312	0.0708
wR2 (all data)	0.1012	0.1074	0.0761	0.1663
max. peak/hole (e.Å^{-3})	0.574/-0.339	0.294/-0.335	0.246/-0.349	1.883/-2.719

Compound	**DPDP·IO$_4$**	**PTAP·IO$_4$**	**TIAP·IO$_4$**
Chemical formula	$C_{18}H_{26}IN_2O_4P$	$C_{15}H_{29}IN_3O_4P$	$C_{12}H_{32}IN_4O_4P$
Formula weight	492.28	473.28	454.28
Temperature	100(2)K	100(2)K	100(2)K
Crystal system	Monoclinic	Monoclinic	Monoclinic
Space group	*Cc*	*P*2$_1$/*n*	*P*2$_1$/*n*
a (Å); α (°)	16.132(5); 90	9.4605(16); 90	9.4556(14); 90
b (Å); β(°)	9.130(3); 103.993(6	15.753(3); 94.485(4)	16.279(2); 95.307(3)
c (Å); γ (°)	14.981(5); 90	13.812(2); 90	13.269(2); 90
V (Å^3); Z	2140.9(11); 4	2052.0(6); 4	2033.7(5); 4
ρ (calc.) g cm^{-3}	1.527	1.532	1.484
μ(Mo K$_\alpha$) mm^{-1}	1.594	1.661	1.673
$2\theta_{max}$ (°)	55.76	55.76	55.74
R(int)	0.0290	0.0638	0.0357
Completeness to θ	100	100	100
Data / param.	4865/211	4897/218	4854/199
GOF	1.023	1.056	1.034
R1 [F>4σ(F)]	0.0175	0.0229	0.0183
wR2 (all data)	0.0411	0.0568	0.0447
max. peak/hole (e.Å^{-3})	0.504/-0.566	0.471/-0.522	0.711/-0.702

4.2.4 Ferroelectric, dielectric and piezoelectric measurements: The ferroelectric polarization measurements were performed on the single crystals of TPAP·BF_4, DPDP·BF_4, DPDP·ClO_4, and DPDP·IO_4 using a Sawyer-Tower circuit at room temperature. For ferroelectric measurements, the conducting copper adhesive was used on both sides of the two opposite ends of the single crystals. The ferroelectric polarization and fatigue measurements were performed on aixACCT TF-2000E model hysteresis loop analyzer. Leakage current density experiments were conducted dynamically for various voltage steps during the hysteresis loop measurements. The dielectric permittivity measurements were performed on the pressed powder pellets of TPAP·BF_4, DPDP·BF_4, TIAP·BF_4, DPDP·ClO_4, TPAP·ClO_4, TIAP·ClO_4 and DPDP·IO_4, respectively. The temperature and frequency dependent dielectric constants were measured in a Novocontrol Dielectric Spectrometer. The dielectric constants for all the composite films were carried out with an applied operating frequency between 5 Hz and 5 kHz, which corresponds to the electrical field of 10 V at room temperature. The d_{33} measurements were performed on a Piezotest meter model PM300 on the single crystals of TPAP·BF_4, DPDP·BF_4, TIAP·BF_4, DPDP·ClO_4, TPAP·ClO_4, TIAP·ClO_4 and DPDP·IO_4.[30] To confirm the presence of polarization in these phosphonium salts, preliminary theoretical dipole moment ONIOM calculations were performed by using Gaussian 09 program. For in this purpose, the anionic parts were taken as the high layer and the cationic segments were chosen as the lower layer. These dipole moment calculations were performed by using the density functional theory (DFT) methods.[31]

4.2.5 Non-Linear Optical Properties: The second harmonic generation (SHG) analysis of all the synthesized compounds was measured by using Kurtz and Perry method. The irradiation frequency of 1064 nm was generated by using Q- switched Nd:YAG laser. The as-grown single crystals of all the synthesized phosphonium compounds were ground in the form of unsieved powders which were then filled into a capillary tube for the measurements. The powdered KDP was used as a reference material for all the SHG measurements.[32]

4.2.6 General procedure for the preparation of the phosphonium salt/TPU composites and devices: The general procedure for the fabrication of the phosphonium Salt/TPU composite devices involves the dissolution of the appropriate quantities of the ferro- and/or piezoelectric crystallites into a homogeneous solution containing TPU in tetrahydrofuran (THF). The mixture was further homogenized by heating at 70° C for 15 minutes, followed by vortex mixing for 15 minutes. The homogeneous reaction mixtures of the composite solutions were poured into a glass mould and then dried at room temperature for 24 hours. The dried free-standing TPAP·BF_4/TPU, DPDP·BF_4/TPU, TIAP·BF_4/TPU and DPDP·PF_6/TPU polymeric films of various weight percentages (wt %) in 5, 10, 15 and 20 were subsequently peeled off from the glass mould (Schemes 4A.1-4A.2 and Table 4A.8, Appendix 4). The device architectures were subsequently completed by placing copper adhesive tapes on either side of the films and the electrodes were finally covered with the 0.1 mm thick PDMS polymer.

4.3 Results and discussion

4.3.1 Synthesis, characterization and crystal structures: The organoamino phosphonium salts of $[Ph_3(^{i}PrNH)P]\cdot BF_4$ (TPAP·BF_4), $[Ph_3(^{i}PrNH)P]\cdot ClO_4$ (TPAP·ClO_4), $[Ph_3(^{i}PrNH)P]\cdot IO_4$ (TPAP·IO_4), $[Ph_2(^{i}PrNH)_2P]\cdot BF_4$ (DPDP·BF_4), $[Ph_2(^{i}PrNH)_2P]\cdot ClO_4$ (DPDP·ClO_4), $[Ph_2(^{i}PrNH)_2P]\cdot IO_4$ (DPDP·IO_4), $[Ph(^{i}PrNH)_3P]\cdot BF_4$ (PTAP·BF_4), $[Ph(^{i}PrNH)_3P]\cdot ClO_4$ (PTAP·ClO_4), $[Ph(^{i}PrNH)_3P]\cdot IO_4$ (PTAP·IO_4), $[(^{i}PrNH)_4P]\cdot BF_4$ (TIAP·BF_4), $[(^{i}PrNH)_4P]\cdot ClO_4$ (TIAP·ClO_4) and $[(^{i}PrNH)_4P]\cdot IO_4$ (TIAP·IO_4) containing tetrahedral anions were synthesized by the anion exchange reactions of their corresponding bromide or chloride salts (Schemes 4.1-4.4).[26] All the newly synthesized phosphonium salts were characterized by ^{1}H, ^{13}C, ^{31}P, ^{11}B and ^{19}F-NMR spectroscopy, mass spectrometry and single crystal X-ray diffraction analysis (Figures 4A.1-4A.4, Appendix 4).

Scheme 4.5: Schematic diagrams of the synthesized organo-amino phosphonium salts of tetrahedral multi-atomic anions.

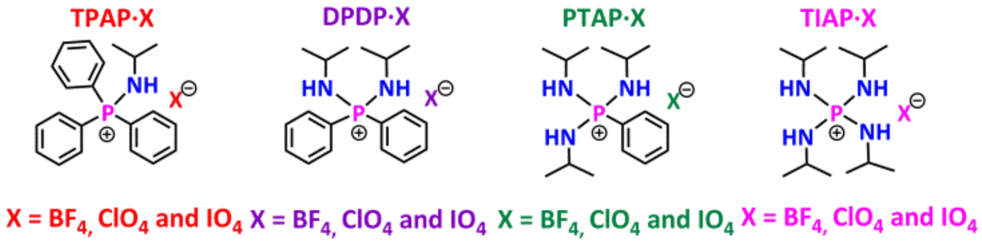

While the earlier studied DPDP·PF_6 salt adopts a monoclinic polar space group *Cc*, the other two salts TPAP·PF_6 and PTAP·PF_6 were found to crystallize in the centrosymmetric space groups. This could be due to the presence of octahedral PF_6^- ions exhibiting a structure-directing role.[26] Thus, we employed the lower symmetric tetrahedral BF_4^-, ClO_4^- and IO_4^- anions in crystallization with the phosphonium cations having one, two, three and four amino groups to improve the possibility of obtaining H-bonded polar assemblies. The single-crystal X-ray diffraction analysis showed that eight among the twelve phosphonium salts, TPAP·BF_4, TPAP·ClO_4, DPDP·BF_4, DPDP·ClO_4, DPDP·IO_4, PTAP·ClO_4, TIAP·BF_4, and TIAP·ClO_4 were solved in the acentric space groups with six of them crystallizing in the polar space groups. The other salts, TPAP·IO_4, PTAP·BF_4, PTAP·IO_4 and TIAP·IO_4 were solved in the centrosymmetric space groups (Figure 4.1a-l).

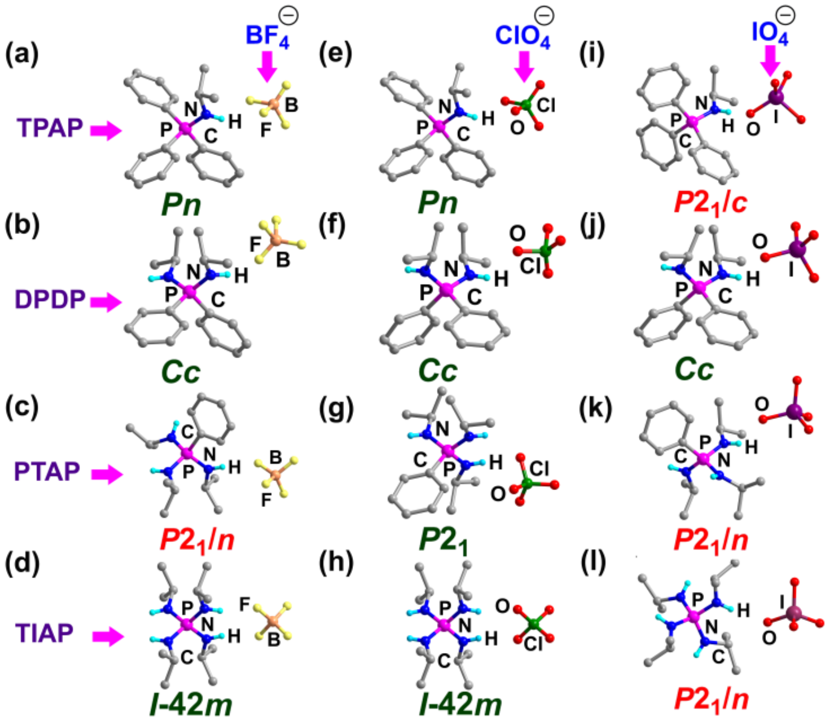

Figure 4.1: *Crystal structures of the organoamino phosphonium salts of tetrahedral anions in their prevalent space groups (a-l).*

Moreover, three phosphonium salts were found to exhibit a phase transition below room temperature between two distinct polar space groups. The TPAP·ClO_4 shows phase transition from monoclinic *Pc* to monoclinic *Pn* upon sweeping the temperature from 150 to 200 K. The salts DPDP·BF_4 and DPDP·ClO_4 were found to crystallize in the monoclinic space group *Pn* at 100 K. However, at higher temperatures (150 K for DPDP·BF_4 and 125 K for DPDP·ClO_4), they crystallized in the monoclinic space group *Cc* (Tables 4.1 and 4A.1, Appendix 4).

All these phosphonium salts exhibit interesting arrays of H-bonding interactions, due to the presence of one or more donor amino protons and four H-bond acceptor sites on each of the anionic moieties. Thus, the unique amino protons in all the salts of TPAP cation were H-bonded to one of the four electronegative atoms of the anions (F or O), resulting in a binary assembly of cations and anions in their corresponding crystal lattice (Figures 4A.5-4A.7, Appendix 4). The weak non-classical C-H···X bonds facilitate further propagation of these assemblies. In the DPDP series, the two amino protons are oriented in a divergent manner (in the *Cc* space group) and involved in a corrugated 1D-chain like structure via N-H···X type interactions (X = F or O) along the polar b-axis (Figures 4.2a-c, 4A.8 and 4A.9, Appendix 4).

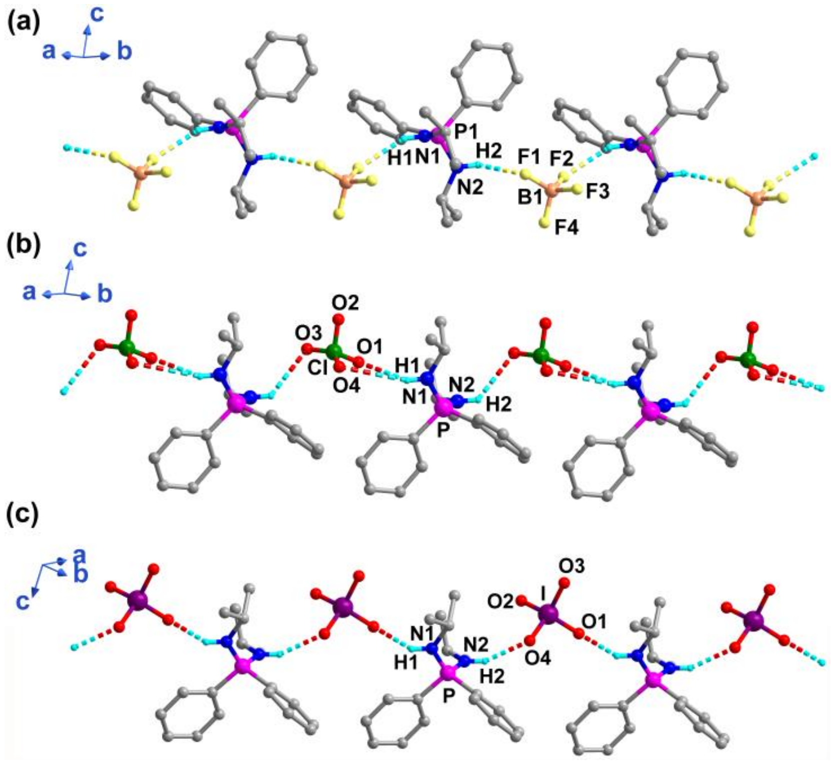

Figure 4.2: *1D-hydrogen bonded corrugated chain-like structures of (a) DPDP·BF_4, (b) DPDP·ClO_4 and (c) DPDP·IO_4 mediated by classical N-H···F or N-H···O hydrogen bonds.*

Each of the three tris-amino substituted PTAP salt exhibits different types of H-bonded assemblies. The polar structure of PTAP·ClO_4 (monoclinic $P2_1$) contains four independent molecules in the asymmetric unit forming three unique types of 1D-chains (two Zigzag chains along the b-axis and one linear-chain along the a-axis) (Figure 4A.10, Appendix 4). Formation of these chains involve a number of H-bonds including chelating and bridging motifs in which the chelating interactions are assisted by a pair of double N-H donors from two of the three amino groups forming graph set $R_2^2(8)$ type rings. In contrast, the centrosymmetric crystals of PTAP·BF_4 (monoclinic $P2_1/n$) and PTAP·IO_4 (monoclinic $P2_1/n$) form extended two-dimensional H-bonded assemblies built on one or more macrocycles (Figures 4A.11 and 4A.12, Appendix 4). The 2D-assembly of PTAP·BF_4 is built on only one type of macrocycle represented by graph set $R_6^6(24)$ rings in 'hcb' (3-c uninodal net) topology. Whereas the 2D-assembly in PTAP·IO_4 consists of smaller $R_4^4(16)$ and larger $R_8^8(32)$ macrocycles arranged in 'fes' (3-c uninodal net) topology.[33]

In contrast, the tetra-amino substituted TIAP salts were shown to exhibit two different types of H-bonding (Figures 4A.13b,d and 4A.14b, Appendix 4). A simplistic twisted-linear chain structure consisting of well-known $R_2^2(8)$ rings were observed in the tetragonal structures of TIAP·BF_4 and TIAP·ClO_4. The four amino groups in each of these assemblies act like the double H-donors on either side of the phosphorus center. In return, the tetrahedral BF_4^- and ClO_4^- anions bind to two phosphonium cations via chelating interactions (Figure 4A.13, Appendix 4). In contrast, the TIAP·IO_4 forms a three-dimensional H-bonded network. Each phosphonium unit is connected to four IO_4^- anions and each IO_4^- unit is H-bonded with four phosphonium cations resulting in the formation of a 3D-net of 'crb' (4-c uninodal net) topology. Construction of this network is accompanied by the formation of three different macrocycles represented by the graph set $R_4^4(16)$, $R_6^6(24)$, and $R_8^8(32)$ rings (Figure 4A.14, Appendix 4).

The variable-temperature single-crystal X-ray diffraction analysis (VT-SCXRD) of these phosphonium salts, except those of TPAP·ClO_4, DPDP·BF_4 and DPDP·ClO_4, show no phase transitions at all the measured temperatures between 100 and 473 K (Figures 4A.15-4A.21, Appendix 4). However, the polar crystal symmetries of these three salts were preserved from room temperature and above. A small volume change observed at higher temperatures for some of these phosphonium salts may be attributed to the mere thermal expansion of the unit cell boundaries. The variable-temperature powder X-ray diffraction (VT-PXRD) analysis of these salts signifies the bulk phase purity of these samples for wide temperature ranges (Figures 4A.22a, 4A.23a, 4A.24a and 4A.25, Appendix 4). The thermal analysis (TG/DTA) of TPAP·BF_4, DPDP·BF_4 and TIAP·BF_4 salts shows two heat anomalies about their melting points (well below 505 K) followed by their decomposition points (below 600 K) supporting the high thermal and phase stabilities of these salts (Figures 4A.22b, 4A.23b and 4A.24b, Appendix 4). The room temperature second harmonic generation (SHG) measurement was performed on the samples of TPAP·BF_4, TPAP·ClO_4, DPDP·BF_4, DPDP·ClO_4, DPDP·IO_4, TIAP·BF_4, and TIAP·ClO_4 to confirm their non-centrosymmetric crystal symmetry. The finely grounded and unsieved powder samples of these phosphonium salts gave the respective SHG efficiencies of 0.25, 0.29, 1.17, 0.29, 0.13, 0.25 and 0.17, corresponding to the standard potassium dihydrogen phosphate (KDP) sample.

4.3.2 Ferroelectric, dielectric and piezoelectric studies

Crystals of TPAP·BF_4, TPAP·ClO_4, DPDP·BF_4, DPDP·ClO_4, DPDP·IO_4 and PTAP·ClO_4 were solved in the polar acentric space group suitable for ferroelectric behavior. Accordingly, the *P-E* loop measurements performed on single crystals of the polar salts of TPAP·BF_4, DPDP·BF_4, DPDP·ClO_4 and DPDP·IO_4 by using a Sawyer-Tower circuit gave a rectangular hysteresis loop at room temperature. However, polar TPAP·ClO_4 and PTAP·ClO_4 salts did not yield any signature hysteresis loops due to the poor quality of their single crystals. The observed remnant polarization (P_r) and coercive field (E_c) of TPAP·BF_4, DPDP·BF_4, DPDP·ClO_4, and DPDP·IO_4 were found to be 0.22, 35.36, 21.83, 21.12 μC cm^{-2} and 0.42, 1.38, 0.87, 2.36 kV cm^{-1}, respectively (Figures 4.3a-c and 4A.26, Appendix 4). The computed dipole moments from the ONIOM calculations support the presence of ferroelectric polarization in these phosphonium salts (Table 4A.2, Appendix 4).

The origin of ferroelectricity in the salts of DPDP·BF_4, DPDP·ClO_4, DPDP·IO_4 and TPAP·BF_4 can be tracked to their asymmetric ionic lattice coupled with their H-bonded 1D-chain structures that helps in the alignment of dipoles responsible for their long-range polar order. It is to be noted that the polarization observed for the DPDP salts is relatively higher than that of TPAP·BF_4. This can be attributed to the formation of infinite 1D-hydrogen bonded structures in the DPDP salts mediated by strong N-H···X bonds that facilitates the long-range order along the polar b-axis.

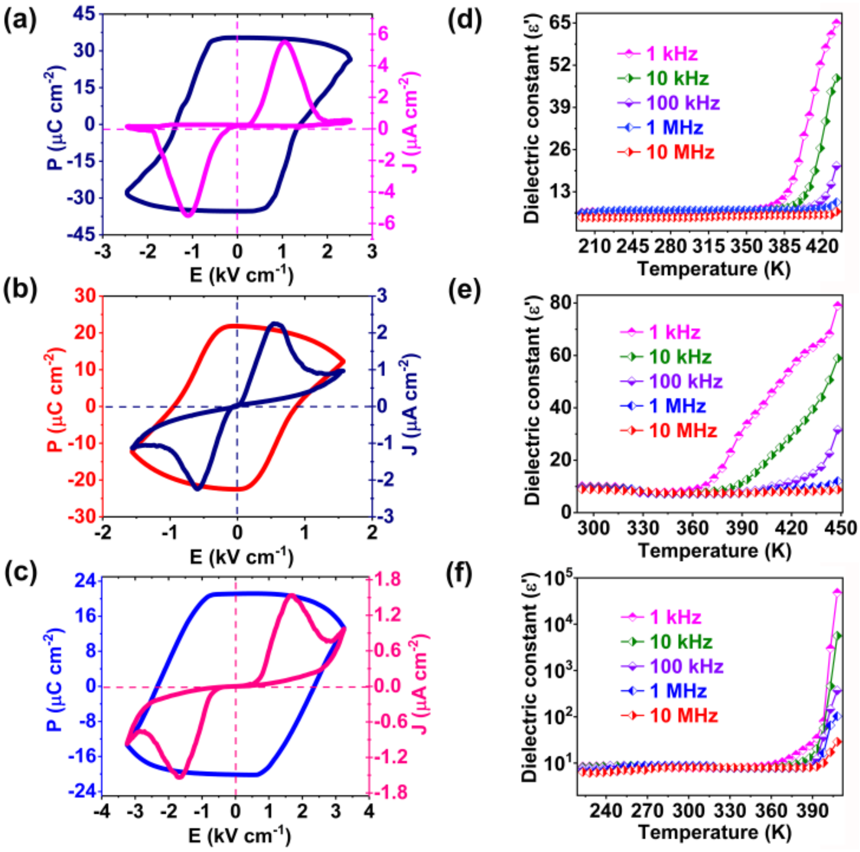

Figure 4.3: *The P-E hysteresis loops and leakage current density plots of (a) DPDP·BF_4, (b) DPDP·ClO_4 and (c) DPDP·IO_4. Temperature dependence of ε' plots of (d) DPDP·BF_4, (e) DPDP·ClO_4 and (f) DPDP·IO_4 at various frequencies.*

However, the ionic salt of TPAP·BF_4 shows a discrete binary structure supported by N-H···F bonds. Much weaker C-H···F bonds loosely connect these discrete units via one of the aromatic meta C-H groups that presumably support only a weakened dipolar ordering along the b-axis. Nevertheless, it is to be noted that, the magnitude of ferroelectric polarization depends on several factors such as the individual functionalities of molecular components, long-range ordering, quality of the single crystals, the polarizing ability of cations and anions and also the thermal and electrical response of single crystals used for the measurements.[34-39]

The observed P_r values are higher than earlier known organo and amino phosphonium salts; phosphonium stabilized metal-organic frameworks and other charge-separated hybrid materials.[26,32,40-45] Furthermore, the current density measurements of all these four samples show peaks at the domain switching points along with low leakage current densities confirming the ferroelectric nature of their *P-E* loops. Also, the fatigue measurement studies on these crystals suggest the retention of ferroelectric polarization even after 10^6 cycles (Figure 4A.27, Appendix 4).

The dielectric permittivity measurements of TPAP·BF_4, TPAP·ClO_4, DPDP·BF_4, DPDP·ClO_4, DPDP·IO_4, TIAP·BF_4 and TIAP·ClO_4 were performed on their compressed pellets at different temperature intervals at constant operating frequencies from 1 kHz to 10 MHz (Figures 4.3d-f and 4A.28-4A.34, Appendix 4). For all these compounds, the real part of the dielectric constants (ε') was found to increase linearly upon increasing the temperatures, which further increases rapidly near to their corresponding melting points, indicating the presence of more polarizable dipoles (charge carriers and ionic mobility) in those temperature regions. Interestingly, no notable curie points (ferroelectric to paraelectric phase) were observed for any of these salts between 200 K and their respective melting points, which are unusual in most of the known molecular ferroelectric materials. This can be attributed to the presence of stable supramolecular H-bonding interactions coupled with strong ionic bonding in their crystal structures.[46-48] The observed ε' (293 K and 1 MHz) values of TPAP·BF_4, TPAP·ClO_4, DPDP·BF_4, DPDP·ClO_4, DPDP·IO_4, TIAP·BF_4 and TIAP·ClO_4 were found to be 9.28, 16.21, 7.26, 9.08, 8.75, 16.67 and 16.88, respectively. The dielectric loss factors (tan δ) as a function of temperature indicate the low dielectric loss nature of these salts. The frequency dependent ε' and tan δ measurements of these ionic salts show similar trends to those observed in the temperature dependent ε' measurements.

The direct piezoelectric coefficient (d_{33}) measurements were performed on the single crystals of several of these phosphonium salts with an externally applied force of 0.25 N and the operating frequency of 110 Hz using the Berlincourt method.[49] The observed d_{33} values of 3, 4, 7, 12, 8, 3 and 3 pC N^{-1} for the single crystals of TPAP·BF_4, TPAP·ClO_4, DPDP·BF_4, DPDP·ClO_4, DPDP·IO_4, TIAP·BF_4 and

TIAP·ClO_4, respectively, are comparable to those observed for well-known small-molecule based piezo- and ferroelectric materials.[50-52]

4.3.3 Fabrication and characterization of the phosphonium salt-polymer composites

Inspired by our earlier observation of DPDP·PF_6 as a ferroelectric flexible mechanical energy harvesting device in the form of a PDMS polymer composite, we set out to examine the utility of the entire family of these compounds for this application. Owing to the shock-sensitive nature of the ClO_4^- and IO_4^- salts, only the BF_4^- salts of these phosphonium salts were subjected for the energy generation through impact force measurements. Except for PTAP·BF_4, which is centrosymmetric, all the other BF_4^- stabilized phosphonium cations showed high thermal and structural stabilities along with ferro- and/or piezoelectric properties and thus are suitable for this application. In view of preparing all organic, flexible salt-polymer composites, we chose to employ thermoplastic polyurethane (TPU) as a polymer matrix.

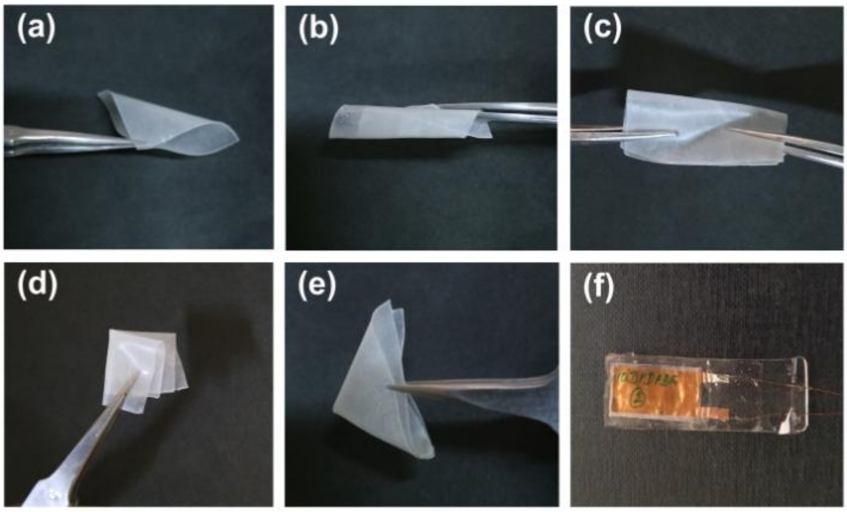

Figure 4.4: *Photographs of the 10 wt % of DPDP·BF_4/TPU composite films showing (a) folding, (b) rolling, (c) stretching and (d, e) multi-fold bending operations. (f) Image of the as-made 10 wt % DPDP·BF_4/TPU device.*

The preparation of the phosphonium salt/TPU composites involves the dissolution of the appropriate quantities of phosphonium salt crystallites into a homogeneous solution containing TPU in tetrahydrofuran (THF) followed by heating and mechanical stirring. The homogeneous solutions were poured into a mould and the freestanding TPAP·BF_4/TPU, DPDP·BF_4/TPU and TIAP·BF_4/TPU polymeric films of various (5, 10, 15 and 20) weight percentages (wt %) of the phosphonium salts were subsequently peeled off from it (Table 4A.3, Schemes 4A.1 and 4A.2, Appendix 4). All these films were shown to exhibit high degrees of flexibility for folding, rolling, stretching and multi-fold bending operations (Figure 4.4a-e). A similar set of TPU composites of the earlier reported DPDP·PF_6 salt (DPDP·PF_6/TPU) has also been prepared and studied for comparison.

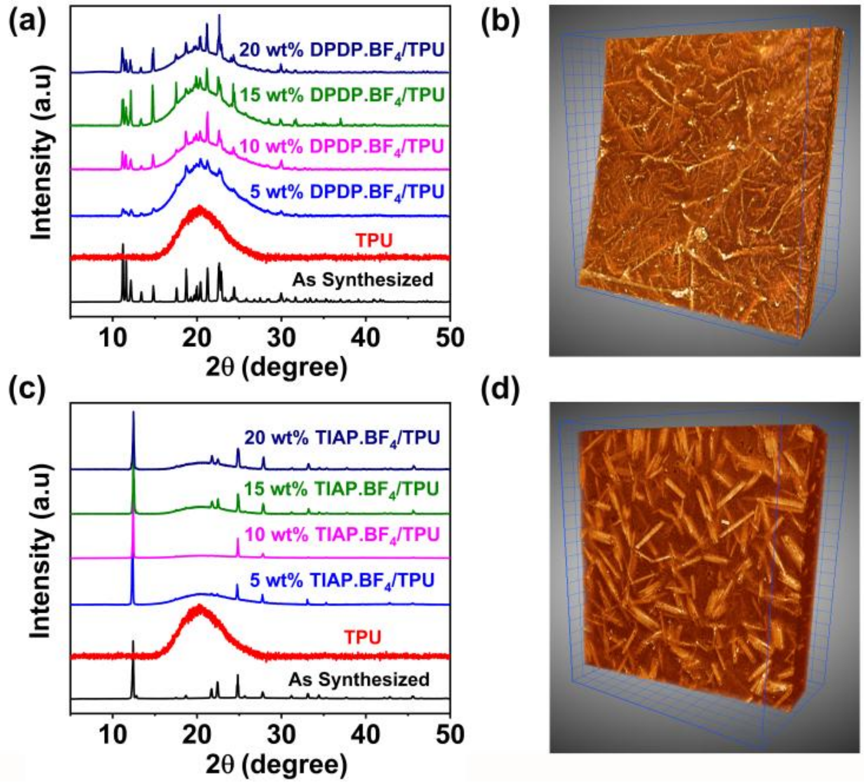

Figure 4.5: *The PXRD patterns of (a) DPDP·BF_4/TPU and (c) TIAP·BF_4/TPU films and the X-ray 3D-tomography images of the corresponding 10 wt % composites of (b) DPDP·BF_4/TPU and (d) TIAP·BF_4/TPU (grid-scale: 100 μm).*

The phase purity of the embedded phosphonium salt particles in all the wt % phosphonium salt-TPU composites was identified by performing the X-ray diffraction analysis. These results indicate that the crystalline nature of the phosphonium salts is unaffected in all the instances. Also, as the loading of particles increases (5 to 20 wt %), the phase purity of phosphonium salts was found to be more prominent with a concomitant increase in the crystalline nature of the composite films (Figures 4.5a,c and 4A.35, Appendix 4).

The structural morphologies of all the polymeric composite films were characterized by performing the X-ray 3D-tomography analysis. These studies reveal the presence of the phosphonium salt crystallites in the embedded polymer composite films. The magnified X-ray 3D-tomography images of the various organic salt-TPU composites are shown in Figures 4.5b,d and 4A.36-4A.41, Appendix 4. These images reveal the highly crystalline nature of the embedded particles in the composite matrices in a homogenous distribution. Also, from the tomography images, an increase in the particle distribution and density of the composites can be observed upon increasing the loading from 5 to 20 wt %. Moreover, the morphologies of the embedded particles were found to be significantly different with respect to each other for all the phosphonium salt/TPU composite films. The composite films were subsequently electroded and covered with a layer of PDMS polymer to eliminate surface static charges during the measurements (Figure 4.4f).

4.3.4 Energy harvesting performance of the composite devices

The mechanical energy generation responses of the as-made phosphonium salt-TPU composite devices were tested with the help of an in-house built impact setup coupled with an oscilloscope. The electromechanical performance of all the fabricated non-poled devices was shown to exhibit excellent output voltages and output currents for the prepared 5, 10, 15 and 20 wt % composites films. An optimized mechanical force of 22 N and the frequency of 8 Hz were found to yield the best results for all the composite devices. The maximum output peak to peak voltages (V_{PP}) and output peak to peak currents (I_{PP}) of 7.37, 8.95, 4.75, 6.73 V and 0.61, 0.89, 0.41, 0.47 μA, respectively, were observed for the 10 wt % composites of TPAP·BF_4/TPU, DPDP·BF_4/TPU, TIAP·BF_4/TPU and DPDP·PF_6/TPU (Figure 6a-d). For other weight percentages, both the V_{PP} and I_{PP} values were found to decrease by a few units with 20 wt % devices showing a notable decrease (Figures 4A.42-4A.53, Appendix 4). The best current density (CD) and power density (PD) values in this series were again observed for the 10 wt % devices. Thus, the 10 wt % devices of TPAP·BF_4/TPU, DPDP·BF_4/TPU, TIAP·BF_4/TPU and DPDP·PF_6/TPU gave the CD values of 0.16, 0.23, 0.11, 0.12 μA cm^{-2} and PD values of 4.77, 10.16, 2.16, 2.83 μW cm^{-3}, respectively (Figures 4.7a,b, 4A.54 and Table 4A.4, Appendix 4). As seen in the trends of the V_{PP} and I_{PP} values, the CD and PD values of these devices first increase with the increase in the wt % loading of the phosphonium salts and sharply decline after attaining the maximum at 10 wt %. It is also visible that within a given anionic series, the V_{PP} (and power densities) of the optimal 10 wt % composites having ferroelectric TPAP·BF_4 and DPDP·BF_4 salts are higher than the device with only piezoelectric TIAP·BF_4 salt.

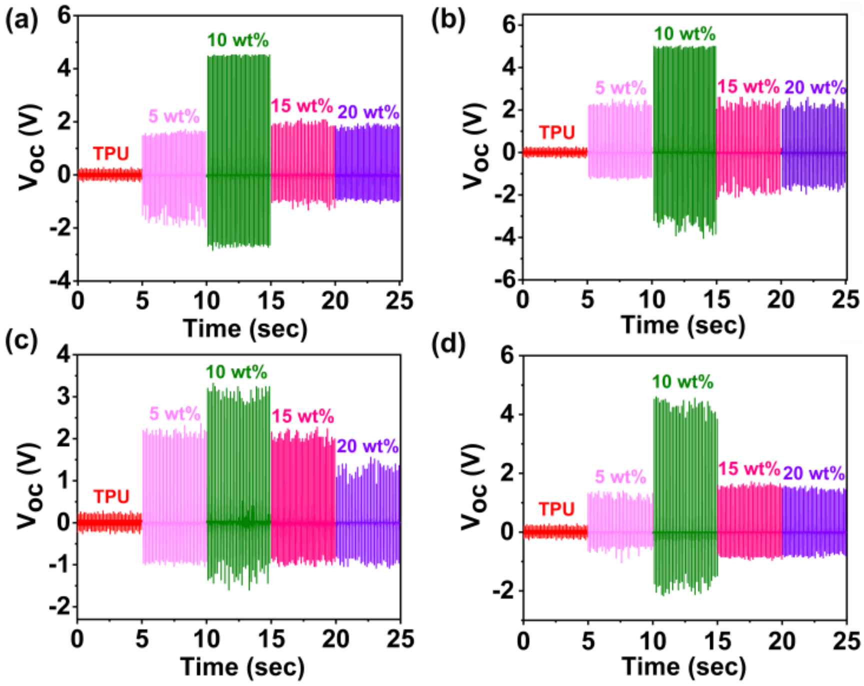

Figure 4.6: *The output voltage data of the various wt % (a) TPAP·BF_4/TPU, (b) DPDP·BF_4/TPU, (c) TIAP·BF_4/TPU and (d) DPDP·PF_6/TPU devices.*

Interestingly the output performance of the DPDP·PF_6/TPU films observed in the present instance (Figures 6d, 7b, 4A.51-4A.54 and Table 4A.4, Appendix 4) is comparable to that of the previously recorded DPDP·PF_6/PDMS films, which indicates that the energy harvested from these devices are mostly derived from the crystallites of the organic salts. The output performances of these new devices are comparable with other TPU based piezoelectric devices and have an additional advantage of being all-organic in composition.[53-55]

The decrease in the overall output performance of the devices at higher concentrations can be attributed to the agglomeration of the polar crystallites, which affects randomization of the dipoles responsible for their piezo-response.[56-57] This effect can predominantly be seen in the measured dielectric constant values of all the composite films at various frequencies at 10 V (Figures 4.7c,d, 4A.55 and 4A.56, Appendix 4).

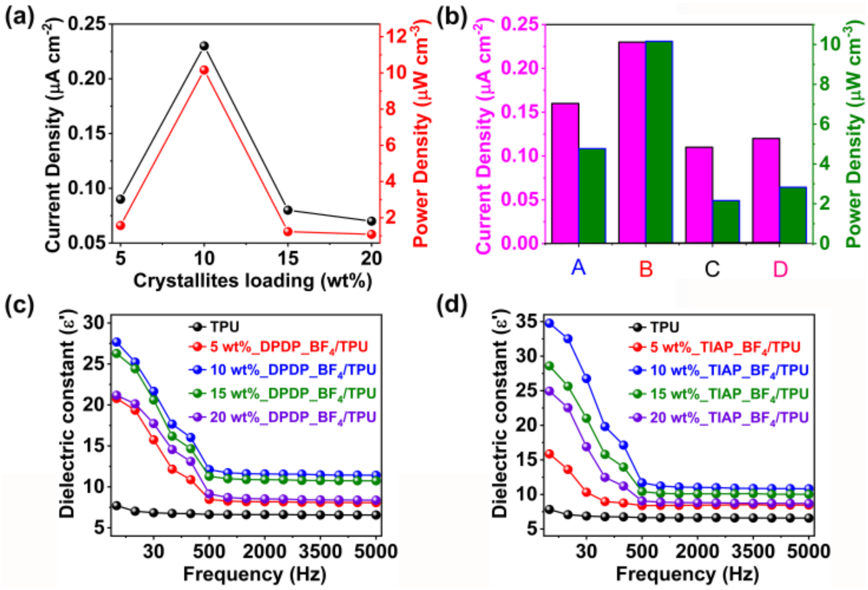

Figure 4.7: *(a) The output current density and power density plots for all the DPDP·BF_4/TPU composites and (b) the comparative bar diagram of current and power density data for the 10 wt % composite devices of TPAP·BF_4/TPU (A), DPDP·BF_4/TPU (B), TIAP·BF_4/TPU (C) and DPDP·PF_6/TPU (D). The comparative ε' data for the composite films of (c) DPDP·BF_4/TPU and (d) TIAP·BF_4/TPU.*

In all the cases, the maximum values of ε' has been observed for the 10 wt % films, while for the other compositions, especially for the 15 and 20 wt % composites, a visible decrease in the ε' values has been noted. This effect is more prominent, particularly in the lower frequency regimes where the dipole responses from the ferro- and/or piezoelectric crystallites are dominant in the environment of the bulk composites. The observed trends in the dielectric constant values of the composite films correlate well with the recorded output performance values of the corresponding devices. In general, the energy harvesting activity of any composite material is influenced by several factors including the thickness of composite, the strength of the mechanical force, applied frequency, the morphology of crystallites and ratio of the polymer to piezoelectric crystallites and by choice of supporting organic polymer.[58] Furthermore, we have measured the energy harvesting performance for the 10 wt % composite devices after a period of six months to check the mechanical durability of these samples. These experiments showed no voltage drop even after a resting period of six months. Furthermore, the fatigue studies performed on the 10 wt % DPDP·BF_4/TPU composite film showed excellent durability and retention of its output voltage even after 8000 cycles at a continuously applied force of 22 N with 8 Hz frequency (Figures 4A.57 and 4A.58, Appendix 4).

The energy storage capability of the 10 wt % of composites was determined by connecting the devices through a 100 μF capacitor by employing a full-wave bridge four diode rectifier circuit with an applied external force of 22 N. The voltage accumulated in the capacitor saturates in less than 60 s for all the composite devices with the stored energy (E) and measured charges (Q) of 74.42, 89.78, 50, and 61.61 μJ and 122, 134, 100 and 111 μC for the respective 10 wt % TPAP·BF_4/TPU, DPDP·BF_4/TPU, TIAP·BF_4/TPU and DPDP·PF_6/TPU films. The stored voltages at the saturation limits were found to be 1.22, 1.34, 1.00 and 1.11 for the 10 wt % of TPAP·BF_4/TPU, DPDP·BF_4/TPU, TIAP·BF_4/TPU and DPDP·PF_6/TPU films (Figures 4.8a,b, 4A.59 and 4A.60, Appendix 4). It is to be noted that the stored voltages across the capacitor were found to be less than the corresponding output voltages (V_{PP}), which can be attributed either to the voltage utilized in rectifying the diodes or leakage of the energy stored in the capacitors.[59-60]

The mechanical (viscoelastic) properties of the 10 wt % composites of TPAP·BF_4/TPU, DPDP·BF_4/TPU, TIAP·BF_4/TPU and DPDP·PF_6/TPU films were measured at room temperature by using a dynamic mechanical analyzer and compared with that of neat TPU.[61] All these composites exhibited high storage (E') and low loss (E”) modulus combined with a low damping behavior than that of the pure TPU, signifying a good interface and structural reinforcement between the phosphonium salt and the polymer within the composite architecture (Figures 8c,d and 4A.61, Appendix 4).

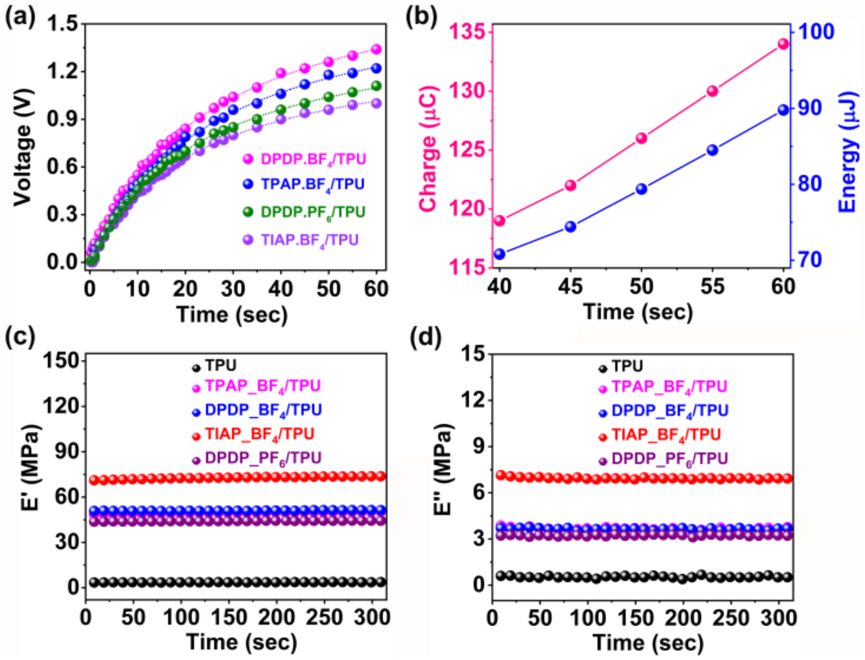

Figure 4.8: *(a) Capacitor charging of all the 10 wt % composite devices. The solid curves tracing the points are provided as a guide to the eye. (b) The measured charges and stored energy for the 10 wt % DPDP·BF$_4$/TPU device. The viscoelastic properties of all the 10 wt % composite films showing their (c) storage and (d) loss moduli.*

Since the crystalline nature of the phosphonium salts is unaffected in all the polymer composites (as confirmed by XRD, Figures 4.5a,c and 4A.35, Appendix 4), the mechanical reinforcement of TPU in substantially high in all of them. It is interesting to note that TIAP·BF$_4$/TPU composites show a significant enhancement in storage modulus (~20 times) as compared to other composites, which concurs well with X-ray tomography images (Figures 4.5d, 4A.37 and 4A.40, Appendix 4) where we could observe thick high aspect ratio fibrillar network of TIAP crystals within TPU matrix.

4.4 Conclusion

In summary, we have synthesized twelve new examples of specifically designed organo-amino phosphonium cations that are supported by non-coordinating BF_4^-, ClO_4^-, and IO_4^- anions. The *P-E* loop measurements gave the P_r values of 0.22, 35.36, 21.83 and 21.12 μC cm^{-2} for the 1D-hydrogen bonded assemblies of TPAP·BF_4, DPDP·BF_4, DPDP·ClO_4 and DPDP·IO_4 salts supported by N-H···X interactions. Further, all-organic composites films of TPAP·BF_4/TPU, DPDP·BF_4/TPU, TIAP·BF_4/TPU and DPDP·PF_6/TPU were prepared and shown to harvest mechanical energy by using an impact force setup. These experiments gave the maximum output voltages of 7.37, 8.95, 4.75, 6.73 V for the 10 wt % of TPAP·BF_4/TPU, DPDP·BF_4/TPU, TIAP·BF_4/TPU and DPDP·PF_6/TPU composite films. All these 10 wt % devices were found to exhibit notable output current and power density values. The capacitor charging experiment has demonstrated the utility of these devices for energy storage process. These outcomes suggest a promising development for the use of organic ferroelectric salts as all-organic energy harvesting devices that are envisioned to have a greater impact on future smart-home technologies.

4.5 References

(1) Lines, M. E.; Glass, A. M. *Principles and Applications of Ferroelectrics and Related Materials*; Oxford University Press: New York, 1977.

(2) Tang, Y. Y.; Li, P. F.; Liao, W. Q.; Shi, P. P.; You, Y. M.; Xiong, R. G. *J. Am. Chem. Soc.* **2018**, *140*, 8051–8059.

(3) Eerenstein, W.; Mathur, N, D.; Scott, J. F. *Nature* **2006**, *442*, 759–765.

(4) Martin, L. W.; Rappe, A. M. *Nat. Rev. Mater.* **2016**, *2*, 16087.

(5) Asadi, K.; van der Veen, M. A. *Eur. J. Inorg. Chem.* **2016**, *27*, 4332–4344.

(6) Shi, P. P.; Tang, Y. Y.; Li, P. F.; Liao, W. Q.; Wang, Z. X.; Ye, Q.; Xiong, R. G. *Chem. Soc. Rev.* **2016**, *45*, 3811–3827.

(7) Haertling, G. H. *J. Am. Ceram. Soc*. **1999**, *82*, 797–818.

(8) Park, B. H.; Kang, B. S.; Bu, S. D.; Noh, T. W.; Lee, J.; Jo, W. *Nature* **1999**, *401*, 682–684.

(9) Scott, J. F. *Science* **2007**, *315*, 954–959.

(10) Yang, S. Y.; Seidel, J.; Byrnes, S. J.; Shafer, P.; Yang, C. H.; Rossell, M. D.; Yu, P.; Chu, Y. H.; Scott, J. F.; Ager, J. W.; Martin, L. W.; Ramesh, R. *Nat. Nanotechnol*. **2010**, *5*, 143–147.

(11) Hoffman, J.; Pan, X.; Reiner, J. W.; Walker, F. J.; Han, J. P.; Ahn, C. H.; Ma, T. P. *Adv. Mater.* **2010**, *22*, 2957–2961.

(12) Bowen, C. R.; Kim, H. A.; Weaver, P. M.; Dunn, S. *Energy Environ. Sci*. **2014**, *7*, 25–44.

(13) Ellabban, O.; Abu-Rub, H.; Blaabjerg, F. *Renewable Sustainable Energy Rev.* **2014**, *39*, 748–764.

(14) Tao, P.; Ni, G.; Song, C.; Shang, W.; Wu, J.; Zhu, J.; Chen, G.; Deng, T. *Nat. Energy* **2018**, *3*, 1031–1041.

(15) Ray, T. R.; Choi, J.; Bandodkar, A. J.; Krishnan, S.; Gutruf, P.; Tian, L.; Ghaffari, R.; Rogers, J. A. *Chem. Rev.* **2019**, *119*, 5461–5533.

(16) Invernizzi, F.; Dulio, S.; Petrini, M.; Guizzetti, G.; Mustarelli, P. *Chem. Soc. Rev*. **2016**, *45*, 5455–5473.

(17) Xie, M.; Hisano, K.; Zhu, M.; Toyoshi, T.; Pan, M.; Okada, S.; Tsutsumi, O.; Kawamura, S.; Bowen, C. *Adv. Mater. Technol.* **2019**, *4*, 180026.

(18) Chae, I.; Jeong, C. K.; Ounaies, Z.; Kim, S. H. *ACS Appl. Bio Mater.* **2018**, *1*, 936–953.

(19) Chen, B.; Yang, Y.; Wang, Z. L. *Adv. Energy Mater.* **2019**, *9*, 1802906.

(20) Shepelin, N. A.; Glushenkov, A. M.; Lussini, V. C.; Fox, P. J.; Dicinoski, G. W.; Shapter, J. G.; Ellis, A. V. *Energy Environ. Sci.* **2019**, *12*, 1143–1176.

(21) Wang, Z. L.; Song, J. *Science* **2006**, *312*, 242–246.

(22) Li, J.; Wang, X. *APL Mater.* **2017**, *5*, 073801.

(23) Persano, L.; Dagdeviren, C.; Su, Y.; Zhang, Y.; Girardo, S.; Pisignano, D.; Huang, Y.; Rogers, J. A. *Nat. Commun.* **2013**, *4*, 1633.

(24) Lu, X.; Qu, H.; Skorobogatiy, M. *ACS Nano* **2017**, *11*, 2103–2114.

(25) Ram, F.; Ambone, T.; Sharma, A.; Murugesan, R.; Kajale, D.; Borkar, V.; Ali, S. F.; Balu, P. K.; Kumaraswamy, G.; Shanmuganathan, K. *J. Phys. Chem. C* **2018**, *122*, 16540–16549.

(26) Vijayakanth, T.; Srivastava, A. K.; Ram, F.; Kulkarni, P.; Shanmuganathan, K.; Praveenkumar, B.; Boomishankar, R. *Angew. Chem. Int. Ed.* **2018**, *57*, 9054–9058.

(27) Gupta, A. K.; Nicholls, J.; Debnath, S.; Rosbottom, I.; Steiner, A.; Boomishankar, R. *Cryst. Growth Des.* **2011**, *11*, 555–564.

(28) Sheldrick, G. M. *Acta Crystallogr. Sect. A* **2008,** *64*, 112–122.

(29) Spek, A. L. *Acta Crystallogr., Sect. D* **2009**, *D65*, 148–155.

(30) Cain, M. G. *Characterization of ferroelectric bulk materials and thin films*. Springer, 2014.

(31) Frisch, M.; Trucks, G.; Schlegel, H. *Gaussian 03, Revision B. 05, Gaussian, Inc., Wallingford*, CT, **2004**.

(32) Vijayakanth, T.; Pandey, R.; Kulkarni, P.; Praveenkumar, B.; Kabra, D.; Boomishankar, R. *Dalton.Trans.* **2019**, *48*, 7331–7336.

(33) Akhmetshina, T. G.; Blatov, V. A.; Proserpio, D. M.; Shevchenko, A. P. *Acc. Chem. Res*. **2018**, *51*, 21–30.

(34) Sato, O. *Nat. Chem*. **2016**, *8*, 644–656.

(35) Anetai,H.; Takeda, T.; Hoshino, N.; Kobayashi, H.; Saito, N.; Shigeno, M.; Yamaguchi, M.; Akutagawa, T. *J. Am. Chem. Soc.* **2019**, *141*, 2391–2397.

(36) Horiuchi, S.; Tokunaga, Y.; Giovannetti, G.; Picozzi, S.; Itoh, H.; Shimano, R.; Kumai, R.; Tokura, Y. *Nature* **2010**, *463*, 789–792.

(37) Ai, Y.; Chen, X. G.; Shi, P. P.; Tang, Y. Y.; Li, P. F.; Liao, W. Q.; Xiong, R. G. *J. Am. Chem. Soc.* **2019**, *141*, 4474–4479.

(38) Srivastava, A. K.; Divya, P.; Praveenkumar, B.; Boomishankar, R. *Chem. Mater.* **2015**, *27*, 5222–5229.

(39) Yadav, A.; Kulkarni, P.; Steiner, A.; Praveenkumar, B.; Boomishankar, R. *Chem. Eur. J.* **2018**, *24*, 14639–14643.

(40) Sante, D. D.; Stroppa, A.; Jian, P.; Picozzi, S. *J. Am.Chem. Soc*. **2013**, *135*, 18126–18130.

(41) Tammam, A. K.; El-Dean, T. S.; Mostafa, M. F. *Ferroelectrics* **2015**, *481*, 34–40.

(42) Zhou, L.; Shi, P. P.; Liu, X. M.; Feng, J. C.; Ye, Q.; Yao, Y. F.; Fu, D. W.; Li, P. F.; You, Y. M.; Zhang, Y.; Xiong, R. G. *NPJ Asia Materials*. **2019**, *11*, 15–23.

(43) Ye, H. Y.; Liao, W. Q.; Hu, C. L.; Zhang, Y.; You, Y. M.; Mao, J. G.; Li, P. F.; Xiong, R. G. *Adv. Mater.* **2016**, *28*, 2579–2586.

(44) Liao, W. Q.; Zhang, Y.; Hu, C. L.; Mao, J. G.; Ye, H. Y.; Li, P. F.; Huang, S. D.; Xiong, R. G. *Nat. Commun*. **2015**, *6*, 7338.

(45) Pan, Q.; Liu, Z. B.; Tang, Y. Y.; Li, P. F.; Ma, R. W.; Wei, R. Y.; Zhang, Y.; You, Y. M.; Ye, H. Y.; Xiong, R. G. A *J. Am. Chem. Soc.* **2017**, *139,* 3954–3957.

(46) Narayanan, A.; Cao, D.; Frazer, L.; Tayi, A. S.; Blackburn, A. K.; Sue, A. C. H.; Ketterson, J. B.; Stoddart, J. F.; Stupp, S. I. *J. Am. Chem. Soc.* **2017**, *139*, 9186–9191.

(47) Kobayashi, K.; Horiuchi, S.; Ishibashi, S.; Murakami, Y.; Kumai, R. *J. Am. Chem. Soc.* **2018**, *140*, 3842–3845.

(48) Horiuchi, S.; Kobayashi, K.; Kumai, R.; Ishibashi, S. *Nat. Commun.* **2017**, *8*, 14426.

(49) You, Y. M.; Liao, W. Q.; Zhao, D.; Ye, H. Y.; Zhang, Y.; Zhou, Q.; Niu, X.; Wang, J.; Li, P. F.; Fu, D. W.; Wang, Z.; Gao, S.; Yang, K.; Liu, J.; Li, J.; Yan, Y.; Xiong, R. G. *Science* **2017**, *357*, 306–309.

(50) Ye, H. Y.; Tang, Y. Y.; Li, P. F.; Liao, W. Q.; Gao, J. X.; Hua, X. N.; Cai, H.; Shi, P. P.; You, Y. M.; Xiong, R. G. *Science* **2018**, *361*, 151–155.

(51) Liao, W. Q.; Zhao, D.; Tang, Y. Y.; Zhang, Y.; Li, P. F.; Shi, P. P.; Chen, X. G.; You, Y. M.; Xiong, R. G. *Science* **2019**, *363*, 1206–1210.

(52) Yang, C. K.; Chen, W. N.; Ding, Y. T.; Wang, J.; Rao, Y.; Liao, W. Q.; Tang, Y. Y.; Li, P. F.; Wang, Z. X.; Xiong, R. G. *Adv. Mater.* **2019***, 31,* 1808088.

(53) Siddiqui, S.; Lee, H. B.; Kim, D. L.; Duy, L. T.; Hanif, A.; Lee, N. E. *Adv. Energy Mater.* **2018**, *8*, 1701520–170152.

(54) Moody, M. J.; Marvin, C. W.; Hutchison, G. R. *J. Mater. Chem. C* **2016**, *4*, 4387–4392.

(55) Li, X.; Chen, Y.; Kumar, A.; Mahmoud, A.; Nychka, J. A.; Chung, H. J. *ACS Appl. Mater. Interfaces* **2015**, *7*, 20753–20760.

(56) Ding, R.; Liu, H.; Zhang, X.; Xiao, J.; Kishor, R.; Sun, H.; Zhu, B.; Chen, G.; Gao, F.; Feng, X.; Chen, J.; Chen, X.; Sun, X.; Zheng, Y. *Adv. Funct. Mater.* **2016**, *26*, 7708–7716.

(57) Siddiqui, S.; Kim, D. Il; Roh, E.; Duy, L. T.; Trung, T. Q.; Nguyen, M. T.; Lee, N. E. A *Nano Energy* **2016**, *30*, 434–442.

(58) Alluri, N. R.; Chandrasekhar, A.; Vivekananthan, V.; Purusothaman, Y.; Selvarajan, S.; Jeong, J. H.; Kim, S. J. *ACS Sustain. Chem. Eng.* **2017**, *5*, 4730–4738.

(59) Xu, S.; Hansen, B. J.; Wang, Z. L. *Nat. Commun*. **2010**, *1*, 93.

(60) Yan, J.; Jeong, Y. G. *ACS Appl. Mater. Interfaces* **2016**, *8*, 15700–15709.

(61) Li, J.; Zhu, Z.; Fang, L.; Guo, S.; Erturun, U.; Zhu, Z.; West, J. E.; Ghosh, S.; Kang, S. H. *Nanoscale* **2017**, *9*, 14215–14228.

End of Chapter 4

Chapter 5

Piezoelectric Energy Harvesting from a Ferroelectric Hybrid Salt $[Ph_3MeP]_4[Ni(NCS)_6]$ Embedded in a Polymer Matrix

5.1 Introduction

Organic-inorganic hybrids are an exciting class of materials for their myriad applications in the area of energy and next-generation electronics.[1-3] Hybrid ABX_3 type perovskite materials with light-harvesting properties are utilized in solar cell devices with very high power conversion efficiencies.[4-8] The superior performance of these devices are driven by their solution processability, strong optical absorption, high charge mobility, photoconductivity and tunable bandgap properties.[9-11] In addition to their extensive optoelectronic applications, more recently, they have been investigated as potential thermoelectric and piezoelectric energy harvesters.[12-15] The multifaceted utility of these substances can be attributed to the individual characteristics of the organic and inorganic components that are present in a single-phase crystalline structure. Piezoelectric effect offers an attractive source of alternate energy in which the conversion of mechanical energy into electrical energy can be achieved by ambient forces of nature and biomechanical movements.[16-18] Typical piezoelectric energy harvesters have been fabricated from traditional materials such as ZnO, CdS, ZnS, GaN, $PbZrTiO_3$, $BaTiO_3$, $PbTiO_3$, $ZnSnO_3$, $LiNbO_3$ and $NaNbO_3$ and organic piezoelectric sources such as PVDF or its copolymers.[19-21] Lately, perovskite structured lead- and tin-halide salts supported by organic cations have been utilized as efficient piezoelectric energy harvesters in the form of polymer composites.[22-24] The highest output voltage of 23 V and a power density value of 35.05 mW cm^{-2} have been realized for the $FASnI_3$ embedded PVDF films.[25] Despite their high performance, several of these materials suffer from air and moisture stability due to reactive metal-halide bonds and pose environmental concerns due to the presence of toxic heavy metal ions.[26-29] One of the viable solutions to tackle this problem is to employ light-weight 3d metal ions in combination with pseudo-halogenometallate counter-anions within the framework of organic-inorganic hybrid structures. Known examples of hybrid pseudo-halogenometallate salts exist in several compositions such as ABX_3, A_2BX_4, A_3BX_6 and A_4BX_6 (where A is the monovalent organic cation, B is the transition metal ion and X = $HCOO^-$, CN^-, SCN^-, NCS^-, N_3^- and $N(CN)_2^-$, etc.).[30-32] However, most of them, barring a few examples of metal-formates, tend to crystallize in the centrosymmetric space groups that are incompatible with the non-linear dielectric (piezoelectric, pyroelectric, or ferroelectric) properties. This is particularly due to the symmetrical octahedral coordination environment around the metal ions provided by these pseudo-halogenometallate anions and also the poor ordering of the organic cations employed in their synthesis.[33-35] We envisioned that by introducing lower-symmetric distorted tetrahedral organophosphonium cations with heteroleptic substituents, these assemblies would potentially crystallize with polar point group symmetries.

Herein, we show that the discrete A_4MX_6 type of compound $[Ph_3MeP]_4[Ni(NCS)_6]$ (**1**) is noncentrosymmetric and displays ferro- and piezoelectric properties. The polarization (*P*) versus electric field (*E*) hysteresis loop measurements on single-crystals of this compound show a high remnant polarization (P_r) of 18.71 μC cm^{-2}, at room temperature. Polymeric composite films with various weight percentages (5, 10, 15 and 20 wt %) of **1** embedded in thermoplastic polyurethane (TPU) polymer were prepared and utilized for mechanical energy harvesting applications. The maximum output voltage and output current of 19.29 V and 14 μA, respectively, were recorded for the composite with 15 wt % of **1**-TPU. The viscoelastic studies of these composite films show very high storage and low loss modulus over neat TPU polymer. The obtained voltages and currents were further utilized for charging capacitors with a wide range of capacitance values. To the best of our knowledge, this is the first report for a ferroelectric hybrid pseudo-halogenometallate complex of a 3d metal ion that serves as an efficient mechanical energy harvesting and storage system.

5.2 Experimental section

5.2.1 General remarks

The starting materials triphenylmethyl phosphonium bromide ($Ph_3PMe{\cdot}Br$), sodium rhodanide (NaSCN), nickel (II) nitrate hexahydrate ($Ni(NO_3)_2{\cdot}6H_2O$), nickel (II) chloride hexahydrate ($NiCl_2{\cdot}6H_2O$) potassium hexacyanoferrate (III) {$K_3[Fe(CN)_6]$}, potassium hexacyanocobaltate (III) {$K_3[Co(CN)_6]$} and polydimethylsiloxane (PDMS) were purchased from Sigma Aldrich and used as received. The thermoplastic polyurethane (TPU) polymer (Elastollan 85 A) was purchased from BASF and used as received. The ESI and MALDI-TOF spectra were carried out by using Waters Synapt G2 and the Applied Biosystem MALDI-TOF spectrometer, respectively. The thermogravimetric (TGA) and differential thermal analysis (DTA) was obtained by performing the PerkinElmer STA-6000 analyzer with a heating rate of 10 °C/min in a nitrogen atmosphere. Melting point analysis was performed by using a Buchi M-560 melting point apparatus and were uncorrected. FT-IR spectrum was performed on a Perkin-Elmer spectrometer with samples prepared as KBr pellets in the ranges between 400 and 4000 cm^{-1}. The Raman active modes of neat TPU and the all different wt % composite films were recorded by using Raman spectroscopy (λ_{exc} = 633 nm) with a Raman microscope (LabRAM HR, HorbiaJobinYvon) and 50X objective lens. The variable temperature powder X-ray diffraction data (VT-PXRD) were measured in the 2-theta range of 5° to 50° on a Bruker-D8 Advance X-ray diffractometer. The field-emission scanning electron microscopy (FE-SEM) analysis of piezo and ferroelectric crystallites and their different wt % composites films were characterized by using Zeiss ultra plus FE-SEM instrument. The 2D and 3D microstructures of the composite films were extracted by using the non-invasive X-ray microtomography imaging technique which consists of a Carl Zeiss Versa 510 microscope. For this experiment, the used input applied X-ray energy was noted to be 50 kV. The second harmonic generation (SHG) analysis of **1** was measured by adopting a similar reported procedure.[36] The UV-Visible spectra of **1** were performed at room temperature by using Shimadzu UV-3600 spectrophotometer in an optical glass cuvette with the whole visible region range of 400–800 nm. The optical band gap was calculated from absorption spectra by following the literature procedure.[50] The piezoelectric coefficient (d_{33}) measurements were performed on the single crystal of compound **1** by using Piezotest meter model PM300.

5.2.2 Synthesis

The compound **1** was synthesized by following the modified literature procedure.[37-38] To a stirred solution of triphenyl methyl phosphonium bromide (TPMP·Br), [2.46 g, 0.0069 mol] in methanol (25 mL), sodium rhodanide (NaSCN), [0.8363 g, 0.0103 mol)] in water (15 mL) was slowly added and the reaction mixture was stirred at room temperature for a further period of 10-15 min. Subsequently, the nickel(II) nitrate hexahydrate ($Ni(NO_3)_2{\cdot}6H_2O$), [0.5 g, 0.0017 mol] was added into an above solution and filtered through celite. The obtained green colored solution was left for crystallization at room temperature. Dark green-colored crystals of

$[Ph_3MeP]_4[Ni(NCS)_6]$ (**1**) were obtained after 7 days.Yield: 1.43 g (55 %). M.P. 130-135 °C. ^{31}P NMR (162 MHz, CD_3OD) δ 21.80). FT-IR data in KBr pellet (cm^{-1}): 3043, 3014, 2969, 2871, 2805, 2063, 1617, 1580, 1491, 1337, 1015, 921, 753, 705 and 645. Anal. Calcd. For $C_{82}H_{72}N_6NiP_4S_6$: C 64.95; H 4.79; N 5.54. Found: C 64.91; H 4.73; N 5.55.

5.2.3 Crystallography: The single-crystal X-ray diffraction analyses of **1**.H_2O and **1** at various temperatures were performed on a Bruker Smart Apex Duo diffractometer by using Mo Kα radiation (λ= 0.71073Å). The crystal structures were solved by using intrinsic methods and then refined by full-matrix least-squares against F^2 using all data by using SHELXL-2014/7 built in the Apex-3 package.[39]

Table 5.1: Crystallographic data for the ferroelectric organic-inorganic hybrid compound 1.H_2O and 1 at different temperatures.

Compound	**Compound 1.H_2O**	**Compound 1 (RT)**	**Compound 1 (HT)**
Chemical formula	$C_{82}H_{74}N_6NiOP_4S_6$	$C_{82}H_{72}N_6NiP_4S_6$	$C_{82}H_{72}N_6NiP_4S_6$
Formula weight	1534.42	1516.40	1516.40
Temperature	100(2)K	294(2)K	373(2)K
Crystal system	Monoclinic	Monoclinic	Monoclinic
Space group	Cc	Cc	Cc
a (Å); α (°)	22.805(4); 90	22.946(5); 90	23.027(3); 90
b (Å); β(°)	13.659(3); 91.742(7)	13.767(3); 91.247(6)	13.862(2); 91.132(3)
c (Å); γ (°)	24.579(5); 90	24.688(5); 90	24.753(4); 90
V ($Å^3$); Z	7653.(3); 4	7797.(3); 4	7900.(2); 4
ρ (calc.) g cm^{-3}	1.332	1.292	1.275
μ(Mo K_α) mm^{-1}	0.551	0.539	0.532
$2\theta_{max}$ (°)	50.7	52.74	53.46
R(int)	0.1376	0.0787	0.0612
Completeness to θ	99.9	99.9	99.9
Data / param.	13395/914	15931/896	14129/896
GOF	0.964	1.004	1.009
R1 [F>4σ(F)]	0.0562	0.0518	0.0500
wR2 (all data)	0.1228	0.1212	0.1103
max. peak/hole (e.$Å^{-3}$)	0.356/-0.432	0.789/-0.270	0.411/-0.248

The crystallographic refinement data for **1**.H_2O and **1** at different temperatures are listed in (Table 5.1). All the non-hydrogen atoms were refined anisotropically if not stated otherwise. Hydrogen atoms were constructed in geometric positions to their parent atoms.[40] The DIAMOND-3.1 and Mercury software package was used to describe the bond length, bond angles and various structural illustrations of **1**.H_2O and **1**.

5.2.4 Hirshfeld surface analysis: The Hirshfeld surface mapping of all the non-covalent molecular interactions of **1**.H_2O and **1** was performed by using Crystal Explorer 3.1 program.[43] For this study, the single-crystal X-ray crystallographic information file (CIF) was utilized to visualize all the different type of interactions which are present on the Hirshfeld surface. These interactions were obtained as 3D color mapping images such as normalized contact distance (dnorm), shape index and curvedness. The diverse surface color mappings of **1**.H_2O and **1** were generated on the Hirshfeld surface by various color codings based on strong (red), medium (blue) and weak (white) interactions. The dimensionless quantity (shape index) indicates the local shape of the concave and convex region based on the features of the Hirshfeld surface. The maximum and best range of the surface index was used between 1.0 and -1.0 which corresponds to the most convex and concave regions. For the minimal surface regions, these values were fixed to be 0. The other term curvedness denotes a measure of how much the shape can get curved from the Hirshfeld surface which has a general useful range of -4.0 to 0.4, respectively. In continuation, the 2D fingerprint plot for the same compound **1**.H_2O and **1** can be constructed by the distance of an atom which is nearest to the interior (di) and exterior (de) of the generated Hirshfeld surface. The different contours (blue and grey color) that are present in the 2D fingerprint plot explains the various types of molecular interactions, specific and all the contact information, based on the Hirshfeld surface. The surface generation of the Hirshfeld images can be constructed with an iso-value of a weight function of 0.5 au.

5.2.5 Ferroelectric and dielectric studies: The *P-E* hysteresis loop measurements were performed on the single crystals of **1** using a Sawyer-Tower circuit at room temperature. The conductive copper adhesive tape was used on opposite sides of the single crystals which were presented as top and bottom of the electrodes. The frequency-dependent ferroelectric polarization and fatigue measurements were performed on aixACCT TF-2000E model hysteresis loop analyzer. Leakage current density experiments were conducted dynamically for various voltage steps during the hysteresis loop measurements. The temperature and frequency-dependent dielectric constants and dielectric loss measurements were performed on the pressed powder pellets of **1** by using Novocontrol Dielectric Spectrometer. The dielectric constants for all the wt % composite films were carried out with an applied voltage of 10 V and the operating frequencies range from 100 to 5000 Hz at room temperature. The piezoelectric coefficient (d_{33}) measurements were performed on the single crystal of compound **1** by using Piezotest meter model PM300.

5.2.6 Viscoelastic Properties and Stress-Strain Analysis: The viscoelastic properties (storage and loss modulus) of pure TPU polymer and all the wt % of **1**-TPU composite films were carried out on a Dynamical Mechanical Analyzer (TA Instruments RSA III) at room temperature.[60] A time sweep test was conducted to measure the storage modulus, loss modulus and tan delta at 0.05 % strain and frequency of 1 Hz. For the stress vs. strain measurements, the films were stretched up to 50 % strain and the stress developed during stretching was recorded on a Dynamical Mechanical Analyzer (TA Instruments RSA III) at room temperature with a strain rate of 0.5 mm/s. Toughness values were calculated from respective stress-strain plots. For selected best performing composite film of 15 wt % **1**-TPU, the stress versus strain experiment was performed on Micro tensile tester with a strain rate of 0.5 mm/s.

5.2.7 General procedure for the preparation of the hybrid 1-TPU composite films: Polymeric composite films were prepared by solution casting method at room temperature. A known quantity (1 g) of TPU was dissolved in tetrahydrofuran (THF) and heated at 70° C for 15 minutes until the clear homogeneous solution was formed. A precalculated amount (for example, 177 mg for 15 wt % composite) of ferroelectric crystalline particles were added into a transparent homogenous TPU mixture and the suspension was continuously stirred at room temperature for 2 to 4 h followed by vortex mixing for 5 min. Subsequently, the homogeneous composite reaction mixture was transferred into a glass slide and dried at room temperature for 12 h. A completely dried free-standing green colored composite film was peeled off from the glass slide. A similar procedure was followed to prepare 5, 10 and 20 wt % of composite films. Further, the composite devices were fabricated with an appropriate selective area of 1.3 x 3 cm^2 and a thickness of 0.02 cm. The copper adhesive tapes were applied on either side of the films. The final device architecture for each wt % of the composite devices was obtained by enclosing the films within a neat PDMS polymer layer that serves to protect the device from any physical damages. Further, the energy harvesting performance of all the **1**-TPU composite devices was carried out by using a home-built impact measurement setup as described by us earlier.[53]

5.3 Results and discussion

5.3.1 Synthesis, characterization and crystal structures: The hybrid assembly of **1** was synthesized by adding a mixture of $Ph_3MeP{\cdot}Cl$ (TPMP·Br) and NaSCN into an aqueous solution containing $Ni(NO_3)_2{\cdot}6H_2O$ or $NiCl_2{\cdot}6H_2O$. Greenish-blue colored crystals of **1**·H_2O were directly obtained from the reaction mixture after seven days. The unsolvated phase **1** was obtained by standing the crystals at room temperature for one day (Figure 5A.1, Appendix 5). We have also synthesized few other examples of the cyanometallates $[DPDP]_3[M(CN)_6]$ (M = Fe, Co) for the realier reported diisopropylaminophosphonium (DPDP) cations. These compounds were synthesized by using slow evaporation method with an equivalent amount of aqueous solution containing potassium hexacyanoferrate (III) or potassium hexacyanocobaltate (III) and diphenyl diisopropylaminophosphonium bromide (DPDP·Br) in methanol at room temperature. The large plates like crystals of these hybrid assemblies were formed after seven days. The X-ray single-crystal diffraction analysis of these compounds was shown to crystallize in the monoclinic *Cc* space group with a discrete type of A_3MX_6 hybrid assemblies of $[Ph_2(^iPrNH)_2P]_3[Fe(CN)_6]$ and $[Ph_2(^iPrNH)_2P]_3[Fe(CN)_6]$, respectively (Figure 5A.2, Appendix 5). However, these two compounds did not show any ferroelectric behaviour as anticipated and hence are not discussed further in this chapter.

The single-crystal X-ray diffraction (SCXRD) analysis reveals that **1** crystalizes in the polar acentric monoclinic space group *Cc*, which corresponds to one of the 10 polar point groups (Table 5.1). The asymmetric unit shows the presence of one $[Ni(NCS)_6]^{4-}$ motif featuring the nickel (II) ion in an octahedral coordination and four phosphonium $[(Ph_3PMe)]^+$ cations (Figures 5.1a and 5A.3-5A.7, Appendix 5). The borderline Lewis acidity of Ni^{2+} ion is perfectly compatible with the borderline Lewis basicity of the N-coordinated isothiocyanate (SCN^-) ions giving rise to the symmetric assembly of $[Ni(NCS)_6]^{4-}$.[41-42] In order to track the existence of any structural phase transition in this assembly, the unit cell parameters of **1**·H_2O were extracted at various temperatures from 100 to 373 K which showed no major changes in its lattice parameters and retention of the crystal space-group at all the measured temperatures (Figure 5A.8, Appendix 5). The thermogravimetric (TGA) analysis, coupled with the differential scanning calorimetric (DTA) studies of **1**, further confirms this observation giving anomaly peaks due to the melting and decomposition points of the compound (Figures 5A.9 and 5A.10, Appendix 5). The Ni-N-C bond angles of **1** measured from the 100 and 373 K data range between 159.3(6) and 170.7(5)°. This indicates the absence of any drastic motional changes in the SCN^- ions that can impact the phase transition in the crystal. However, the N-C-S angles due to all the six thiocyanate ions are close to linearity. All the phosphonium cations in **1** show distorted tetrahedral geometries, in which the C-P-C angles range from 107.6(3) to 111.0(4)º at 294 K. These values were found to show minimal deviations for the datasets collected at both lower (100 K) and higher (373 K) temperatures (Tables 5A.1-5A.2, Appendix 5). Furthermore, variable temperature powder X-ray diffraction (VT-PXRD) profiles collected from 294 to 373 K confirms the absence of any phase transitions and the retention of phase purity of **1** at all the measured temperatures (Figure 5A.11, Appendix 5).

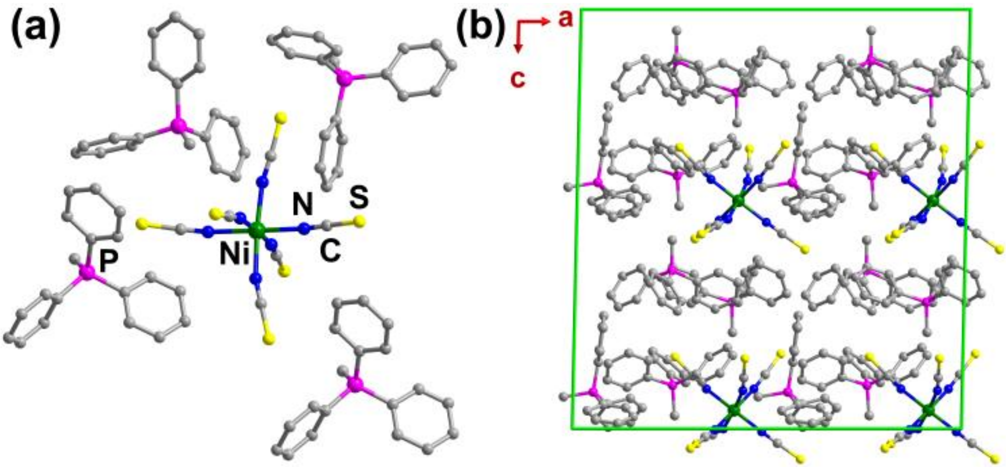

Figure 5.1: *(a) Molecular structure of* ***1*** *and (b) its crystal packing diagram along the crystallographic [0 1 0] plane. The methyl and phenyl group protons are omitted for clarity.*

The packing structure of **1** consists of four units of the anionic [Ni(NCS)6]$^{4-}$ fragments and sixteen phosphonium cations (Figure 5.1b). These cationic and anionic motifs were involved in several non-classical interactions mediated by C-H…S and C-H…N contacts (Figures 5.2c and 5A.5, Appendix 5). Further, the presence of diverse non-covalent interactions and their specific contacts were visualized by Hirshfeld surface analysis using the two dimensional (2D) finger-print plots and three dimensional (3D) color surface mapping built in the Crystal Explorer 3.1 program (Figures 5.2a,b and 5A.12-5A.16, Appendix 5).[43-45]

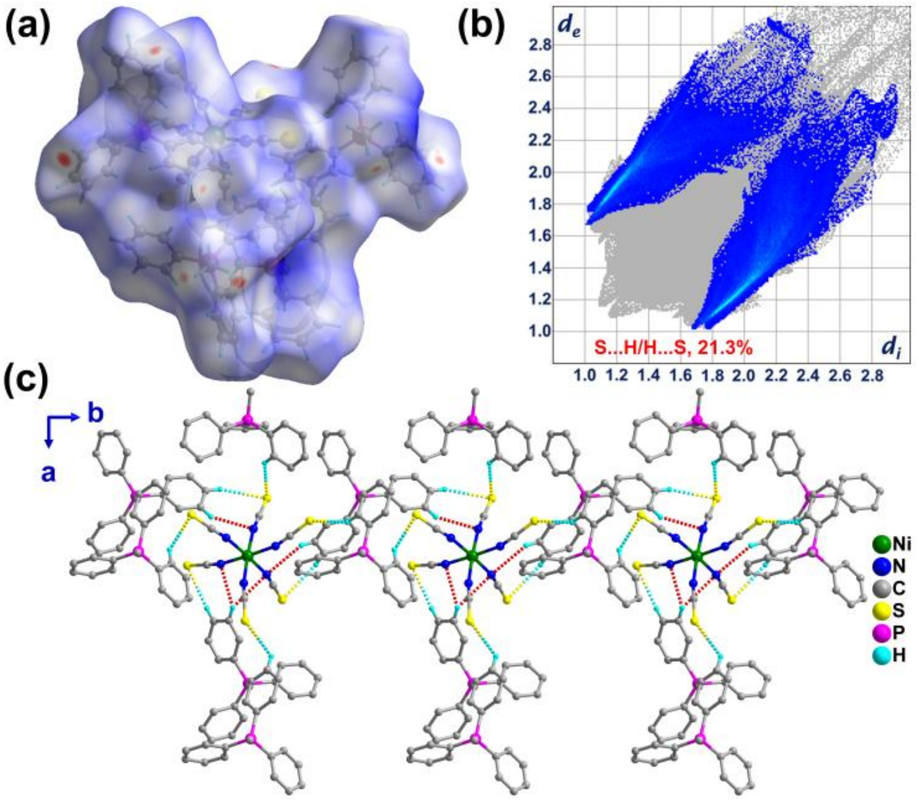

Figure 5.2: *(a) Hirshfeld surface view of **1** and (b) the two-dimensional fingerprint plot of C-H···S interactions. (c) The hydrogen bonded structure of **1** at 294 K along the polar b-axis mediated by C-H···S and C-H···N interactions.*

The non-covalent interactions were mapped via the normalized distances from a point on the surface to the nearest nucleus outside (de) and inside (di) of the surface. From the 3D-surface color mapping, the proximity of the contacts defined as close (red), moderate (white) and long (blue), between the two interacting nuclei, can be derived. The Hirshfeld surface built from the 294 K SCXRD structure of **1** shows several types of molecular interactions such as S⋯H, N⋯H, C⋯S, C⋯C, C⋯H and H⋯H with an overall percentage contribution of 21.3, 4.3, 1.1, 2.2, 28.5 and 42.4 %, respectively (Figure 5A.16, Appendix 5). The hydrogen bonding contributes 25.6 % of interactions, while dispersion and van der Walls contacts contribute 74.2 % of the interactions.

Despite the higher contributions from the later (dispersion and van der Walls) contacts, they account for a short-range order in the molecule with a lower stabilization energy of 0.4-4 kJ mol^{-1}. However, the hydrogen bonding (C-H⋯X; X = N and S) and ionic interactions account for the strong long-range order with the structure stabilization energy of 12-30 KJ mol^{-1}.[46-47] A detailed inspection of the hydrogen bonding interactions in **1** shows the involvement of the C-H (meta or para) groups of the phosphonium phenyl rings and the S and N atoms of the SCN$^-$ ions. A cumulative effect of these interactions leads to a closely-knit 3D H-bonded structure in which the interactions along the polar b-axis are dominated by C-H⋯S and C-H⋯N interactions (Figure 5.2c).

The second harmonic generation (SHG) measurement on **1** was performed at room temperature, which confirms its non-centrosymmetric nature. The fine unsieved powdered sample gave a sizable SHG efficiency of 0.75, with respect to the reference KDP sample. The optical bandgap characteristic of **1** was determined by UV-visible absorption spectroscopy on its powdered sample (Figure 5A.17, Appendix 5). The Tauc plot derived from the spectral profile yielded the optical band gap (Eg) value of 4.07 eV. The observed Eg value is comparable with well-known ferroelectric metal oxides and organic-inorganic hybrid systems.[48-50] The presence of direct piezoelectric polarization in **1** was probed by using the Berlin-court method.[51] These measurements gave a piezoelectric coefficient (d_{33}) value of 8 pC N^{-1} with an applied compressive force of 0.25 N and the operating frequency of 110 Hz on the single-crystals of **1**. Furthermore, the piezoelectric voltage/potential coefficient (g_{33}) value of **1** was calculated through the relationship between the piezoelectric coefficient (d_{33}) and the dielectric permittivity (ε_r) of the material ($g_{33} = d_{33}/\varepsilon_r$). The observed maximum g_{33} (63.27 10^{-3} V m N^{-1}) value for **1** was found to be comparable with most of the known piezo and ferroelectric compounds derived from small molecules and polymeric compounds.[52]

5.3.2 Ferroelectric, dielectric and piezoelectric studies

The polar nature of **1** was confirmed by performing ferroelectric polarization switching (*P*) versus electric field (*E*) measurements on its single crystals by using a Sawyer-Tower circuit at an operating frequency of 0.3 Hz (Figures 5.3a and 5A.18, Appendix 5). These measurements gave a well-saturated rectangular hysteresis loop at room temperature with high remnant polarization (P_r) and low coercive electric field (E_c) values of 18.71 μC cm^{-2} and 0.58 kV cm^{-1}, respectively, along with the crystallographic [0 1 0] plane (Figure 5.3a). The origin of the polarization in **1** can be tracked to its stable charge-separated structure composed by the cationic phosphorus centers and the octahedrally coordinated $Ni(NCS)_6]^{4-}$ ions, and their non-covalent interactions along the polar b-axis. The obtained polarization values were comparable with those observed for the organophosphonium salts containing various organic and inorganic anions.[53-55]

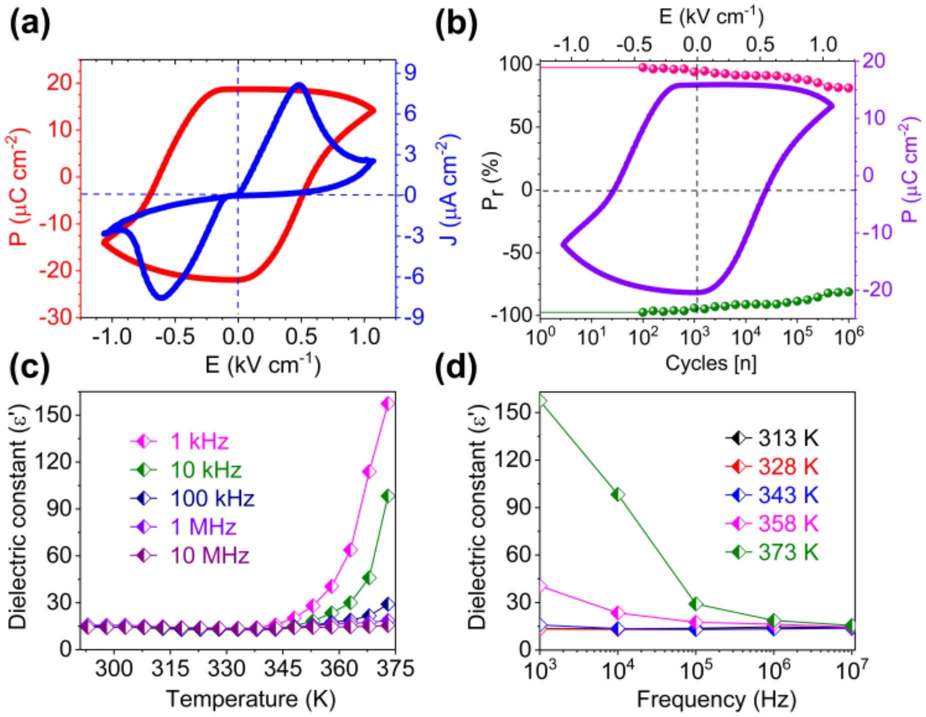

Figure 5.3: *(a) Ferroelectric P vs. E hysteresis loop and leakage current density plot on a single crystal of* ***1****. (b) Fatigue data up to* 10^6 *cycles and the P-E loop trace after the fatigue cycles (inset). Temperature (c) and frequency (d) dependent dielectric constant measurements on a compacted pellet of* ***1****.*

The leakage current density (J) values, measured along *P-E* loop trace, were found to be in the order of 8.14 μA cm^{-2} and displayed peaks at the switching coercive fields corresponding to the ferroelectric domain inversion in **1** (Figure 5.3a). The *P-E* loop cycling measurements were performed up to 10^6 cycles, which showed the retention of ferroelectric hysteresis loop and the fatigue-free polarization behavior of **1** (Figure 5.3b).

The polarization in the bulk compacted powdered sample of **1** was probed by the temperature and frequency dependent dielectric permittivity measurements at various frequencies from 1 kHz to 10 MHz (Figure 5.3c,d). The real part of the dielectric constant (ε') was found to gradually increase upon increasing the temperature at a constant interval of 5 K and shows an abrupt rise beyond 345 K. The observed trends in the ε' values indicate the absence of Curie point in **1** as noted earlier from its DTA profile. The absence of structural phase transitions in **1** can be attributed to the effective coordination modes between Ni-N bonds in $Ni(NCS)_6]^{4-}$ ions and its intricate non-classical H-bonding interactions with the four phosphonium motifs. The room temperature (294 K) ε' value of **1** at 10 MHz was recorded to be 14.29. Further, the observed dissipation of the electrical energy (dielectric loss, tan δ) in the temperature plots indicates a low dielectric loss behavior in **1**. Similar trends have been observed for the frequency dependent ε' and tan δ vales of **1** as well (Figure 5A.19, Appendix 5).

5.3.3 Fabrication and characterization of the organic-inorganic hybrid phosphonium salt-polymer composites

Spurred by the dielectric, piezoelectric and ferroelectric properties of **1**, we investigated its mechanical energy harvesting behavior in the form of its polymer composites. For this, we employed the non-piezoelectric thermoplastic polyurethane (TPU) polymer as a flexible polymer substrate composite films with 5, 10, 15 and 20 weight percentage (wt %) compositions were prepared by solution casting method (Figures 5A.20-5A.21, Scheme 5A.1 and Table 5A.3, Appendix 5). The composite films were further characterized by X-ray powder diffraction and Raman spectral analysis which shows the phase purity and crystalline nature of ferroelectric particles at all the wt % compositions (Figures 5A.22-5A.24, Appendix 5). The PXRD profiles of these films indicate that the peak intensities of the ferroelectric particles increases upon increasing the loading of ferroelectric crystallites in the composite films (from 5 to 20 wt %) (Figures 5A.22-5A.23, Appendix 5). From the PXRD profiles it is evident that the crystallites are randomly oriented within the bulk polymer matrix showing all the characteristic hkl peaks that are present in the bulk powdered sample of **1** (Figure 5A.23, Appendix 5). Such kinds of composites with the random alignment of crystals within the bulk polymer matrix have also been reported for ceramic materials.[56-57] The Raman spectra recorded on all the wt % compositions of **1**-TPU films shows peaks due to both **1** and TPU (Figure 5A.24, Appendix 5).[58-59]

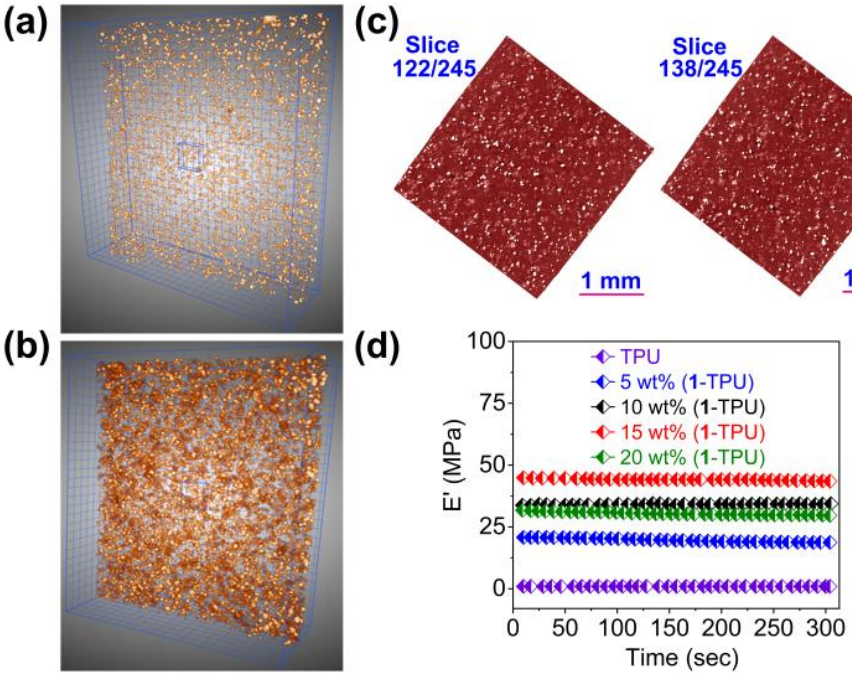

Figure 5.4: *The X-ray 3D-microtomography images of the (a) 5 wt % and (b) 15 wt %* ***1****-TPU composite films (grid-scale: 100 μm). 2D-microtomography images of 15 wt %* ***1****-TPU composite films at different slices. (d) The storage modulus (E') of* ***1****-TPU films.*

The X-ray 3D-tomography images were obtained for all the wt % of composite films of **1**-TPU to qualitatively understand the distribution of the salt crystals of **1** within the bulk of the composite films (Figures 5.4a,b and 5A.25-5A.29, Appendix 5). These studies reveal the uniform distribution of the ferroelectric crystalline particles in the polymeric TPU films. From the X-ray 3D-tomography images, it is evident that the size of the particles and density of the films increase upon increasing the wt % of **1** (from 5 to 20 %) in the composites (Figures 5.4a,b and 5A.29, Appendix 5). In fact, the 20 wt % composite solution shows a visible tint of green due to the increased concentration of the Ni(II) ions in it (Figure 5A.20, Appendix 5). These images also indicate the progressive aggregation of ferroelectric crystallites in the polymeric TPU films upon increasing the wt % of **1** from 5 to 20 wt %. The 2D-horizontal and vertical slices extracted from the 3D-tomography images (approximately 500 slices) show the homogeneous composition of the embedded crystallites via the reconstruction of the 3D-crystallites at every slice of the film interiors (Figures 5c and 5A.25-5A.28, Appendix 5).

The elastic and viscous (viscoelastic) nature of the composite films was examined at room temperature by using a dynamic mechanical analyzer and compared with that recorded for neat TPU (Figure 5.4c and d).[60] All the composite films show excellent storage (E′) and low loss (E″) moduli coupled with low damping (tan δ) behavior in comparison with neat TPU illustrating a structural and interfacial interaction between the ferroelectric particles and TPU (Figures 5A.30 and 5A.31, Appendix 5). A higher storage modulus of 44.87 MPa was observed for the 15 wt % **1**-TPU indicating the maximum reinforcement of the ferroelectric crystallites within the polymer matrix at this composition. The higher stiffness of all the composites can be attributed to the uniform dispersion/distribution of the crystallites of **1** as observed from their 3D-microtomography images.

Furthermore, the room temperature stress-strain relationship of all the composite films was evaluated as a function of strain. These films were easily stretchable up to 50 % strain and the resultant stress (toughness) values at 50 % strain were found to be 3.51, 3.53, 3.93, 4.46 and 3.53 MPa for TPU, 5, 10, 15 and 20 wt % **1**-TPU composite films, respectively (Figure 5A.32, Appendix 5). In fact, the 15 wt % **1**-TPU composite film was confortably stretched upto 300 % strain without any damage demonstrating the very high flexibility of the **1**-TPU composites. The sustained stress value of the 15 wt % **1**-TPU film at 300 % strain was found to be 5.66 Mpa (Figure 5A.33, Appendix 5).

5.3.4 Energy harvesting performance of the hybrid composite devices

The piezoelectric nanogenerators were fabricated from all the composite films and their energy-harvesting properties were probed with an in-house built impact set up attached with an oscilloscope. The maximum output peak to peak voltage (V_{PP}) and calculated output peak to peak current (I_{PP}) values was found to increase with an increase in the wt % percentage of **1**-TPU from 0 to 5 to 15 %. An impetuous increase in V_{PP} and I_{PP} values to the tune of 19.29 V and 14 μA, respectively, is observed for the 15 wt % **1**-TPU device at an optimized mechanical force of 17 N and an operating frequency of 8 Hz (Figures 5.5a and 5A.34-5A.37, Appendix 5).

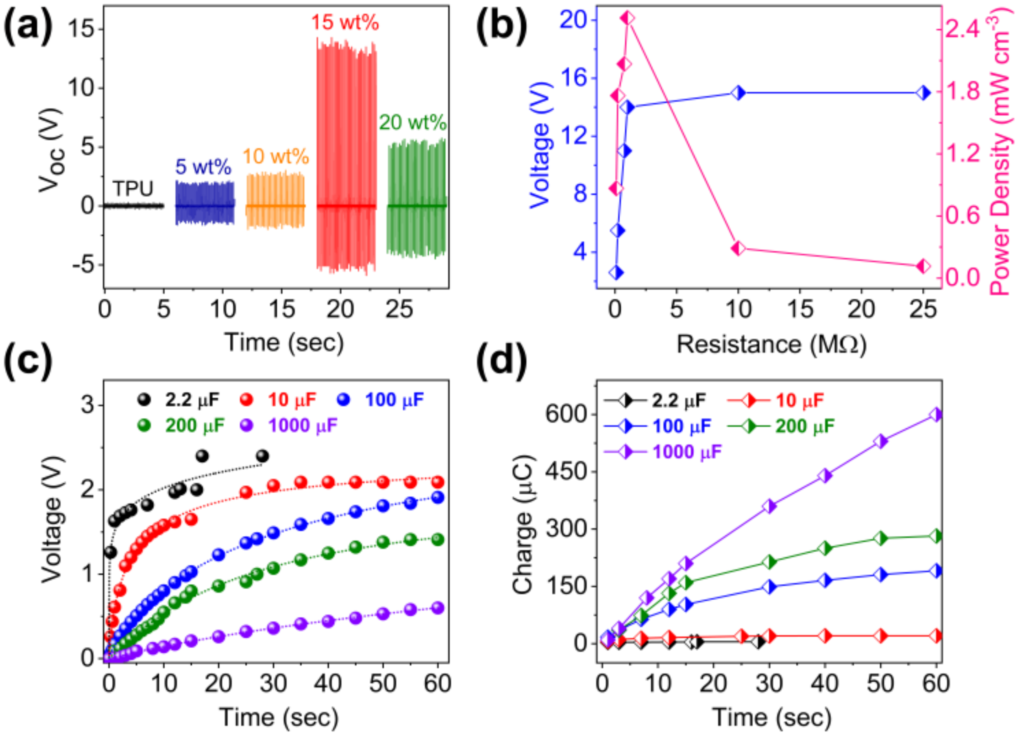

Figure 5.5: *The piezoelectric energy harvesting performance of* ***1****-TPU (a) output voltage recorded for all wt % composite devices. (b) The plot of observed trends in the output voltage and power density data of 15 wt %* ***1****-TPU film under various load resistances. (c) Capacitor charging traces and (d) the plot of accumulated charges data for the capacitors with varied capacitance values employing the 15 wt %* ***1****-TPU as a piezoelectric power source.*

The maximum current density (CD) value of 3.59 μA cm^{-2} and power density (PD) value of 2.51 mW cm^{-3} were obtained again for the 15 wt % **1**-TPU film (Figure 5A.38 and Table 5A.4, Appendix 5). The observed power density values are the highest known so far for any organic and organic-inorganic hybrid composite piezoelectric energy harvester fabricated from a non-piezoelectric polymer matrix.[24, 28, 53-54, 61-63] Further increase in the loading of **1** to 20 wt %, however, shows an abrupt decrease in the output performance which can be attributed to higher-particle agglomeration at this concentration as observed from its 3D-tomography images (Figures 5.4a,b, 5A.29 and Table 5A.4, Appendix 5).

In addition, the output voltages and calculated output currents of the best performing 15 wt % **1**-TPU device were determined under a wide range of external load resistances from 0.1 to 25 MΩ (Figures 5.5b and 5A.39, Appendix 5). The output voltages were shown to increase gradually with an increase in the values of resistance and attain saturation at 25 MΩ. A maximum power density of 2.51 mW cm^{-3} was obtained at a threshold load resistance of 1 MΩ and a maximum current density of 6.67 μA cm^{-2} was recorded at the lowest load resistance of 0.1 MΩ (Figure 5A.40, Appendix 5). Furthermore, we performed the durability (Figure 5A.41, Appendix 5). and the cyclic stability (up to 4000 cycles, Figure 5A.42, Appendix 5) experiments for the 15 wt % **1**-TPU composite device. The cycling experiments show no apparent drop in output voltage, while the durability experiment indicate the retention of more than 90 % of the piezoelectric voltage even after a resting period of eight months.

To gain further insights on the observed trends in the output energy harvesting performances of these **1**-TPU devices, the dielectric permittivity of all the wt % composite films was measured as a function of frequency (100 to 1 kHz) with an applied voltage of 10 V at 294 K (Figure 5A.43, Appendix 5). These measurements gave the ε' values of 6.64, 13.07, 15.97, 20.05 and 16.81 at 1 kHz for neat TPU, 5, 10, 15, and 20 wt % of **1**-TPU composite films, respectively (Table 5A.5, Appendix 5). Notably, the observation of the highest ε' values for the 15 wt % device corroborates well with its maximum device output values. The lower ε' values observed for the 20 wt % device (than the 15 wt % device) suggests the reduction in the long-range dipole-dipole interactions for the ferroelectric particles in it. Typically, upon increasing the concentration of ferro/piezoelectric particles, stiffness and total dipole moment of the composite increases due to effective stress transfer between active particles and polymer which could translate into a higher voltage output. However, an optimal minimum concentration is required to obtain a noticeable enhancement at resonance, which is observed to be of 15 wt % in our device architecture. The observed trends in the output voltages indicate that the surface charge density due to the interfacial structure in 5 and 10 wt % **1**-TPU films are almost the same and lower in comparison with the 15 wt % **1**-TPU composite device. For higher concentrations beyond the optimal loading the agglomeration in the composites affects effective stress transfer and result in the randomization of the dipoles which is responsible for the lower performance of the 20 wt % **1**-TPU device. Such a reduction in the output device performance was also found in many piezoelectric energy harvesters made-up of inorganic ceramic oxides, polymers, organic and organic-inorganic hybrid composite materials.[64-70]

To test the energy storage capabilities of these devices, a full-wave bridge four diode rectifier circuit was constructed by integrating the best performing 15 wt % **1**-TPU nanogenerator in to a charging capacitor with different capacitance values (2.2, 10, 100, 200 and 1000 μF). In all the cases, the stored output voltages across the capacitors were shown to increase gradually with time and reach the threshold value within ~ 60 seconds (Figures 5.5c and 5A.44, Appendix 5). The charging time increases from 28 to 60 s as the capacitance of the capacitor increases from 2.2 to 1000 μF. The highest threshold voltage of 2.4 V is recorded for the 2.2 μF capacitor. With 10, 100, 200 and 1000 μF capacitors, the stored voltages were found to be 2.09, 1.91, 1.41 and 0.6 V, respectively. From these voltages, the stored energies (E) and measured charges (Q) were computed to be 6.34, 21.84, 182.41, 198.81 and 180 μJ and 5.28, 20.9, 191, 282 and 600 μC for the respective 2.2, 10, 100, 200 and 1000 μF capacitors (Figures 5.5d and 5A.44, Appendix 5).

5.4 Conclusion

In summary, we have synthesized an organic-inorganic hybrid pseudohalogenometallate salt **1** containing a simple 3d-metal ion that exhibits ferro- and piezoelectric properties. The *P-E* hysteresis loop measurements on **1** gave a high P_r value of 18.71 μC cm^{-2} along the polar b-axis. The crystallites of this salt were further integrated into flexible composite films made up of polymeric TPU with various wt % compositions of **1** which gave a highest output voltage of 19.29 V. The power density values calculated from the output voltages and currents gave a remarkably high value of 2.51 mW cm^{-3} for the 15 wt % **1**-TPU composite. Capacitor charging experiments gave the highest stored energies and measured charges of 198.8 μJ and 600 μC for the respective 200 and 1000 μF capacitors. Such findings are envisioned to bring about paradigm shifts in the area of flexible micropower electronics in the years to come.

5.5 References

(1) Liu, K.; Jiang, Y.; Jiang, Y.; Guo, Y.; Liu, Y.; Nakamura, E. *J. Am. Chem. Soc.* **2019**, *141*, 1406–1414.

(2) Jena, A. K.; Kulkarni, A.; Miyasaka, T. *Chem. Rev.* **2019**, *119*, 3036–3103.

(3) Faustini, M.; Nicole, L.; Ruiz-Hitzky, E.; Sanchez, C. *Adv. Funct. Mater.* **2018**, *28*, 1704158.

(4) Schulz, P.; Cahen, D.; Kahn, A. *Chem. Rev.* **2019**, *119*, 3349–3417.

(5) Mercier, N. *Angew. Chem. Int. Ed.* **2019**, 17912–17917.

(6) Brenner, T. M.; Egger, D. A.; Kronik, L.; Hodes, G.; Cahen, D. *Nat. Rev. Mater.* **2016**, *1*, 15007.

(7) Zhang, W.; Eperon, G. E.; Snaith, H. J. *Nat. Energy* **2016**, *1*, 16048.

(8) Sutherland, B. R.; Sargent, E. H. *Nat. Photonics* **2016**, *10*, 295–302.

(9) Fu, Y.; Zhu, H.; Chen, J.; Hautzinger, M. P.; Zhu, X. Y.; Jin, S. *Nat. Rev. Mater.* **2019**, *4*, 169–188.

(10) Stranks, S. D.; Snaith, H. J. *Nat. Nanotechnol.* **2015**, *10*, 391–402.

(11) Pham, H. D.; Xianqiang, L.; Li, W.; Manzhos, S.; Kyaw, A. K. K.; Sonar, P. *Energy Environ. Sci.* **2019**, *12*, 1177–1209.

(12) Jin, H.; Li, J.; Iocozzia, J.; Zeng, X.; Wei, P. C..; Yang, C.; Li, N.; Liu, Z.; He, J. H.; Zhu,T.; Wang, J.; Lin, Z.; Wang, S. *Angew. Chem. Int. Ed.* **2019**, *58*, 15206–15226.

(13) Wang, H.; Chu, W.; Chen, G. *Adv. Electron. Mater.* **2019**, *5*, 1900167.

(14) Jella, V.; Ippili, S.; Eom, J. H.; Pammi, S. V. N.; Jung, J. S.; Tran, V. D.; Nguyen, V. H.; Kirakosyan, A.; Yun, S.; Kim, D.; Sihn, M. R.; Choi, J.; Kim, Y. J.; Kim, H. J.; Yoon, S. G. *Nano Energy* **2019**, *57*, 74–93.

(15) Kim, Y. J.; Dang, T. Van; Choi, H. J.; Park, B. J.; Eom, J. H.; Song, H. A.; Seol, D.; Kim, Y.; Shin, S. H.; Nah, J.; Yoon, S. G. *J. Mater. Chem. A*, **2016**, *4*, 756–763.

(16) Ray, T. R.; Choi, J.; Bandodkar, A. J.; Krishnan, S.; Gutruf, P.; Tian, L.; Ghaffari, R.; Rogers, J. A. *Chem. Rev.* **2019**, *119*, 5461–5533.

(17) Huang, L.; Lin, S.; Xu, Z.; Zhou, H.; Duan, J.; Hu, B.; Zhou, J. *Adv. Mater.* **2019**, *31*, 1902034.

(18) Wang, Z. L.; Wu, W. *Angew. Chem. Int. Ed.* **2012**, *51*, 11700–11721.

(19) Wang, Z. L.; Song, J. *Science* **2006**, *312*, 242–246.

(20) Bai, Y.; Jantunen, H.; Juuti, J. *Adv. Mater.* **2018**, *30*, 1707271.

(21) Xie, M.; Hisano, K.; Zhu, M.; Toyoshi, T.; Pan, M.; Okada, S.; Tsutsumi, O.; Kawamura, S.; Bowen, C. *Adv. Mater. Technol.* **2019**, *4*, 1800626.

(22) Ippili, S.; Jella, V.; Kim, J.; Hong, S.; Yoon, S. G. *Nano Energy* **2018**, *49*, 247–256.

(23) Ding, R.; Zhang, X.; Chen, G.; Wang, H.; Kishor, R.; Xiao, J.; Gao, F.; Zeng, K.; Chen, X.; Sun, X. W.; Zheng, Y. *Nano Energy* **2017**, *37*, 126–135.

(24) Tusiime, R.; Zabihi, F.; Tebyetekerwa, M.; Yousry, Y. M.; Wu, Y.; Eslamian, M.; Yang,S.; Ramakrishna, S.; Yua, M.; Zhang, H. *J. Mater. Chem. C*, **2020**, *8*, 2643 –2658.

(25) Pandey, R.; Gangadhar, S. B.; Grover, S.; Singh, S. K.; Kadam, A.; Ogale, S.; Waghmare, U. V.; Rao, V. R.; Kabra, D. *ACS Energy Lett*. **2019**, *4*, 1004 –1011.

(26) Ding, R.; Zhang, X.; Sun, X. W. *Adv. Funct. Mater*. **2017**, *27*, 1702207.

(27) Zhang, Y.; Jie, W.; Chen, P.; Liu, W.; Hao, J. *Adv. Mater*. **2018**, *30*, 1707007.

(28) Ippili, S.; Jella, V.; Eom, J. H.; Kim, J.; Hong, S.; Choi, J. S.; Tran, V. D.; Hieu, N. V.; Kim, Y. J.; Kim, H. J.; Yoon, S. G. *Nano Energy* **2019**, 57, 911–923.

(29) Coll, M.; Gomez, A.; Marza, E. M.; Almora, O.; Belmonte, G. G.; Quiles, M. C.; Bisquert, J. *J. Phys. Chem. Lett.* **2015**, *6*, 1408–1413.

(30) Li, W.; Wang, Z.; Deschler, F.; Gao, S.; Friend, R. H.; Cheetham, A. K. *Nat. Rev. Mater.* **2017**, *2*, 16099.

(31) Gao, P.; Bin Mohd Yusoff, A. R.; Nazeeruddin, M. K. *Nat. Commun.* **2018**, *9*, 5028.

(32) Tang, Y. Y.; Li, P. F.; Liao, W. Q.; Shi, P. P.; You, Y. M.; Xiong, R. G.; *J. Am. Chem. Soc.* **2018**, *140*, 8051–8059.

(33) Shi, C.; Bin Han, X.; Zhang, W. *Coord. Chem. Rev.* **2019**, *378*, 561–576.

(34) Grancini, G.; Nazeeruddin, M. K. *Nat. Rev. Mater.* **2019**, *4*, 4–22.

(35) Xu, W. J.; Du, Z. Y.; Zhang, W. X.; Chen, X. M. *CrystEngComm* **2016**, *18*, 7915–7928.

(36) Kurtz, S. K.; Perry, T. T. *J. Appl. Phys*. **1968**, *39*, 3798–3813.

(37) Liu, J. Y.; Zhang, S. Y.; Zeng, Y.; Shu, X.; Du, Z. Y.; He, C. T.; Zhang, W. X.; Chen, X. M. *Angew. Chem. Int. Ed*. **2018**, *57*, 8032–8036.

(38) Li, Q.; Shi, P. P.; Ye, Q.; Wang, H. T.; Wu, D. H.; Ye, H. Y.; Fu, D. W.; Zhang, Y. *Inorg. Chem*. **2015**, *54*, 10642–10647.

(39) Sheldrick, G. M. *Acta Crystallogr., Sect. A* **2008,** *64*, 112–122.

(40) Spek, A. L. *Acta Crystallogr., Sect. D* **2009**, *D65*, 148–155.

(41) Pearson, R. G. *J. Am. Chem. Soc.* **1963**, *85*, 3533–3539.

(42) Parr, R. G.; Pearson, R. G. *J. Am. Chem. Soc.* **1983**, *105*, 7512–7516.

(43) Turner, M. J.; McKinnon, J. J.; Wolff, S. K.; Grimwood, D. J.; Spackman, P. R.; Jayatilaka, D.; Spackman, M. A. *Crystal Explorer 3.1*. The University of Western Australia, 2012.

(44) Spackman, M. A.; Jayatilaka, D. *CrystEngComm* **2009**, *11*, 19−32.

(45) McKinnon, J. J.; Jayatilaka, D.; Spackman, M. A. *Chem. Commun*., **2007**, 3814–3816.

(46) Hobza, P.; Řezáč, J. *Chem. Rev.* **2016**, *116*, 4911–4912.

(47) Müller-Dethlefs, K.; Hobza, P. *Chem. Rev.* **2000**, *100*, 143–167.

(48) Grinberg, I.; West, D. V.; Torres, M.; Gou, G.; Stein, D. M.; Wu, L.; Chen, G.; Gallo, E. M.; Akbashev, A. R.; Davies, P. K.; Spanier, J. E.; Rappe, A. M. *Nature* **2013**, *503*, 509–512.

(49) Li, L.; Liu, X.; Li, Y.; Xu, Z.; Wu, Z.; Han, S.; Tao, K.; Hong, M.; Luo, J.; Sun, Z. *J. Am. Chem. Soc.* **2019**, *141*, 2623–2629.

(50) Shi, P. P.; Lu, S. Q.; Song, X. J.; Chen, X. G.; Liao, W. Q.; Li, P. F.; Tang, Y. Y.; Xiong, R. G. *J. Am. Chem. Soc.* **2019**, *141*, 18334–18340.

(51) Liao, W. Q.; Zhao, D.; Tang, Y. Y.; Zhang, Y.; Li, P. F.; Shi, P. P.; Chen, X. G.; You, Y. M.; Xiong, R. G. *Science* **2019**, *363*, 1206–1210.

(52) Chen, X. G.; Song, X. J.; Zhang, Z. X.; Li, P. F.; Ge, J. Z.; Tang, Y. Y.; Gao, J. X.; Zhang, W. Y.; Fu, D. W.; You, Y. M.; Xiong, R. G. *J. Am. Chem. Soc.* **2020**, *142*, 1077–1082.

(53) Vijayakanth, T.; Srivastava, A. K.; Ram, F.; Kulkarni, P.; Shanmuganathan, K.; Praveenkumar, B.; Boomishankar, R. *Angew. Chem. Int. Ed.* **2018**, *57*, 9054–9058.

(54) Vijayakanth, T.; Ram, F.; Praveenkumar, B.; Shanmuganathan, K.; Boomishankar, R. *Chem. Mater.* **2019**, *31*, 5964–5972.

(55) Zhou, L.; Shi, P. P.; Liu, X. M.; Feng, J. C.; Ye, Q.; Yao, Y. F.; Fu, D. W.; Li, P. F.; You, Y. M.; Zhang, Y.; Xiong, R. G. *NPJ Asia Materials*. **2019**, *11*, 15–23.

(56) Jung, J. H.; Chen, C. Y.; Yun, B. K.; Lee, N.; Zhou, Y.; Jo, W.; Chou, L. J.; Wang, Z. L. *Nanotechnology*, **2012**, *23*, 375401.

(57) Surmenev, R. A.; Orlova, T.; Chernozem, R. V.; Ivanova, A. A.; Bartasyte, A.; Mathur, S.; Surmeneva, M. A. *Nano Energy* **2019**, *62*, 475−506.

(58) Li, X.; Chen, Y.; Kumar, A.; Mahmoud, A.; Nychka, J. A.; Chung, H. J. *ACS Appl. Mater. Interfaces* **2015**, 7, 20753–20760.

(59) Tammam, A. K.; El-Dean, T. S.; Mostafa, M. F. *Ferroelectrics* **2015**, *481*, 34–40.

(60) Ferry, J. D. *Viscoelastic properties of polymers*. Wiley 3rd edition, 1980.

(61) Ding, R.; Liu, H.; Zhang, X.; Xiao, J.; Kishor, R.; Sun, H.; Zhu, B.; Chen, G.; Gao, F.; Feng, X.; Chen, J.; Chen, X.; Sun, X.; Zheng, Y. *Adv. Funct. Mater.* **2016**, *26*, 7708–7716.

(62) Dahiya, A. S.; Morini, F.; Boubenia, S.; Nadaud, K.; Alquier, D.; Poulin-Vittrant, G. *Adv. Mater. Technol.* **2017**, *3*, 1700249.

(63) Jella, V.; Ippili, S.; Eom, J. H.; Choi, J.; Yoon, S. G. *Nano Energy* **2018**, *53*, 46–56.

(64) Shepelin, N. A.; Glushenkov, A. M.; Lussini, V. C.; Fox, P. J.; Dicinoski, G. W.; Shapter, J. G.; Ellis, A. V. *Energy Environ. Sci.* **2019**, 12, 1143–1176.

(65) Zhang, C.; Fan, Y.; Li, H.; Li, Y.; Zhang, L.; Cao, S.; Kuang, S.; Zhao, Y.; Chen, A.; Zhu, G.; Wang, Z. L. *ACS Nano* **2018**, *12*, 4803–4811.

(66) Yang, Z.; Zhou, S.; Zu, J.; Inman, D. *Joule* **2018**, 2, 642–697.

(67) Hua, D.; Yaoa, M.; Fanb, Y.; Mac, C.; Fana, M.; Liu, M. *Nano energy* **2019**, *55*,288–304.

(68) Vivekananthan, V.; Alluri, N. R.; Chandrasekhar, A.; Purusothaman, Y.; Gupta, A.; Kim, S. J. *J. Mater. Chem. C,* **2019**, *7*, 7563–7571.

(69) Siddiqui, S.; Kim, D. I.; Roh, E.; Duy, L. T.; Trung, T. Q.; Nguyen, M. T.; Lee, N. E. *Nano Energy* **2016**, *30*, 434–442.

(70) Ding, R.; Zhang, X.; Chen, G.; Wang, H.; Kishor, R.; Xiao, J.; Gao, F.; Zeng, K.; Chen, X.; Sun, X. W.; Zheng, Y. *Nano Energy* **2017**, *37*, 126–135.

End of Chapter 5

In summary, this thesis presents the synthesis of non-centrosymmetric polar organic and organic-inorganic hybrid organo phosphonium P(V) salts for piezoelectric energy harvesting applications. The molecular symmetry, size and the diverse interactions of all the synthesized organic salts played a significant role in determining the centric as well as acentric structures of the studied systems. In this context, we first prepared a series of organoamino phosphonium salts of formula $[Ph_nP(NH^iPr)_{4-n}]X$ *for various monoatomic halide ions (n = 0, 1, 2 and 3; X = Cl, Br and I) to obtain structures in mostly non-centrosymmetric symmetries that are required for studying their piezo and ferroelectric property. Interestingly, salts of* $[Ph_2P(NH^iPr)_2]^+$ *cation shows a potential ferroelectric polarization behaviour, high dielectric constants with no Curie points and good piezoelectric responses (Chapter 2). Subsequently, we synthesized the hexafluorophosphate salts for some of these cations* $[Ph_nP(NH^iPr)_{4-n}]^+$ *(n = 1, 2 and 3) wherein the* $Ph_2P(NH^iPr)_2]PF_6$ *salt crystallizes in the non-centrosymmetric monoclinic Cc space group. Remarkably, P-E hysteresis loop measurements on this compound showed a higher ferroelectric polarization at room temperature. We have also shown that polymer composites of this ferroelectric salt can be prepared with poly(dimethyl)siloxane that can be utilized as mechanical energy harvesters. These are the first examples all-organic piezoelectric energy harvesters, which gave an output voltage of ~8 V and power density of 1.74 μW* cm^{-3} *for the composite with 10 weight percentage (wt %) ferroelectric salt (Chapter 3).*

Furthermore, we synthesized 12 new derivatives of these amino phosphonium salts that are supported by low symmetric tetrahedral anions (BF_4^-*,* ClO_4^- *and* IO_4^- *anions). Remarkably, eight of these assemblies crystallize in non-centrosymmetric structures that are compatible with ferro- and piezoelectric behaviour. Particularly salts of the diphenyl diisopropyl phosphonium cation show high polarization values than those of the other phosphonium derivatives. All-organic piezoelectric energy harvesters based on the thermoplastic polyurethane (TPU) polymer and the* BF_4^- *supported salts were prepared and studied for mechanical energy harvesting applications that showed good output performance values. Moreover, it is to be mentioned that the high ferroelectric polarization of these organic salts can play a vital role in influencing the overall output performance of the composite devices (Chapter 4). Finally, we demonstrated the piezo and ferroelectric behaviour in an* *organic-inorganic hybrid salt $[Ph_3MeP]_4[Ni(NCS)_6]$. It has been found that the individual contributions of the organic and inorganic counterparts can alter the molecular symmetry, the type of molecular interactions and the dimensionality of the overall frameworks which further leads to the influence of piezo and ferroelectric polarization of such materials. The stable ferroelectric polarization nature of this A_4BX_6 type organic-inorganic hybrid salt $[Ph_3MeP]_4[Ni(NCS)_6]$ has been utilized for the piezoelectric energy harvesting and storage applications in the form of its TPU composite. It should be mentioned that the observed output performance of these composite devices is comparable with some of the best performing composite materials made up of small molecular weight organic-inorganic hybrid systems (Chapter 5).*

All these exciting findings demonstrated in this thesis would be significance towards the development of new flexible piezo and ferroelectric energy harvesting systems that can potentially substitute the traditional heavy metal-containing ceramic systems. However, most of the piezoelectric energy harvester based devices produce relatively small output performance than triboelectric nanogenerators. In the coming years, the next big steps would be on the fabrication of novel triboelectric, pyroelectric and thermoelectric energy harvesting devices based on low molecular weight organic and organic-inorganic hybrid materials. The advantage of multiple energy harvesters lies not only in the enhancement of the output device performances but also in the simultaneous harvesting of energy from various natural sources. Another important factor that can decide on the output performances of the composite device is interfacial interactions between the polymer matrix and the piezoelectric particles. Thus, exploring such materials with deep understandings about interfacial chemistry in polymeric composite materials will improve the output device performance. In the future, these emerging energy harvesting and storage systems can find applications in various platforms such as the internet of things (IoT), molecular electronics, microsensors, capacitors, batteries and blue energy power systems.

****

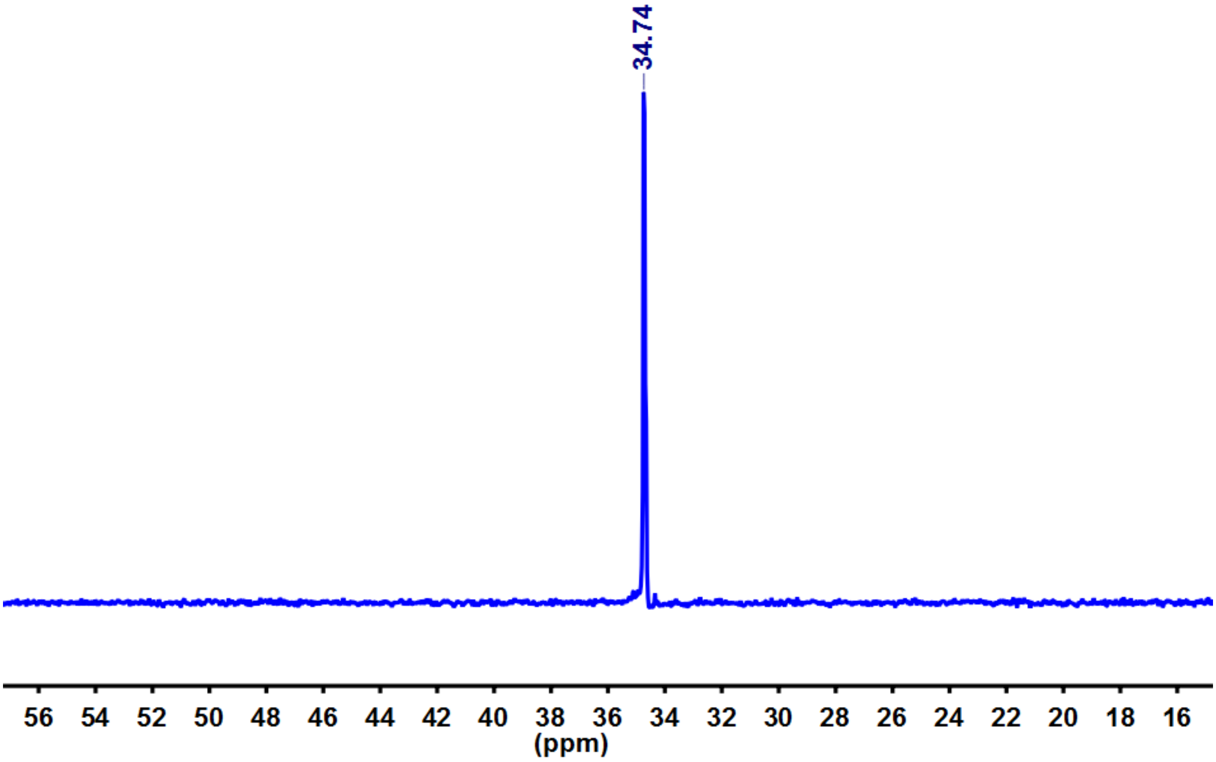

Figure 2A.1: ^{31}P NMR spectrum of DPDP·Cl.

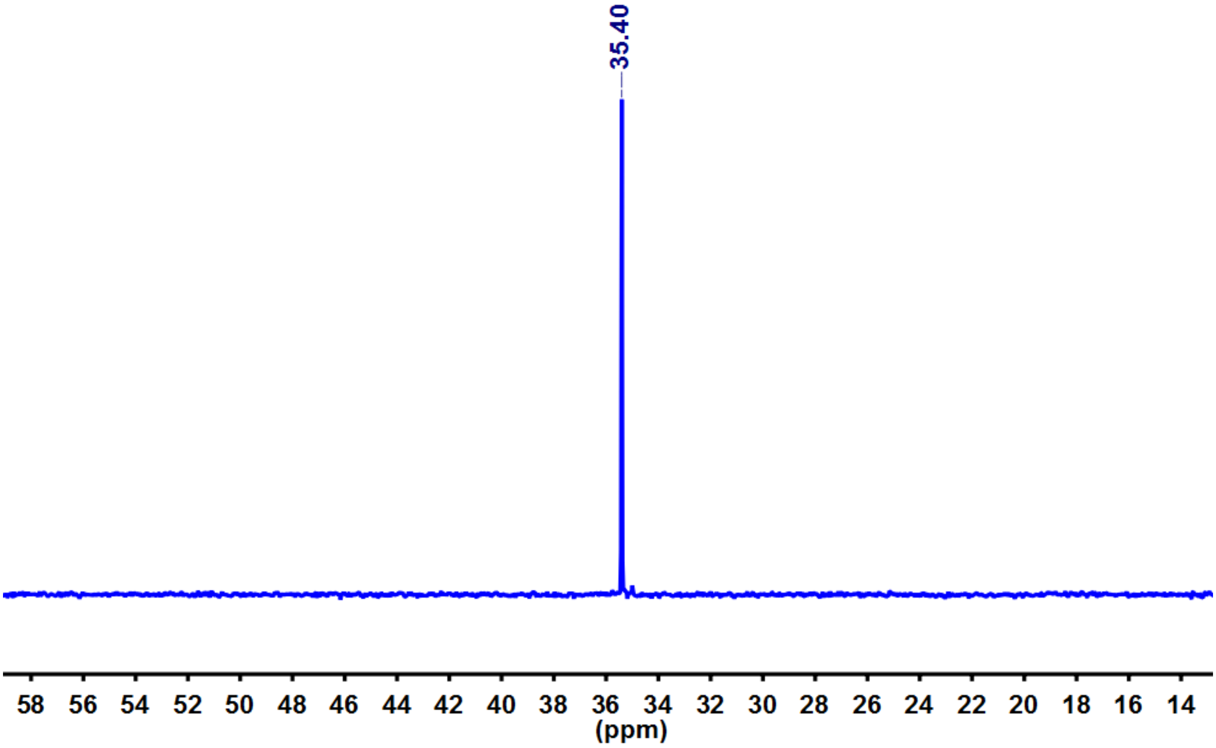

Figure 2A.2: ^{31}P NMR spectrum of DPDP·I (PM1).

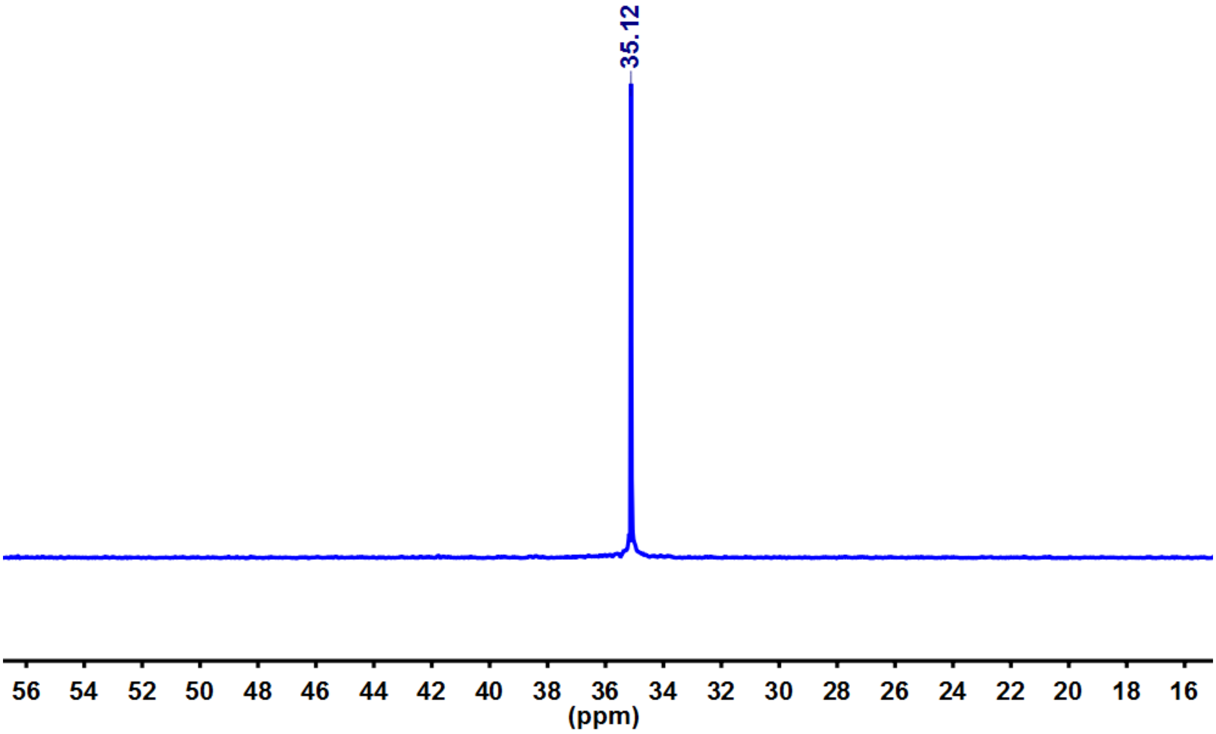

Figure 2A.3: ^{31}P NMR spectrum of DPDP·I (PM2).

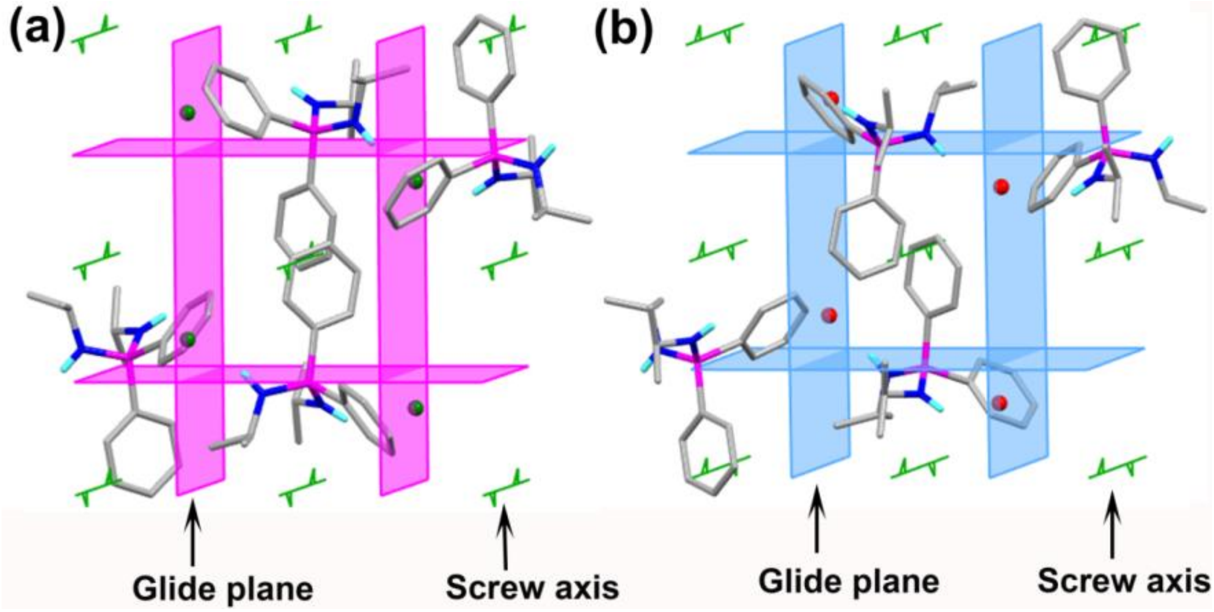

Figure A2.4: Crystal packing diagram for (a) DPDP·Cl and (b) DPDP·Br in the orthorhombic space group *Pna*2_1.

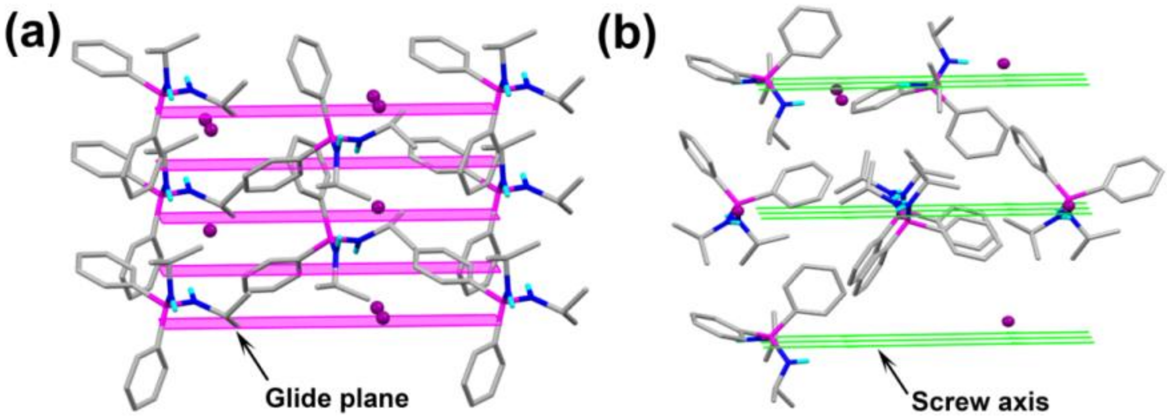

Figure A2.5: Crystal packing diagram for (a) DPDP·I (PM1) and (b) DPDP·I (PM2) in the monoclinic space group (a) *Cc* and (b) $P2_1$.

Table 2A.1: Selected bond lengths [Å] and angles [°] for DPDP·Cl, DPDP·Br and DPDP·I (PM1 & PM2).

Compound	**Bond length**	**Bond angle**
DPDP·Cl	P(1)-N(1): 1.613(3) P(1)-N(2): 1.618(3) N(1)-H(1): 0.8800(1) N(2)-H(2): 0.8800(1)	N(1)-P(1)-N(2): 109.56(15) N(1)-P(1)-C(11): 108.56(12) N(1)-P(1)-C(21): 111.54(14) N(2)-P(1)-C(11): 113.50(13) N(2)-P(1)-C(21): 106.11(13)
DPDP·Br	P(1)-N(1): 1.6325(19) P(1)-N(2): 1.6187(17) N(1)-H(1): 0.8800(2) N(2)-H(2): 0.8800(1)	N(1)-P(1)-N(2): 109.19(9) N(1)-P(1)-C(11): 113.45(8) N(1)-P(1)-C(21): 106.70(8) N(2)-P(1)-C(11): 108.83(8) N(2)-P(1)-C(21): 111.61(9)
DPDP·I (PM1)	P(1)-N(1): 1.6162(26) P(1)-N(2): 1.6271(22) N(1)-H(1): 0.8801(23) N(2)-H(2): 0.8803(25)	N(1)-P(1)-N(2): 120.554(132) N(1)-P(1)-C(11): 103.272(91) N(1)-P(1)-C(21): 107.498(110) N(2)-P(1)-C(11): 108.838(113) N(2)-P(1)-C(21): 106.097(103)
DPDP·I (PM2)	P(1)-N(1): 1.619(4) P(1)-N(2): 1.617(4) P(2)-N(3): 1.616(4) P(2)-N(4): 1.621(4) N(1)-H(1): 0.8799(30) N(2)-H(2): 0.8800(37) N(3)-H(3): 0.8800(32) N(4)-H(4): 0.8799(31)	N(1)-P(1)-N(2): 108.2(2) N(3)-P(2)-N(4): 110.7(2) N(1)-P(1)-C(1P): 107.64(18) N(1)-P(1)-C(7P): 113.17(19) N(2)-P(1)-C(1P): 114.27(19) N(2)-P(1)-C(7P): 105.57(17) N(3)-P(2)-C(13P): 106.28(17) N(3)-P(2)-C(19P): 112.93(18) N(4)-P(2)-C(13P): 112.28(17) N(4)-P(2)-C(19P): 106.23(18)

Table 2A.2: Hydrogen bond data for DPDP·Cl, DPDP·Br and DPDP·I (PM1 & PM2).

Compound	D-H…A	d(D-H)	d(H…A)	d(D-A)	<DHA	Symmetry operations
DPDP·Cl	N(1)-H(1)…Cl(1) N(2)-H(2)…Cl(1)	0.8800(1) 0.8800(1)	2.4248(3) 2.4684(4)	3.228(3) 3.176(3)	152.007(11) 137.856(10)	-x+3/2, y+1/2, z-1/2 x, y, z
DPDP·Br	N(1)-H(1)…Br(1) N(2)-H(2)…Br(2)	0.8800(2) 0.8800(1)	2.6015(5) 2.5247(4)	3.2986(18) 3.3337(18)	136.826(13) 153.126(14)	x, y, z -x+1/2, y-1/2, z+1/2
DPDP·I (PM1)	N(1)-H(1)…I(1) N(2)-H(2)…I(1)	0.8801(23) 0.8803(25)	2.9376(4) 3.0933(3)	3.7496(26) 3.8534(25)	154.204(144) 145.822(163)	x, y, z x-1/2, y-1/2, z
DPDP·I (PM2)	N(1)-H(1)…I(1) N(2)-H(2)…I(1) N(3)-H(3)…I(2) N(4)-H(4)…I(2)	0.8799(30) 0.8800(37) 0.8800(32) 0.8799(31)	2.9785(30) 2.8188(27) 2.8188(25) 3.1277(22)	3.691(5) 3.566(5) 3.586(4) 3.939(5)	139.386(206) 143.6780(258) 146.7033(203) 154.2955(213)	x-1, y, z x, y, z x, y, z+1 -x+1, y+1/2, -z+1

Table 2A.3: Selected torsion and bond angles [°] involved in hydrogen bonding for DPDP·Cl, DPDP·Br and DPDP·I (PM1 & PM2).

Compound	Torsion angle and Bond angle
DPDP·Cl	P(1)-N(1)-H(1)-Cl(1): 134.858(18) P(1)-N(2)-H(2)-Cl(1): 96.745(16) N(1)-Cl(1)-N(2): 140.699(4)
DPDP·Br	P(1)-N(1)-H(1)-Br(1): -95.882(20) P(1)-N(2)-H(2)-Br(1): 137.398(25) N(1)-Br(1)-N(2): 140.856(4)
DPDP·I (PM1)	P(1)-N(1)-H(1)-I(1): -115.030(294) P(1)-N(2)-H(2)-I(1): -118.607(16) N(1)-I(1)-N(2): 137.605 (49)
DPDP·I (PM2)	P(1)-N(1)-H(1)-I(1): 120.696 (282) P(1)-N(2)-H(2)-I(1): 114.769(354) N(1)-I(1)-N(2): 153.953(81) P(2)-N(3)-H(3)-I(2): 97.256(461) P(2)-N(4)-H(4)-I(2): 134.657(442) N(1)-I(1)-N(2): 114.354 (83)

Table 2A.4: Summary of the space groups for all the different derivatives of monoatomic anions supported phosphonium salts.

S.No	Ferro and Piezoelectric Materials	Temperature (K)	Space Group
1	**TPAP·Cl**	100	Monoclinic $P2_1/n$
2	**DPDP·Cl**	100	Orthorhombic $Pna2_1$
3	**PTAP·Cl**	100	Monoclinic $C2/c$
4	**TIAP·Cl**	100	Tetragonal $P\text{-}42_1c$
5	**TPAP·Br**	150	Monoclinic $P2_1/n$
6	**DPDP·Br**	100	Orthorhombic $Pna2_1$
7	**PTAP·Br**	100	Monoclinic $C2/c$
8	**TIAP·Br**	100	Tetragonal $I\text{-}42m$
9	**TPAP·I**	100	Monoclinic $P2_1/c$
10	**DPDP·I (PM1)** **DPDP·I (PM2)**	100 100	Monoclinic Cc Monoclinic $P2_1$
11	**PTAP·I**	100	Orthorhombic $P2_12_12_1$
12	**TIAP·I**	100	Tetragonal $I\text{-}42m$

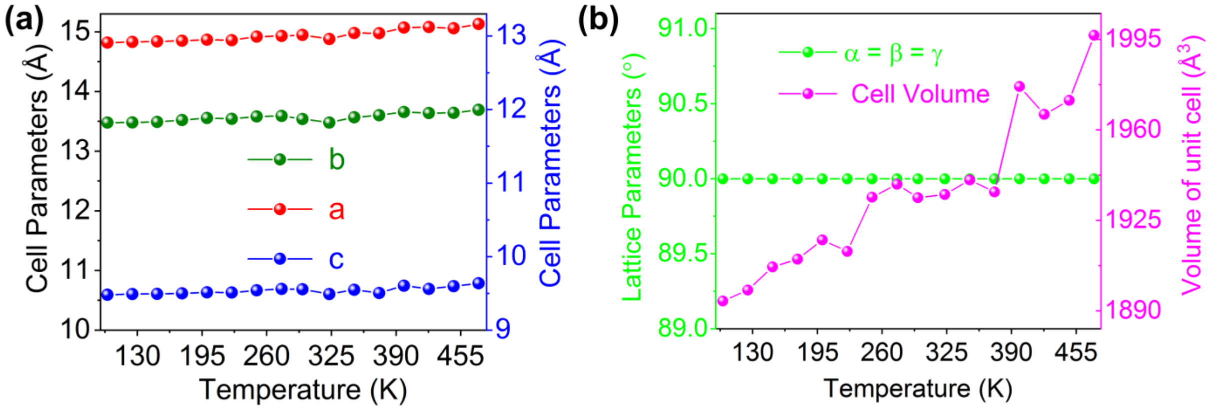

Figure 2A.6: Variable temperature unit-cell parameters for DPDP·Cl.

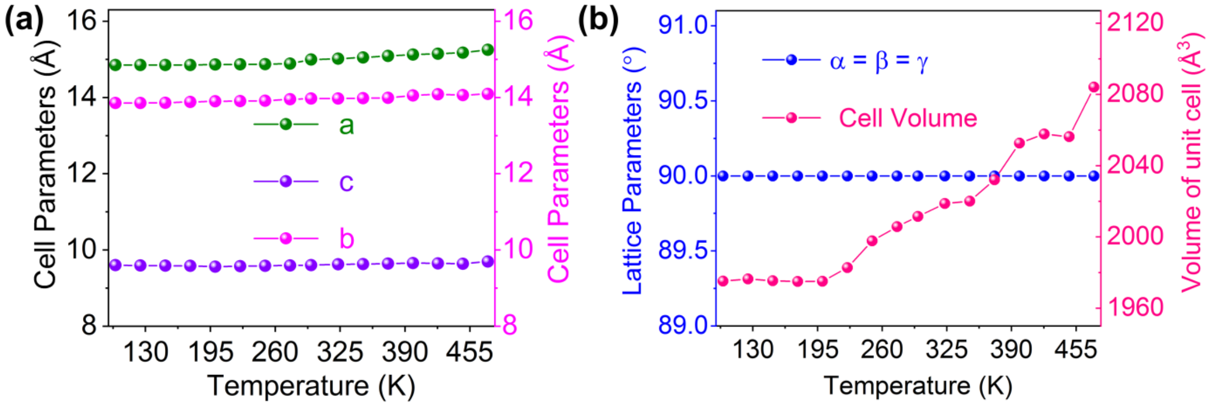

Figure 2A.7: Variable temperature unit-cell parameters for DPDP·Br.

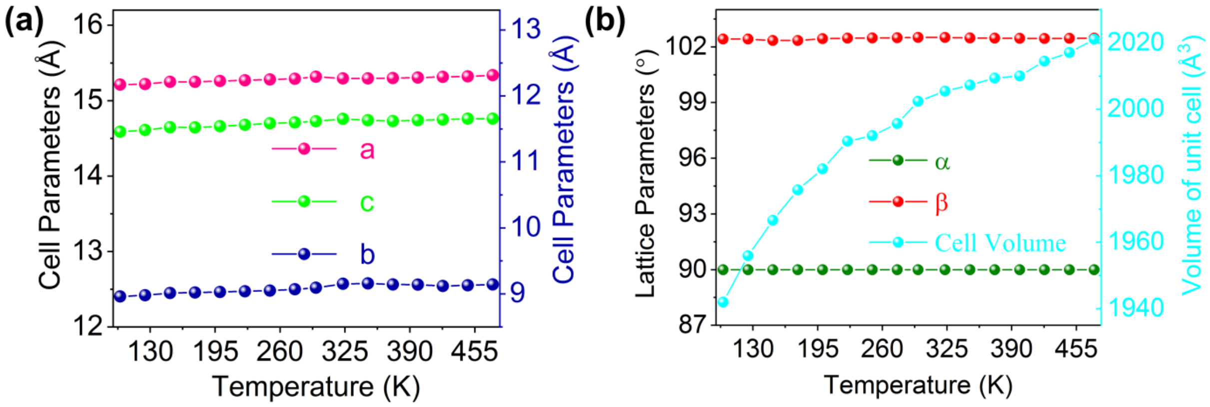

Figure 2A.8: Variable temperature unit-cell parameters for DPDP·I (PM1).

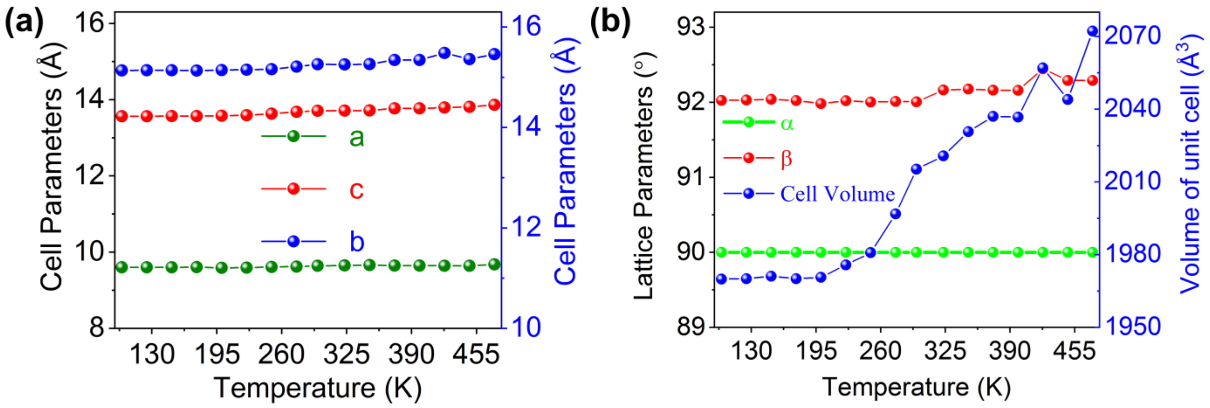

Figure 2A.9: Variable temperature unit-cell parameters for DPDP·I (PM2).

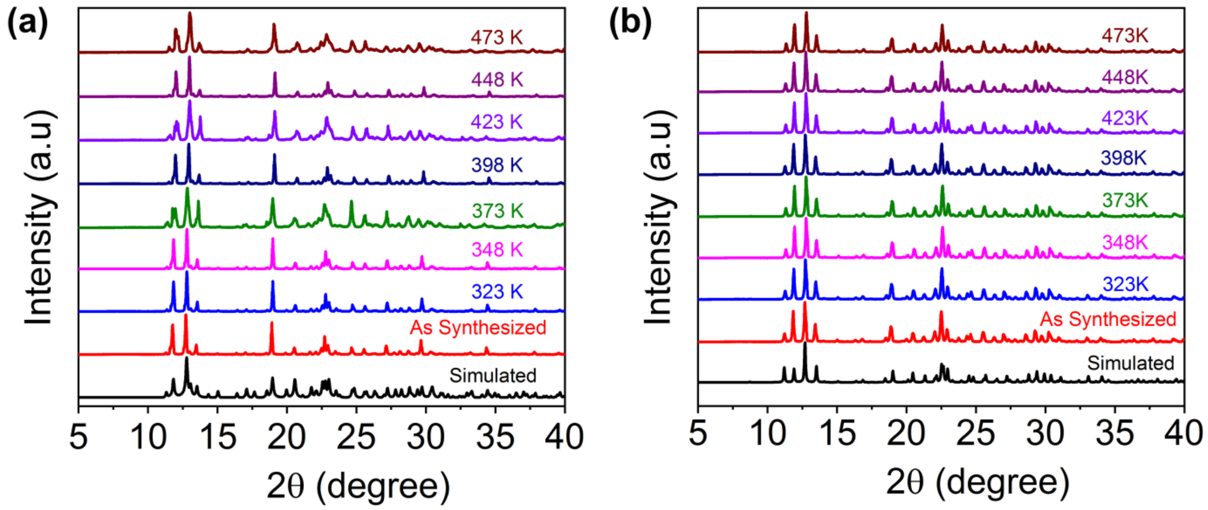

Figure 2A.10: Variable temperature powder pattern of (a) DPDP·Cl and (b) DPDP·Br.

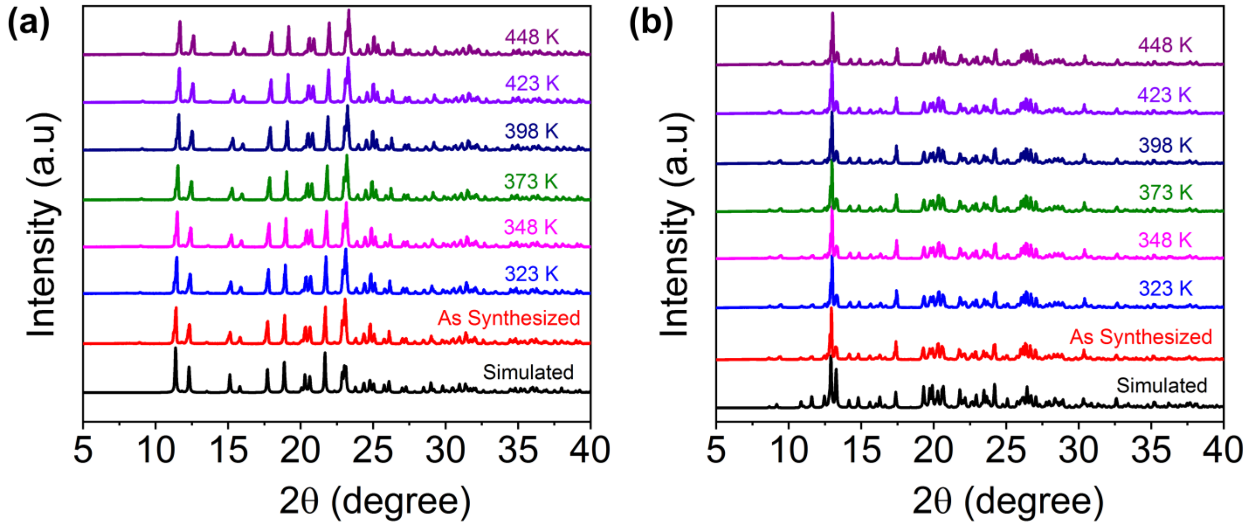

Figure 2A.11: Variable temperature powder pattern of (a) DPDP·I (PM1) and (b) DPDP·I (PM2).

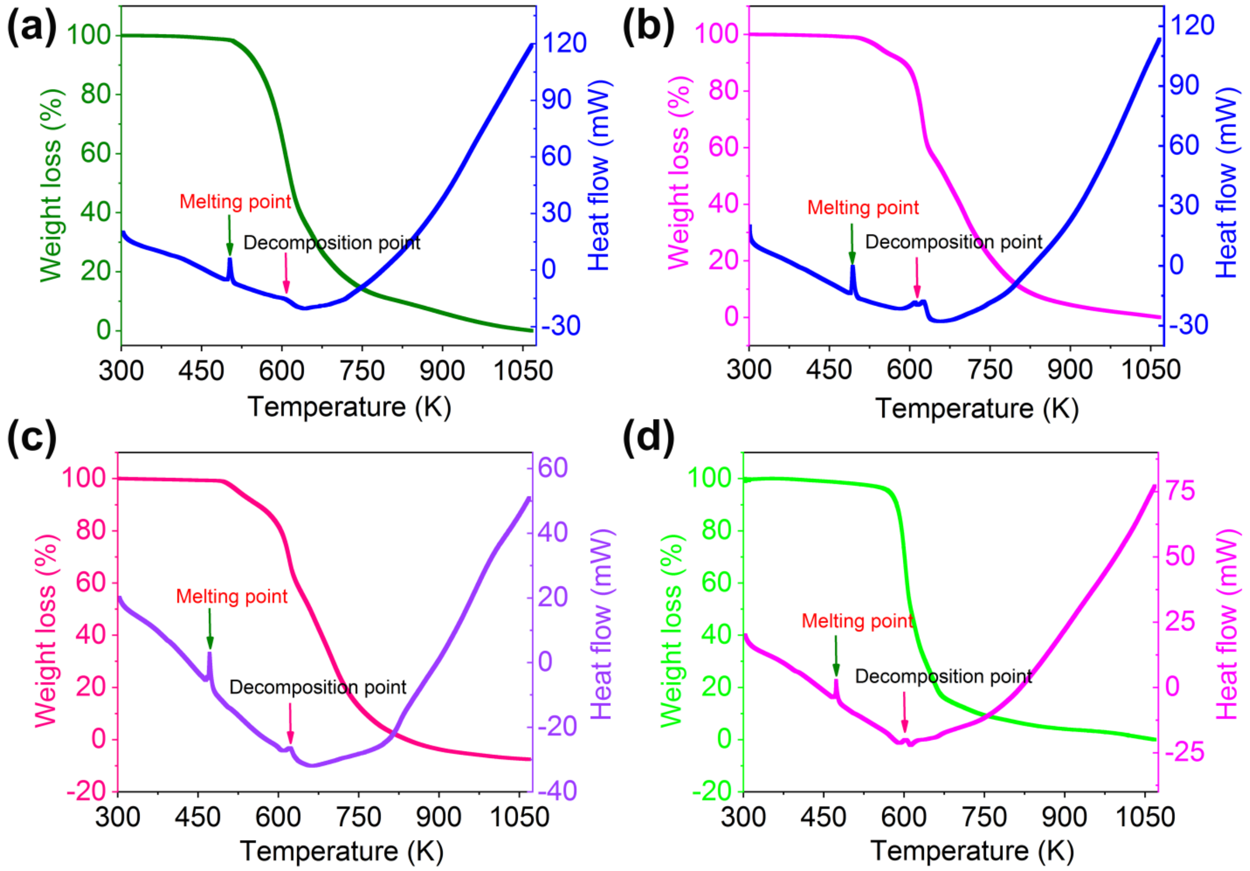

Figure 2A.12: TGA and DTA analysis of (a) DPDP·Cl, (b) DPDP·Br, (c) DPDP·I(PM1) and (d) DPDP·I(PM2).

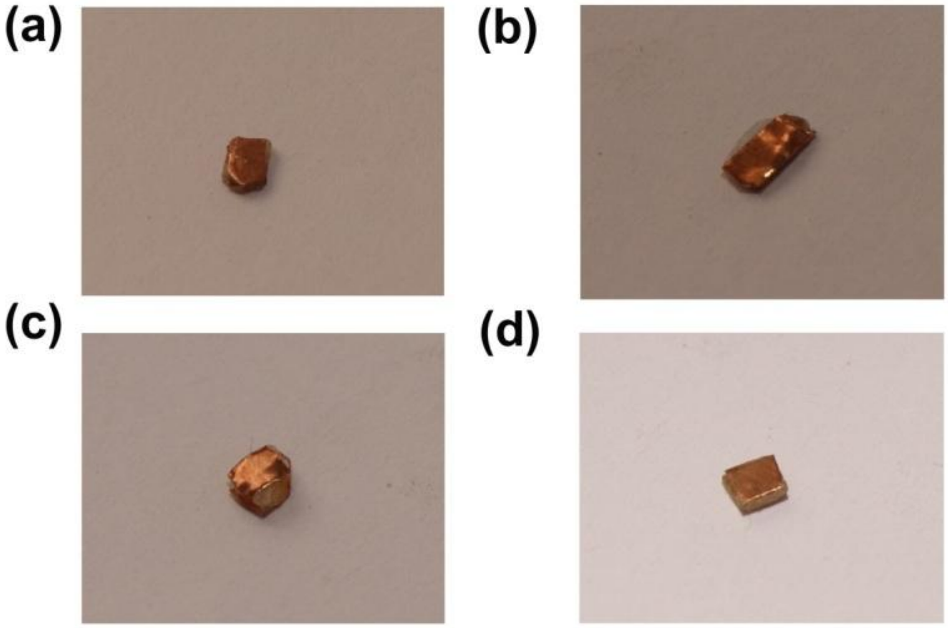

Figure 2A.13: The photo of the measured crystals for (a) DPDP·Cl, (b) DPDP·Br, (c) DPDP·I (PM1) and DPDP·I (PM2).

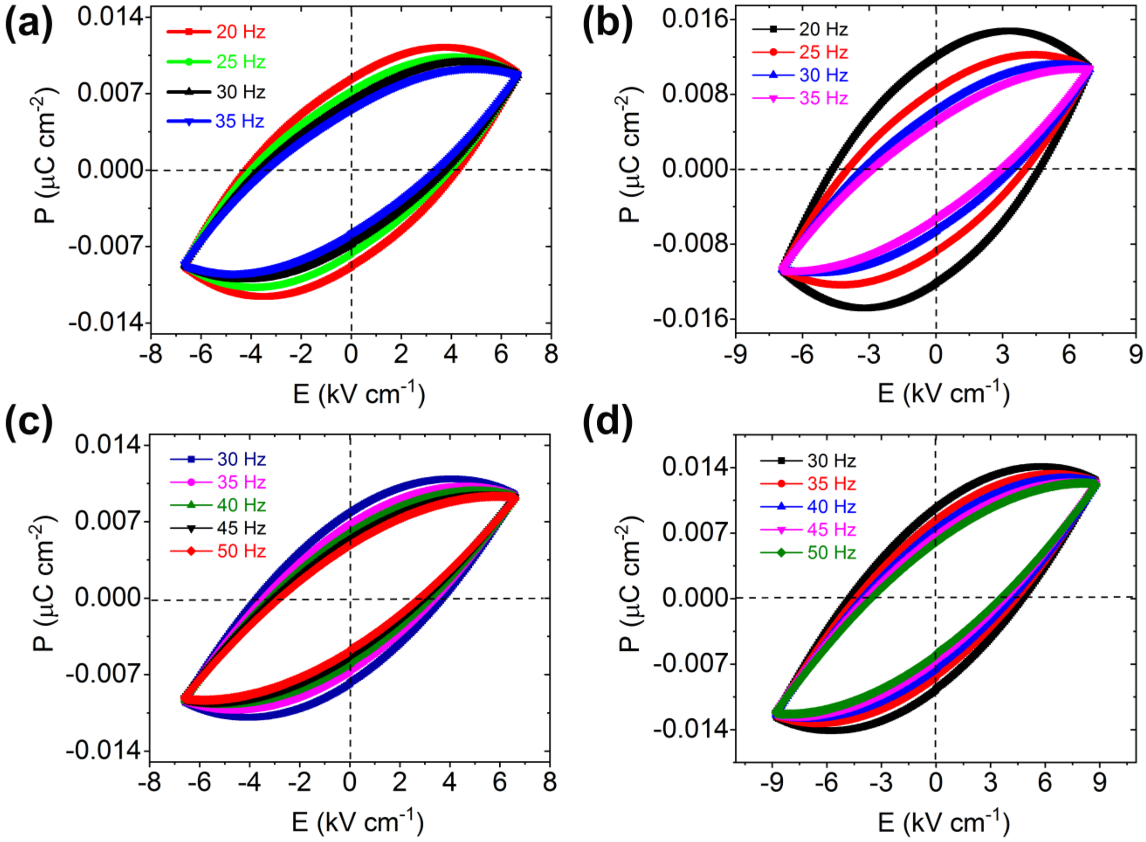

Figure 2A.14: Frequency dependent *P-E* hysteresis loops of (a) DPDP·Cl, (b) DPDP·Br, (c) DPDP·I(PM1) and (d) DPDP·I(PM2).

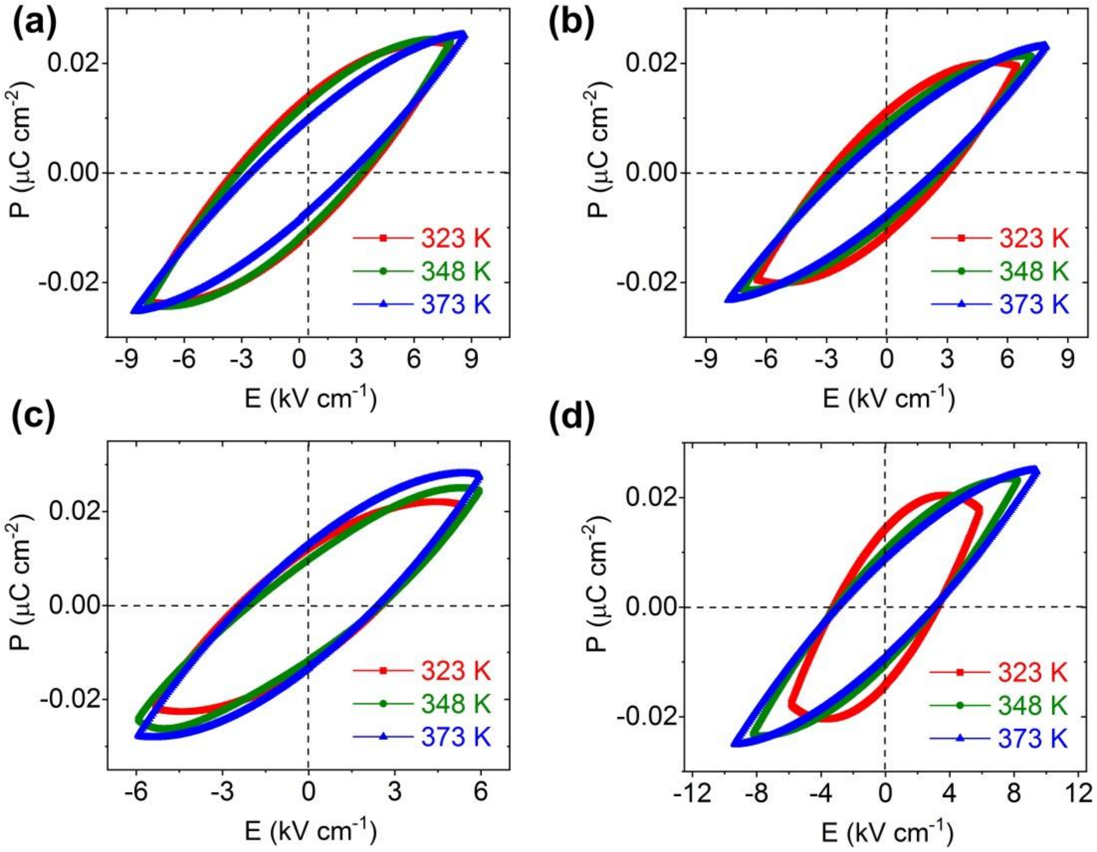

Figure 2A.15: Temperature dependent *P-E* hysteresis loops for (a) DPDP·Cl, (b) DPDP·Br, (c) DPDP·I (PM1) and (d) DPDP·I (PM2).

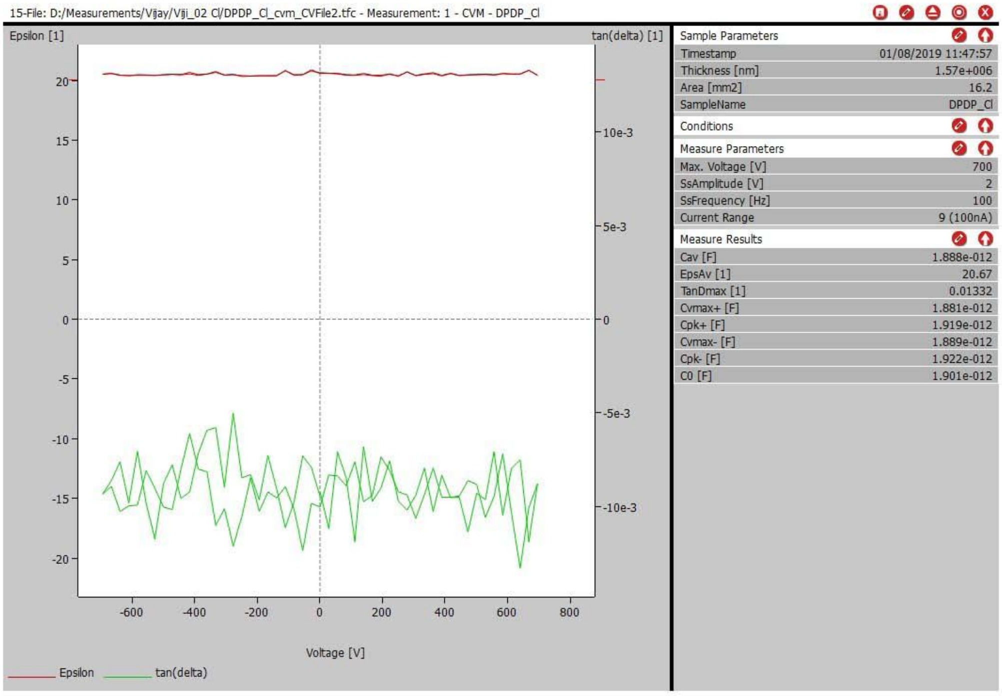

15-File: D:/Measurements/Vijay/Viji_02 Cl/DPDP_Cl_cvm_CVFile2.tfc - Measurement: 1 - CVM - DPDP_Cl

Sample Parameters	
Timestamp	01/08/2019 11:47:57
Thickness [nm]	1.57e+006
Area [mm2]	16.2
SampleName	DPDP_Cl
Conditions	
Measure Parameters	
Max. Voltage [V]	700
SsAmplitude [V]	2
SsFrequency [Hz]	100
Current Range	9 (100nA)
Measure Results	
Cav [F]	1.888e-012
EpsAv [1]	20.67
TanDmax [1]	0.01332
Cvmax+ [F]	1.881e-012
Cpk+ [F]	1.919e-012
Cvmax- [F]	1.889e-012
Cpk- [F]	1.922e-012
C0 [F]	1.901e-012

Figure 2A.16: Electric field dependent dielectric constant of DPDP·Cl.

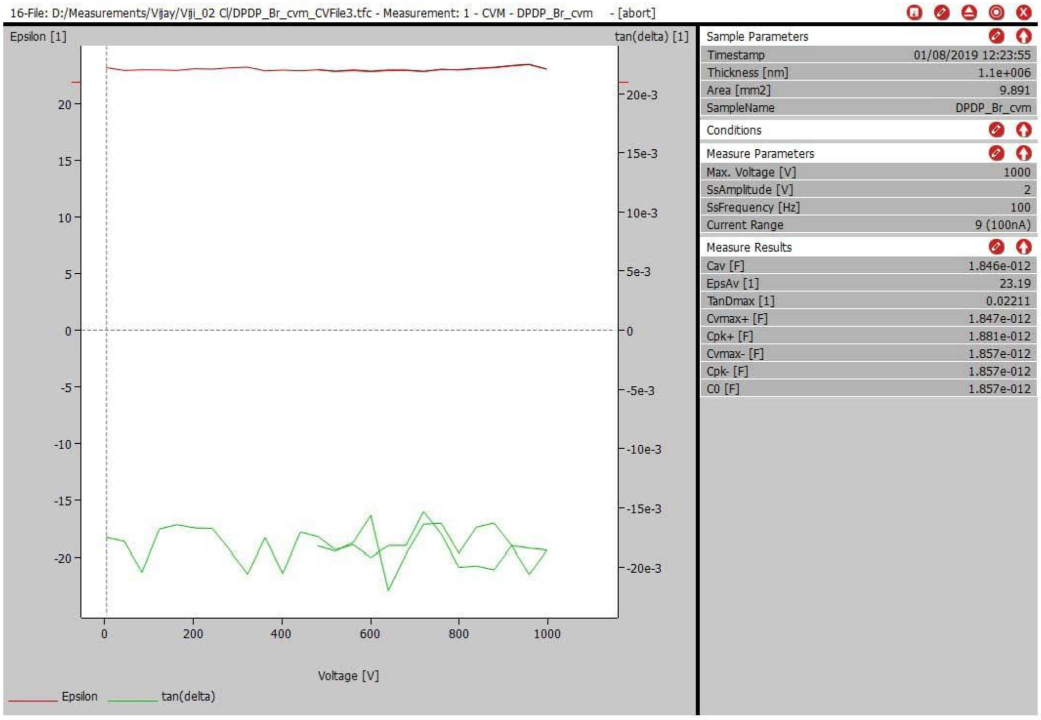

16-File: D:/Measurements/Vijay/Viji_02 Cl/DPDP_Br_cvm_CVFile3.tfc - Measurement: 1 - CVM - DPDP_Br_cvm - [abort]

Sample Parameters	
Timestamp	01/08/2019 12:23:55
Thickness [nm]	1.1e+006
Area [mm2]	9.891
SampleName	DPDP_Br_cvm
Conditions	
Measure Parameters	
Max. Voltage [V]	1000
SsAmplitude [V]	2
SsFrequency [Hz]	100
Current Range	9 (100nA)
Measure Results	
Cav [F]	1.846e-012
EpsAv [1]	23.19
TanDmax [1]	0.02211
Cvmax+ [F]	1.847e-012
Cpk+ [F]	1.881e-012
Cvmax- [F]	1.857e-012
Cpk- [F]	1.857e-012
C0 [F]	1.857e-012

Figure 2A.17: Electric field dependent dielectric constant of DPDP·Br.

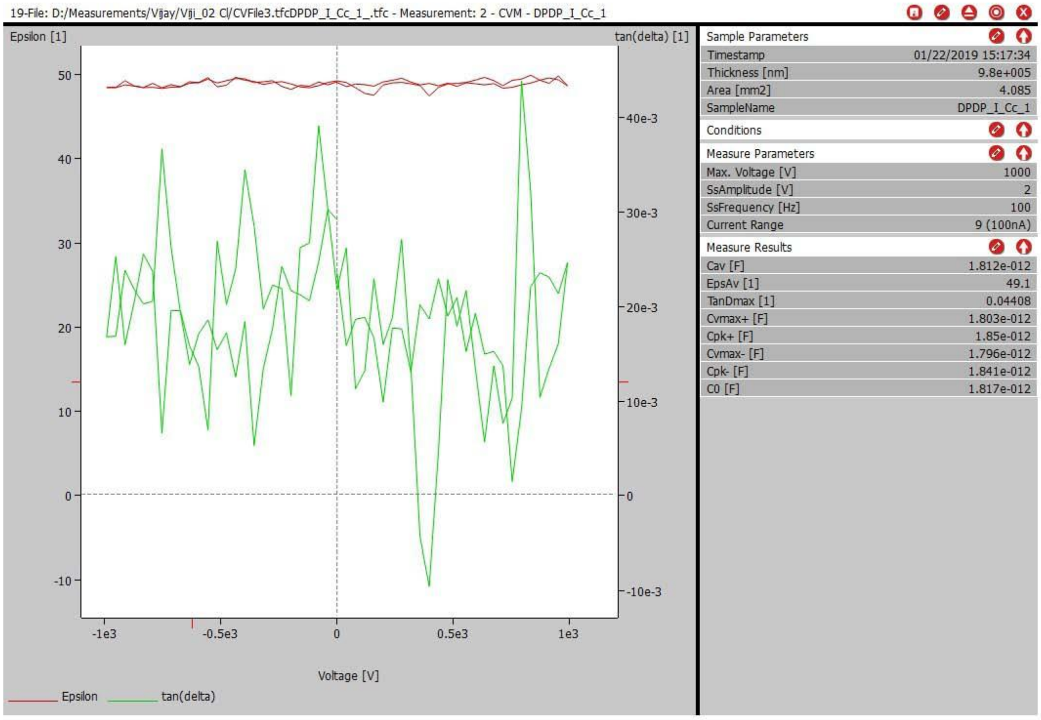

19-File: D:/Measurements/Vijay/Viji_02 Cl/CVFile3.tfcDPDP_I_Cc_1_.tfc - Measurement: 2 - CVM - DPDP_I_Cc_1

Sample Parameters	
Timestamp	01/22/2019 15:17:34
Thickness [nm]	9.8e+005
Area [mm2]	4.085
SampleName	DPDP_I_Cc_1
Conditions	
Measure Parameters	
Max. Voltage [V]	1000
SsAmplitude [V]	2
SsFrequency [Hz]	100
Current Range	9 (100nA)
Measure Results	
Cav [F]	1.812e-012
EpsAv [1]	49.1
TanDmax [1]	0.04408
Cvmax+ [F]	1.803e-012
Cpk+ [F]	1.85e-012
Cvmax- [F]	1.796e-012
Cpk- [F]	1.841e-012
C0 [F]	1.817e-012

Figure 2A.18: Electric field dependent dielectric constant of DPDP·I(PM1).

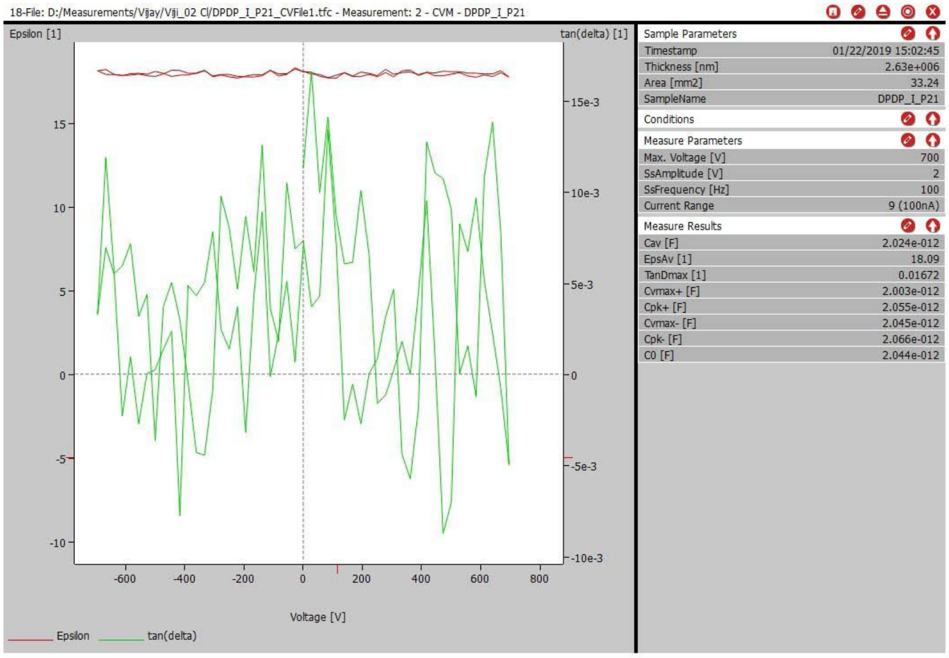
18-File: D:/Measurements/Vijay/Viji_02 Cl/DPDP_I_P21_CVFile1.tfc - Measurement: 2 - CVM - DPDP_I_P21

Sample Parameters	
Timestamp	01/22/2019 15:02:45
Thickness [nm]	2.63e+006
Area [mm2]	33.24
SampleName	DPDP_I_P21
Conditions	
Measure Parameters	
Max. Voltage [V]	700
SsAmplitude [V]	2
SsFrequency [Hz]	100
Current Range	9 (100nA)
Measure Results	
Cav [F]	2.024e-012
EpsAv [1]	18.09
TanDmax [1]	0.01672
Cvmax+ [F]	2.003e-012
Cpk+ [F]	2.055e-012
Cvmax- [F]	2.045e-012
Cpk- [F]	2.066e-012
C0 [F]	2.044e-012

Figure 2A.19: Electric field dependent dielectric constant of DPDP·I(PM2).

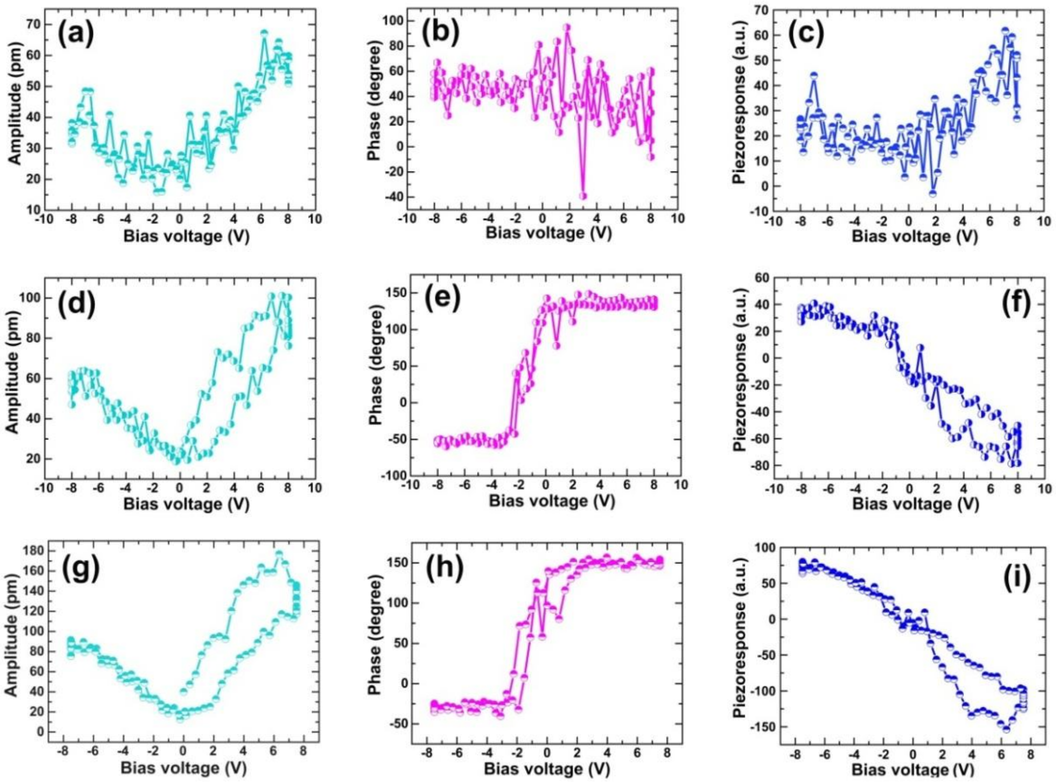

Figure 2A.20: The room temperature V-PFM analysis for DPDP·Br (a,b,c), DPDP·I (PM1) (d,e,f) and DPDP·I (PM2) (g,h,i) showing (a, d, g) amplitude-voltage loops, (b, e, h) phase- voltage loops and (c, f, g) piezoresponse loops.

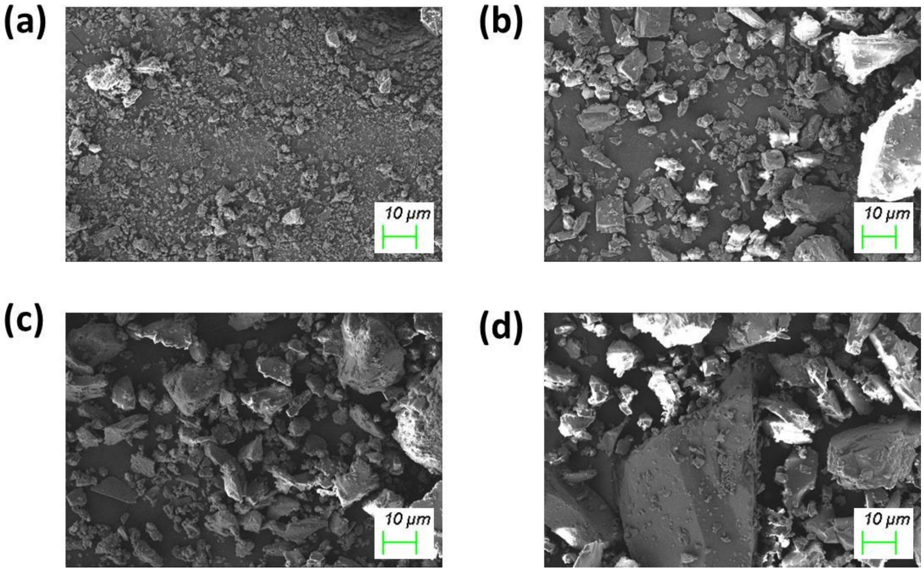

Figure 2A.21: Scanning electron microscopy (SEM) images of (a) DPDP·Cl, (b) DPDP·Br, (c) DPDP·I (PM1) and (d) DPDP·I (PM2).

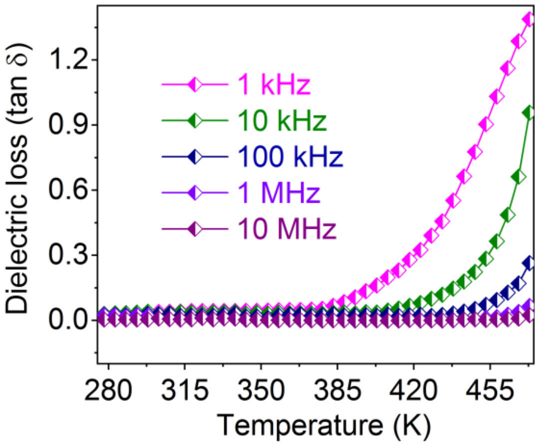

Figure 2A.22: Temperature dependent dielectric loss (tan δ) of DPDP·Cl at various frequencies.

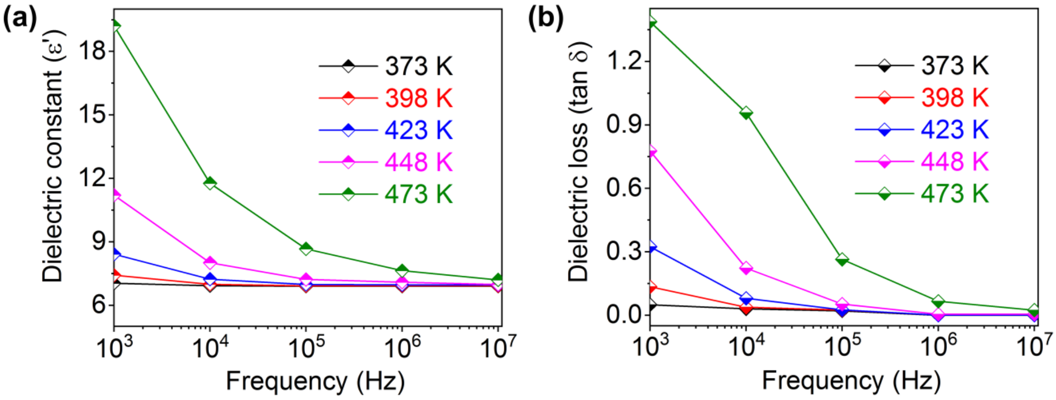

Figure 2A.23: Frequency dependent dielectric constant (ε') and loss (tan δ) of DPDP·Cl at different temperatures.

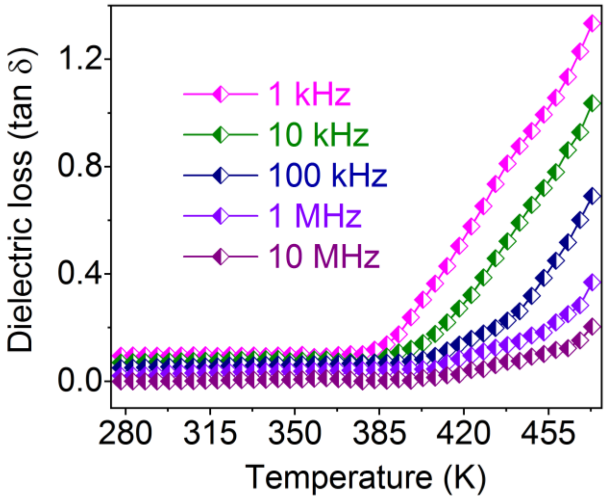

Figure 2A.24: Temperature dependent tan δ of DPDP·Br at various frequencies.

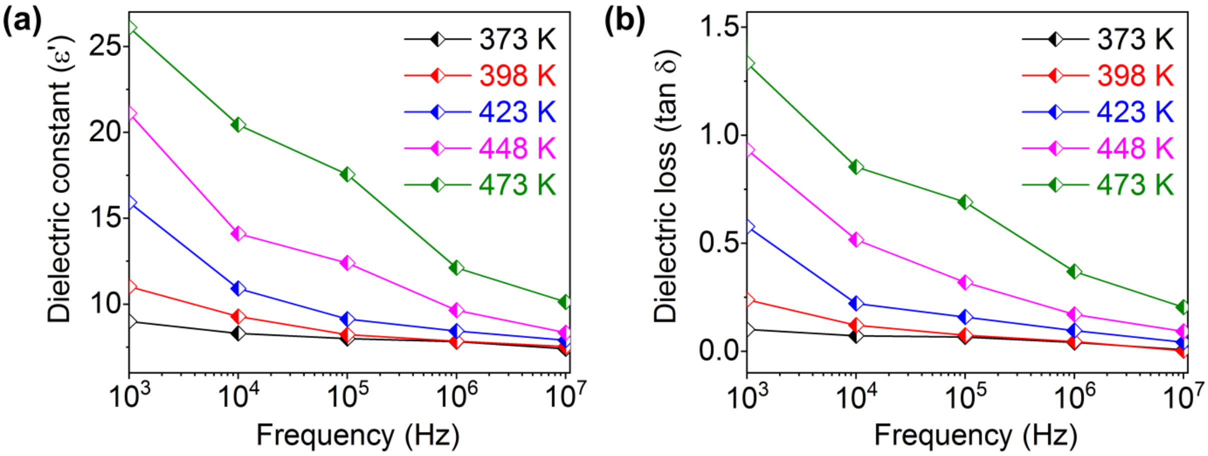

Figure 2A.25: Frequency dependent ε' and tan δ of DPDP·Br at different temperatures.

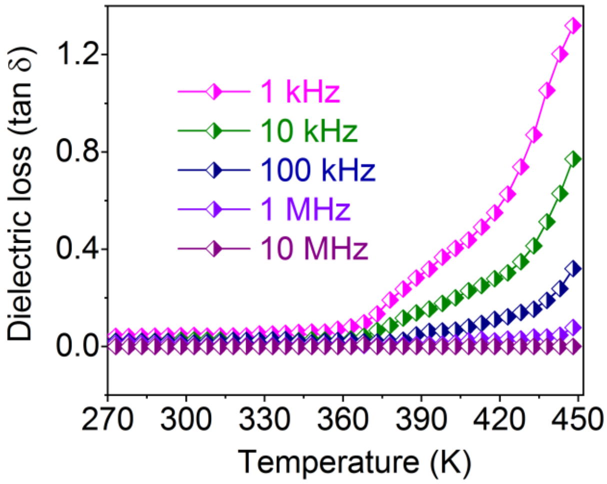

Figure 2A.426: Temperature dependent tan δ of DPDP·I (PM1) at various frequencies.

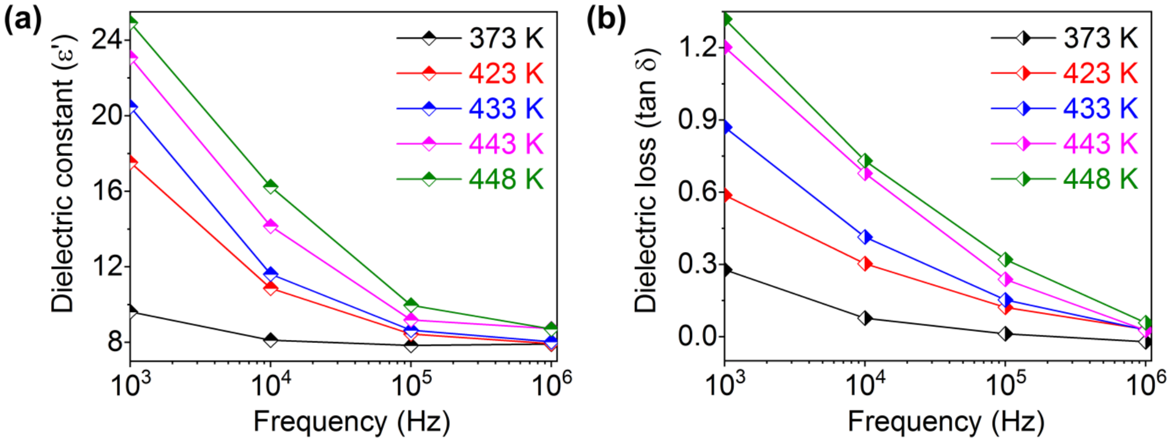

Figure 2A.27: Frequency dependent ε' and tan δ of DPDP·I (PM1) at different temperatures.

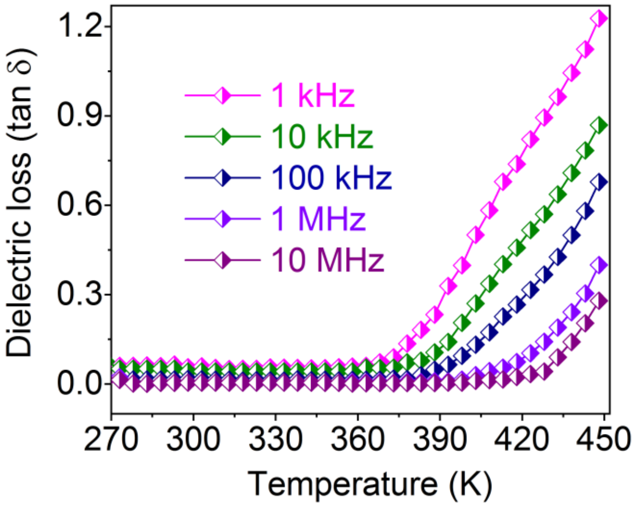

Figure 2A.28: Temperature dependent dielectric loss of DPDP·I (PM2) at various frequencies.

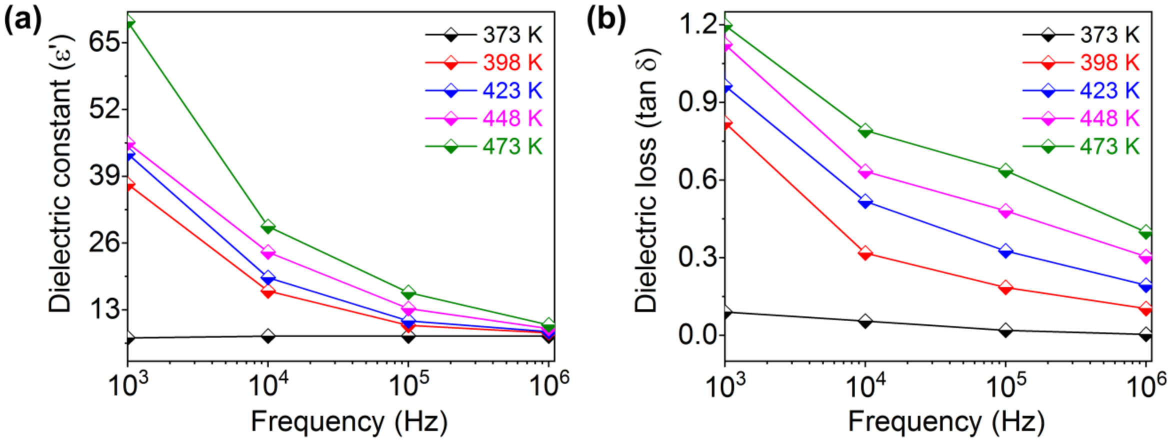

Figure 2A.29: Frequency dependent dielectric constant of DPDP·I (PM2) at different temperatures.

Table 2A.5: Dipole moment calculation of all the phosphonium halides.

S.No	Ferroelectric Materials	Dipole moment (Debye)
1	DPDP·Cl	17.33
2	DPDP·Br	17.97
3	DPDP·I (PM1)	21.29
4	DPDP·I (PM2)	69.14

Table 2A.6: Frequency dependent dielectric constant calculation of DPDP·Cl, DPDP·Br, DPDP·I (PM1) and DPDP·I (PM2).

Compound	Frequency	Dielectric Constant
DPDP·Cl	100 Hz	57.21
	1 kHz	33.37
	10 kHz	31.23
	100 kHz	30.19
	1 MHz	29.4
DPDP·Br	100 Hz	92.29
	1 kHz	40.13
	10 kHz	39.12
	100 kHz	37.12
	1 MHz	37.02
DPDP·I(PM1)	100 Hz	217.83
	1 kHz	124.47
	10 kHz	115.14
	100 kHz	113.27
	1 MHz	111.72
DPDP·I(PM2)	100 Hz	275.36
	1 kHz	111.32
	10 kHz	108.39
	100 kHz	105.46
	1 MHz	102.53

****

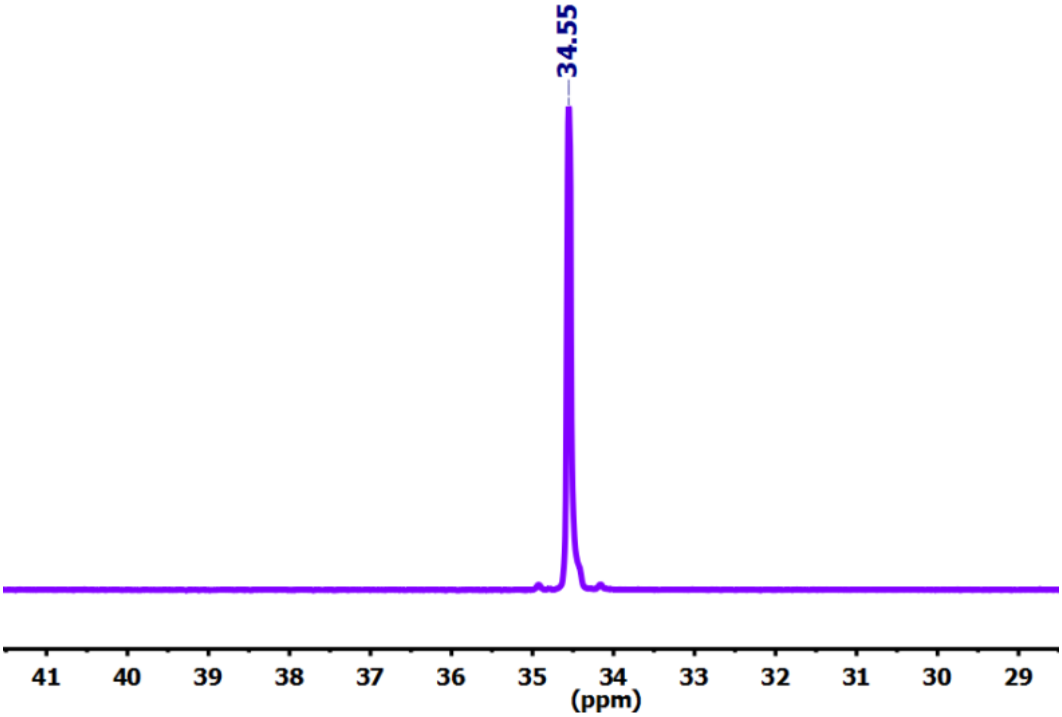

Figure 3A.1: ^{31}P NMR spectrum of DPDP·Br.

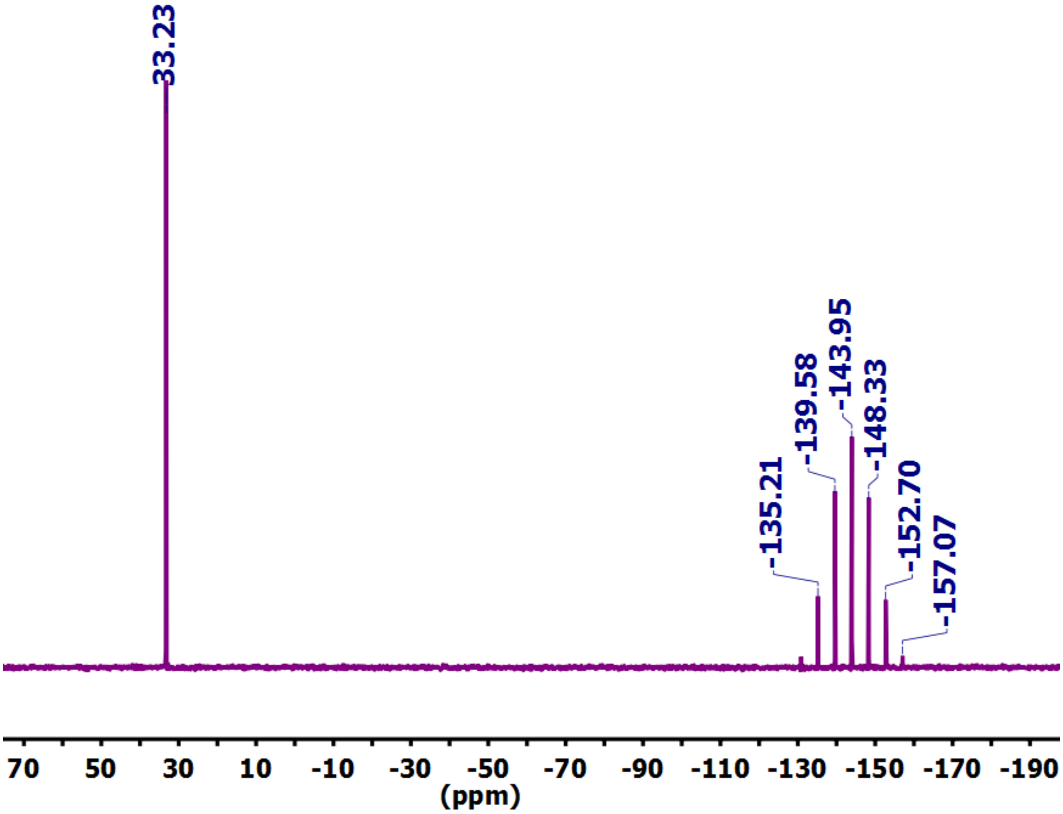

Figure 3A.2: ^{31}P NMR spectrum of DPDP·PF$_6$.

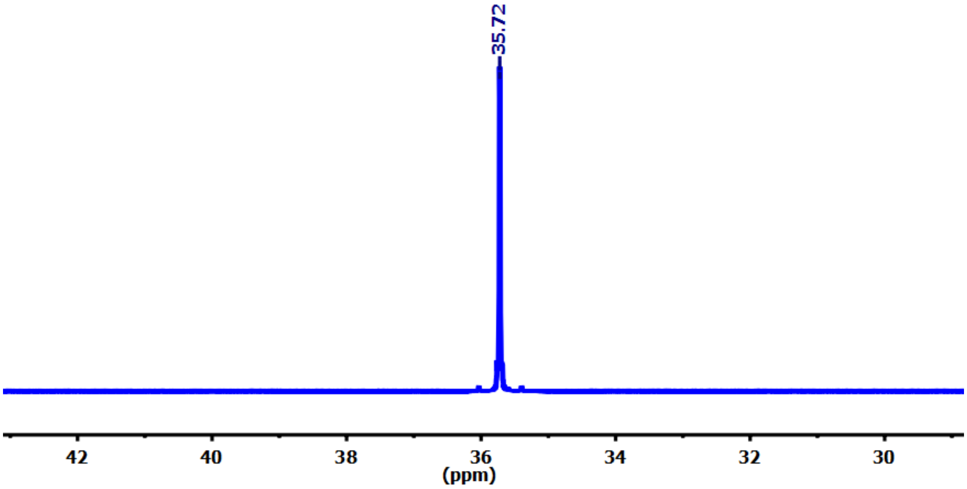

Figure 3A.3: ^{31}P NMR spectrum of TPAP·Br.

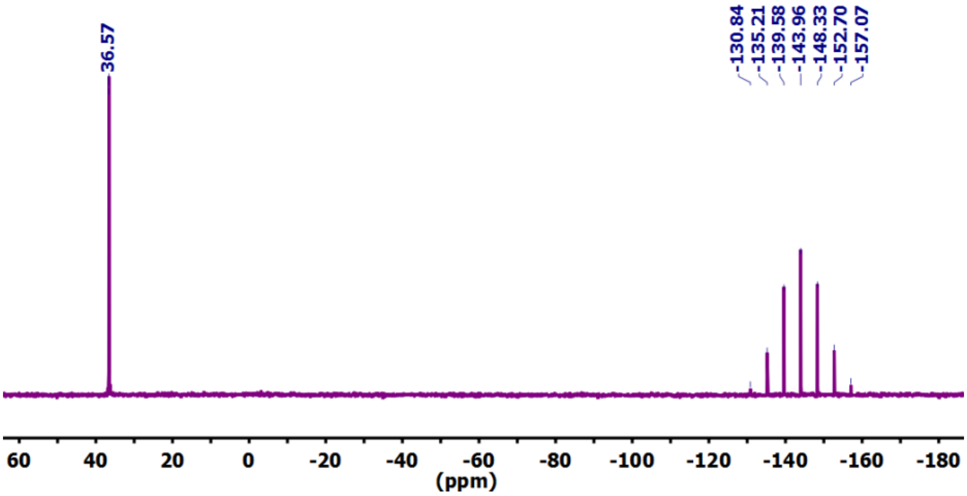

Figure 3A.4: ^{31}P NMR spectrum of TPAP·PF$_6$.

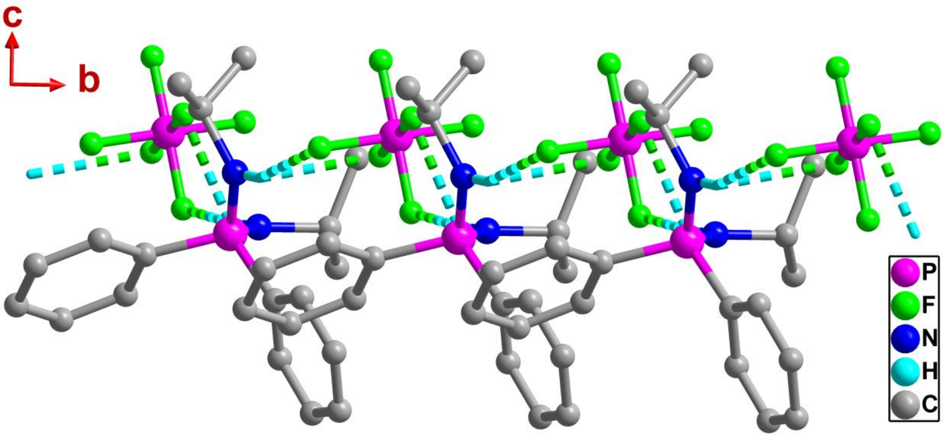

Figure 3A.5: 1D-hydrogen bonded chain structure of DPDP·PF$_6$ shows propagated chains along the b-axis. The observed H…F distances are in the range of 2.26(14) to 2.52(11) Å and the corresponding N-H…F angles are found between 125.6(42) and 162.7(40)°.

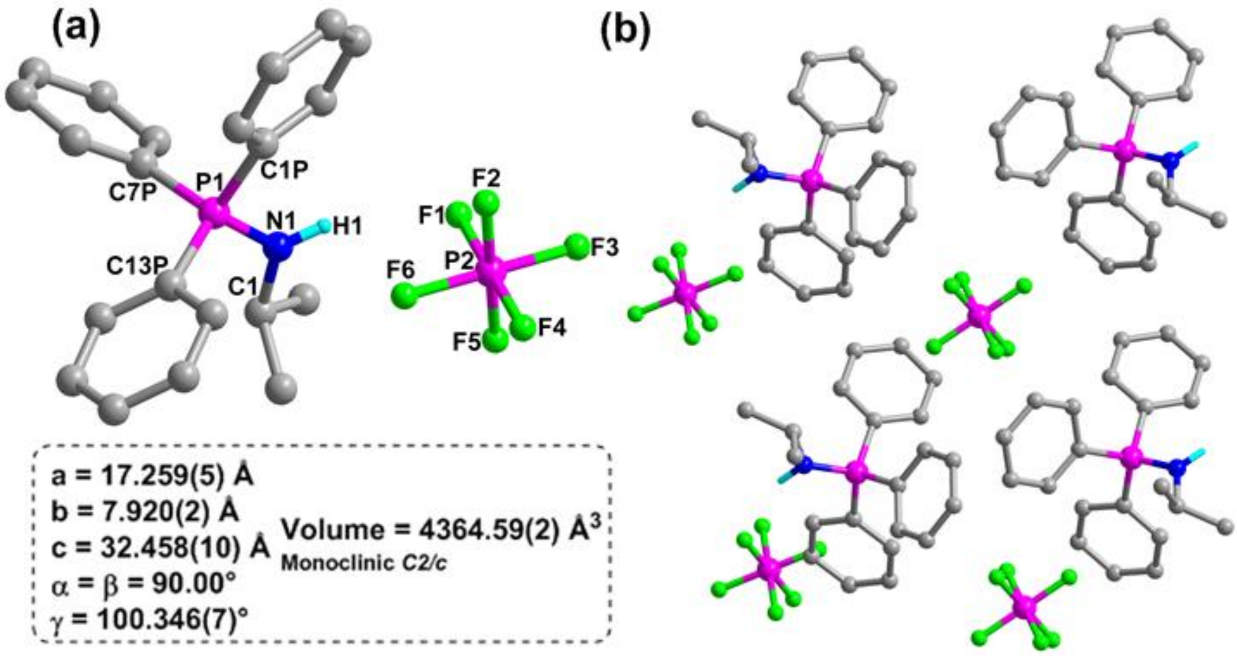

Figure 3A.6: (a) Molecular structure of TPAP·PF$_6$ and (b) its packing diagram along the b-axis.

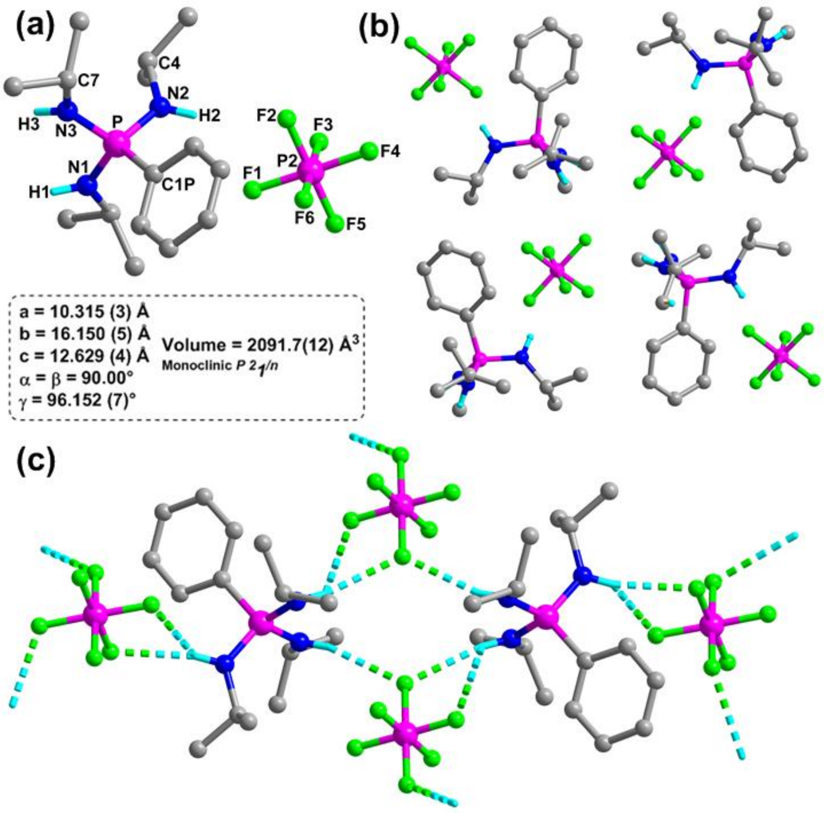

Figure 3A.7: (a) Molecular structure of PTAP·PF$_6$ and (b) its packing diagram along the a-axis. (c) The 2D- structure of PTAP·PF$_6$.

Table 3A.1: Selected bond lengths [Å] and angles [°] for compound DPDP·PF_6, TPAP·PF_6 and PTAP·PF_6.

Compound	**Bond length**	**Bond angle**
DPDP·PF_6	P(1)-N(1): 1.6210(18) P(1)-N(2): 1.6242(19) N(1)-H(1): 0.8800(2) N(2)-H(2): 0.8800(2)	N(1)-P(1)-N(2): 120.76(10) N(2)-P(1)-C(11): 108.34(10) N(2)-P(1)-C(21): 105.94(10) N(1)-P(1)-C(11): 104.93(10) N(1)-P(1)-C(21): 106.34(10)
TPAP·PF_6	P(1)-N(1): 1.633(2) N(1)-H(1): 0.8800(2)	N(1)-P(1)-C(11): 108.90(12) N(1)-P(1)-C(21): 106.24(12) N(1)-P(1)-C(31): 113.32(12)
PTAP·PF_6	P(1)-N(2): 1.617(3) P(1)-N(3): 1.613(3) P(1)-N(1): 1.622(3) N(1)-H(1): 0.8800(2) N(2)-H(2): 0.8800(2) N(3)-H(3): 0.8800(2)	N(3)-P(1)-N(2): 114.58(13) N(3)-P(1)-N(1): 102.27(13) N(2)-P(1)-N(1): 112.56(13) N(2)-P(1)-C(11): 104.07(14) N(3)-P(1)-C(11): 108.71(14) N(1)-P(1)-C(11): 114.97(14)

Table 3A.2: Selected bond lengths [Å] and angles [°] for compound DPDP·PF_6, TPAP·PF_6 and PTAP·PF_6.

Compound	**D-H…A**	**d(D-H)**	**d(H…A)**	**d(D-A)**	**<DHA**
DPDP·PF_6	N(1)-H(1)…F(2)	0.88(3)	2.26(14)	3.112(4)	162.7(40)
	N(1)-H(1)…F(4)	0.88(3)	2.52(11)	3.119(4)	125.6(42)
TPAP·PF_6	N(1)-H(1)…F(2)	0.88(2)	2.41(13)	3.244(4)	156.9(43)
	N(1)-H(1)…F(6)	0.88(3)	2.41(12)	3.244(3)	157.6(42)
PTAP·PF_6	N(1)-H(1)…F(2)	0.88(29)	2.33(34)	3.189(3)	165.7(2)
	N(1)-H(1)…F(6)	0.88(29)	2.62(26)	3.224(4)	126.9(3)
	N(2)-H(2)…F(4)	0.88(29)	2.27(31)	3.136(4)	168.2(2)
	N(2)-H(2)…F(5)	0.88(29)	2.55(50)	3.197(3)	131.1(3)

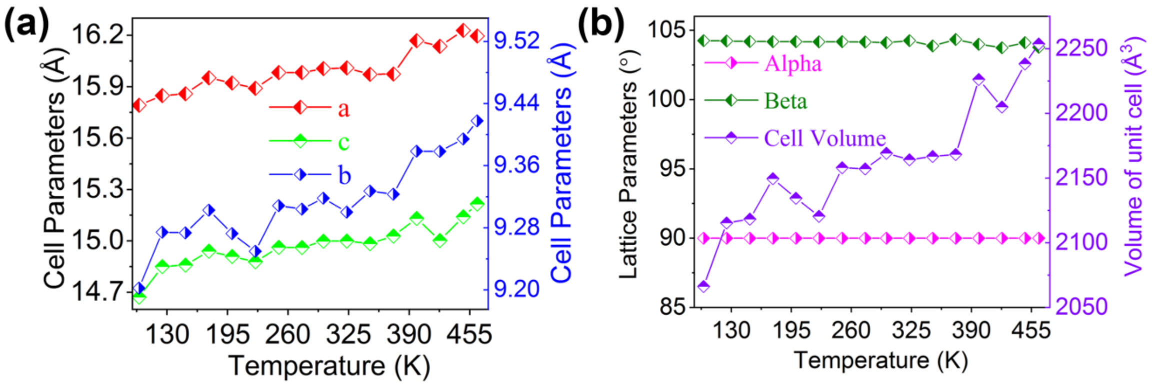

Figure 3A.8: Variable temperature unit-cell parameters of DPDP·PF_6.

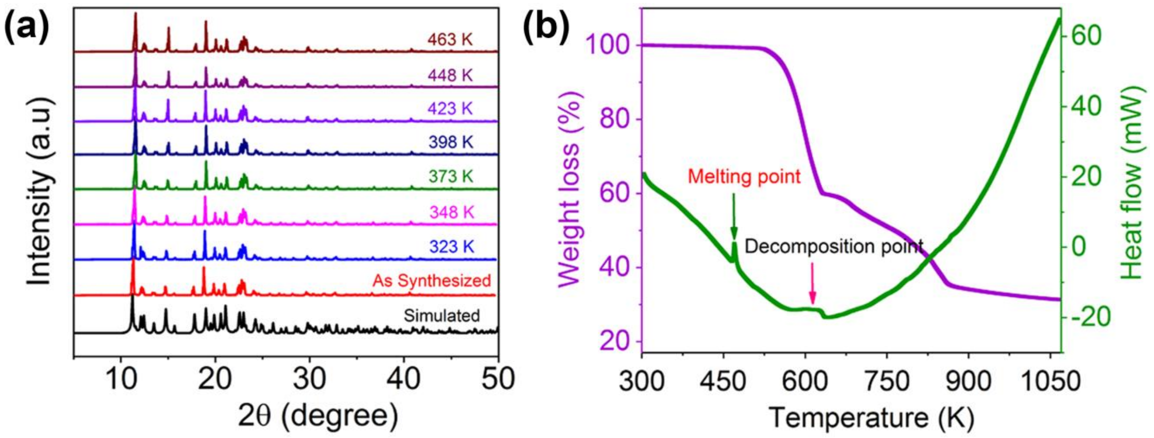

Figure 3A.9: VT-PXRD, TG/DTA analysis of DPDP·PF_6.

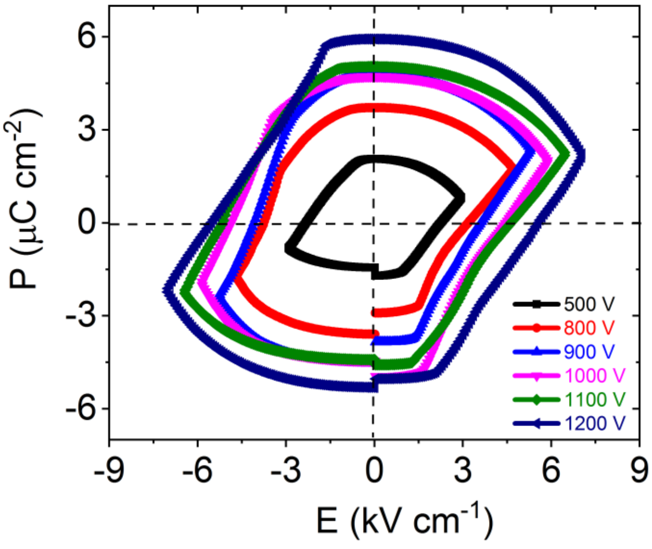

Figure 3A.10: The evolution of *P-E* hysteresis loops at various applied voltages for a single crystal of DPDP·PF_6.

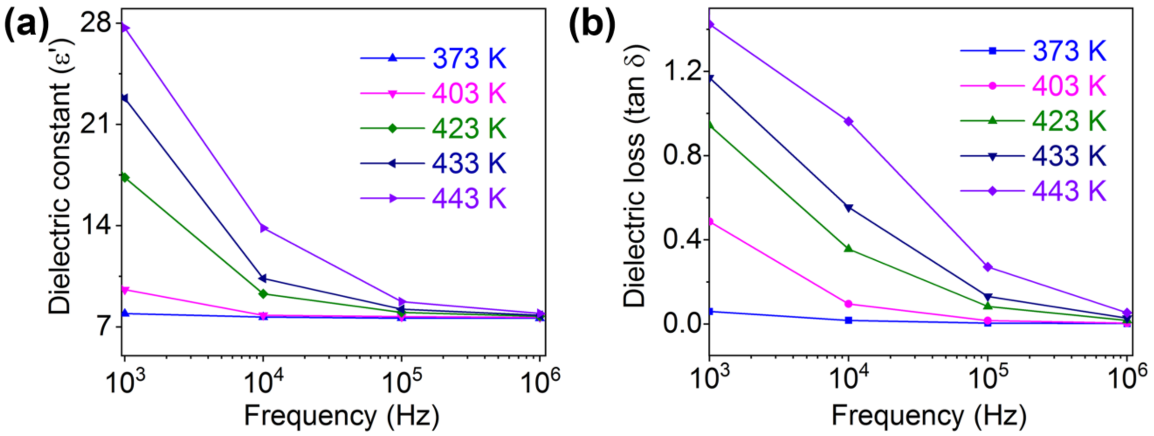

Figure 3A.11: Frequency dependent dielectric constant and loss of DPDP·PF_6 at different temperatures.

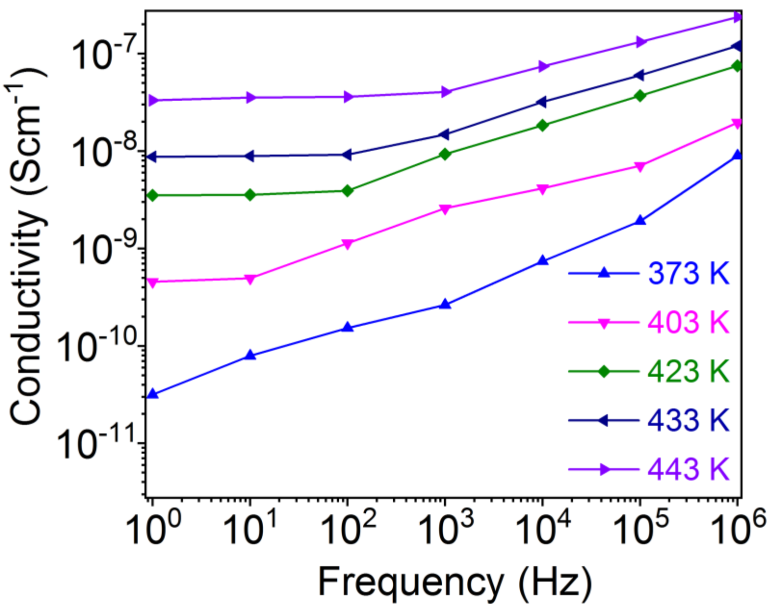

Figure 3A.12: Frequency dependent conductivity plot of DPDP·PF_6 at different temperatures.

Table 3A.3: Detailed weight percentage calculation of used composites.

Composite materials (wt %)	**DPDP·PF_6 (in mg)**	**PDMS + curing agent (in mg)**
3	37.35	1245
5	68	1360
7	93.24	1332
10	150	1350
20	300	1200

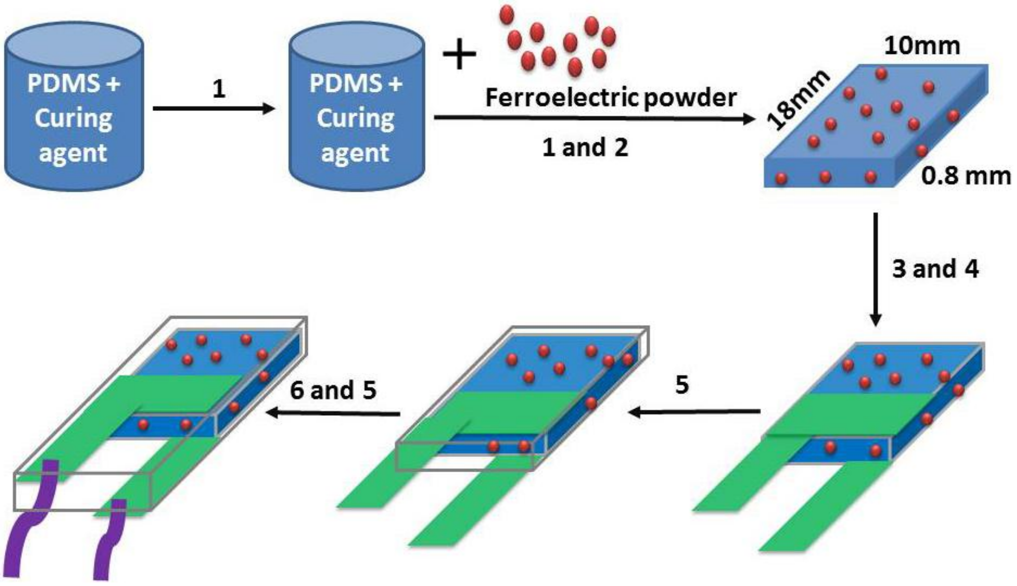

Scheme 3A.1: Device fabrication steps of DPDP·PF_6/PDMS as follows, (1) mixing and degassing of PDMS and curing agent (2) Ferroelectric powder added into PDMS/curing agent and cured in a mouled at 70 °C for 4 hours (3) Silver paste was applied on both sides of the PDMS film for collection of charges during testing and dried at 50 °C for 4 hours (4) Cu electrodes were applied on the silver paste for lead attachment (5) PDMS encapsulation (6) Finally Lead contacts were attached to the copper electrodes.

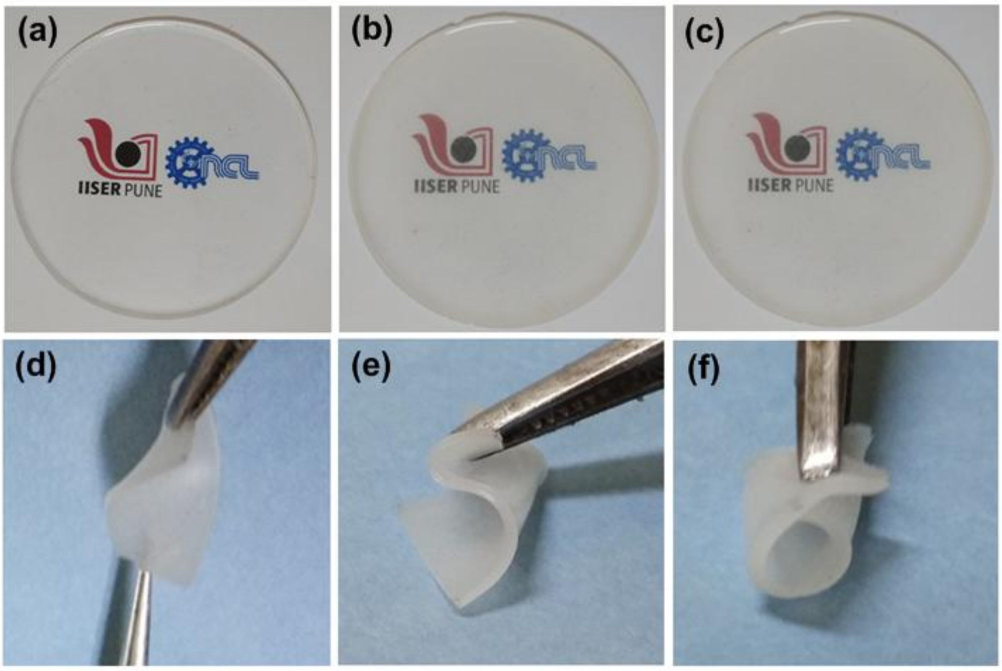

Figure 3A.13: (a), (b) and (c) PDMS, 10, 20 wt % of DPDP·PF_6/PDMS film. Flexibility of DPDP·PF_6/PDMS film (d) twisting (e) two fold bending and (f) rolling.

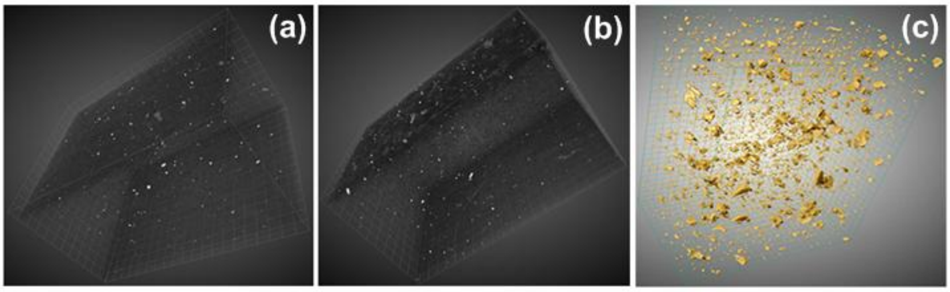

Figure 3A.14: (a), (b) and (c), 3-D Tomography image of DPDP·PF_6 (3, 5 and 20 wt %) embedded in a PDMS matrix (scale bar for single grid 50 μm).

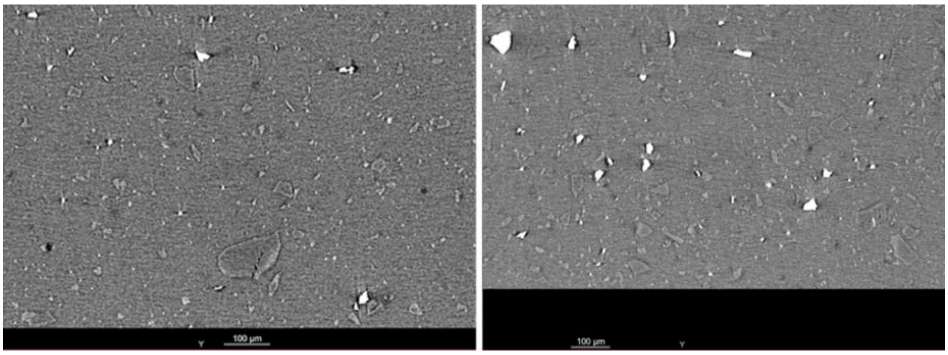

Figure 3A.15: 2-D Tomography image of DPDP·PF_6 (10 and 20 wt %) embedded in a PDMS matrix.

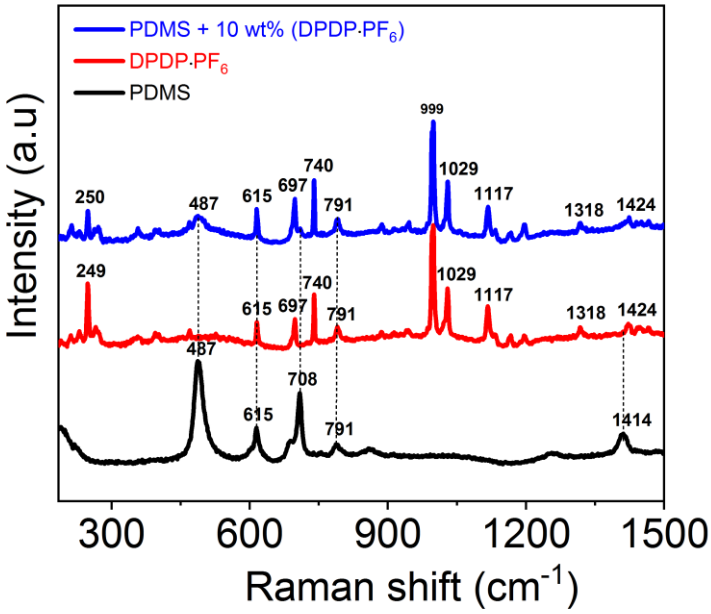

Figure 3A.16: The Raman spectra of DPDP·PF_6/PDMS (10 wt %) and its individual components.

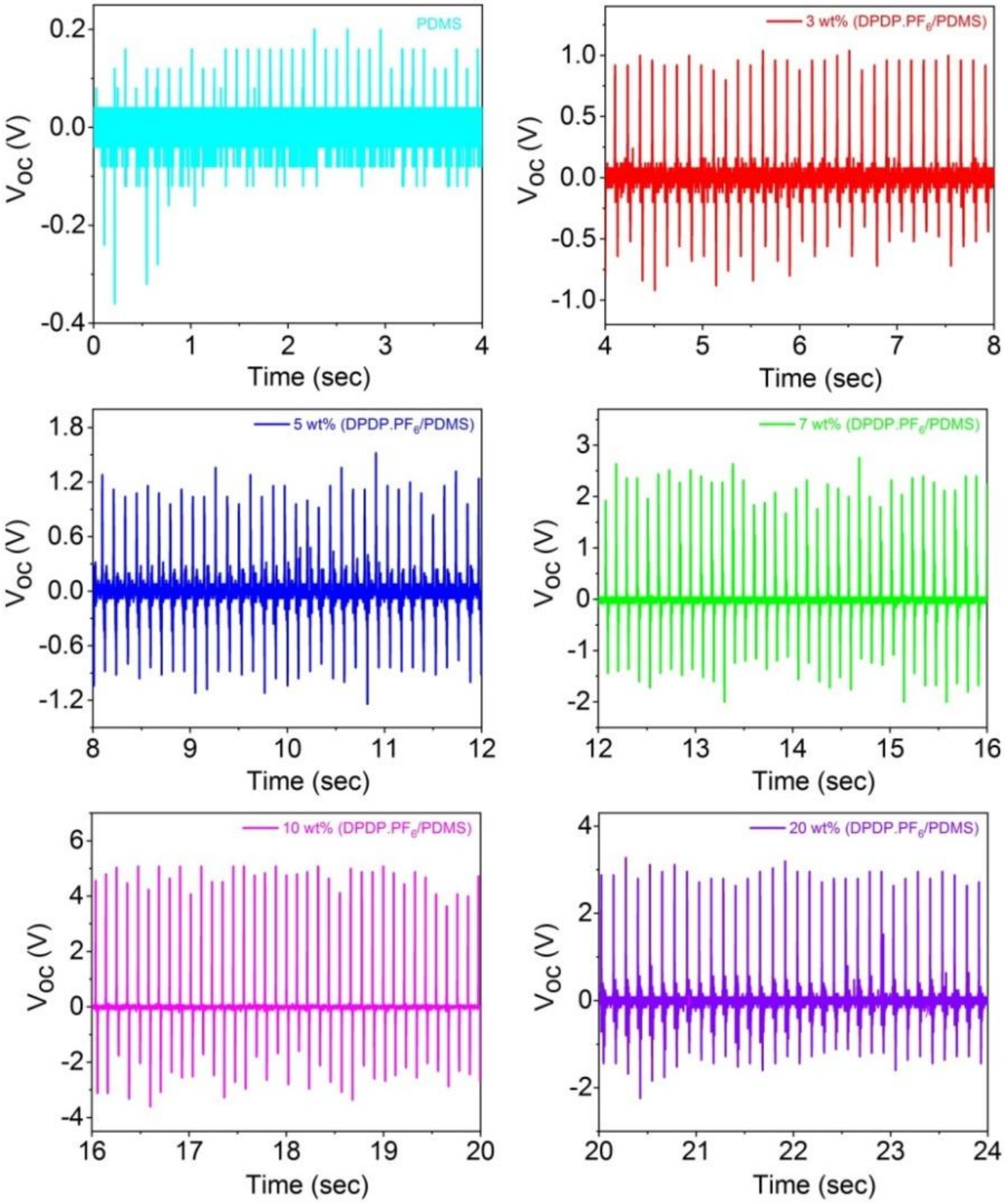

Figure 3A.17: Output voltage measurement for all weight percentage of composite materials.

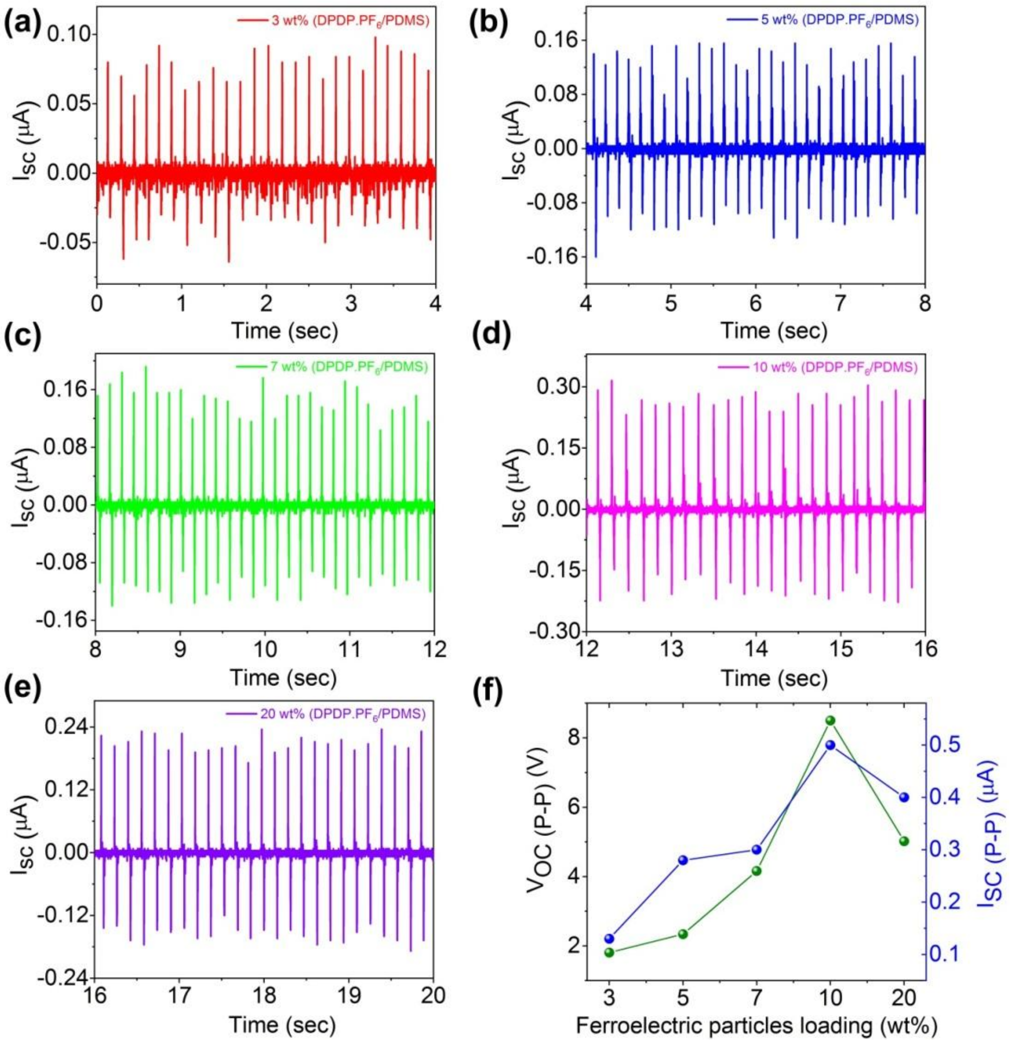

Figure 3A.18: Output current measurement for all weight percentage of composite materials (a) 3 wt % DPDP·PF$_6$ (b) 5 wt % DPDP·PF$_6$ (c) 7 wt % DPDP·PF$_6$ (d) 10 wt % DPDP·PF$_6$ (e) 20 wt % DPDP·PF$_6$ and (f) Variation of output voltage and output current with different loading of composite materials.

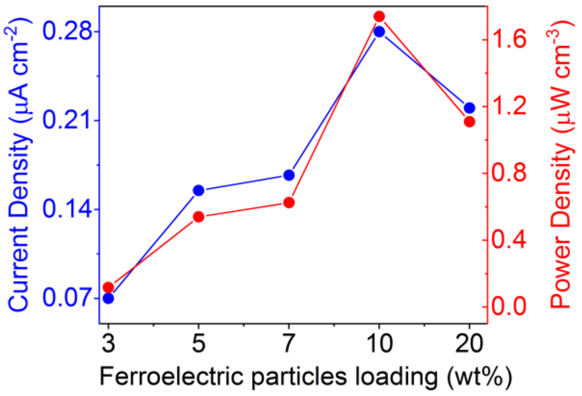

Figure 3A.19: The current and power densities for all the DPDP·PF$_6$/PDMS devices.

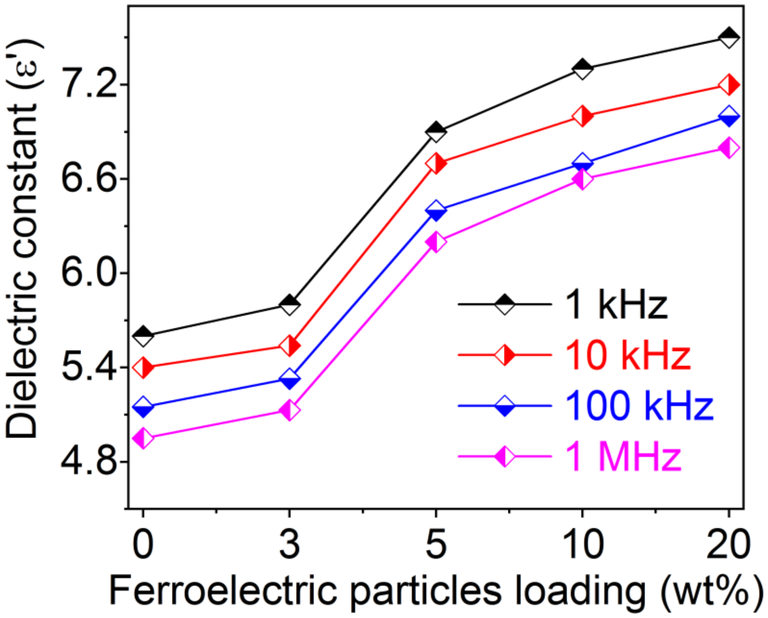

Figure 3A.20: Real part of dielectric permittivity for different compositions of DPDP·PF_6/PDMS films at various frequencies.

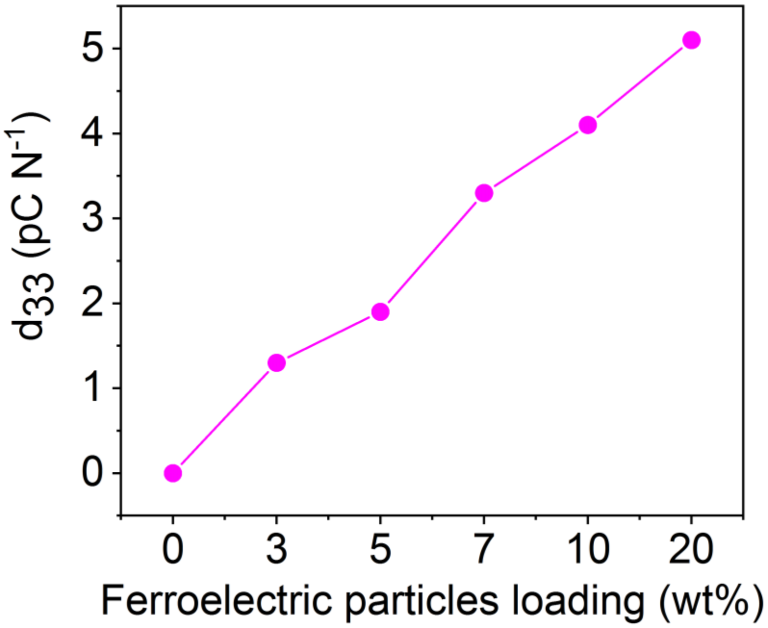

Figure 3A.21: Piezoelectric coefficient for all the DPDP·PF_6/PDMS films.

****

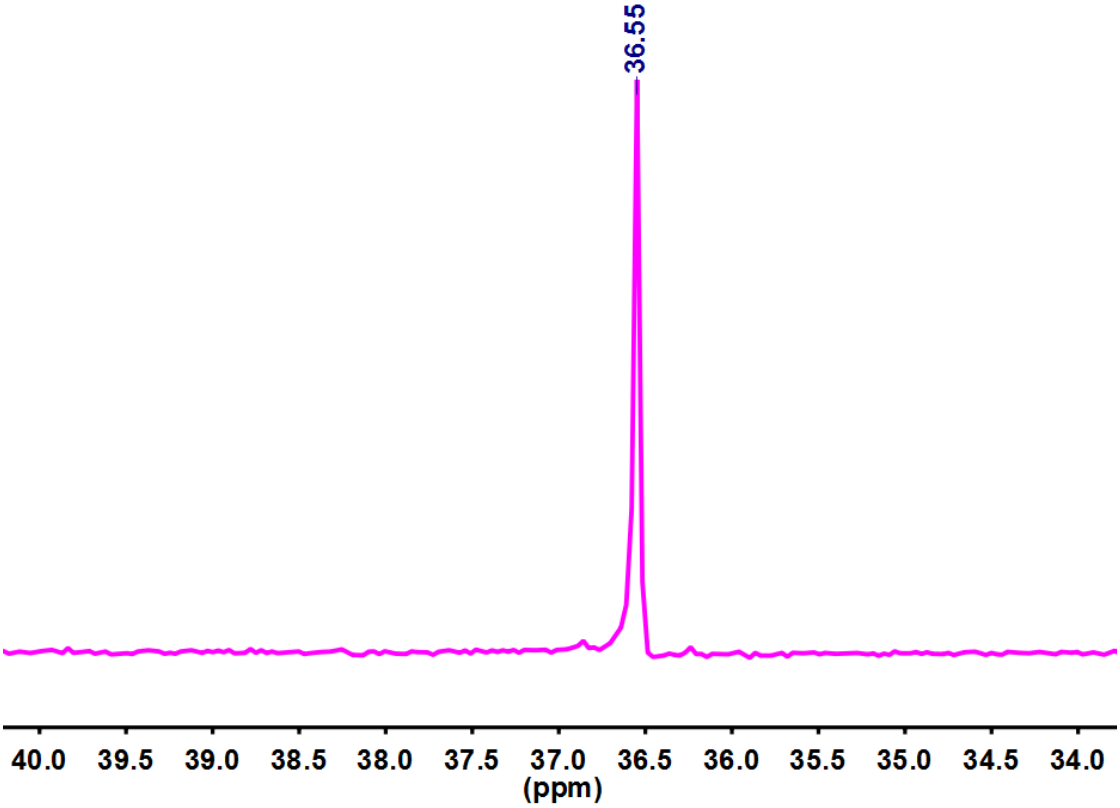

Figure 4A.1: ^{31}P NMR spectrum of TPAP·BF_4.

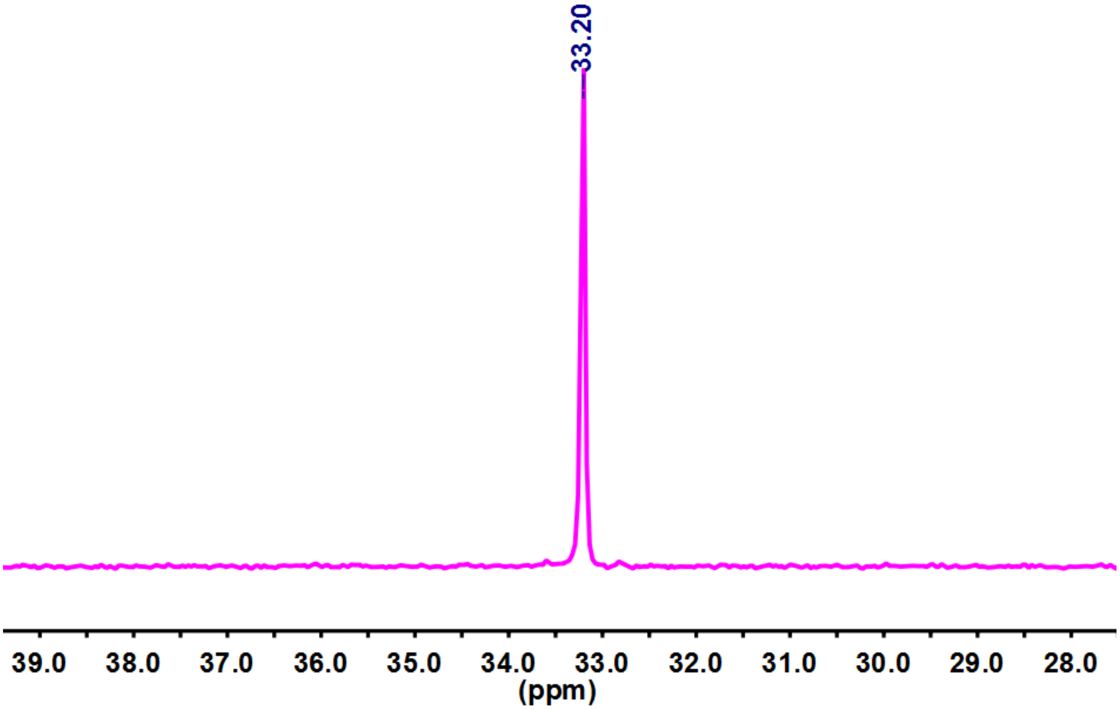

Figure 4A.2: ^{31}P NMR spectrum of DPDP·BF_4

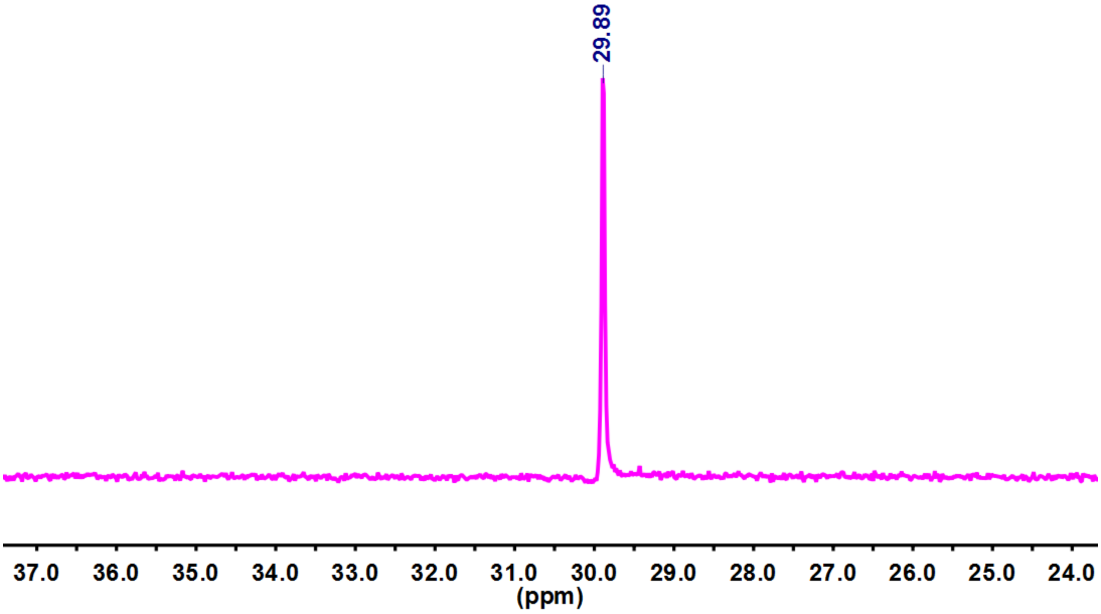

Figure 4A.3: ^{31}P NMR spectrum of $PTAP\cdot BF_4$.

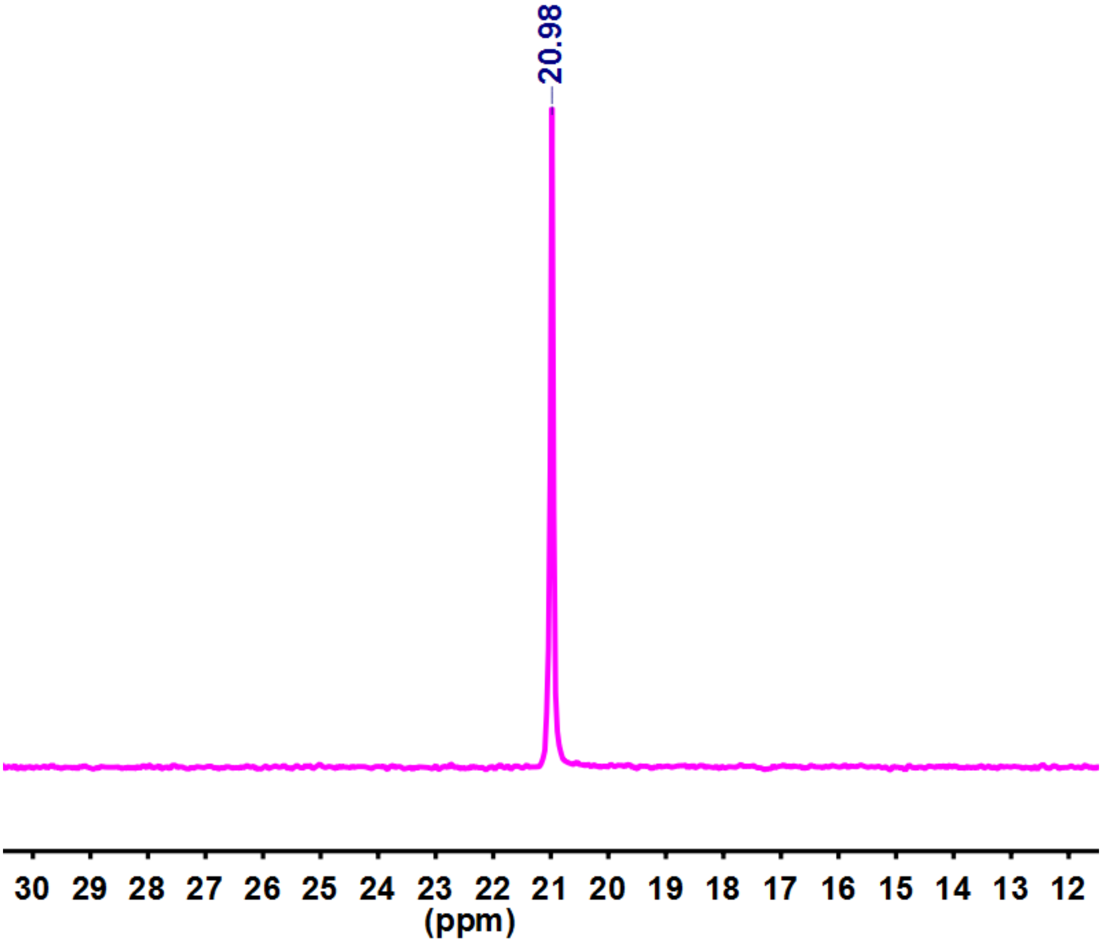

Figure 4A.4: ^{31}P NMR spectrum of $TIAP\cdot BF_4$.

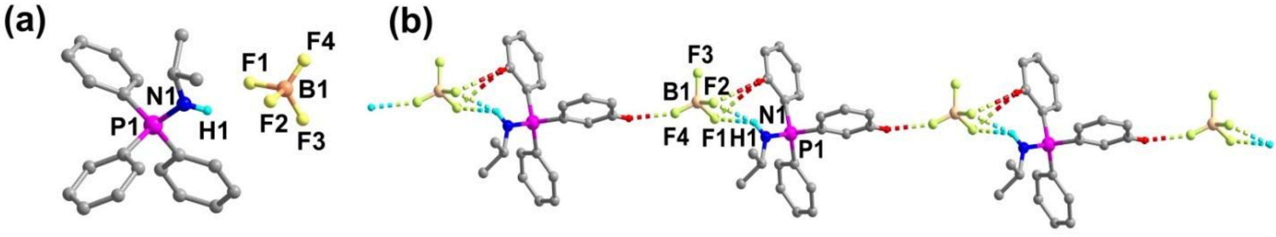

Figure 4A.5: Molecular structure of TPAP·BF_4 at 100 K showing (a) its asymmetric unit and (b) H-bonding interactions along the 'b' axis.

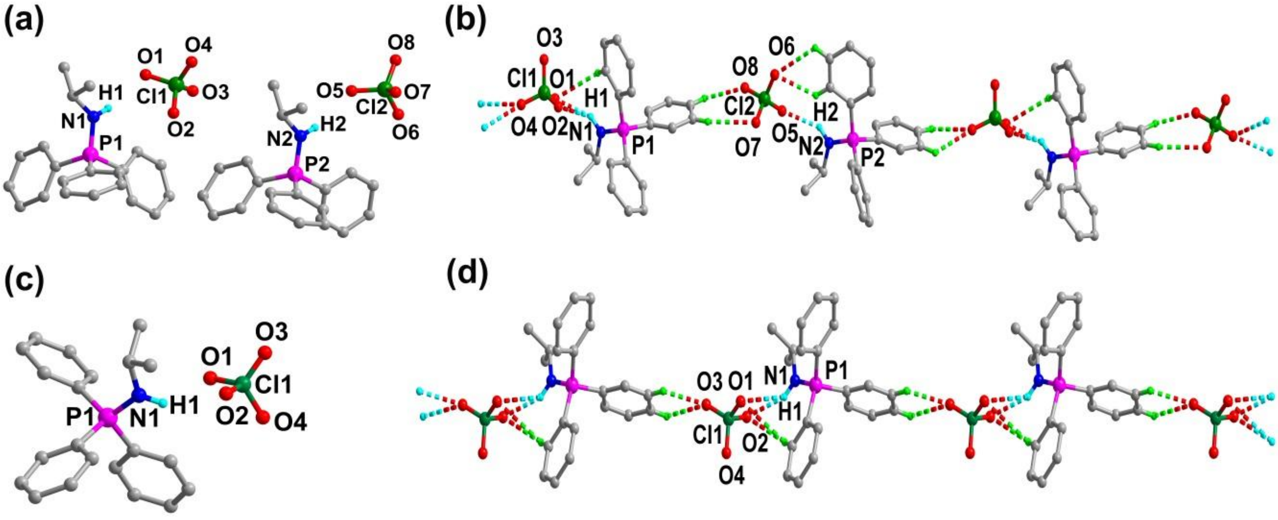

Figure 4A.6: Molecular structure of TPAP·ClO_4 at 150 (a, b) and 200 (c, d) K showing its asymmetric unit (a) and (c) and H-bonding interactions along the 'b' axis (b) and (d).

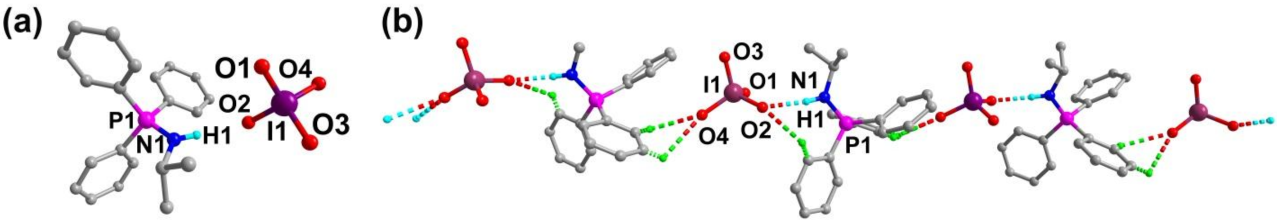

Figure 4A.7: Molecular structure of TPAP·IO_4 at 100 K showing (a) its asymmetric unit and (b) H-bonding interactions along the 'b' axis.

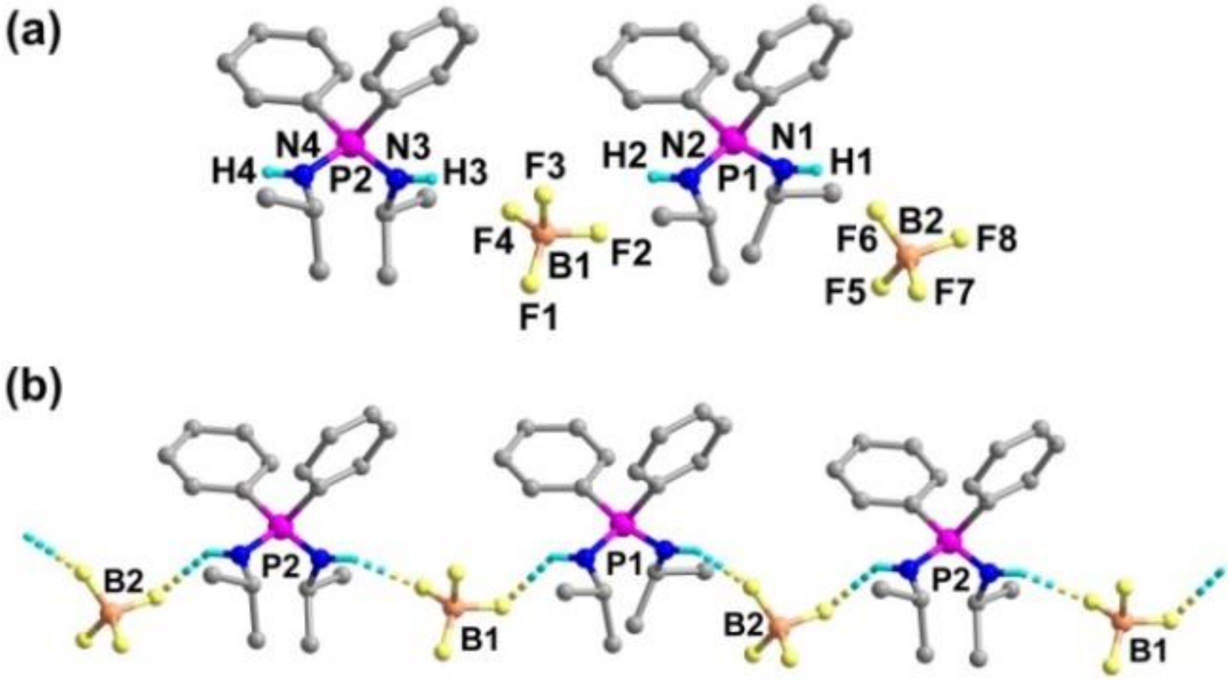

Figure 4A.8: Molecular structure of DPDP·BF_4 at 100 K showing (a) its asymmetric unit and (b) H-bonding interactions along the 'b' axis.

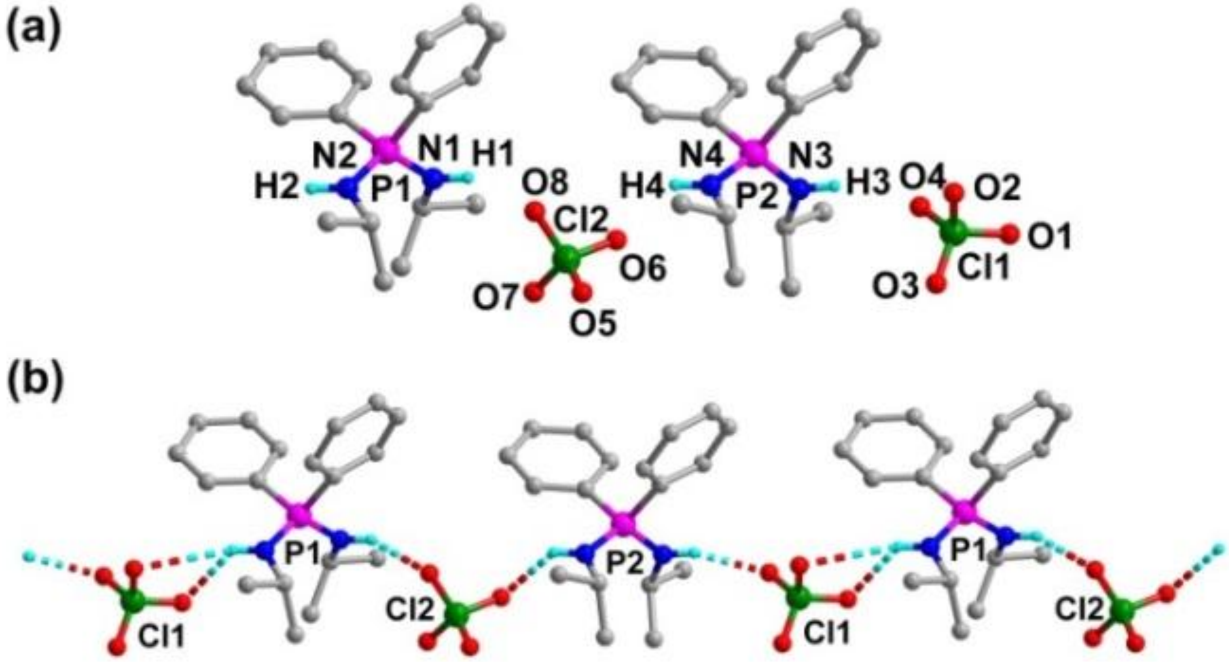

Figure 4A.9: Molecular Structure of DPDP·ClO_4 at 100 K showing (a) its asymmetric unit and (b) H-bonding interactions along the 'b' axis.

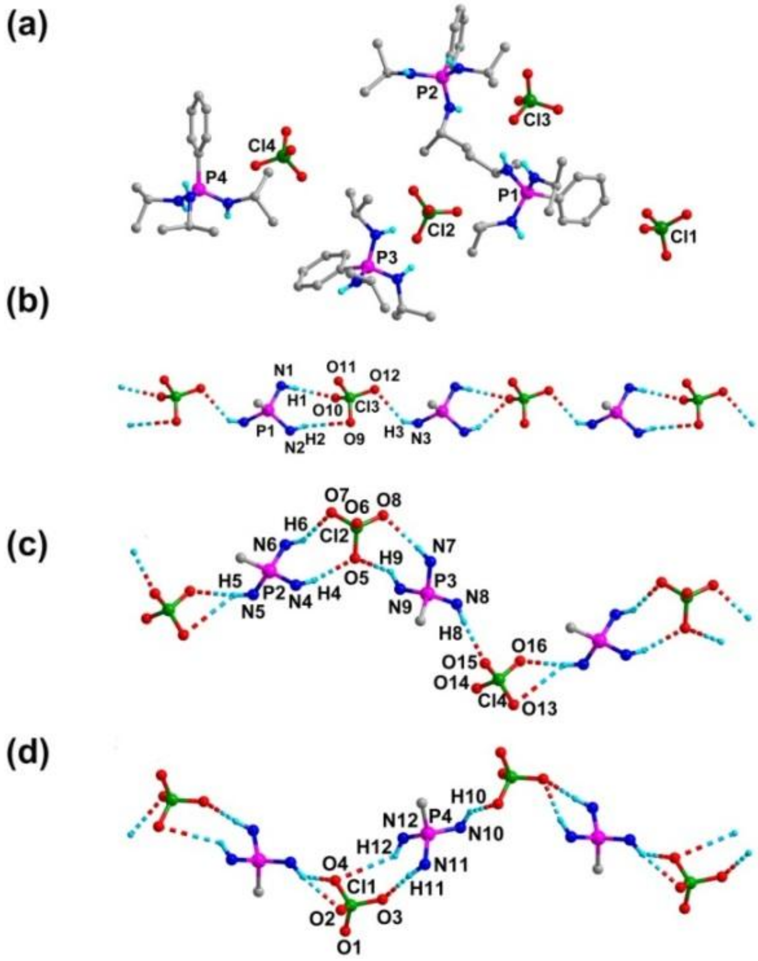

Figure 4A.10: Molecular Structure of PTAP·$\mathrm{ClO_4}$ at 100 K along with its three different H-bonded chains (a) its asymmetric unit (b)1D-chain like structure along the 'a' axis, (c) and (d) the Zig-Zag 1D-chains along the 'b' axis. Phenyl and other alkyl groups are omitted for clarity.

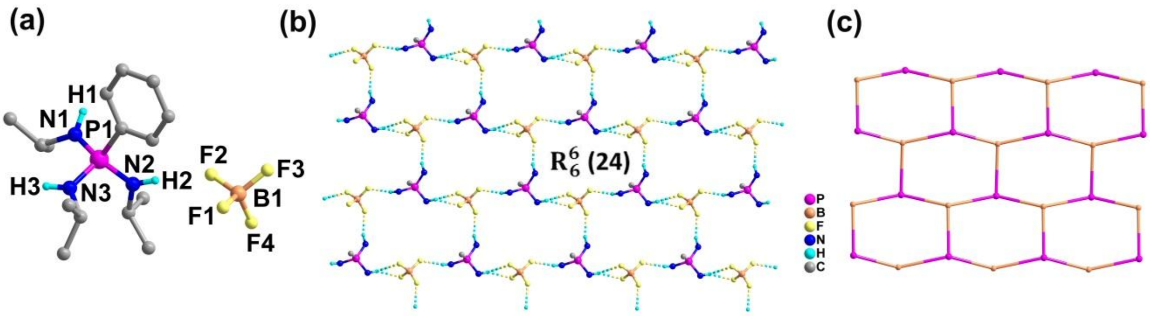

Figure 4A.11: Molecular structure of PTAP·$\mathrm{BF_4}$ at 100 K showing (a) its asymmetric unit and (b) formation of 2D-sheet structure mediated by N-H…F interactions along with the view of a 24-membered macrocyclic ring present in it. Phenyl and other alkyl groups are omitted for clarity. (c) The underlying distorted 2D-net of 'hcb' topology.

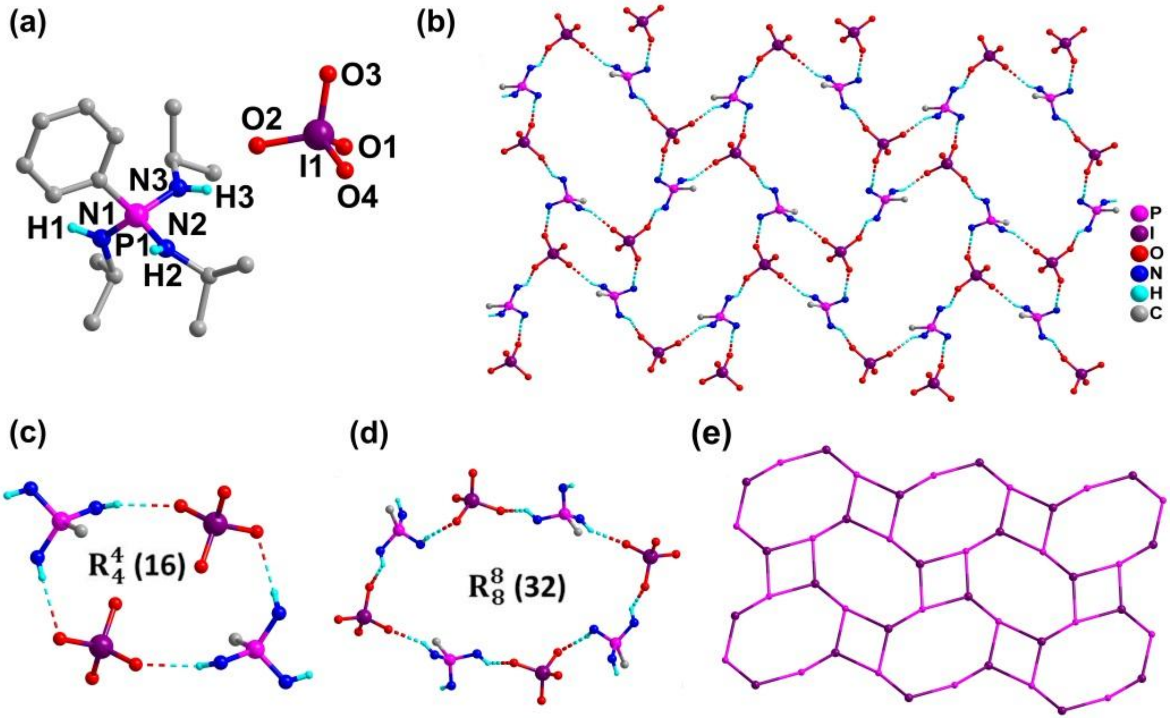

Figure 4A.12: Molecular structure of PTAP·IO_4 at 100 K showing (a) its asymmetric unit and (b) 2D-hydrogen bonded networks viewed parallel to the 'bc' plane. (c) and (d) shows the respective individual 16 and 32 membered macrocycle rings. Phenyl and other alkyl groups are omitted for clarity. (e) The underlying 2D-net of 'fes' topology.

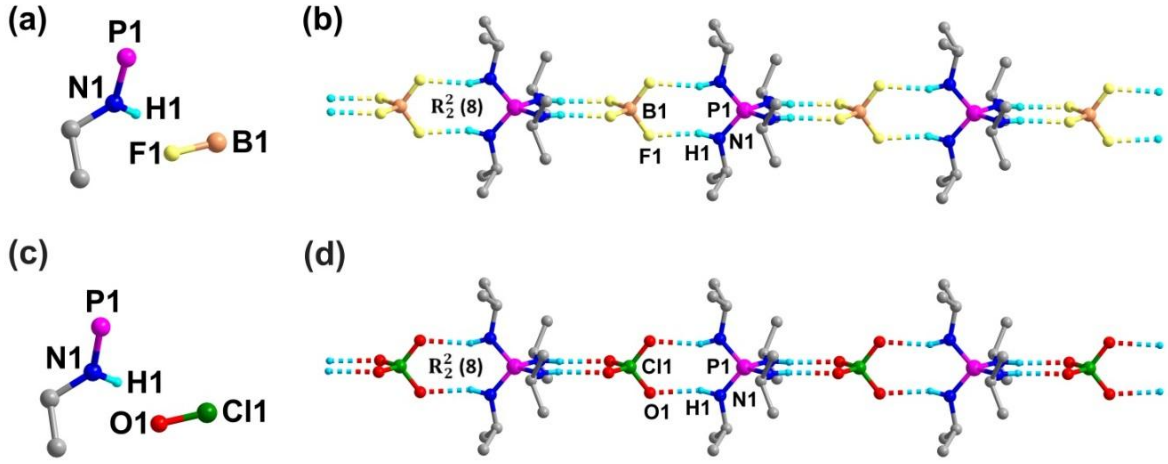

Figure 4A.13: The asymmetric units present in the structures of (a) TIAP·BF_4 and (b) TIAP·ClO_4 at 100 K. (b) and (d) View of their iso-structural of 1D-twisted hydrogen bonded chains along 'c' axis.

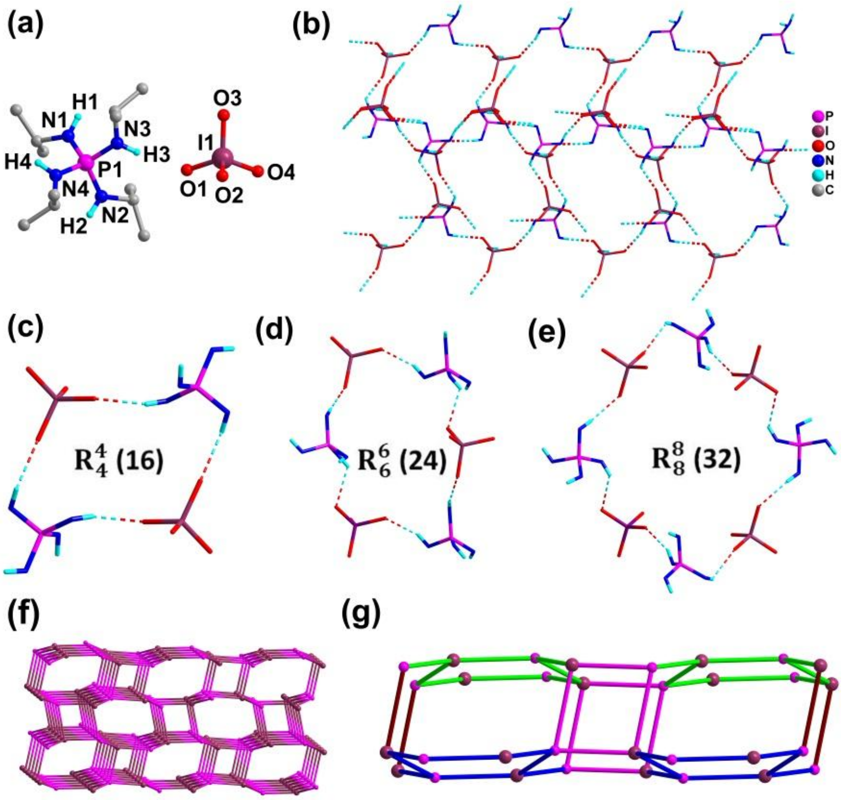

Figure 4A.14: Molecular structure of TIAP·IO_4 at 100 K showing (a) its asymmetric unit and (b) the formation of the 3D-hydrogen bonded network in it. View of the (c) 16-, (d) 24- and (e) 32-membered macrocycle rings within the 3D-lattice. The alkyl groups are omitted for clarity. (f) The underlying 3D-net of 'crb' topology and (g) view of a single layer of 3D-network.

Table 4A.1: Summary of the space groups of all the tetrahedral anion supported phosphonium salts.

S.No	Ferro and Piezoelectric Materials	Temperature (K)	Space Group
1	**TPAP·BF_4**	100	Monoclinic *Pn*
2	**DPDP·BF_4**	100 150	Monoclinic *Pn* Monoclinic *Cc*
3	**PTAP·BF_4**	100	Monoclinic $P2_1/n$
4	**TIAP·BF_4**	100	Tetragonal I-42m
5	**TPAP·ClO_4**	150 200	Monoclinic *Pc* Monoclinic *Pn*
6	**DPDP·ClO_4**	100 296	Monoclinic *Pn* Monoclinic *Cc*
7	**PTAP·ClO_4**	100	Monoclinic $P2_1$
8	**TIAP·ClO_4**	100	Tetragonal I-42m
9	**TPAP·IO_4**	100	Monoclinic $P2_1/c$
10	**DPDP·IO_4**	100	Monoclinic *Cc*
11	**PTAP·IO_4**	100	Monoclinic $P2_1/n$
12	**TIAP·IO_4**	100	Monoclinic $P2_1/n$

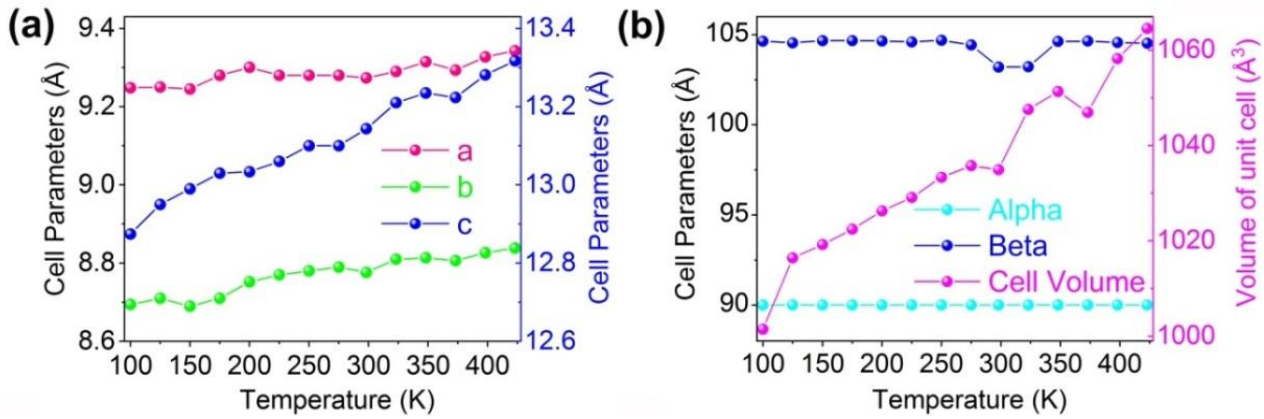

Figure 4A.15: Variable temperature unit-cell parameters of TPAP·BF_4.

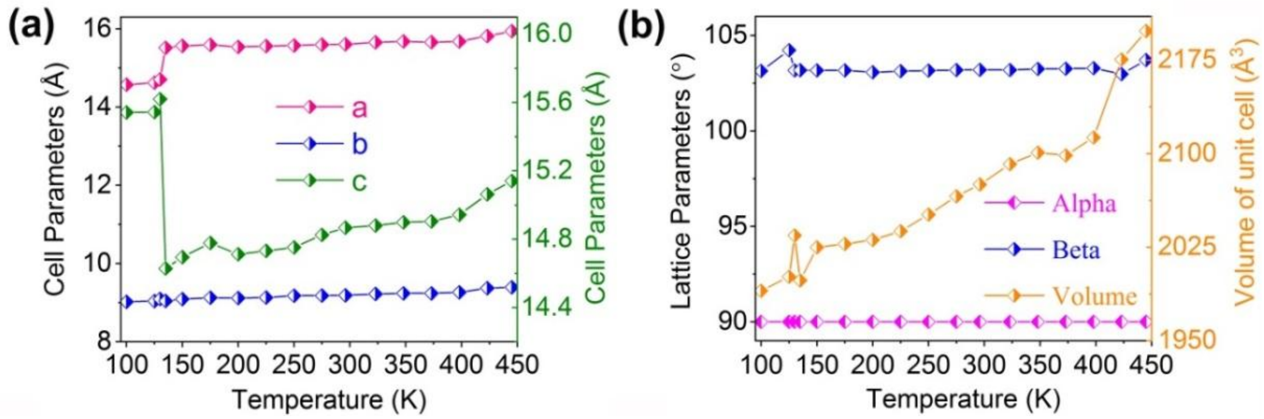

Figure 4A.16: Variable temperature unit-cell parameters of DPDP·BF_4.

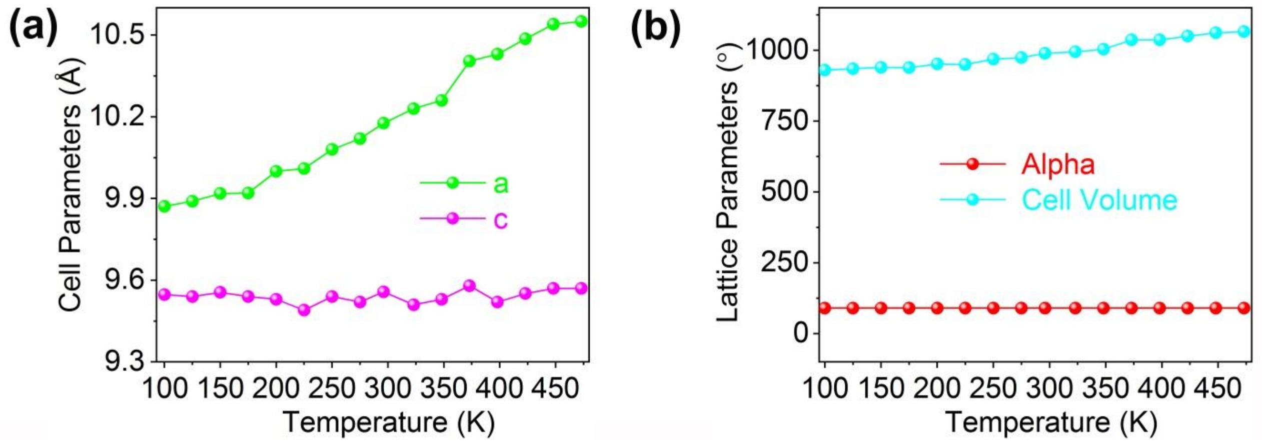

Figure 4A.17: Variable temperature unit-cell parameters of TIAP·BF_4.

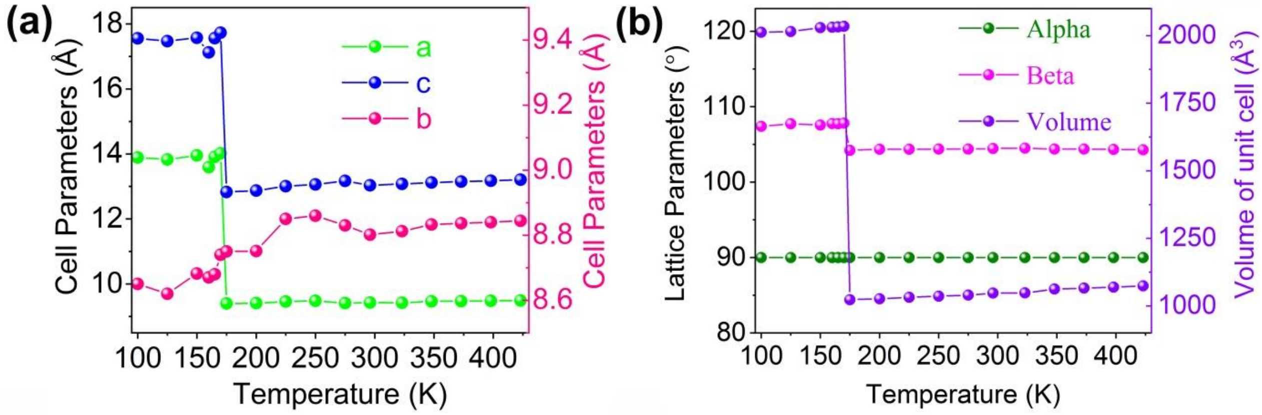

Figure 4A.18: Variable temperature unit-cell parameters of TPAP·ClO$_4$.

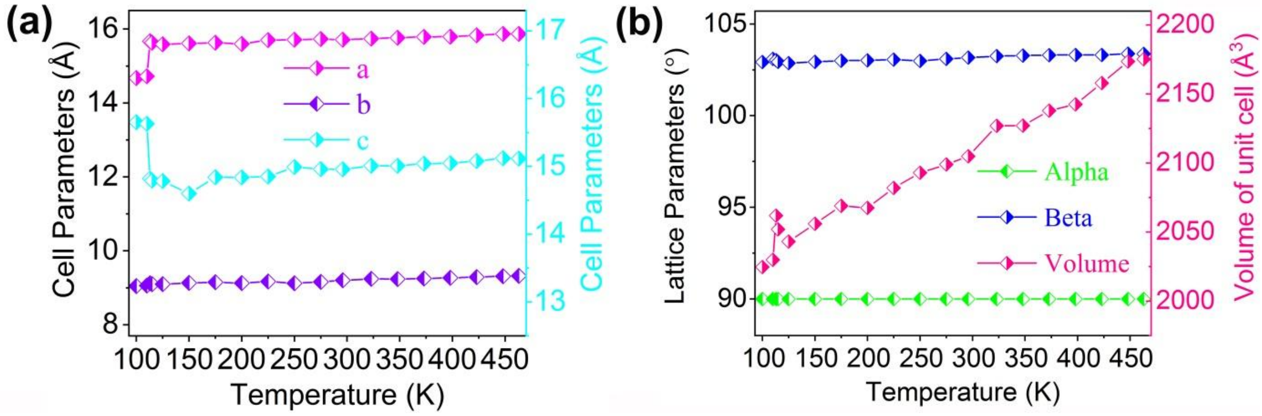

Figure 4A.19: Variable temperature unit-cell parameters of DPDP·ClO$_4$.

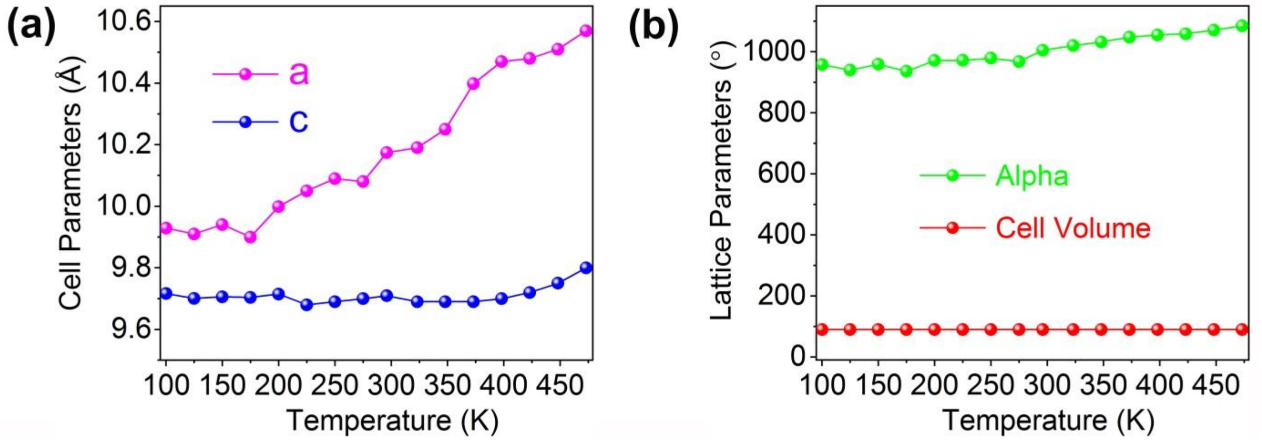

Figure 4A.20: Variable temperature unit-cell parameters of TIAP·ClO$_4$.

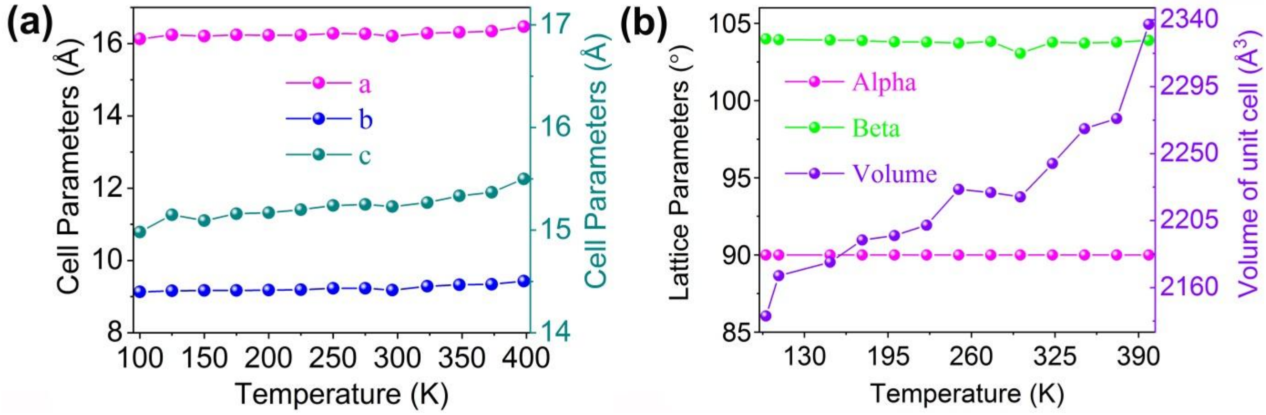

Figure 4A.21: Variable temperature unit-cell parameters of DPDP·IO_4.

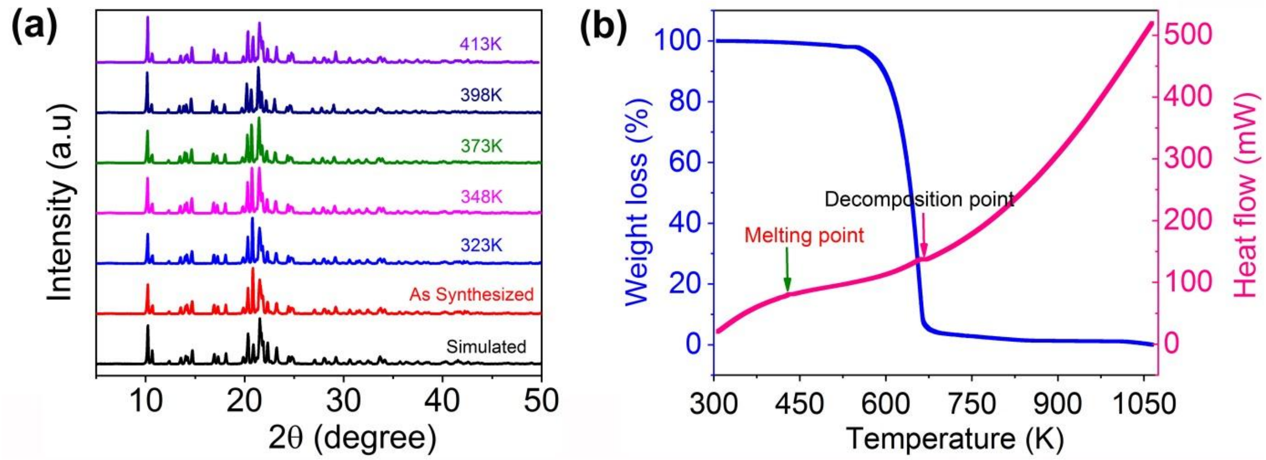

Figure 4A.22: VT-PXRD, TG/DTA analysis of TPAP·BF_4.

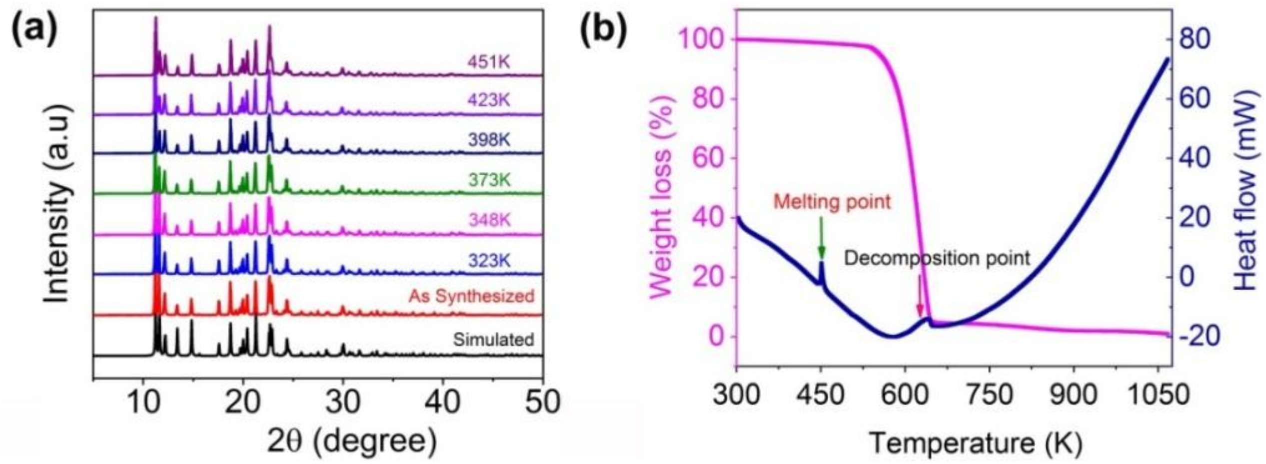

Figure 4A.23: VT-PXRD, TG/DTA analysis of DPDP·BF_4.

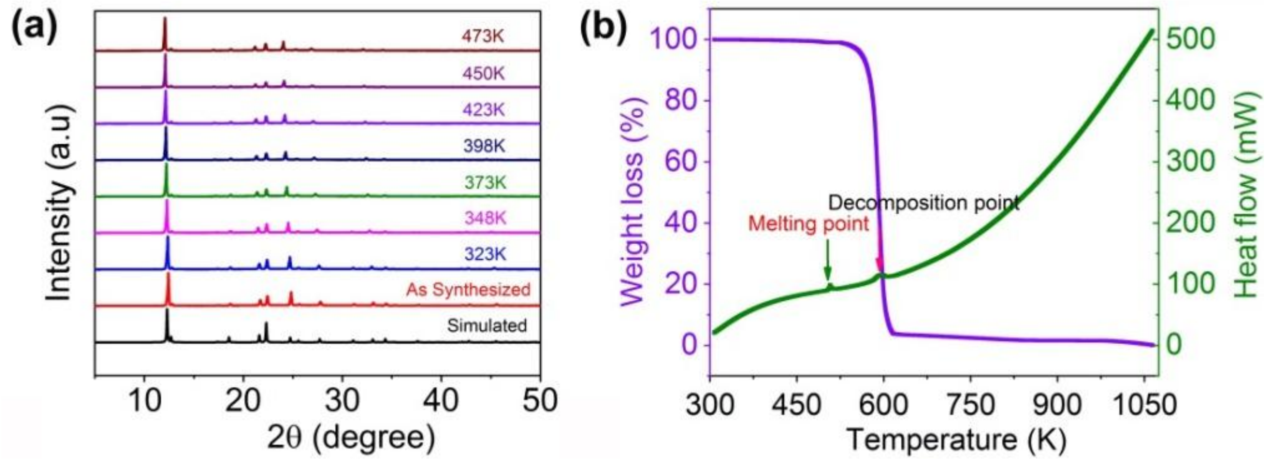

Figure 4A.24: VT-PXRD, TG/DTA analysis of TIAP·BF_4.

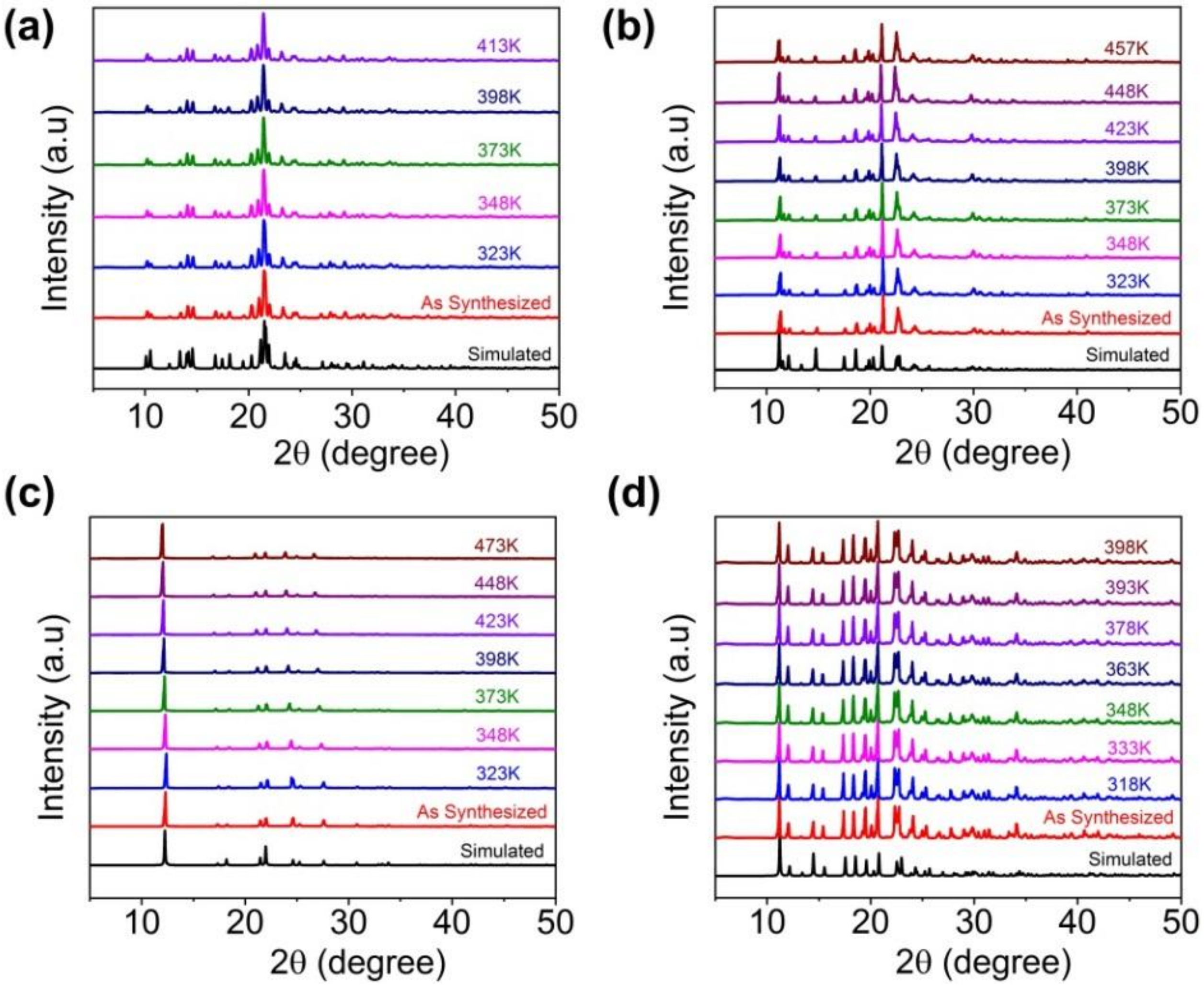

Figure 4A.25: VT-PXRD pattern of (a) TPAP·ClO_4, (b) DPDP·ClO_4, (c) TIAP·ClO_4 and (d) DPDP·IO_4

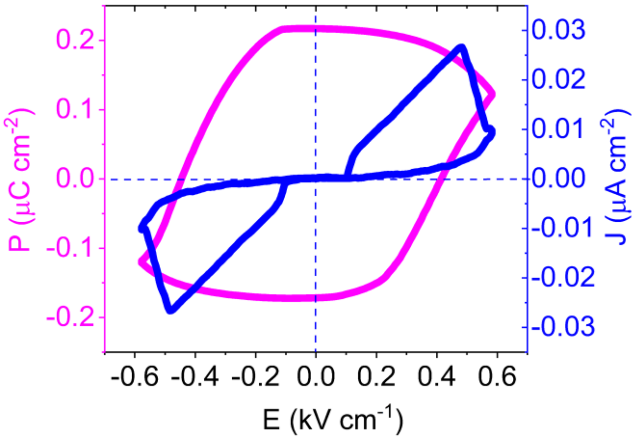

Figure 4A.26: The *P-E* hysteresis loop and leakage current density plots of TPAP·BF_4.

Table 4A.2. Dipole moment calculation of all the ferroelectric phosphonium salts.

S.No	Ferroelectric Materials	Dipole Moment (Debye)
1	**TPAP·BF_4**	18.5745
2	**DPDP·BF_4**	23.4453
3	**DPDP·ClO_4**	22.6718
4	**DPDP·IO_4**	21.9416

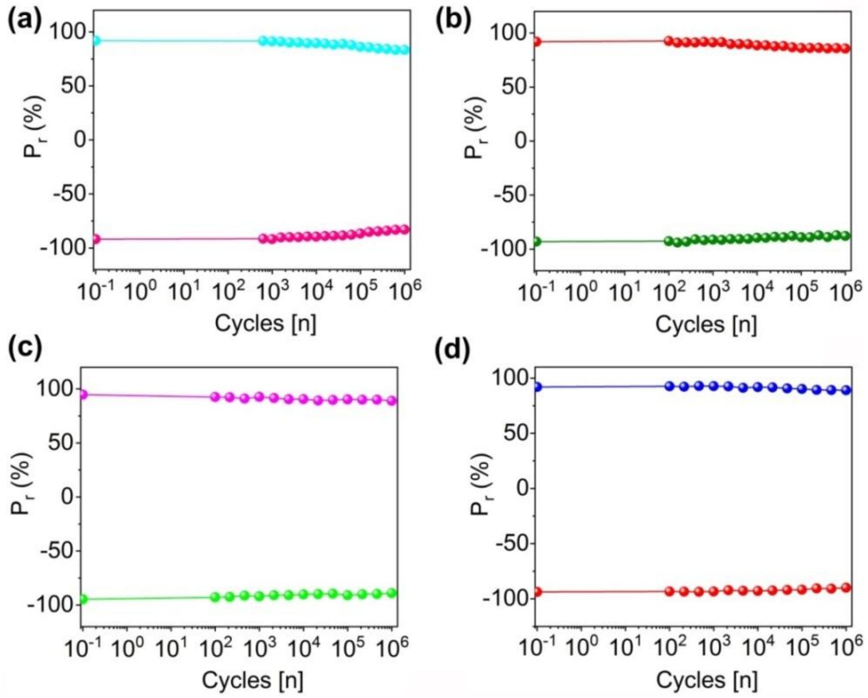

Figure 4A.27: Ferroelectric fatigue data for (a) TPAP·BF_4, (b) DPDP·BF_4, (c) DPDP·ClO_4 and (d) DPDP·IO_4.

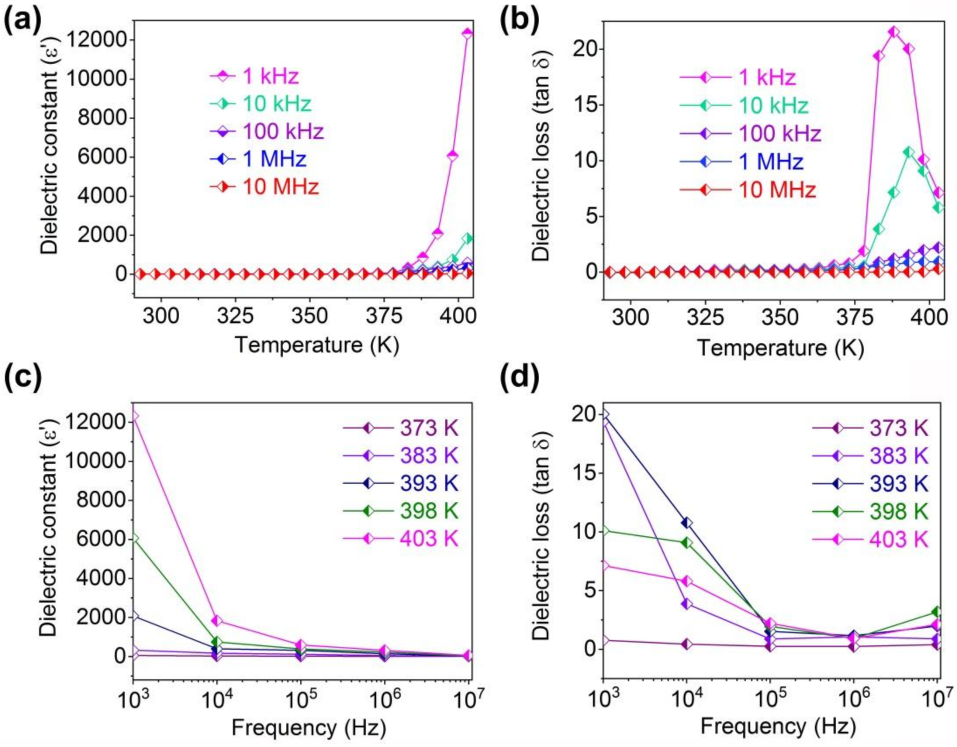

Figure 4A.28: (a and b) temperature and (c and d) frequency dependent dielectric constant (ε') and dielectric loss (tanδ) of TPAP·BF_4.

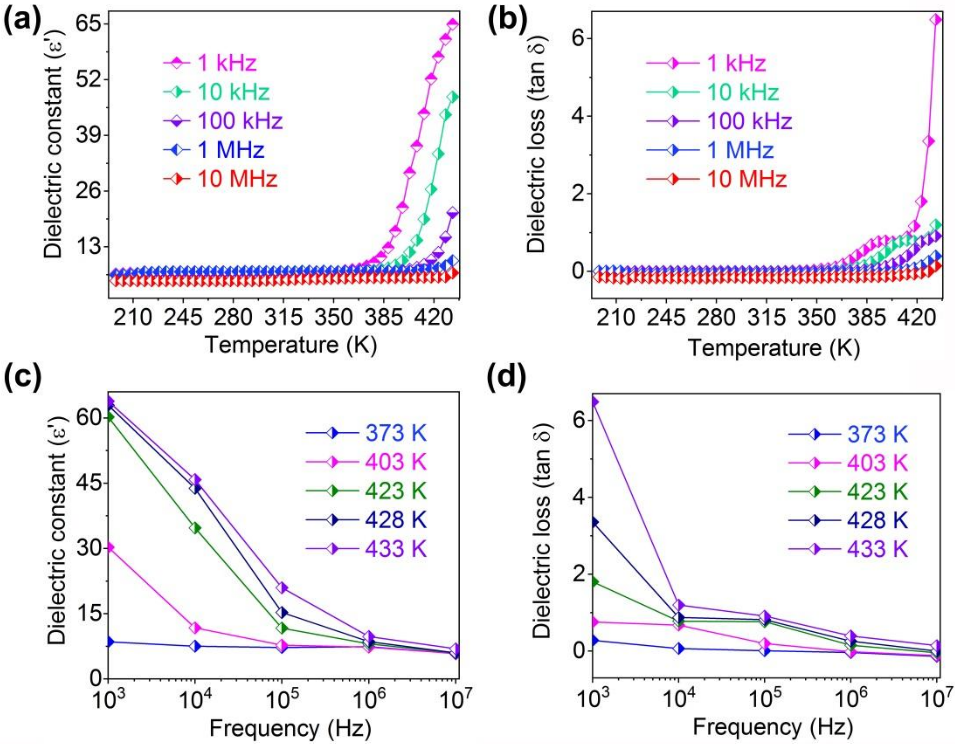

Figure 4A.29: (a and b) temperature and (c and d) frequency dependent ε' and tan δ of DPDP·BF_4.

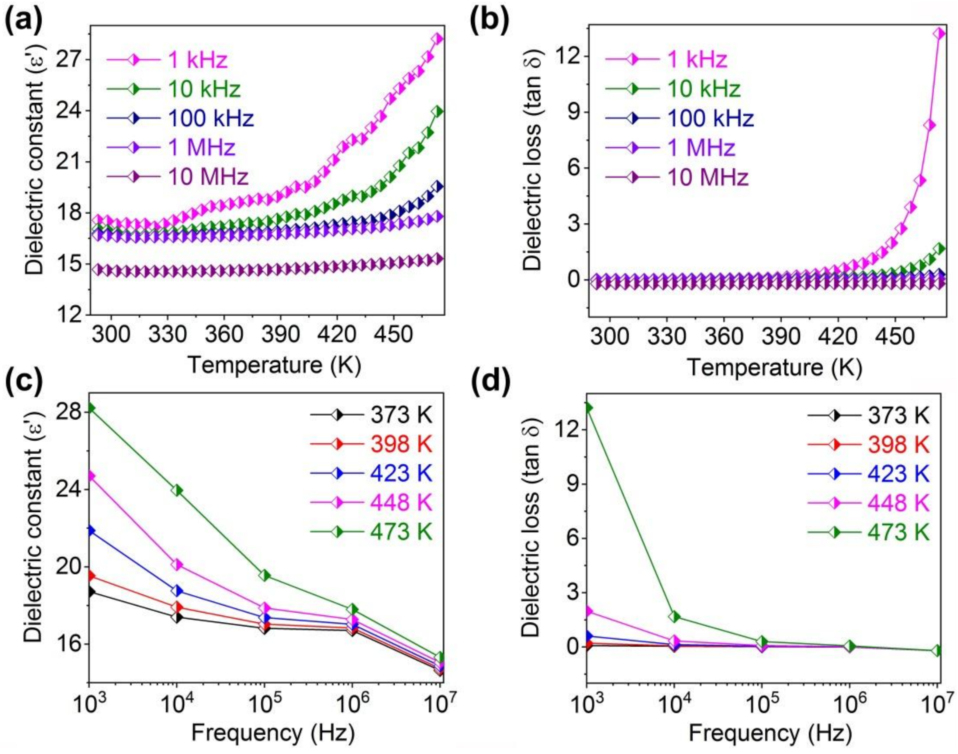

Figure 4A.30: (a and b) temperature and (c and d) frequency dependent ε' and tan δ of TIAP·BF_4.

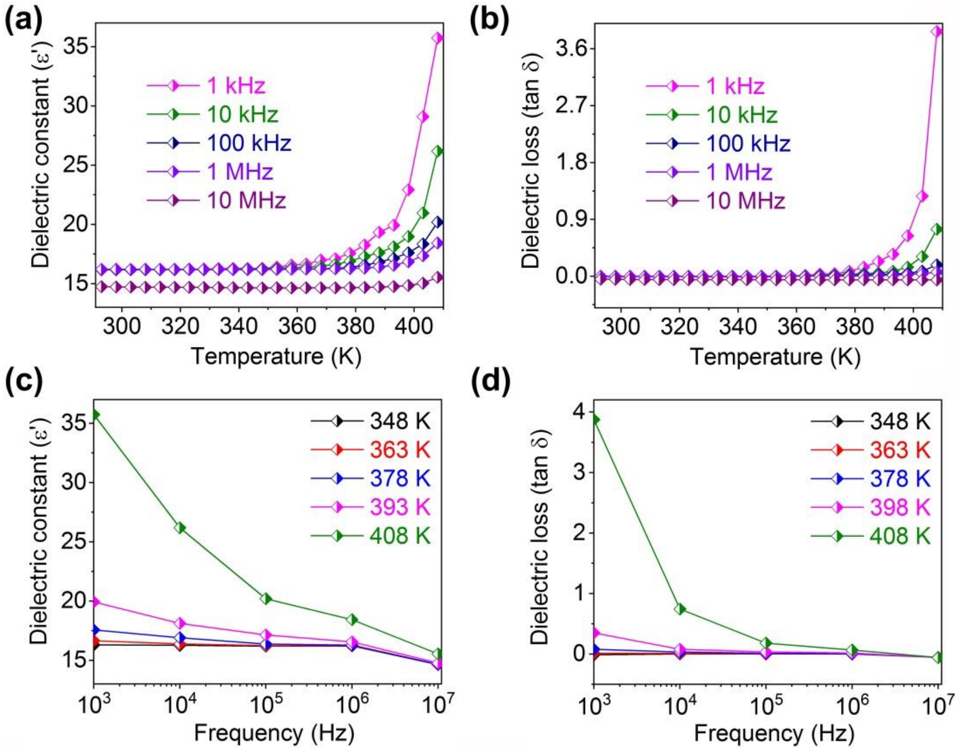

Figure 4A.31: (a and b) temperature and (c and d) frequency dependent ε' and tan δ of TPAP·ClO_4.

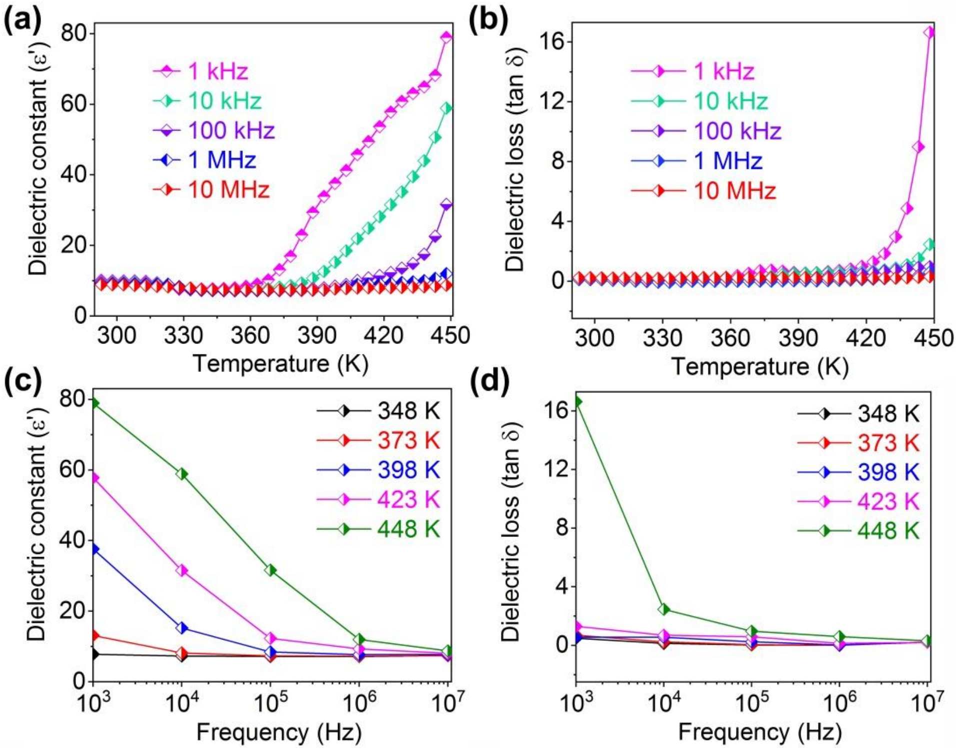

Figure 4A.32: (a and b) temperature and (c and d) frequency dependent ε' and tan δ of DPDP·ClO_4.

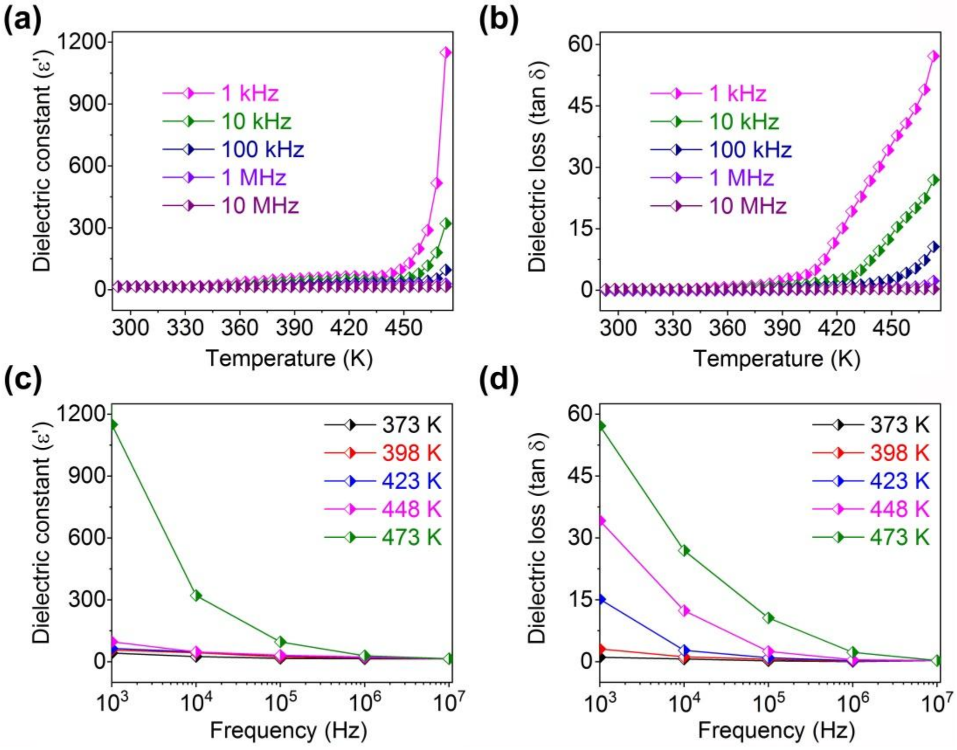

Figure 4A.33: (a and b) temperature and (c and d) frequency dependent ε' and tan δ of TIAP·ClO_4.

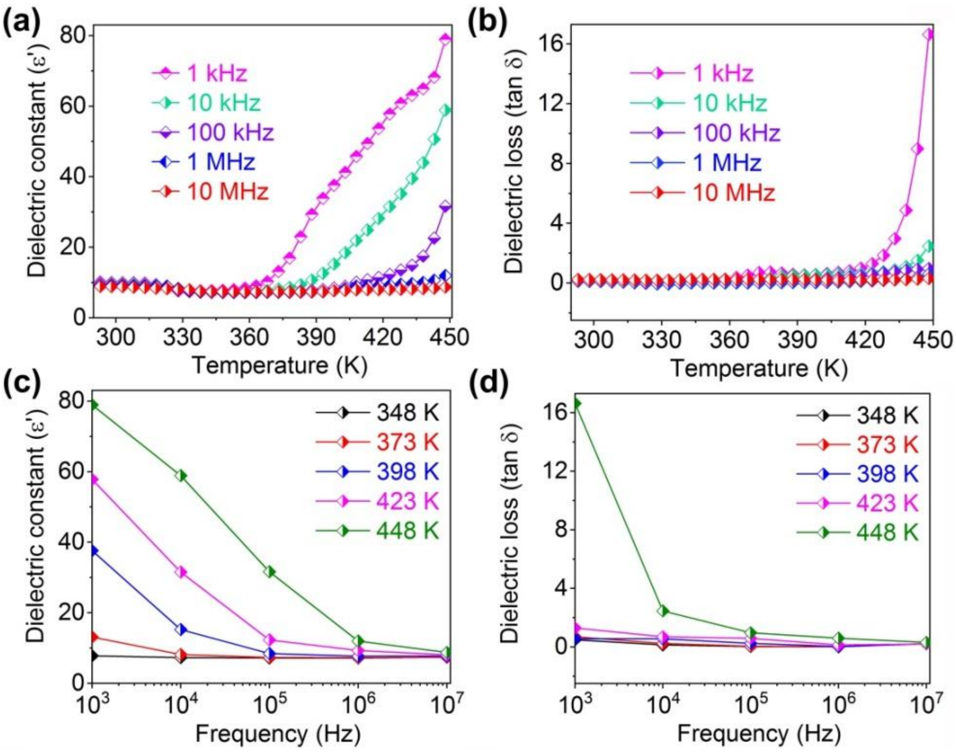

Figure 4A.34: (a and b) temperature and (c and d) frequency dependent ε' and tan δ of DPDP·IO_4.

Table 4A.3. Details about the preparation of various weight percentage (wt %) composites of the organo-amino phosphonium salts.

Organic polymer composites	Composite (wt %)	Salt amount (in mg)	TPU + Organic salts (in mg)
TPAP·BF_4/TPU	5 10 15 20	53 112 177 250	1053 1112 1177 1250
DPDP·BF_4/TPU	5 10 15 20	53 112 177 250	1053 1112 1177 1250
TIAP·BF_4/TPU	5 10 15 20	53 112 177 250	1053 1112 1177 1250
DPDP·PF_6/TPU	5 10 15 20	53 112 177 250	1053 1112 1177 1250

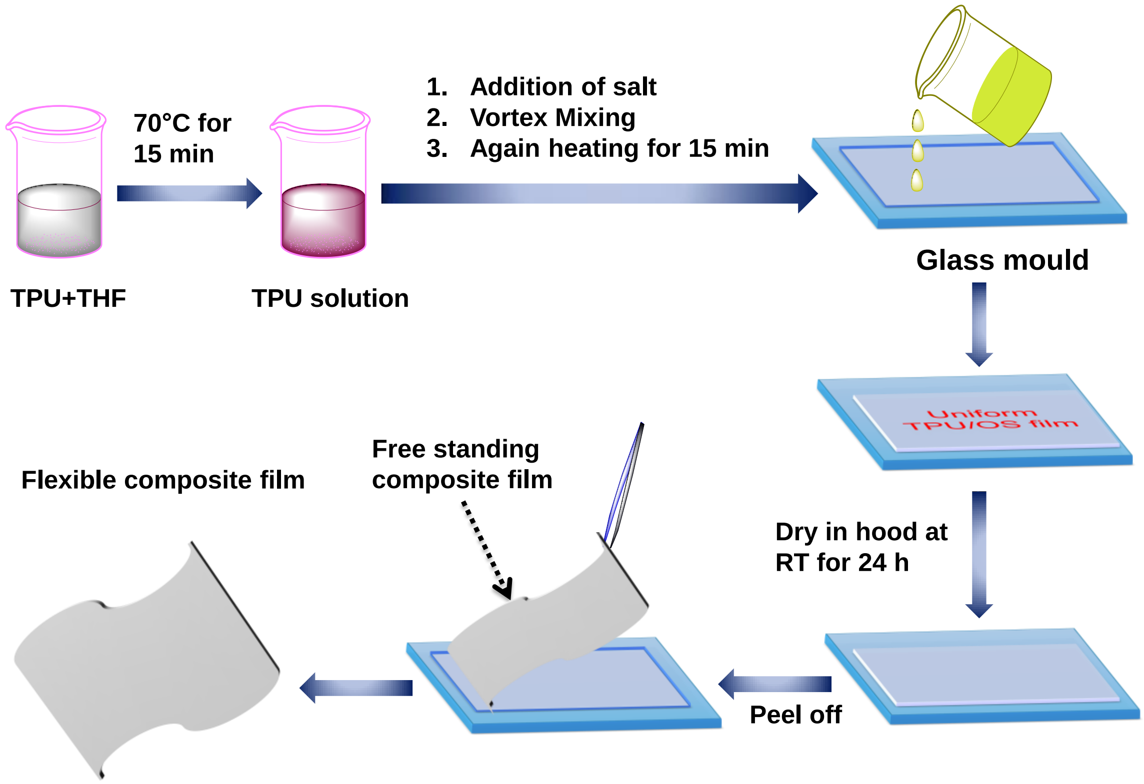

Scheme 4A.1. Detailed procedure involved for making various wt % (5, 10, 15 and 20) polymeric composite films.

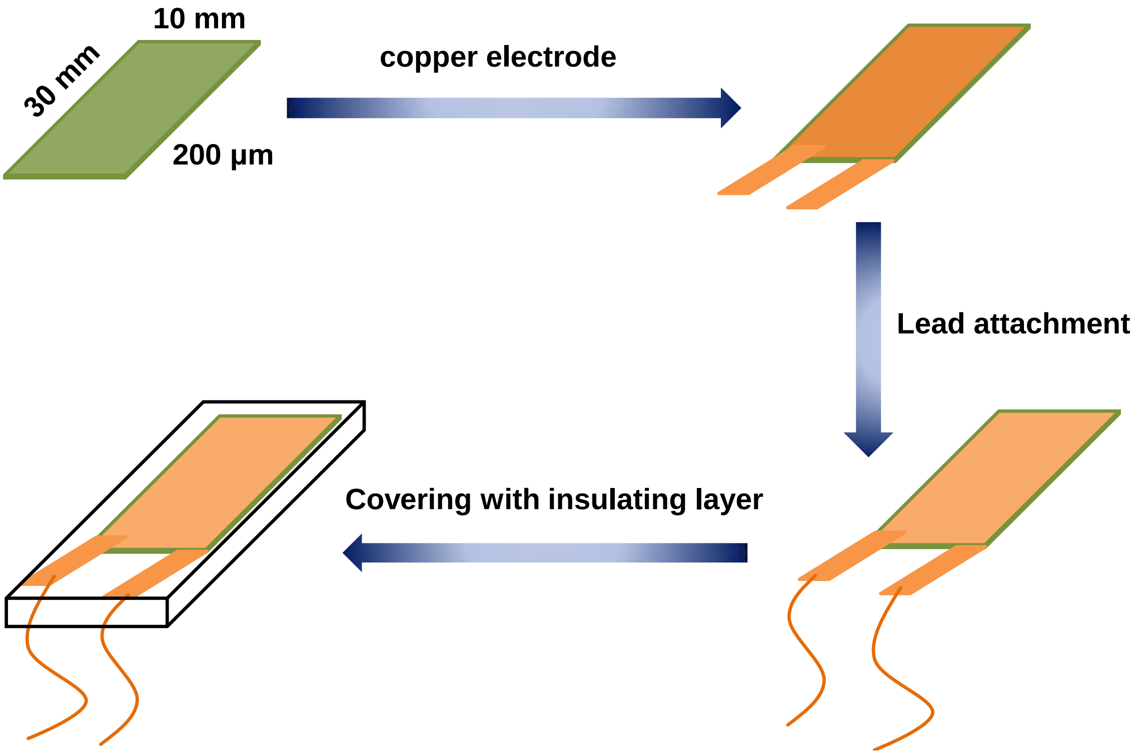

Scheme 4A.2. Device fabrication of all the wt % of (5, 10, 15 and 20) composite films.

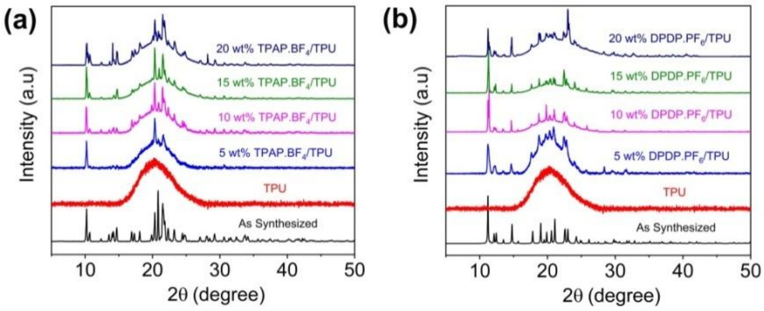

Figure 4A.35: PXRD analysis of all wt % composite films of TPAP.BF$_4$/TPU and DPDP.PF$_6$/TPU.

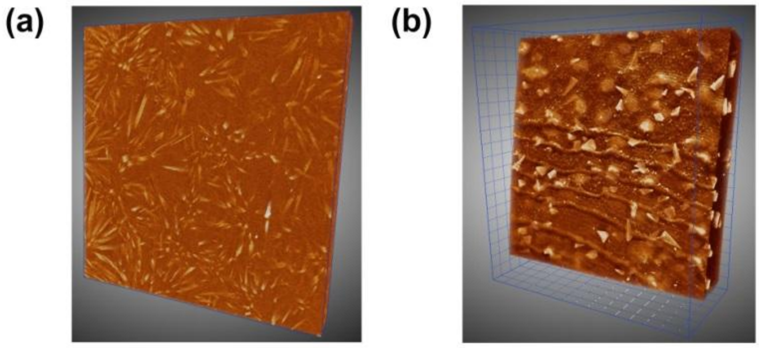

Figure 4A.36: X-ray 3D-tomography analysis of (a) TPAP·BF$_4$/TPU and (b) DPDP·PF$_6$/TPU. The tomography images depicted here is for the corresponding 10 wt % composite films (grid scale: 100 μm).

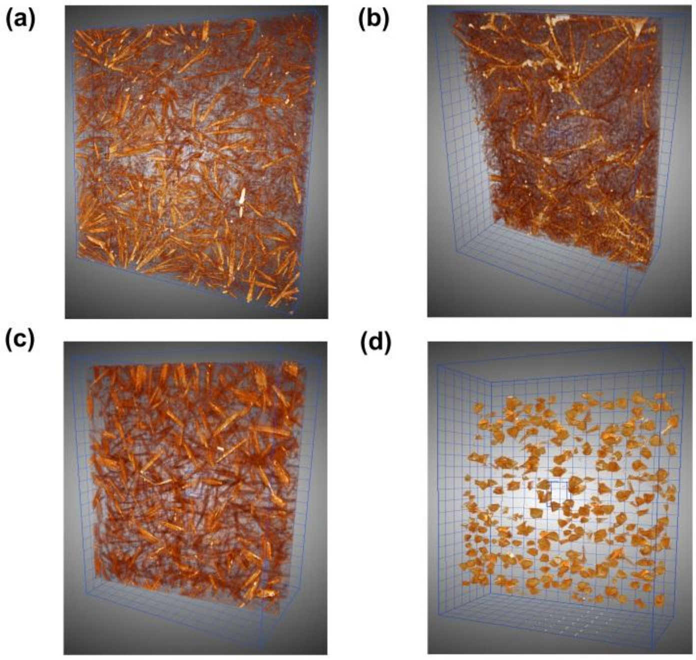

Figure 4A.37: 3D-tomography images of 10 wt % films of (a) TPAP·BF$_4$/TPU (b) DPDP·BF$_4$/TPU (c) TIAP·BF$_4$/TPU and (d) DPDP·PF$_6$/TPU. The polymer background has been corrected to clearly indicate the distribution of the crystallites.

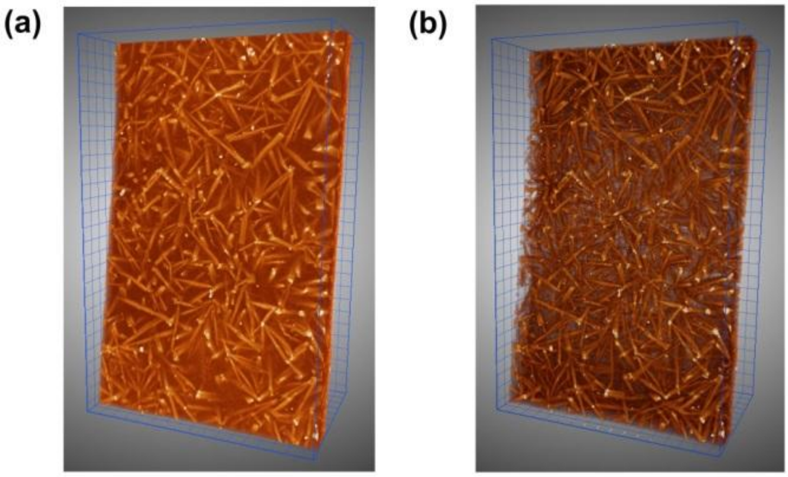

Figure 4A.38: (a) 3D-tomography images of 20 wt %TPAP·BF_4/TPU composite film and (b) image obtained after the polymer background correction.

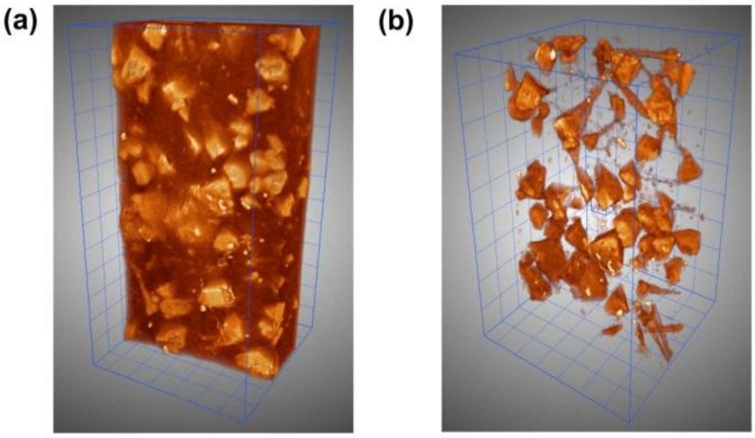

Figure 4A.39: 3D-tomography images of 20 wt % DPDP·BF_4/TPU composite film and (b) image obtained after the polymer background correction.

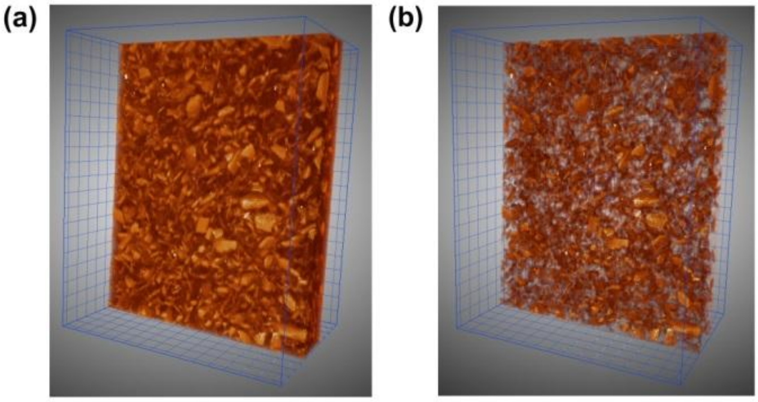

Figure 4A.40: 3D-tomography images of 20 wt % TIAP·BF_4/TPU composite film and (b) image obtained after the polymer background correction.

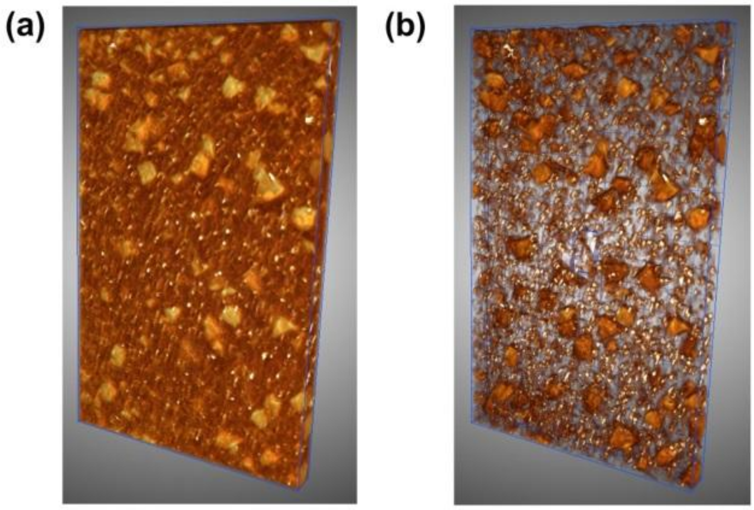

Figure 4A.41: 3D-tomography images of 20 wt % DPDP·PF_6/TPU composite films and (b) image obtained after the polymer background correction.

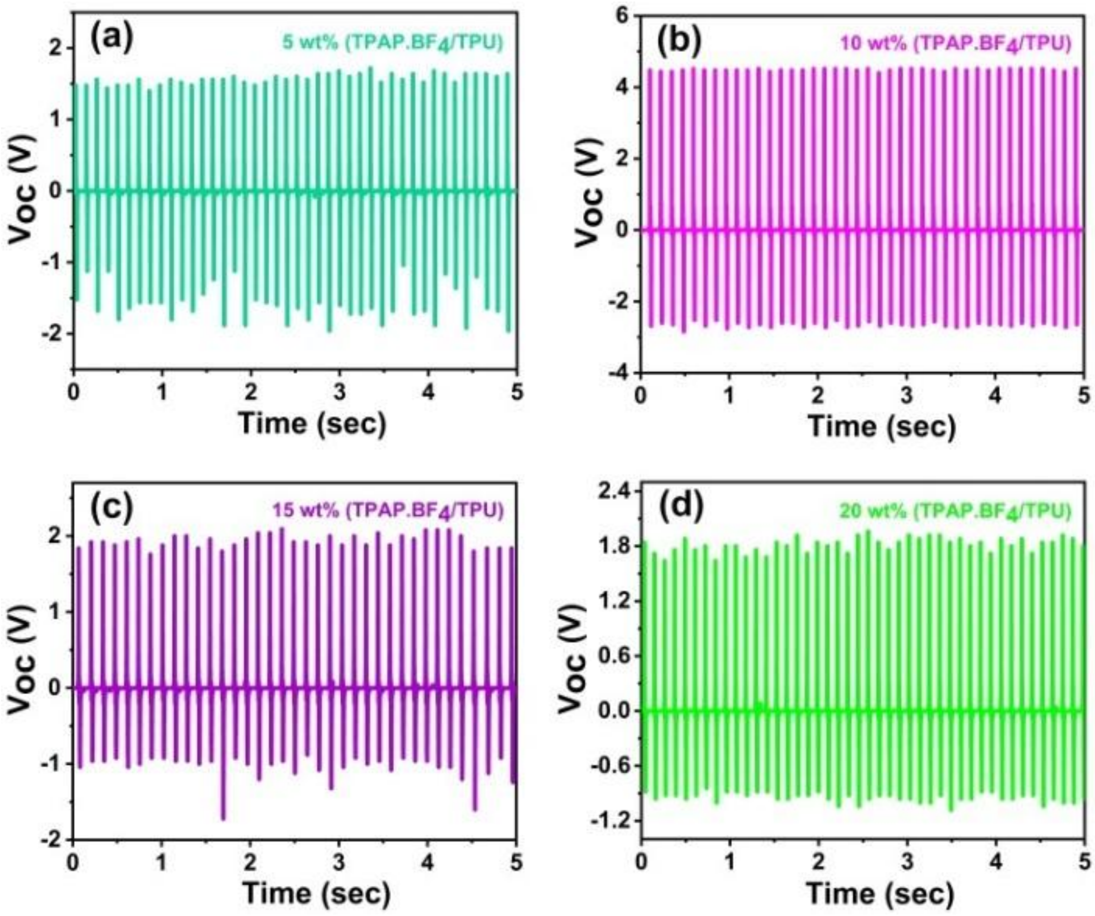

Figure 4A.42: Voltage output performance for TPAP·BF_4/TPU composites (5, 10, 15 and 20 wt %).

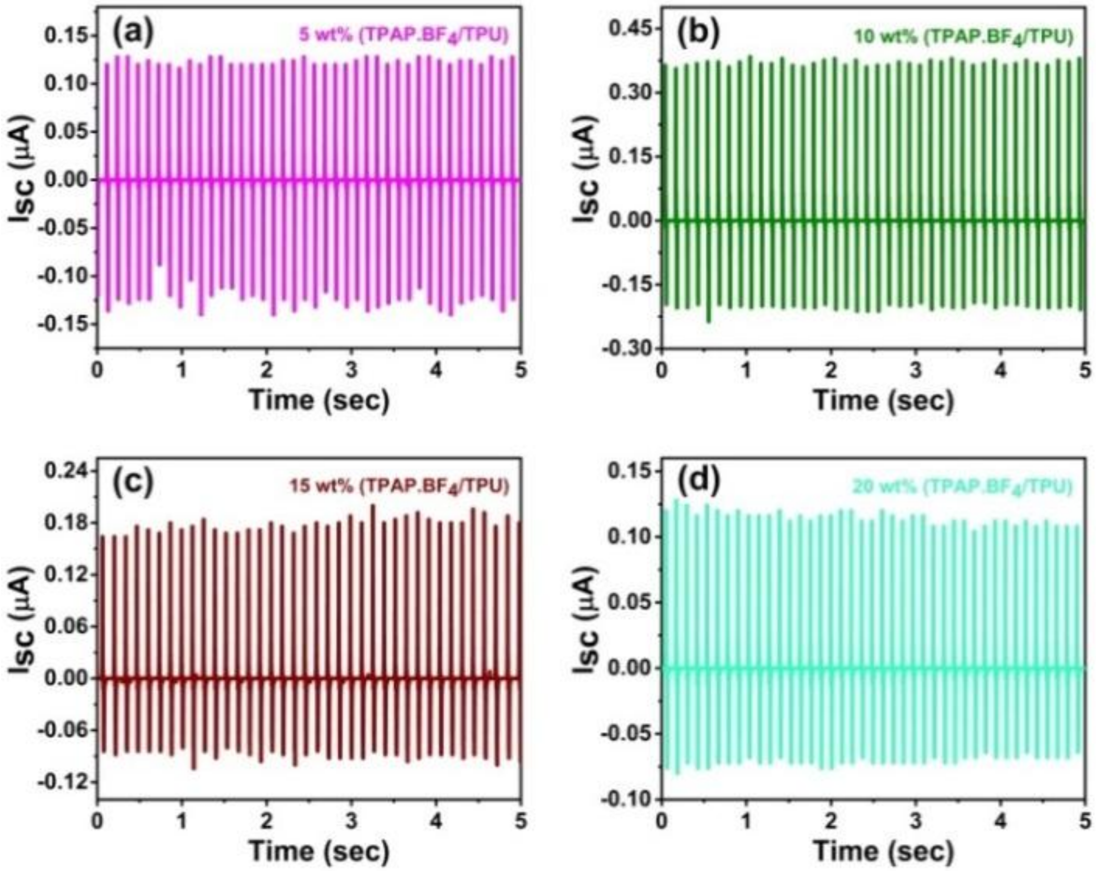

Figure 4A.43: Current output performance for TPAP·BF$_4$/TPU composites (5, 10, 15 and 20 wt %).

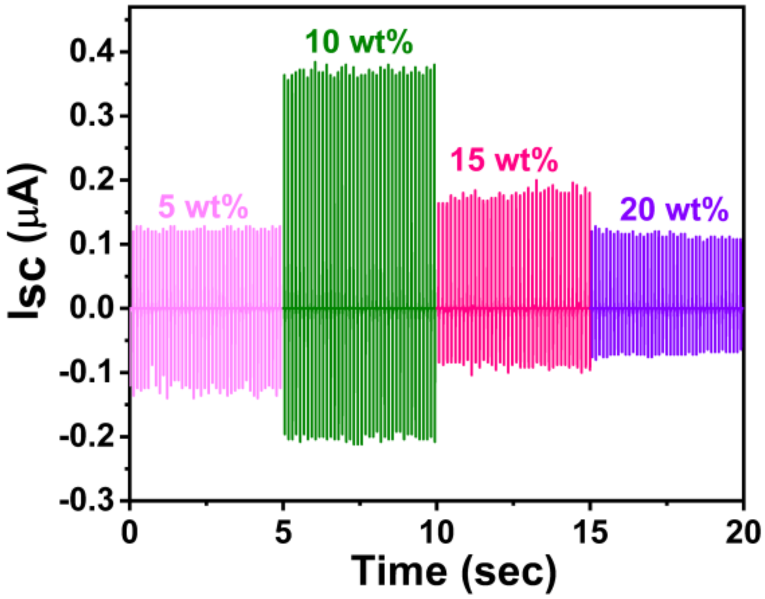

Figure 4A.44: Comparison of the output current performances for the TPAP·BF$_4$/TPU in all wt % composite films.

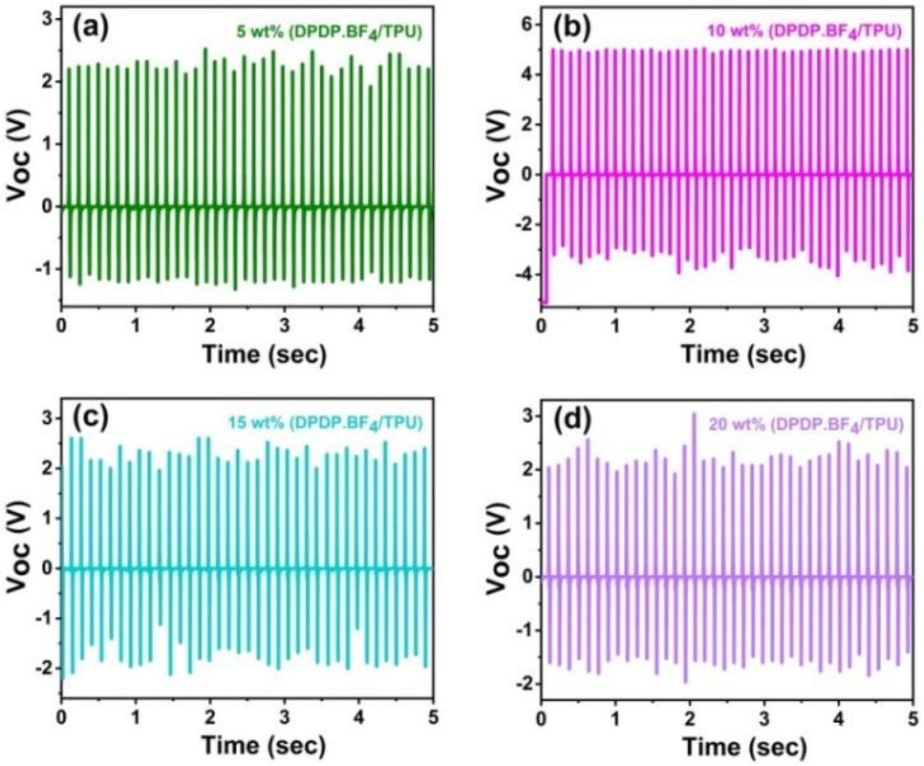

Figure 4A.45: Voltage output performance for DPDP·BF$_4$/TPU composites (5, 10, 15 and 20 wt %).

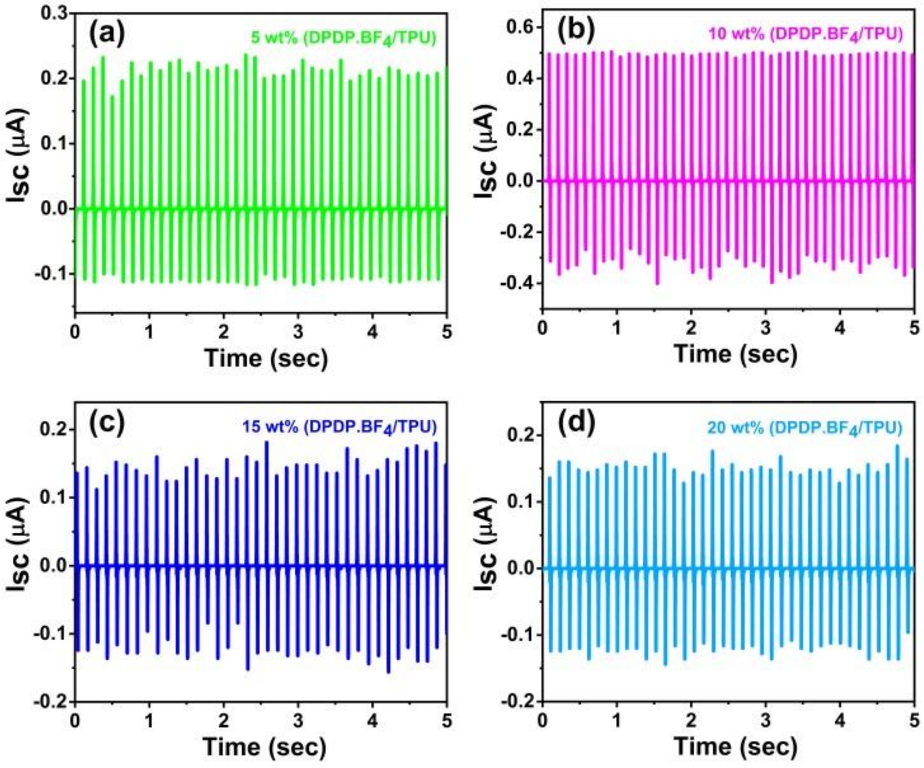

Figure 4A.46: Current output performance for DPDP·BF$_4$/TPU composites (5, 10, 15 and 20 wt %).

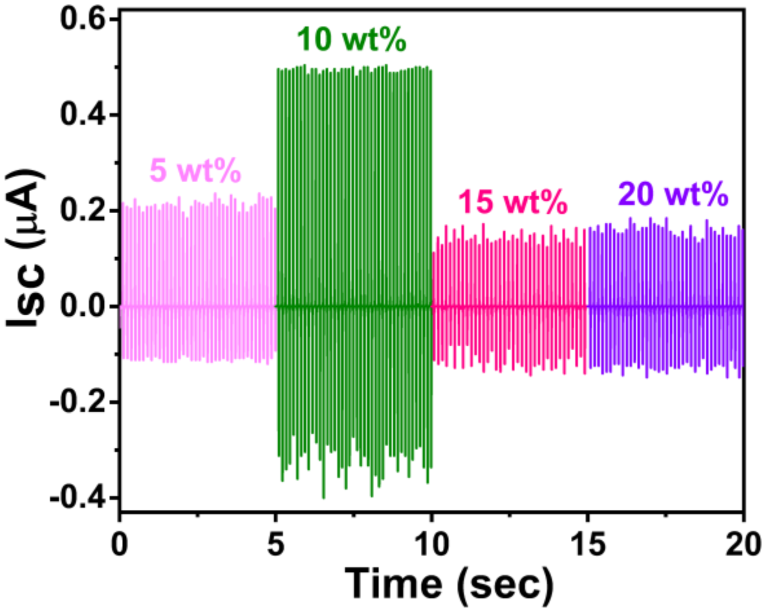

Figure 4A.47: Comparison of output current performance for DPDP·BF_4/TPU in all wt % composite films.

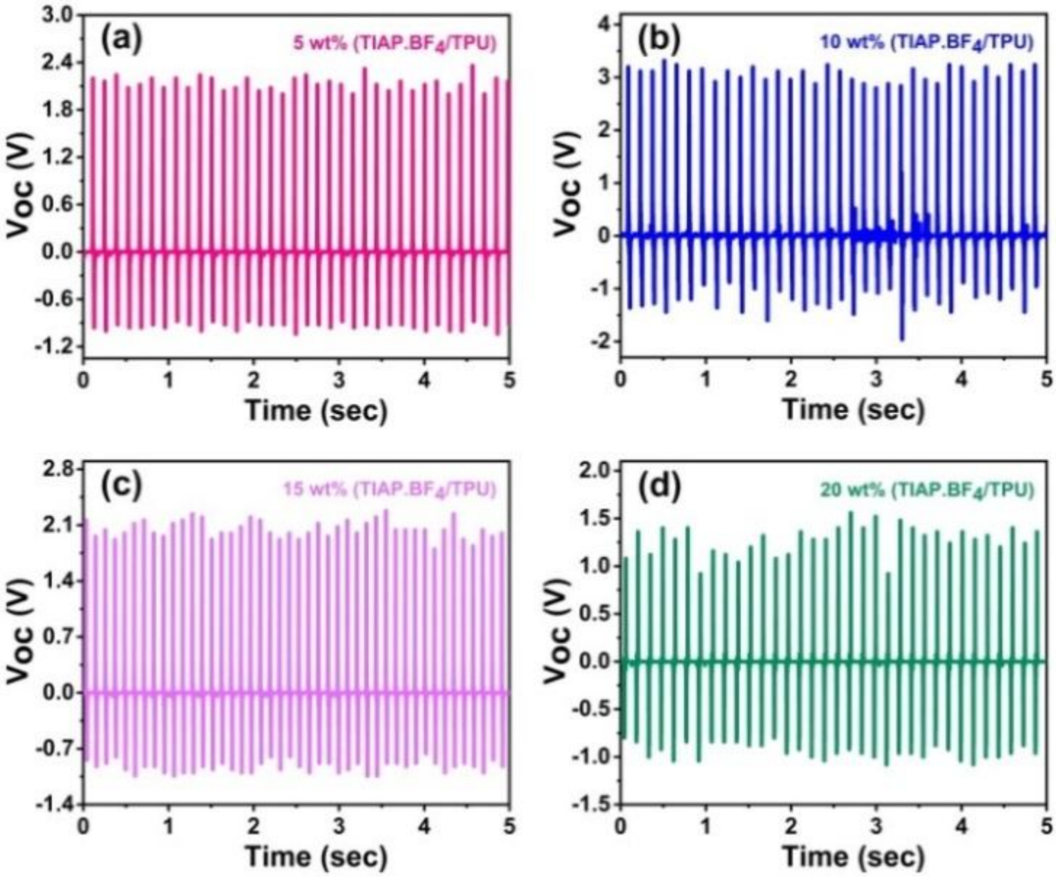

Figure 4A.48: Voltage output performance for TIAP·BF_4/TPU composite films in all wt % composite films.

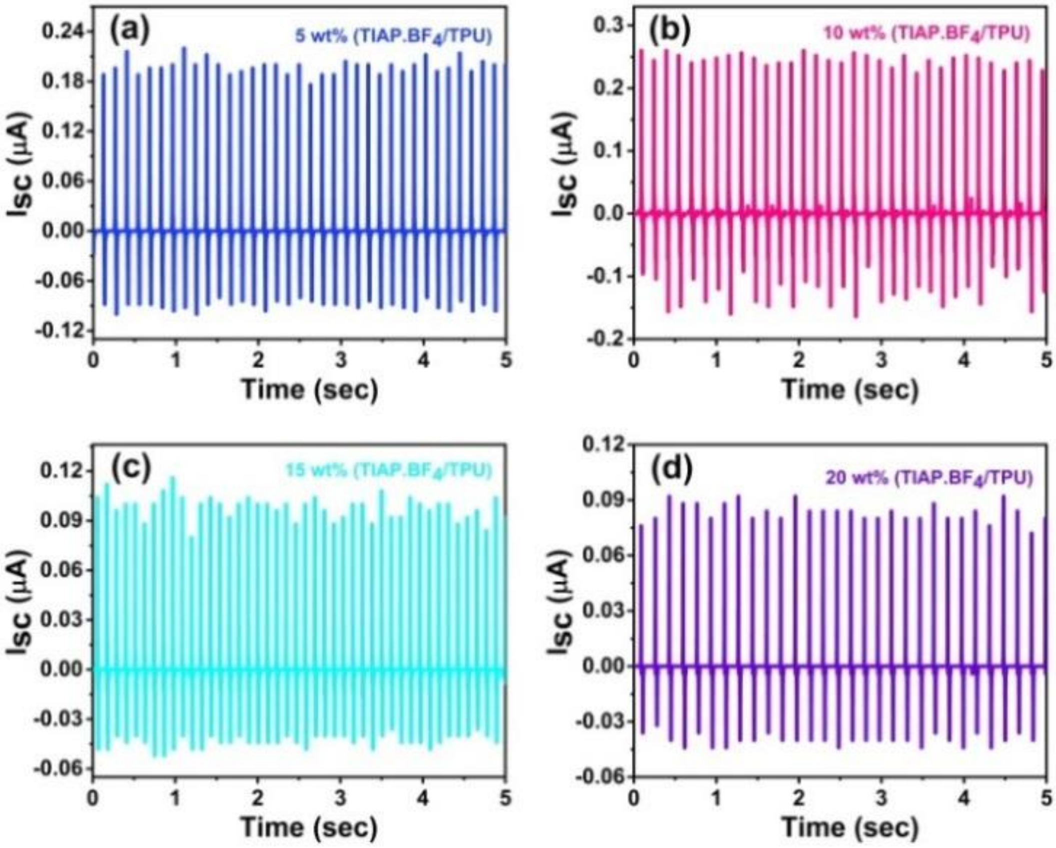

Figure 4A.49: Current output performance for TIAP·BF_4/TPU composite films in all wt% composite films.

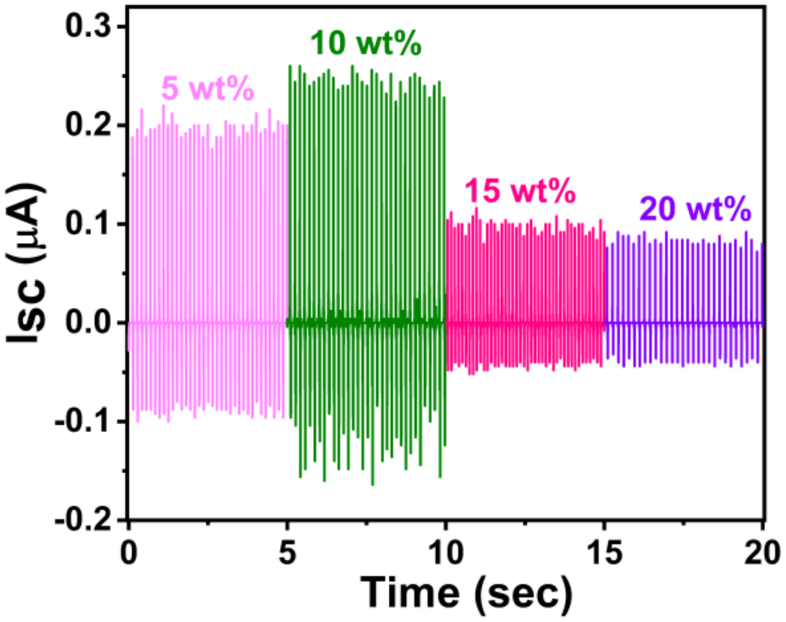

Figure 4A.50: Comparison of output current performance for TIAP·BF_4/TPU composite films in all wt % composite films.

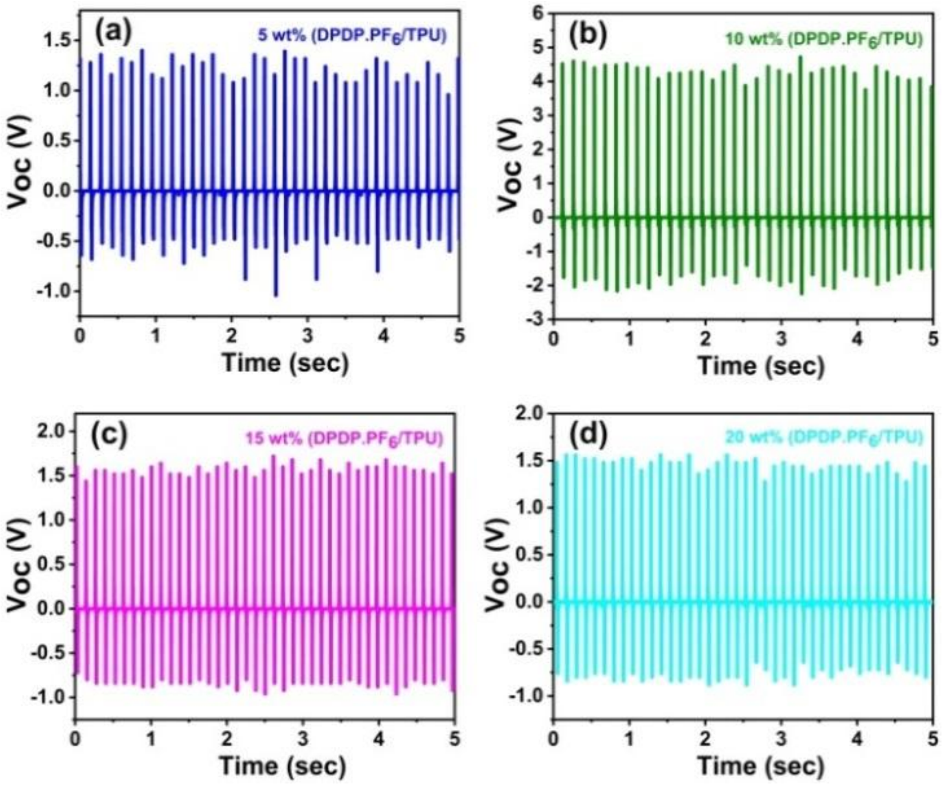

Figure 4A.51: Voltage output performance for DPDP·PF_6/TPU composite films in all wt % composite films.

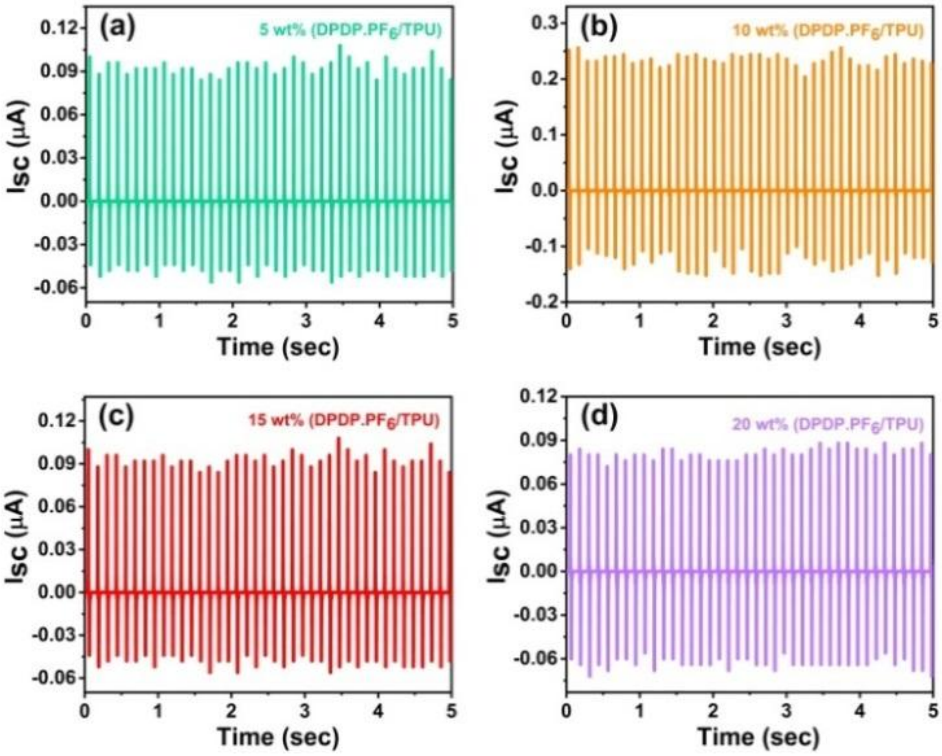

Figure 4A.52: Current output performance for DPDP·PF_6/TPU composite films in all wt % composite films.

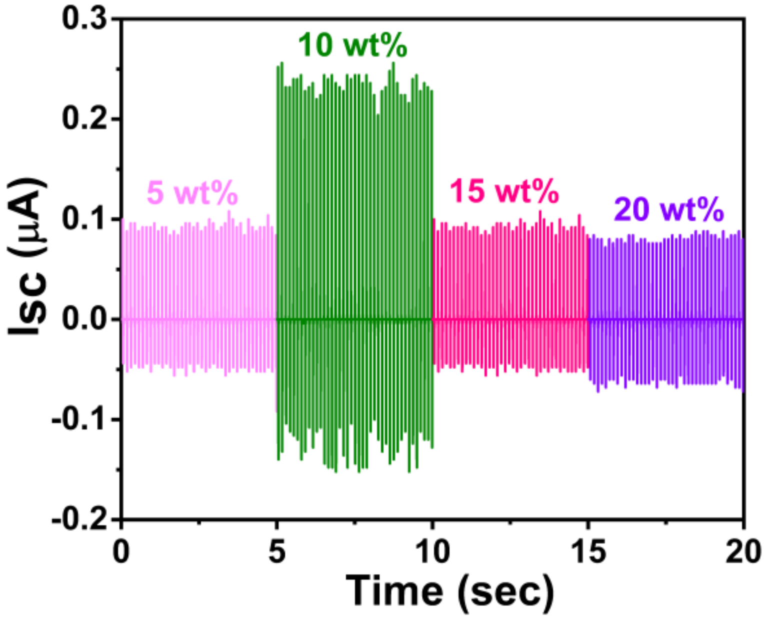

Figure 4A.53: Comparison of output current performance for DPDP·PF_6/TPU composite films in all wt % composite films.

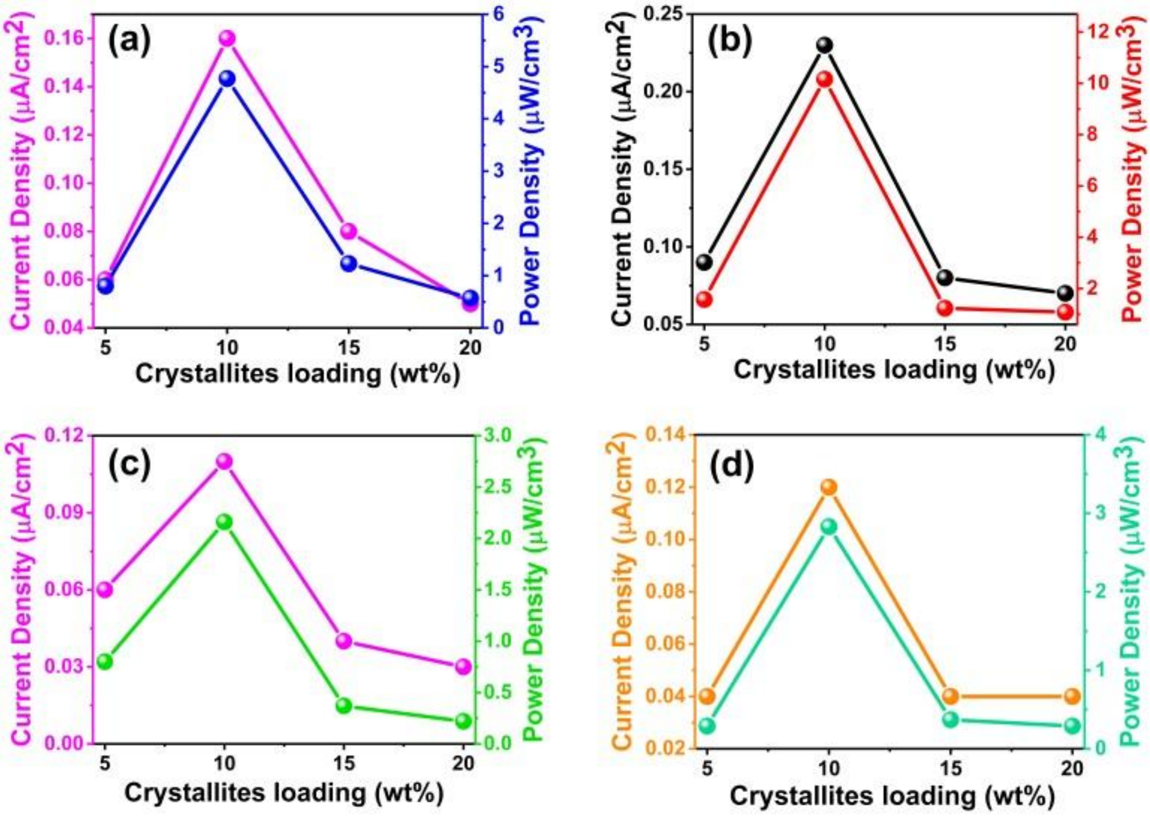

Figure 4A.54: The output current and power density plots for the (a) TPAP·BF_4/TPU, (b) DPDP·BF_4/TPU, (c) TIAP·BF_4/TPU and (d) DPDP·PF_6/TPU devices.

Table 4A.4. Table of device output performance of all the wt % of composites films.

Organic composites	Composites (wt %)	Output voltage (*VPP*)	Output current (*IPP*)	Power density (μW/cm^3)	Current density (μA/cm^2)
TPAP·BF$_4$/TPU	5	3.34	0.25	0.80	0.06
	10	7.37	0.61	4.77	0.16
	15	3.71	0.31	1.23	0.08
	20	2.98	0.21	0.57	0.05
DPDP·BF$_4$/TPU	5	3.64	0.35	1.57	0.09
	10	8.95	0.89	10.16	0.23
	15	4.55	0.31	1.23	0.08
	20	4.16	0.29	1.08	0.07
TIAP·BF$_4$/TPU	5	3.17	0.25	0.80	0.06
	10	4.75	0.41	2.16	0.11
	15	3.26	0.17	0.37	0.04
	20	2.41	0.13	0.22	0.03
DPDP·PF$_6$/TPU	5	2.15	0.15	0.29	0.04
	10	6.73	0.47	2.83	0.12
	15	2.57	0.17	0.37	0.04
	20	2.34	0.15	0.29	0.04

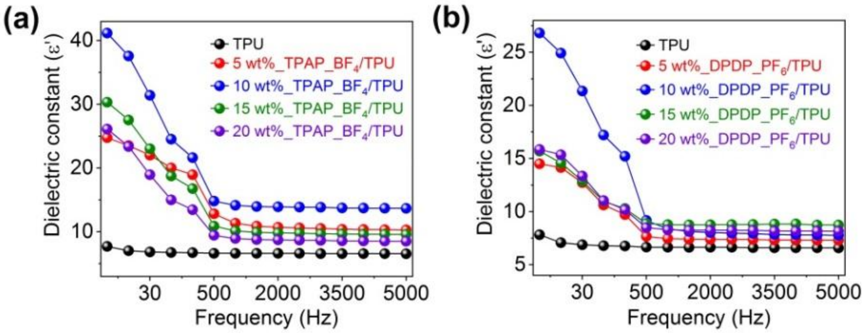

Figure 4A.55: Room temperature ε' data for the composite films of (a) TPAP·BF$_4$/TPU and (b) DPDP·PF$_6$/TPU at an operating electric field of 10 V.

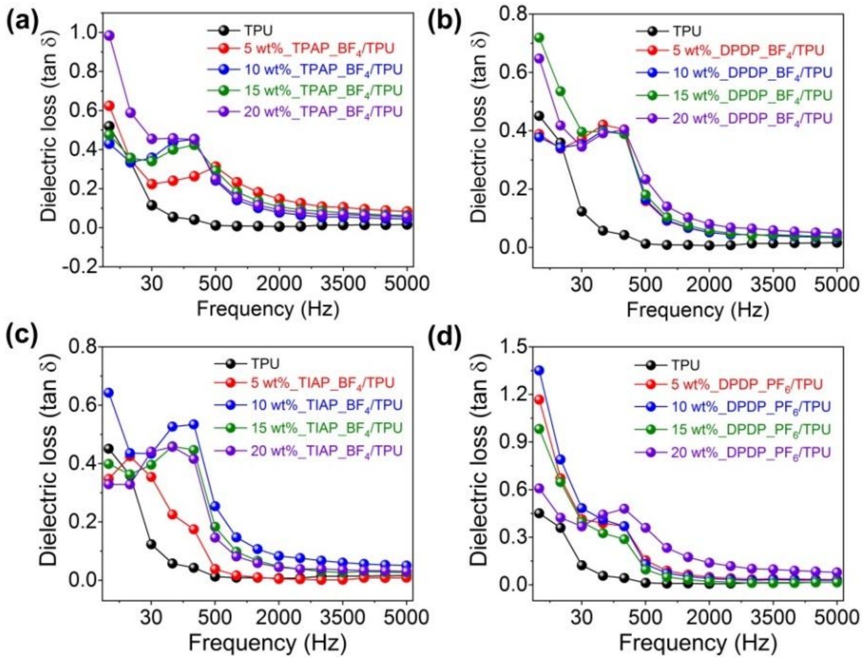

Figure 4A.56: Room temperature tan δ data for all the composite films.

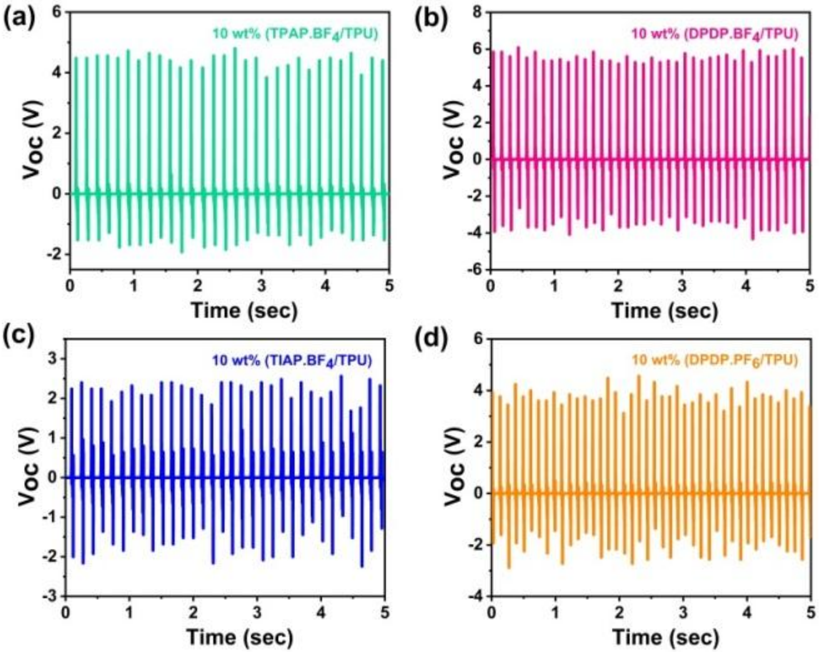

Figure 4A.57: Durability test (after 6 months) for composites (10 wt %) of (a) TPAP·BF$_4$/TPU, (b) DPDP·BF$_4$/TPU, (c) TIAP·BF$_4$/TPU and (d) DPDP·PF$_6$/TPU.

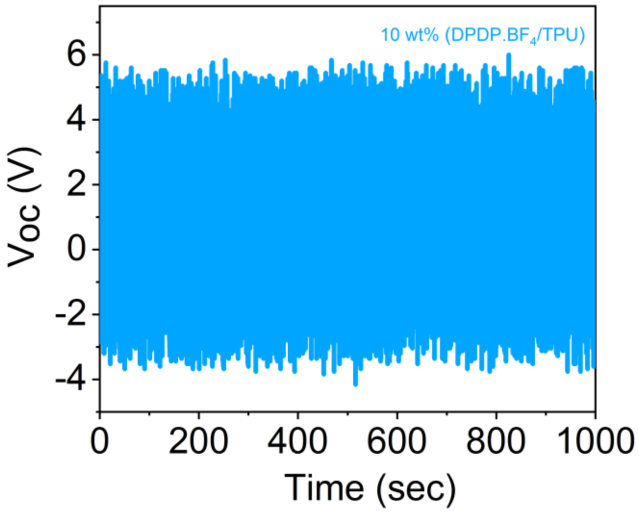

Figure 4A.58: Fatigue test for the 10 wt % DPDP·BF$_4$/TPU composites with a continuous applied frequency of 8 Hz, over a period of 8000 cycles.

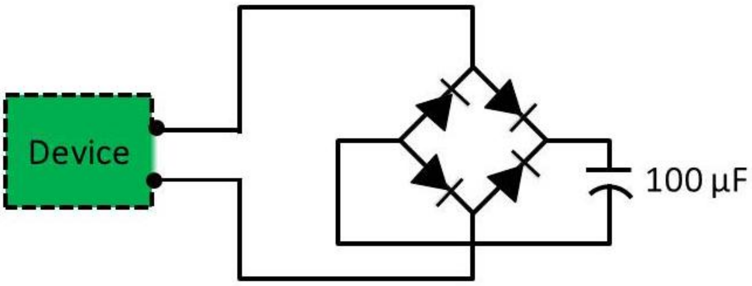

Figure 4A.59: Capacitor charging circuit of full wave-bridge rectifier.

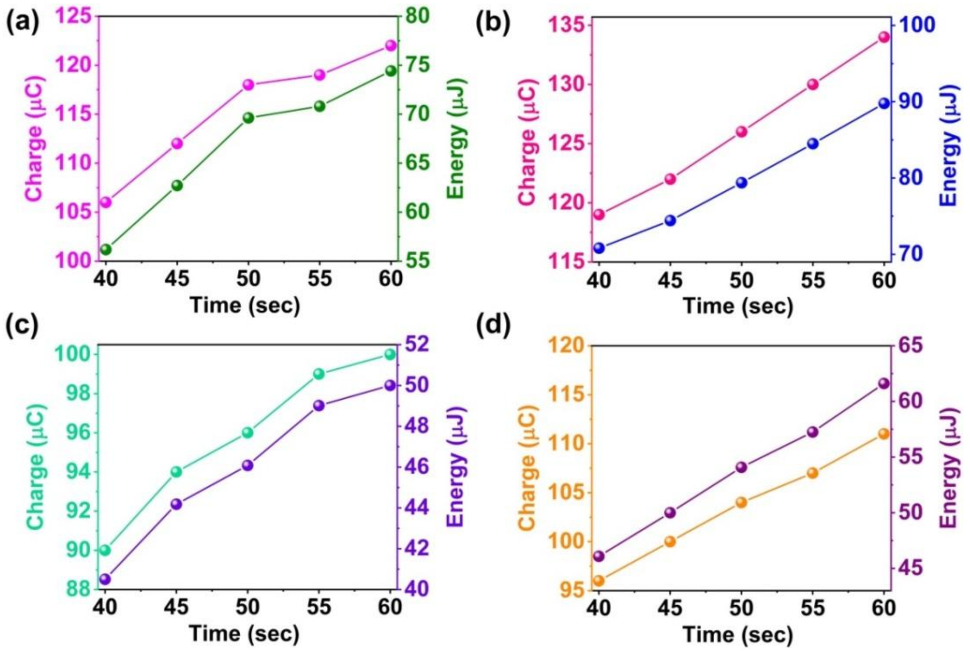

Figure 4A.60: The stored charges (Q) and energies (E) for the 10 wt % composite capacitors of (a) DPDP·BF_4/TPU, (b) TPAP·BF_4/TPU, (c) TIAP·BF_4/TPU and (d) DPDP·PF_6/TPU.

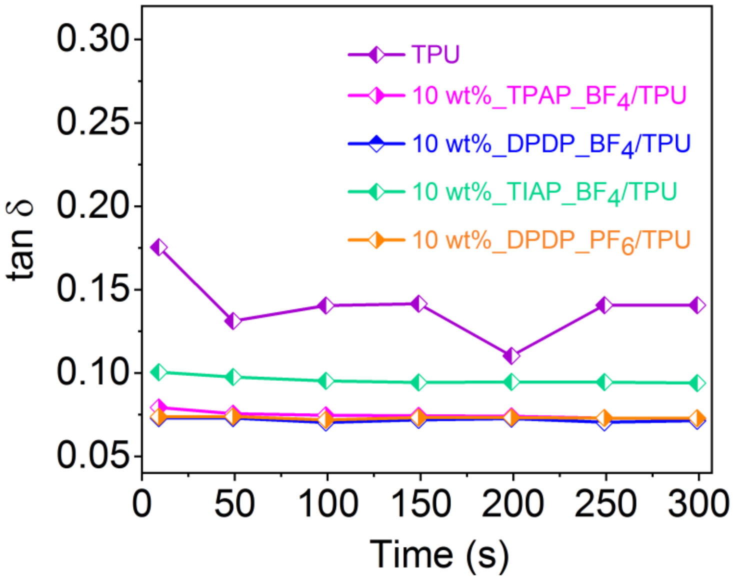

Figure 4A.61: The damping behavior of the neat TPU and 10 wt % composite films of TPAP·BF_4/TPU, DPDP·BF_4/TPU, TIAP·BF_4/TPU and DPDP·PF_6/TPU.

****

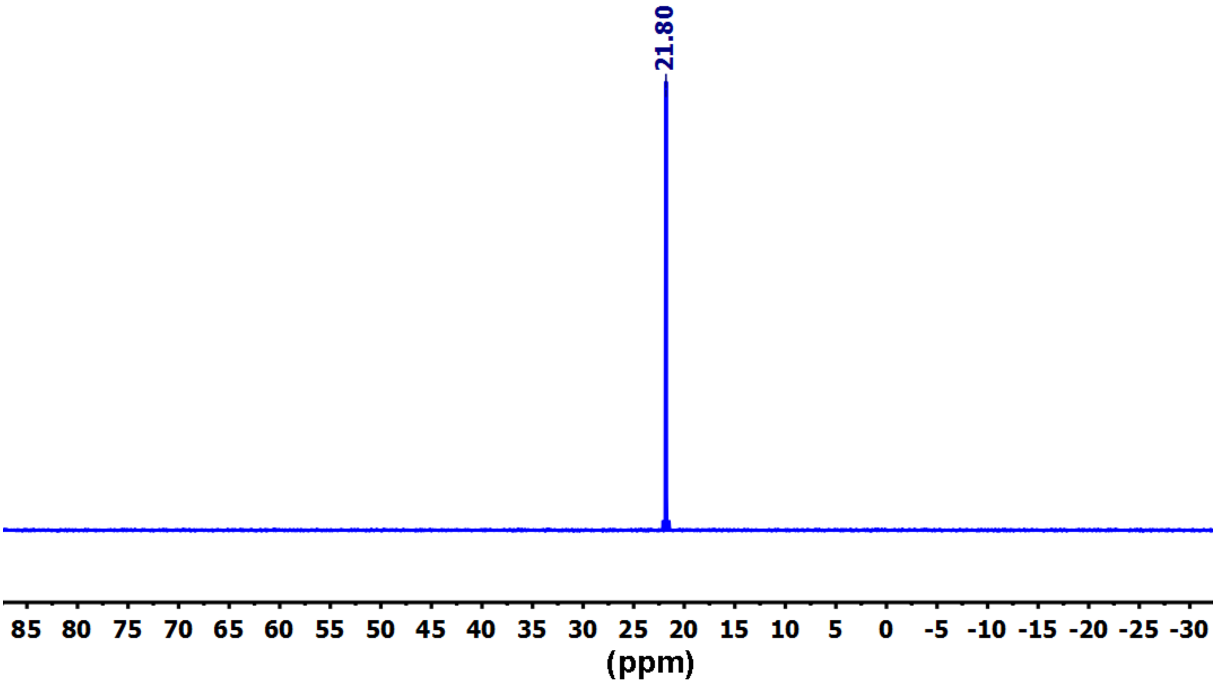

Figure 5A.1: ^{31}P NMR spectrum of **1**.

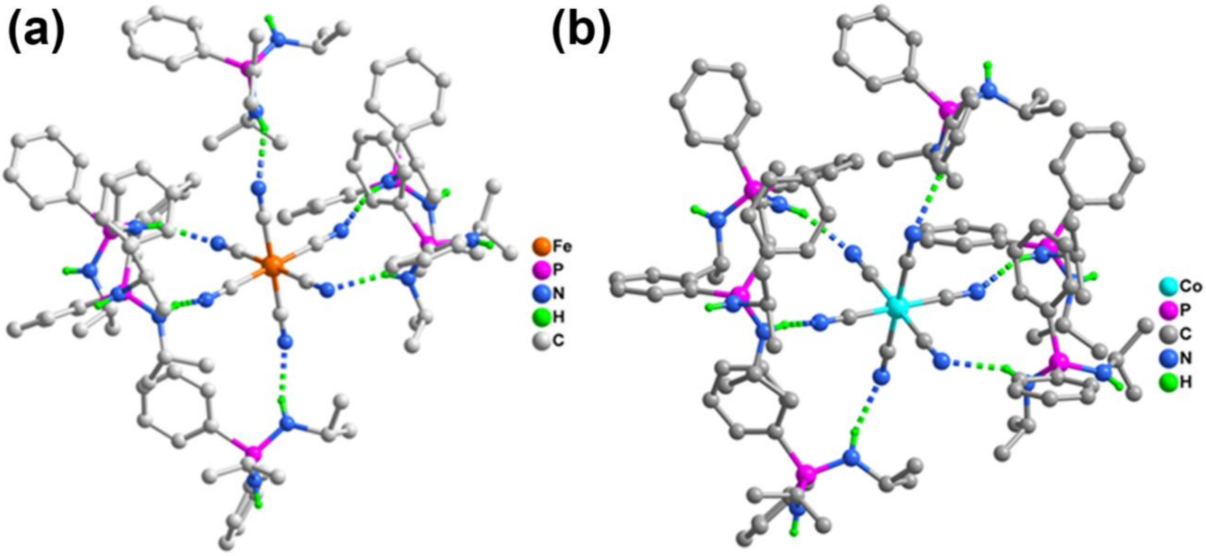

Figure 5A.2: (a) and (b) the view of the N-H···N interactions along the ‘b‘axis at 100 K for $[DPDP]_3[M(CN)_6]$ (M = Fe, Co).

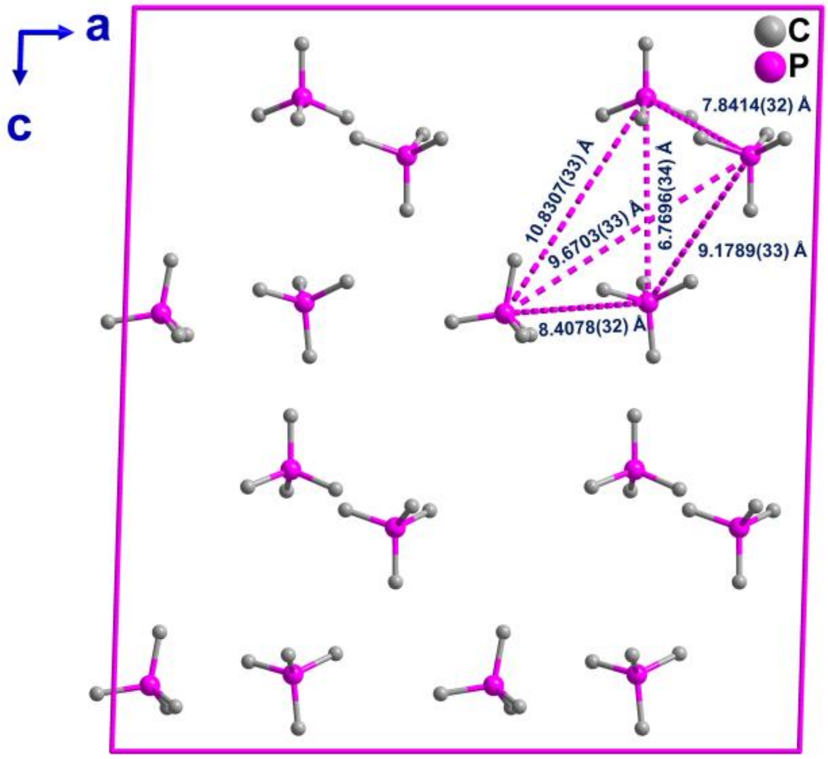

Figure 5A.3: The distance between the adjacent P-P centers in the unit-cell diagram of **1** at 100 K.

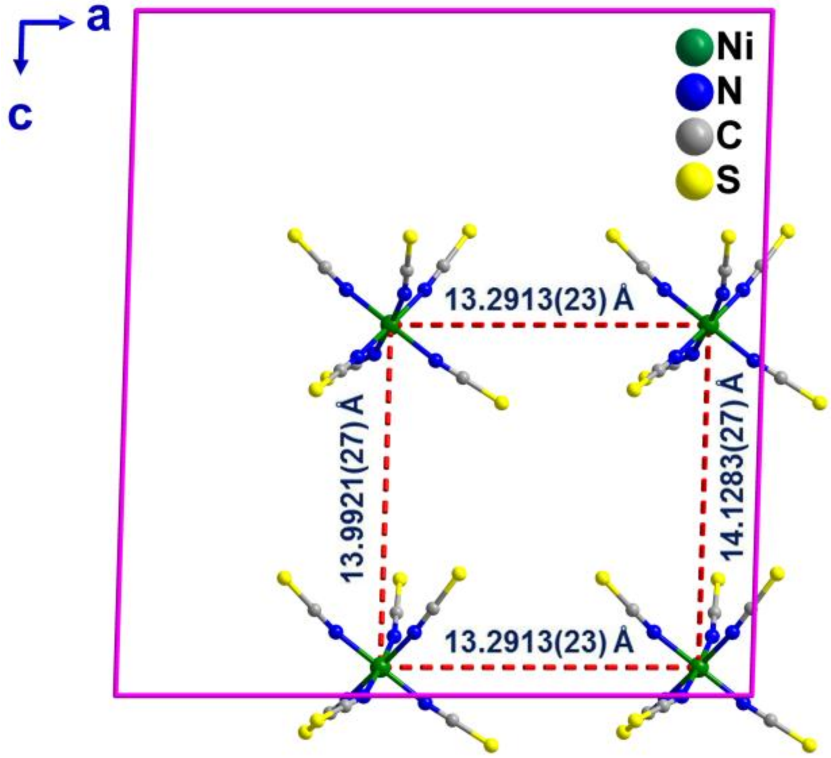

Figure 5A.4: The distance between the adjacent Ni-Ni centers in the unit-cell diagram of **1** at 100 K.

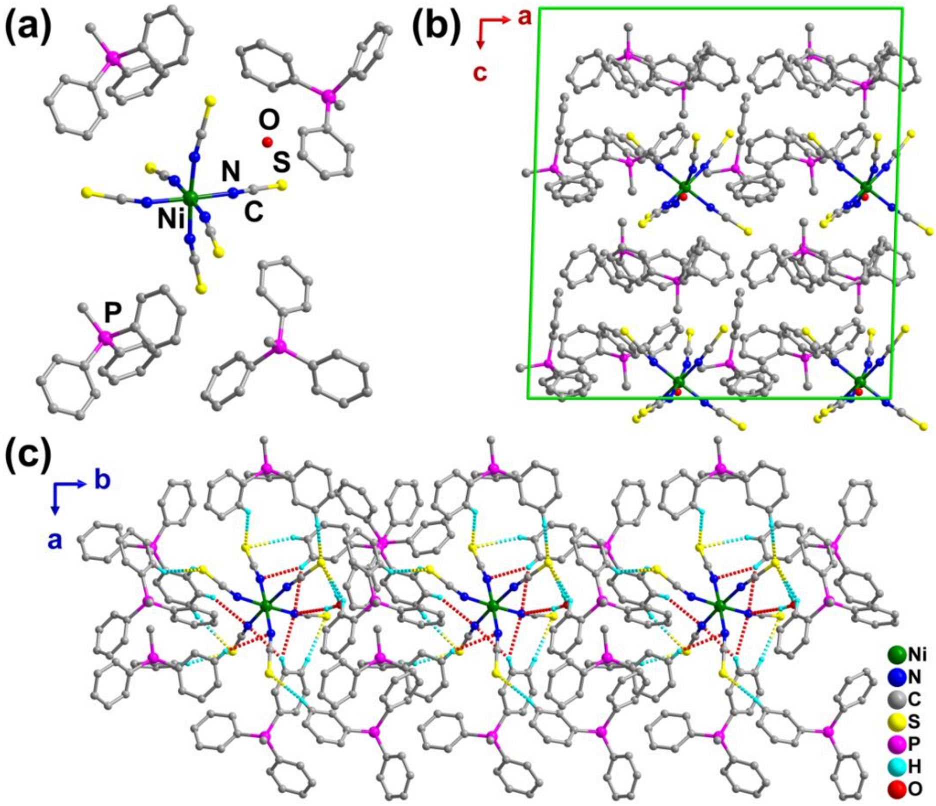

Figure 5A.5: (a) Asymmetric unit of **1**.H_2O. (b) The unit-cell packing diagram and (c) the C-H···S and C-H···N interactions along the 'b' axis at 100 K.

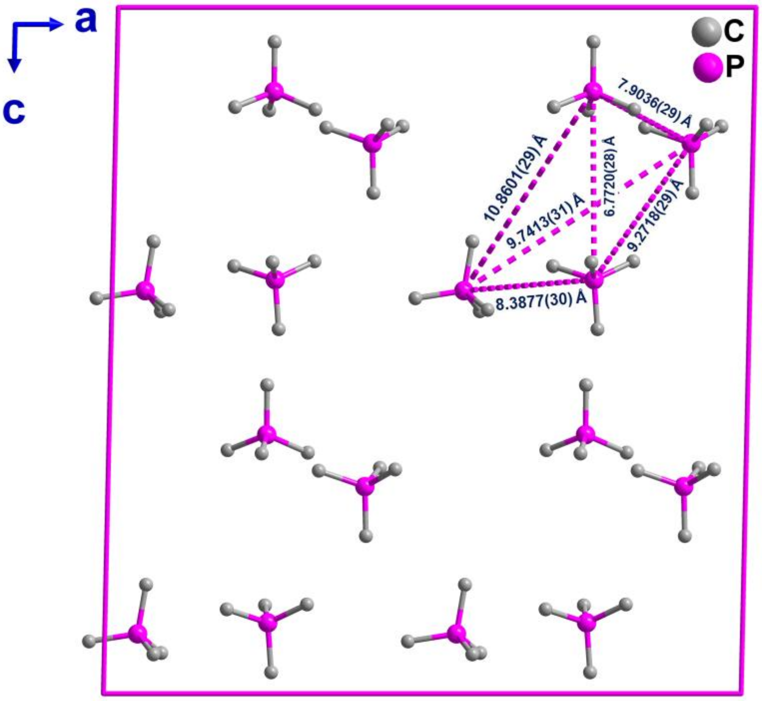

Figure 5A.6: The distance between the adjacent P-P centers in the unit-cell diagram of **1** at 294 K.

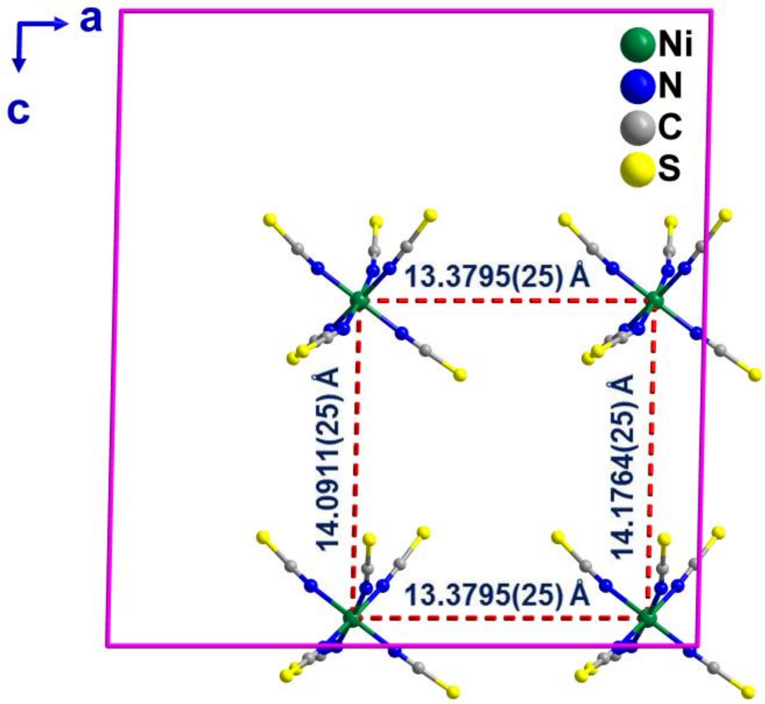

Figure 5A.7: The distance between the adjacent Ni-Ni centers in the unit-cell diagram of **1** at 294 K.

Table 5A.1: Crystallographic data for the ferroelectric organic-inorganic hybrid compound **1**.H_2O (100 K) and **1** (294 K).

1.H_2O and 1	**D-H…A**	**d(D-H)**	**d(H…A)**	**d(D-A)**	**<DHA**	**Symmetry operations**
100 K	C(16P)-H(16P)…S(1M)	0.9495(72)	2.8976(21)	3.552(8)	127.102(446)	0.5+x, -0.5+y, z
	C(28P)-H(28P)…S(1M)	0.9503(99)	2.9571(23)	3.8880(101)	166.670(593)	x, 1-y, 0.5+z
	C(69P)-H(69P)…S(1M)	0.9498(78)	2.9845(22)	3.9129(85)	166.022(475)	0.5+x, 0.5+y, z
	C(40P)-H(40P)…S(2M)	0.9494(89)	2.8370(21)	3.7547(92)	162.845(542)	x, y, z
	C(63P)-H(63P)…S(2M)	0.9496(77)	2.8459(22)	3.5525(81)	132.037(467)	x, 1-y, -0.5+z
	C(26P)-H(26P)…S(3M)	0.9498(87)	2.7879(22)	3.5763(86)	141.002(501)	x, -1+y, z
	C(46P)-H(46P)…S(3M)	0.9476(91)	2.9674(22)	3.7998(90)	147.360(529)	-0.5+x, -0.5+y, z
	C(57P)-H(57P)…S(3M)	0.9504(97)	2.7068(22)	3.4592(99)	136.569(579)	0.5+x, 0.5-y, -0.5+z
	C(32P)-H(32P)…S(4M)	0.9501(76)	2.8166(22)	3.5765(75)	137.657(433)	-0.5+x, -0.5+y, z
	C(52P)-H(52P)…S(4M)	0.9497(84)	2.9288(23)	3.7837(85)	150.398(498)	-0.5+x, 0.5+y, z
	C(70P)-H(70P)…S(4M)	0.9500(85)	2.9504(23)	3.5219(97)	119.921(563)	x, -y, -0.5+z
	C(71P)-H(71P)…S(4M)	0.9490(78)	2.8093(22)	3.4539(81)	126.035(463)	x, -y, -0.5+z
	C(18P)-H(18P)…S(5M)	0.9493(77)	2.9964(22)	3.8297(82)	147.298(473)	x, -1+y, z
	C(44P)-H(44P)…S(5M)	0.951(9)	2.9590(23)	3.7889(100)	146.540(565)	-0.5+x, -0.5+y, z
	C(12P)-H(12P)…S(6M)	0.9496(87)	2.9701(23)	3.7953(89)	146.102(517)	x, y, z
	C(23P)-H(23P)…S(6M)	0.9504(91)	2.9478(24)	3.7615(95)	144.400(559)	-0.5+x, -0.5+y, z
	O(1S)-H(1S)…S(6M)	0.9673(844)	2.4032(950)	3.2990(75)	153.829(695)	x, -1+y, z
	C(21P)-H(21P)…N(1M)	0.9501(86)	2.9679(69)	3.8642(109)	157.803(522)	x, y, z
	C(39P)-H(39P)…N(2M)	0.9488(94)	2.8321(69)	3.6450(115)	144.309(571)	x, y, z
	O(1S)-H(2S)…N(2M)	0.9638(975)	2.3497(980)	3.3061(99)	171.522(753)	x, y, z

	O(1S)-H(2S)…N(6M)	0.9638(975)	2.9176(1020)	3.4340(97)	114.707(583)	x, y, z
	C(51P)-H(51P)…N(2M)	0.9491(78)	2.9343(68)	3.7309(99)	142.320(457)	-0.5+x, 0.5+y, z
	C(21P)-H(21P)…N(3M)	0.9501(86)	2.8797(70)	3.4074(108)	116.191(519)	x, -1+y, z
	C(39P)-H(39P)…N(3M)	0.9488(94)	2.8619(69)	3.6498(116)	141.176(577)	x, y, z
	C(45P)-H(45P)…N(3M)	0.9497(80)	2.7788(68)	3.6663(104)	155.900(492)	-0.5+x, -0.5+y, z
	C(51P)-H(51P)…N(4M)	0.9491(78)	2.6875(69)	3.5679(106)	154.556(502)	-0.5+x, 0.5+y, z
	C(66P)-H(66P)…N(5M)	0.9506(77)	2.7109(73)	3.6319(105)	163.253(482)	x, y, z
	C(66P)-H(66P)…N(6M)	0.9506(77)	2.9263(72)	3.2346(105)	100.314(476)	x, y, z
294 K	C(12P)-H(12P)…S(1M)	0.9309(69)	2.9708(23)	3.7688(73)	144.662(435)	x, y, z
	C(16P)-H(16P)…S(2M)	0.9293(92)	2.9832(23)	3.6712(96)	132.067(577)	0.5+x, 0.5+y, z
	C(27P)-H(27P)…S(3M)	0.9295(72)	2.9243(23)	3.6261(81)	133.364(464)	x, 1-y, -0.5+z
	C(58P)-H(58P)…S(3M)	0.9319(93)	2.8858(23)	3.7868(96)	162.999(573)	x, y, z
	C(21P)-H(21P)…S(4M)	0.9295(98)	2.7757(23)	3.5107(100)	136.768(597)	0.5+x, 1.5-y, -0.5+z
	C(44P)-H(44P)…S(4M)	0.9286(80)	2.8345(23)	3.5995(86)	140.467(512)	x, 1+y, z
	C(64P)-H(64P)…S(4M)	0.9302(91)	2.9956(23)	3.8213(91)	148.739(543)	-0.5+x, 0.5+y, z
	C(35P)-H(35P)…S(5M)	0.9282(79)	2.8650(25)	3.5272(82)	129.334(447)	x, 2-y, -0.5+z
	C(50P)-H(50P)…S(5M)	0.9304(82)	2.8649(24)	3.6017(88)	137.008(505)	-0.5+x, 0.5+y, z
	C(70P)-H(70P)…S(5M)	0.9310(84)	2.9414(25)	3.7980(87)	153.613(513)	-0.5+x, -0.5+y, z
	C(18P)-H(18P)…S(6M)	0.9293(70)	3.0103(23)	3.8303(75)	148.014(437)	x, 1+y, z
	C(30P)-H(30P)…N(1M)	0.9306(72)	2.9960(57)	3.3284(90)	102.813(461)	x, y, z
	C(39P)-H(39P)…N(2M)	0.9313(115)	2.9913(57)	3.8698(120)	157.837(636)	x, 1+y, z
	C(57P)-H(57P)…N(3M)	0.9288(93)	2.7771(47)	3.5752(104)	144.651(577)	x, y, z
	C(39P)-H(39P)…N(4M)	0.9313(115)	2.9039(56)	3.4603(124)	119.622(629)	x, 1+y, z
	C(57P)-H(57P)…N(4M)	0.9288(93)	2.8983(62)	3.6884(109)	143.751(565)	x, y, z
	C(63P)-H(63P)…N(4M)	0.9306(85)	2.8350(61)	3.6939(105)	153.970(539)	-0.5+x, 0.5+y, z
	C(69P)-H(69P)…N(5M)	0.9310(88)	2.7539(57)	3.6097(103)	153.240(539)	-0.5+x, -0.5+y, z
	C(30P)-H(30P)…N(6M)	0.9306(72)	2.7762(55)	3.6766(92)	164.862(459)	x, y, z

Table 5A.2: Selected bond lengths [Å] and angles [°] for compound **1**.H_2O and **1** at different temperatures.

1.H_2O	**Bond length**	**Bond angle**	**1**	**Bond length**	**Bond angle**
100 K	Ni1-N1M: 2.078(7)	N1M-Ni1-N2M: 91.7(3)	**294K**	Ni1-N1M: 2.077(6)	N1M-Ni1-N2M: 91.3(2)
	Ni1-N2M: 2.099(7)	N1M-Ni1-N5M: 91.6(3)		Ni1-N2M: 2.088(6)	N1M-Ni1-N3M: 86.7(2)
	Ni1-N3M: 2.070(7)	N2M-Ni1-N5M: 176.7(3)		Ni1-N3M: 2.086(6)	N1M-Ni1-N5M: 90.9(2)
	Ni1-N4M: 2.068(7)	N3M-Ni1-N1M: 89.3(3)		Ni1-N4M: 2.076(6)	N1M-Ni1-N6M: 93.7(2)
	Ni1-N5M: 2.108(7)	N3M-Ni1-N2M: 88.5(3)		Ni1-N5M: 2.085(6)	N2M-Ni1-N6M: 90.4(2)
	Ni1-N6M: 2.073(7)	N3M-Ni1-N6M: 174.9(3)		Ni1-N6M: 2.119(6)	N3M-Ni1-N2M: 92.9(2)
	N1M-C1M: 1.154(9)	N3M-Ni1-N5M: 91.6(3)		N1M-C1M: 1.147(8)	N3M-Ni1-N6M: 176.7(2)
	N2M-C2M: 1.164(10)	N4M-Ni1-N1M: 177.7(3)		N2M-C2M: 1.139(8)	N4M-Ni1-N1M: 174.7(2)
	N3M-C3M: 1.150(10)	N4M-Ni1-N2M: 90.2(3)		N3M-C3M: 1.141(8)	N4M-Ni1-N2M: 89.2(2)
	N4M-C4M: 1.164(9)	N4M-Ni1-N5M: 86.5(3)		N4M-C4M: 1.148(8)	N4M-Ni1-N3M: 88.0(2)
	N5M-C5M: 1.165(10)	N4M-Ni1-N3M: 89.4(3)		N5M-C5M: 1.147(8)	N4M-Ni1-N5M: 88.8(2)
	N6M-C6M: 1.161(10)	N4M-Ni1-N6M: 90.4(3)		N6M-C6M: 1.146(8)	N4M-Ni1-N6M: 91.6(2)
	C1M-S1M: 1.658(8)	N6M-Ni1-N1M: 91.1(3)		C1M-S1M: 1.641(8)	N5M-Ni1-N2M: 176.6(2)
	C2M-S2M: 1.651(9)	N6M-Ni1-N2M: 86.5(3)		C2M-S2M: 1.652(7)	N5M-Ni1-N3M: 89.9(2)
	C3M-S3M: 1.655(9)	N6M-Ni1-N5M: 93.4(3)		C3M-S3M: 1.643(8)	N5M-Ni1-N6M: 86.8(2)

	C4M-S4M: 1.644(8) C5M-S5M: 1.638(9) C6M-S6M: 1.652(9) O1S-H1S: 0.96(3) O1S-H2S: 0.96(3)	C1M-N1M-Ni1: 167.9(6) C2M-N2M-Ni1: 163.7(6) C3M-N3M-Ni1: 165.9(6) C4M-N4M-Ni1: 169.0(6) C5M-N5M-Ni1: 159.3(6) C6M-N6M-Ni1: 168.5(7) N1M-C1M-S1M: 179.2(8) N2M-C2M-S2M: 179.3(8) N3M-C3M-S3M: 179.3(8) N4M-C4M-S4M: 178.3(8) N5M-C5M-S5M: 177.2(8) N6M-C6M-S6M: 179.4(8) H1S-O1S-H2S: 110.0(10)		C4M-S4M: 1.629(7) C5M-S5M: 1.627(8) C6M-S6M: 1.621(8)	C1M-N1M-Ni1: 166.6(6) C2M-N2M-Ni1: 171.6(6) C3M-N3M-Ni1: 166.3(6) C4M-N4M-Ni1: 165.8(6) C5M-N5M-Ni1: 169.8(6) C6M-N6M-Ni1: 160.3(6) N1M-C1M-S1M: 176.9(7) N2M-C2M-S2M: 179.3(7) N3M-C3M-S3M: 178.3(7) N4M-C4M-S4M: 178.9(7) N5M-C5M-S5M: 178.1(7) N6M-C6M-S6M: 177.3(7)

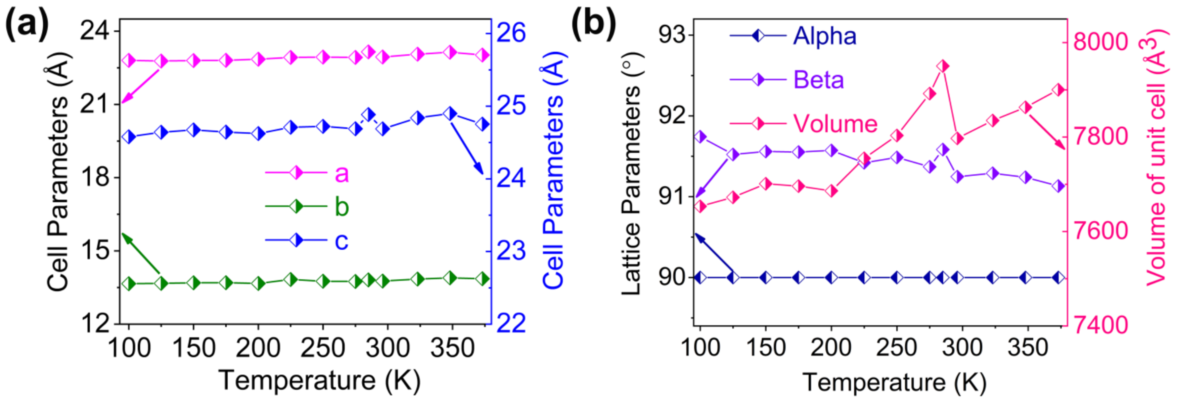

Figure 5A.8: Variable temperature single-crystal X-ray diffraction (VT-SCXRD) unit-cell parameter analysis of **1**.

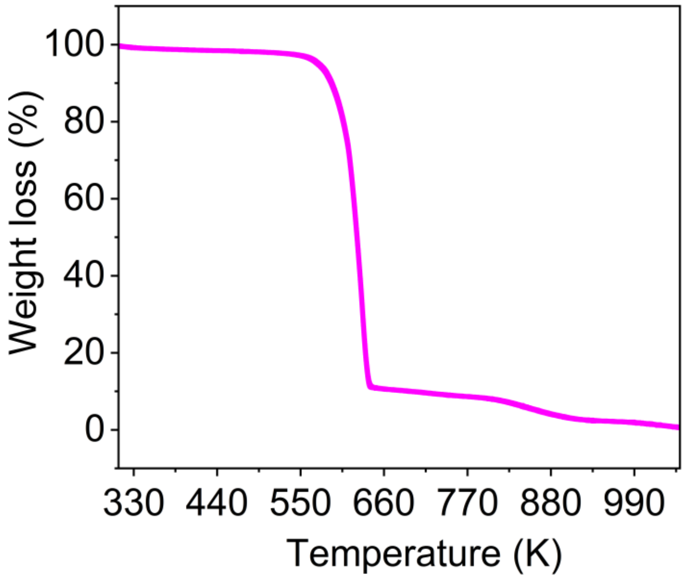

Figure 5A.9: Thermogravimetric (TGA) analysis of **1**.

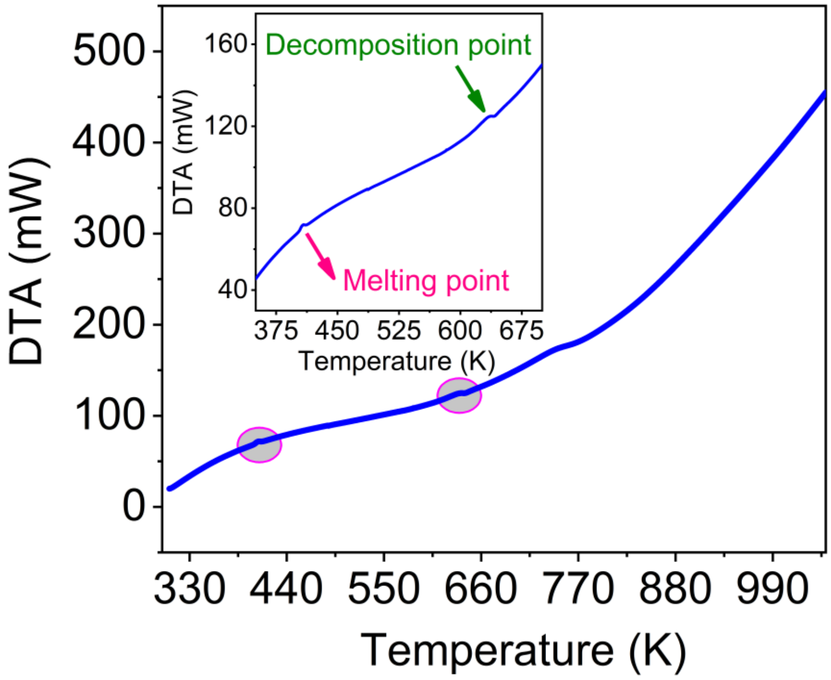

Figure 5A.10: Differential thermal analysis (DTA) of **1**.

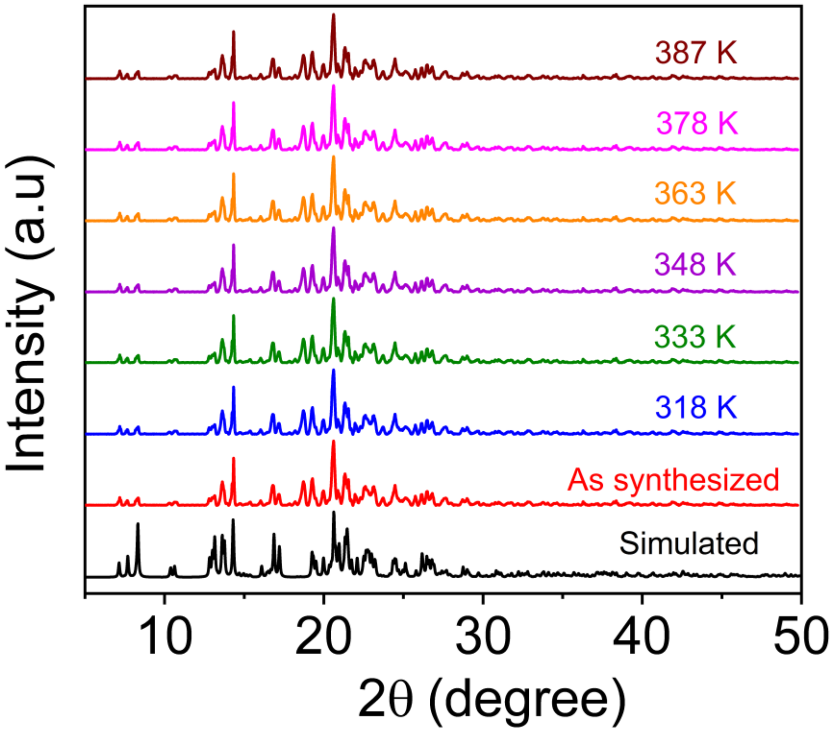

Figure 5A.11: Variable temperature powder X-ray diffraction (VT-PXRD) profiles of **1**.

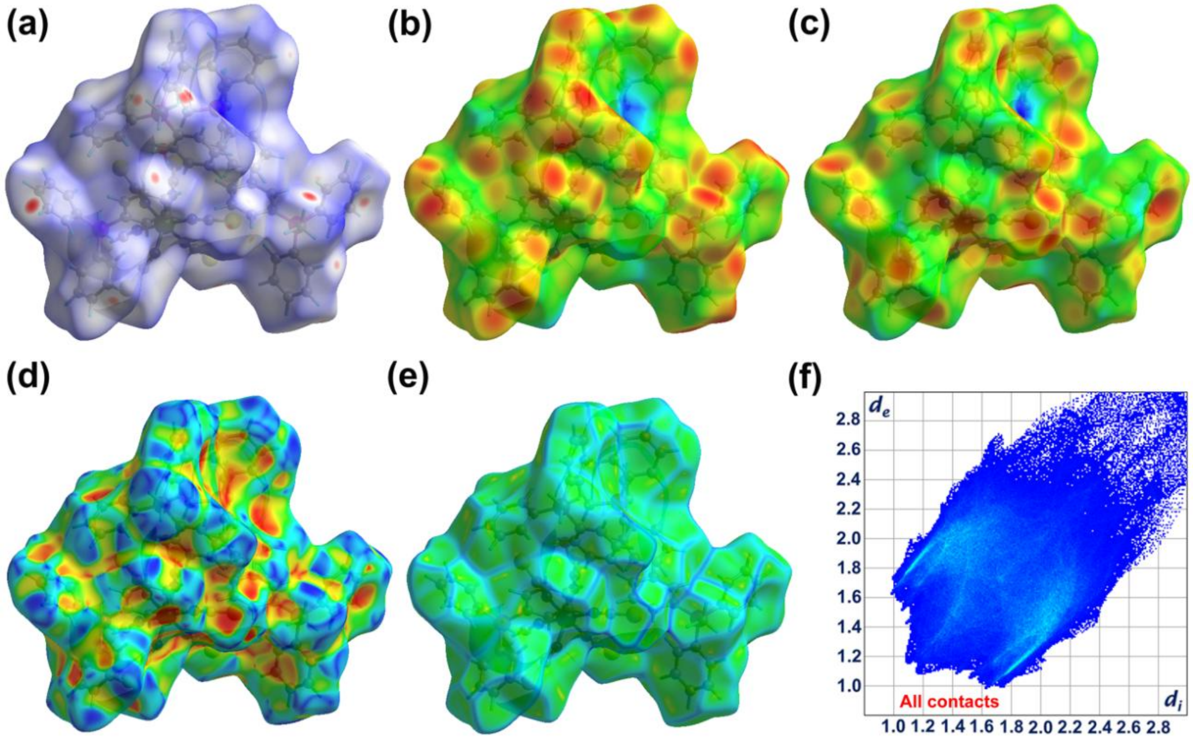

Figure 5A.12: The 3D color mapping over the Hirshfeld surface analysis of **1**.H_2O (100 K) showing (a) dnorm, (b and c) di, de, (d) shape index, (e) curvedness. The 2D fingerprint plot (de vs di) of **1**.

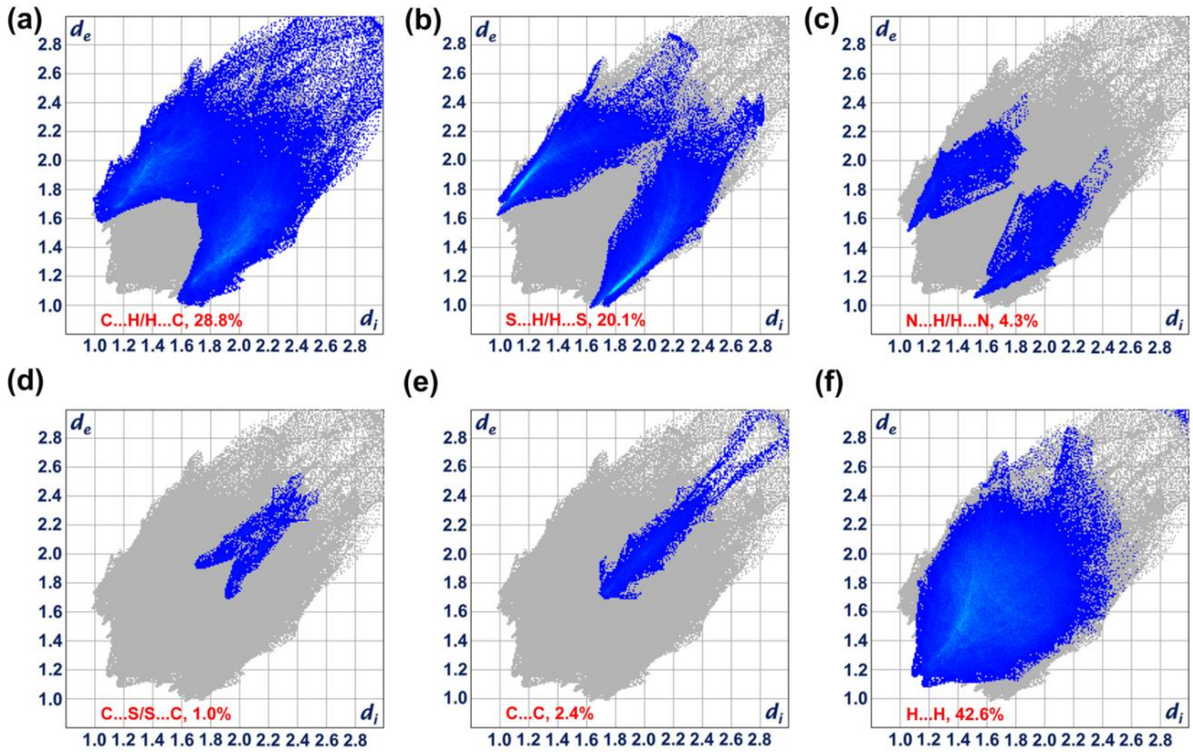

Figure 5A.13: The 2D fingerprint plot (de vs di) of **1**.H_2O at 100 K.

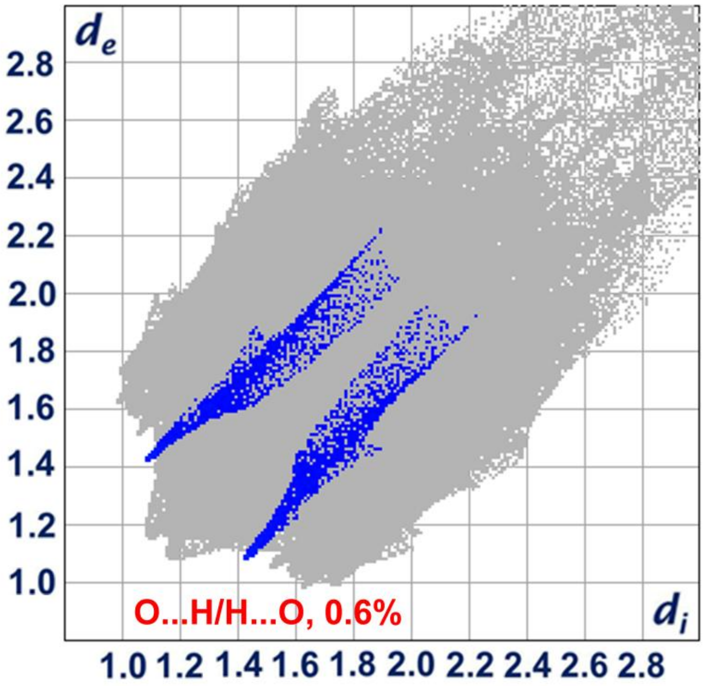

Figure 5A.14: The 2D fingerprint plot (de vs di) of compound **1** at 100 K.

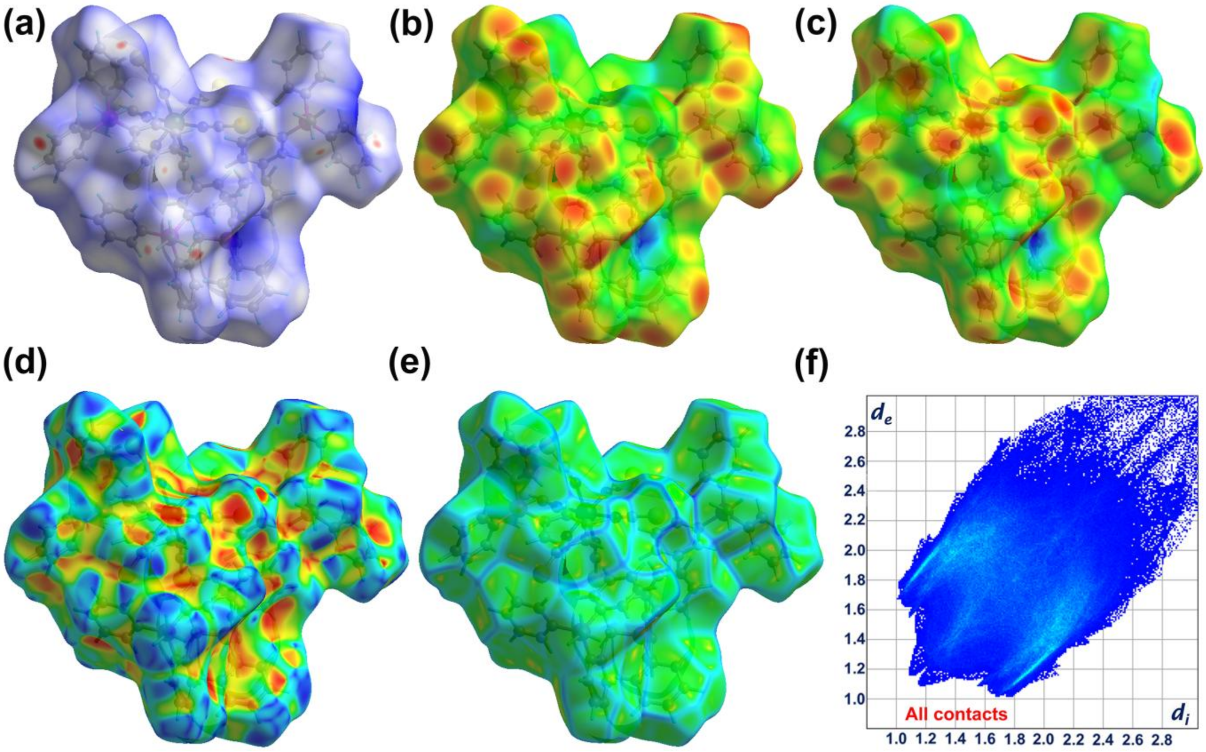

Figure 5A.15: The 3D color mapping Hirshfeld surface analysis of compound **1** (294 K) showing (a) dnorm, (b and c) di, de, (d) shape index, (e) curvedness. The 2D fingerprint plot (de vs di) of **1** at 294 K.

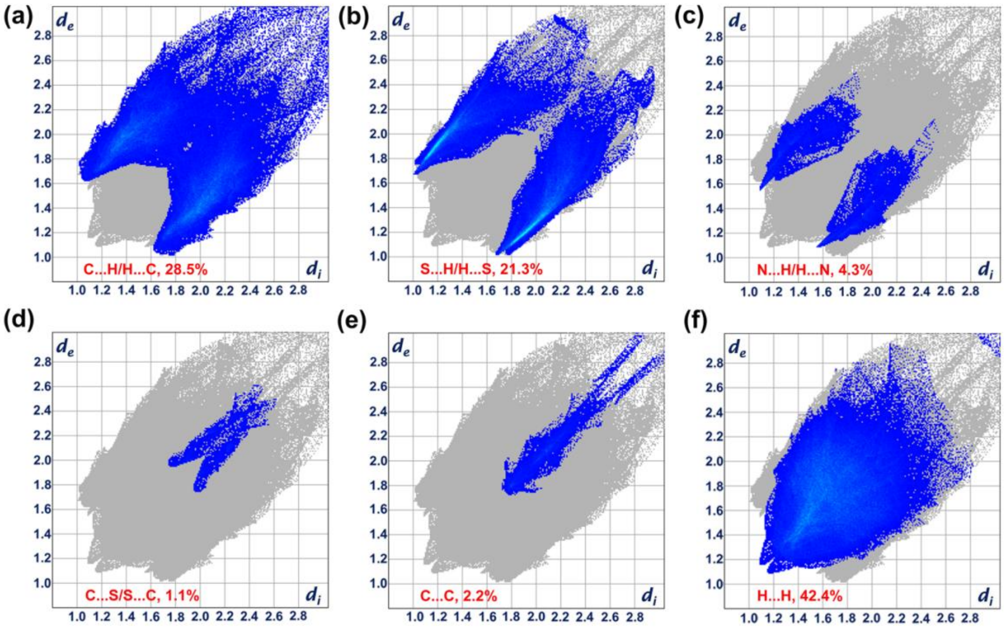

Figure 5A.16: The 2D fingerprint plot (de vs di) of **1** at 294 K.

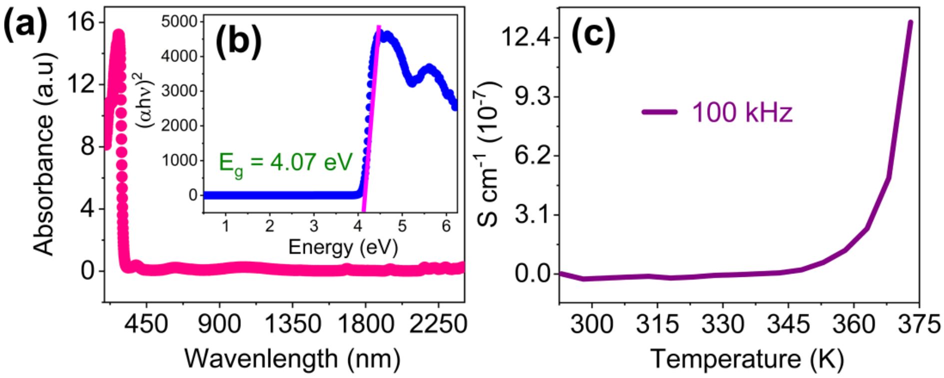

Figure 5A.17: (a) UV-visible Absorption spectra of **1** and it's (b) Tauc plot. (c) Temperature dependent conductivity plot for **1** at 100 kHz.

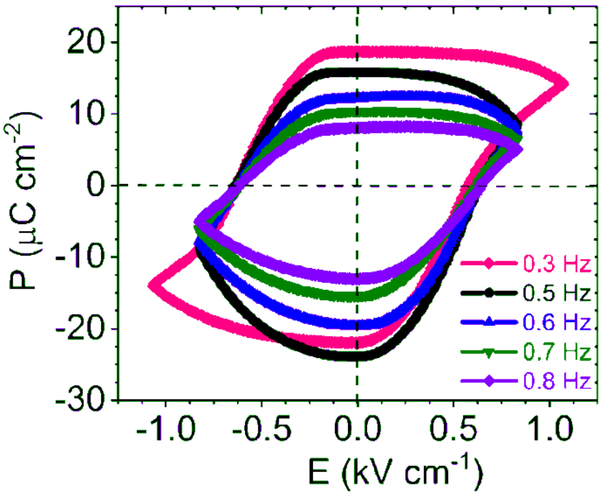

Figure 5A.18: The frequency dependent *P-E* hysteresis loop of **1**.

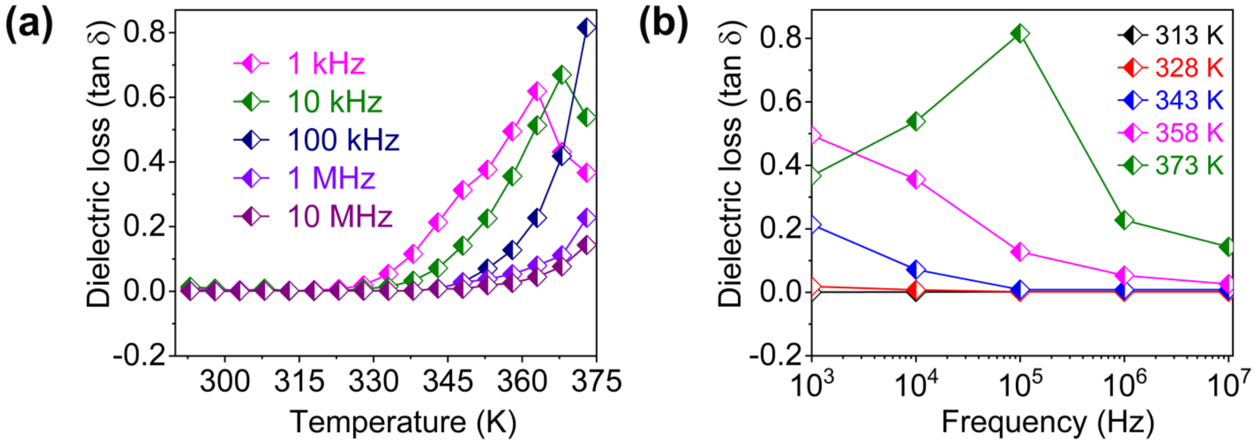

Figure 5A.19: (a) Temperature and (b) frequency-dependent dielectric loss (tan δ) of **1**.

Table 5A.3. Details about the preparation of various weight percentage (wt %) **1**-TPU composites.

Composite (wt %)	**1 (in mg)**	**1 + TPU (in mg)**
5	53	1053
10	112	1112
15	177	1177
20	250	1250

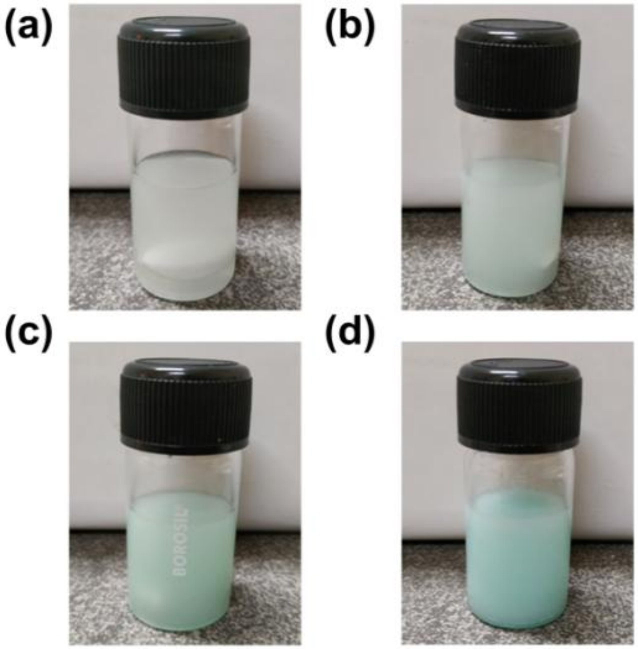

Figure 5A.20: The picture digital photograph of **1**-TPU depicted here indicates the color change of the composite films upon loading of various wt % (5, 10, 15 and 20) of **1**.

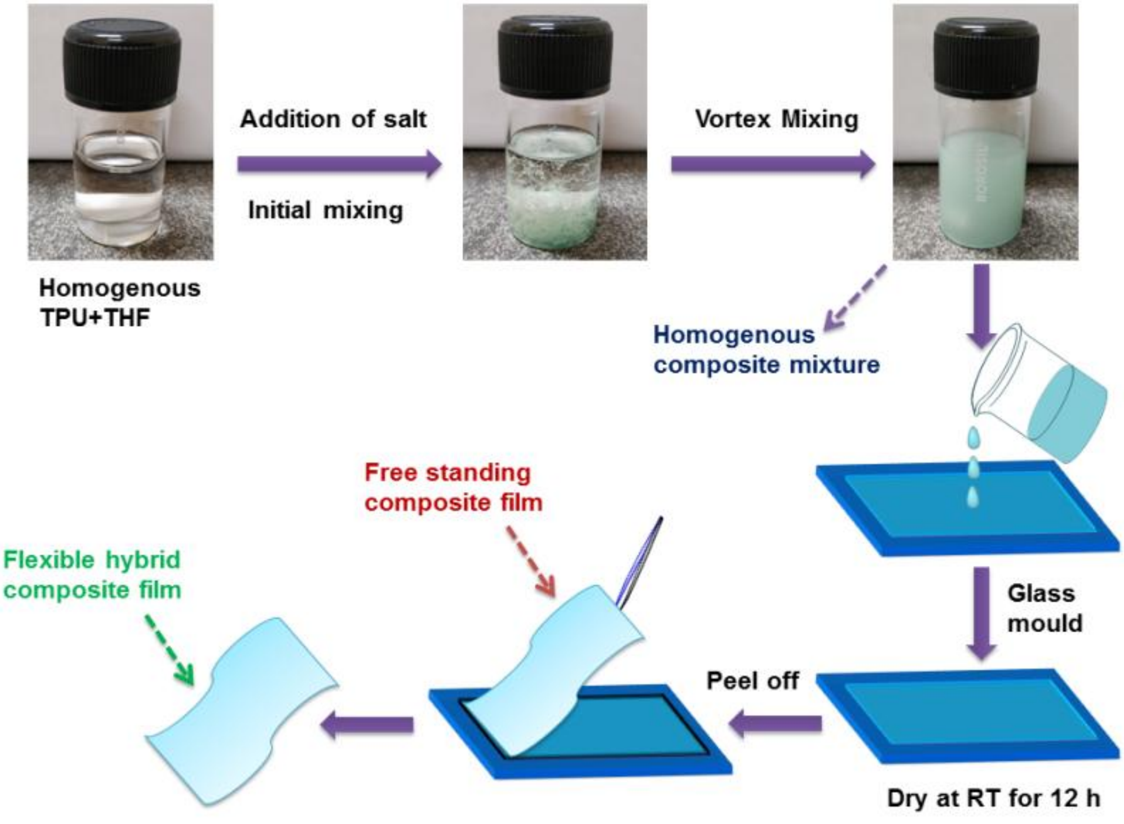

Scheme 5A.1: The detailed procedure involved in the making of **1**-TPU composite films.

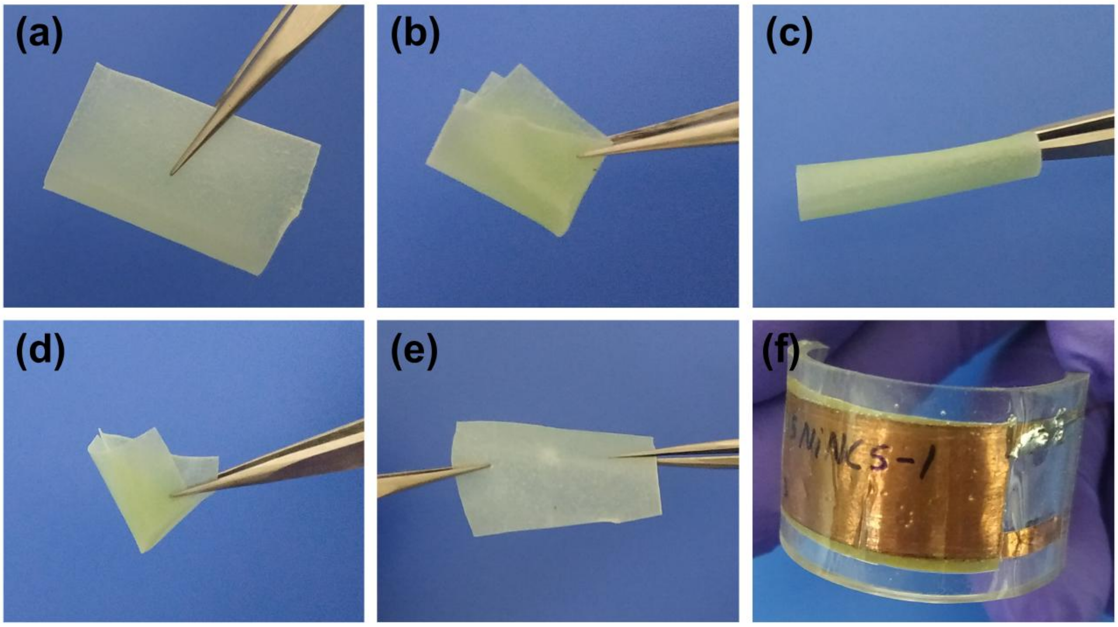

Figure 5A.21: Photographs of the 15 wt % **1**-TPU composite films showing (a) folding, (b) bending, (c) rolling, (d) multifold-bending and (e) stretching operations. (f) Photograph of the as-prepared flexible 15 wt % **1**-TPU composite device.

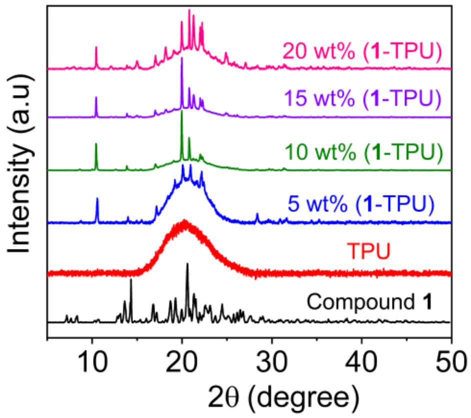

Figure 5A.22: PXRD analysis of all the wt % **1**-TPU composite films.

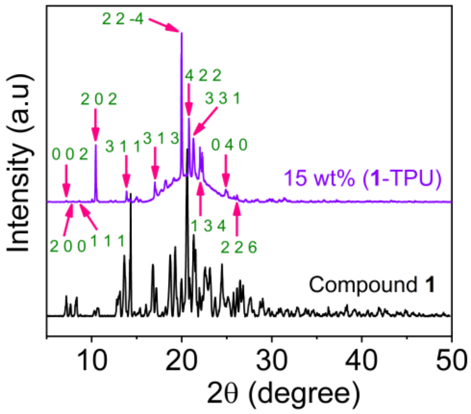

Figure 5A.23: The powder X-ray diffraction pattern and the characteristic hkl peaks for compound **1** and 15 wt % **1**-TPU.

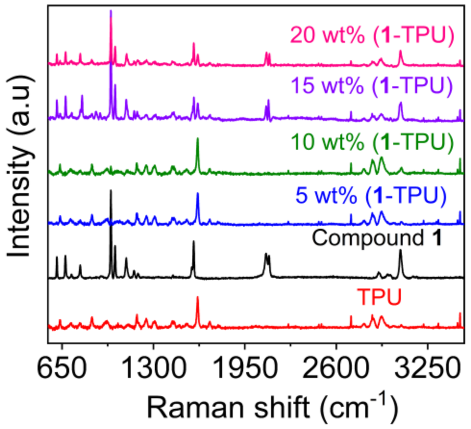

Figure 5A.24: Raman spectral analysis of all the wt % **1**-TPU composite films. The Raman active modes of the pure film of TPU display characteristic peaks at 3480-3325 (N-H stretching modes), 1700 and 1732 (C=O group) cm^{-1} for the urethane linkages in addition to the peaks due to aromatic C-H groups (3062 cm^{-1}) and benzylic CH$_2$ groups (2922 and 2855 cm^{-1}). The powdered crystallites of **1** show distinctive Raman active modes at 3056 (aromatic C-H), 2122-2100 (SCN^{-} group) 1188-1107 (P-C bonds) and 780 (C-S bonds) cm^{-1}.

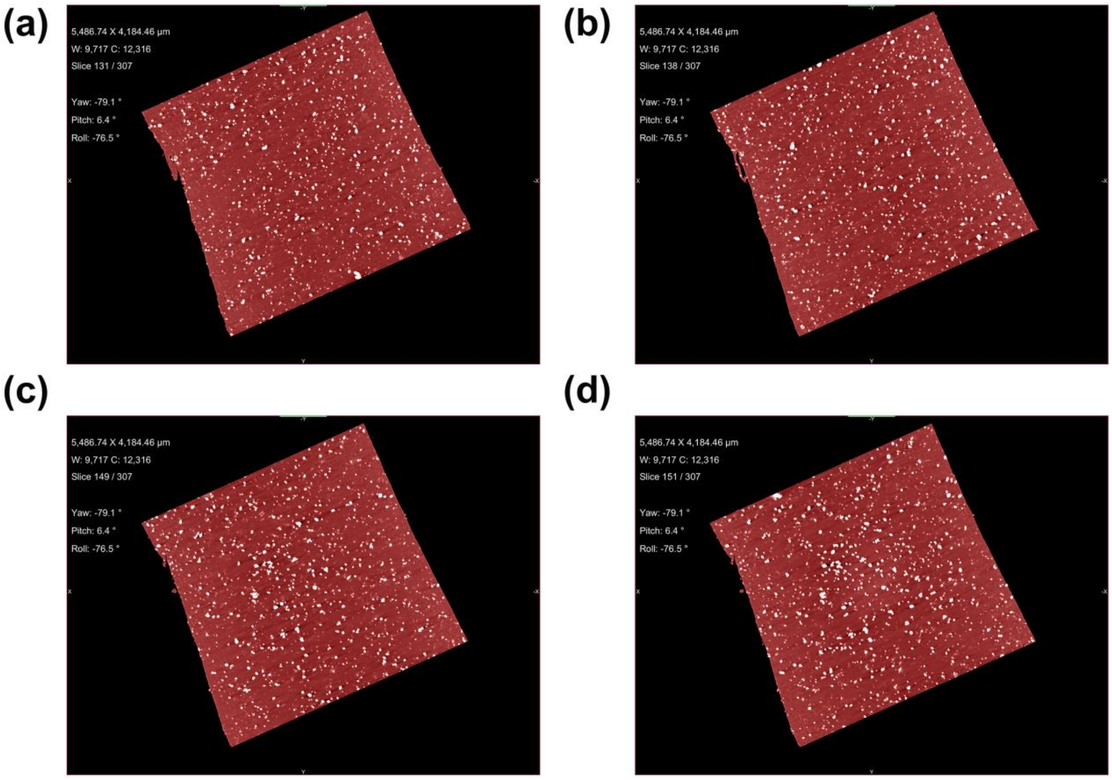

Figure 5A.25: The X-ray 2D-microtomography images of various inner slices of the 5 wt % **1**-TPU composite film (a-d).

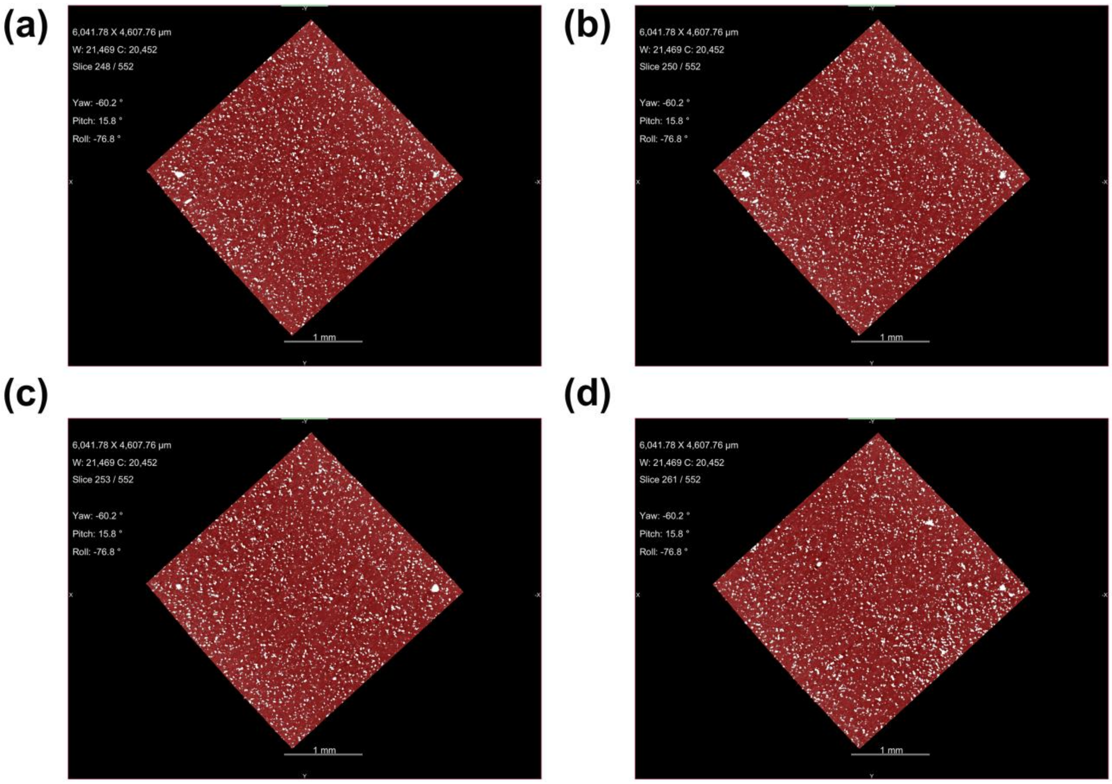

Figure 5A.26: The X-ray 2D-microtomography images of various inner slices of the 10 wt % **1**-TPU composite film (a-d).

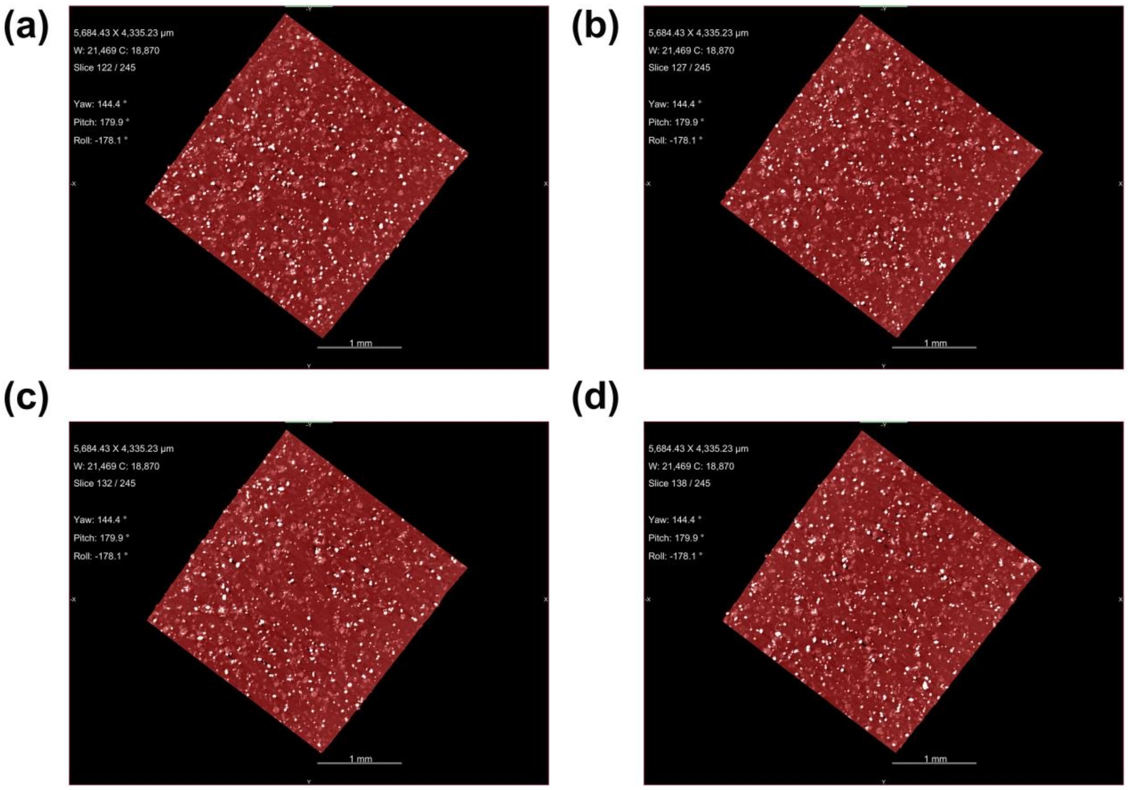

Figure 5A.27: The X-ray 2D-microtomography images of various inner slices of the 15 wt % **1**-TPU composite film (a-d).

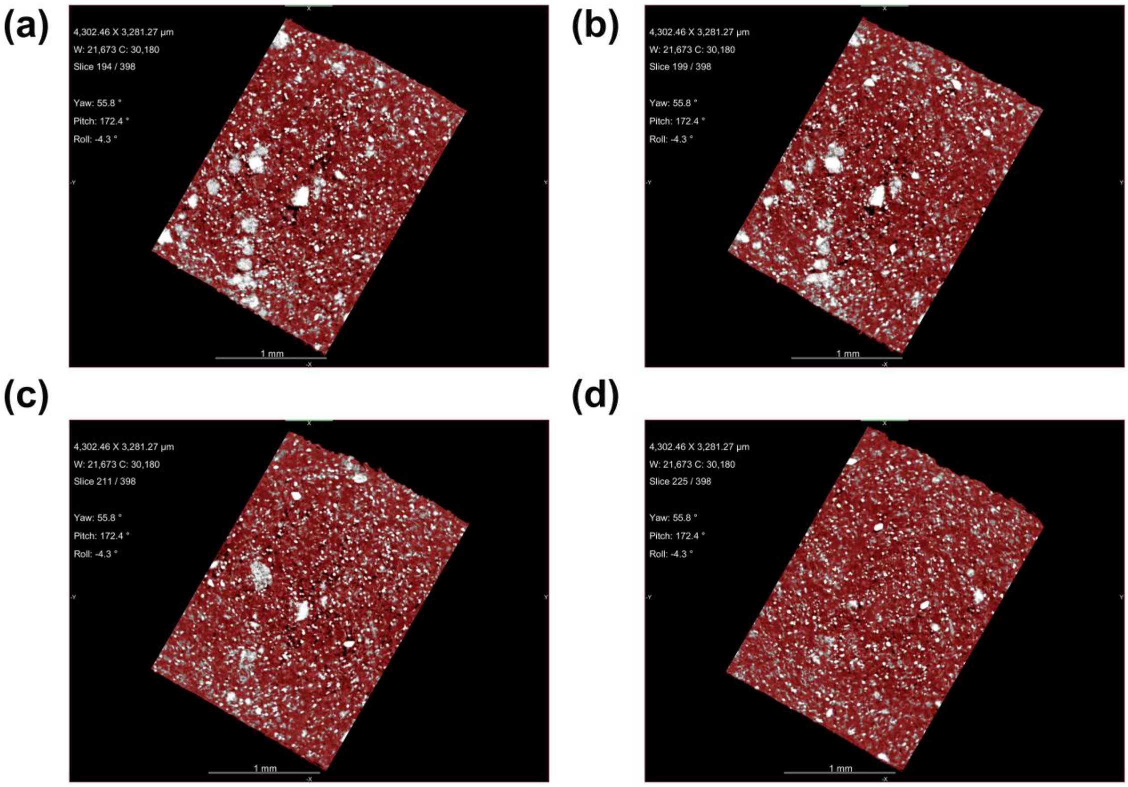

Figure 5A.28: The X-ray 2D-microtomography images of various inner slices of the 20 wt % **1**-TPU composite film (a-d).

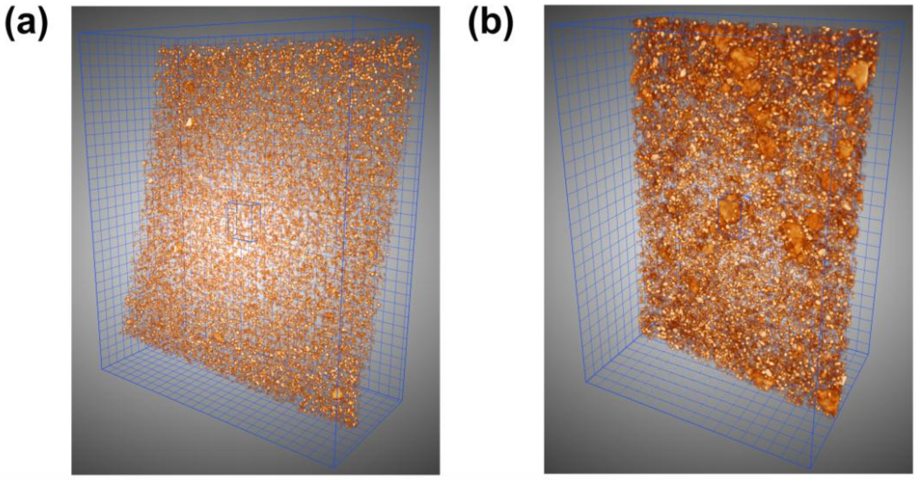

Figure 5A.29: The X-ray 3D-microtomography (a and b) images of 10 and 20 wt % **1**-TPU composite films. The polymer background was corrected to indicate the distribution of ferroelectric particles.

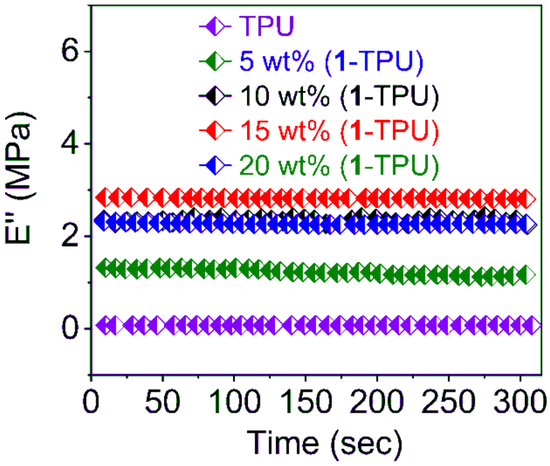

Figure 5A.30: The viscoelastic loss modulus (E”) of neat TPU and the various wt % **1**-TPU composite films.

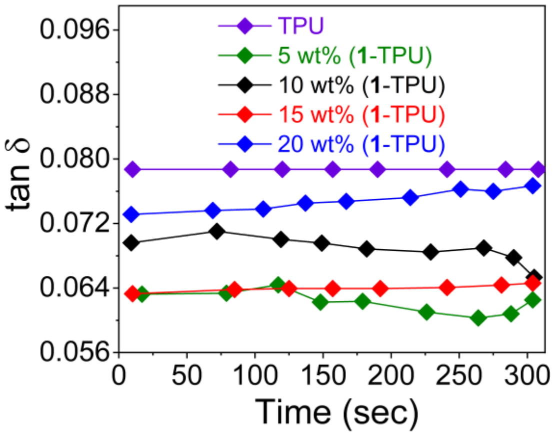

Figure 5A.31: Damping behavior of neat TPU and various wt % **1**-TPU composite films.

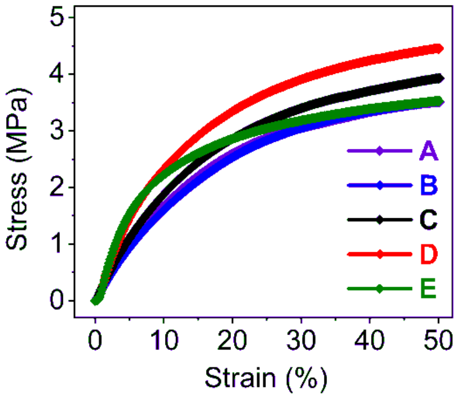

Figure 5A.32: Stress-strain curve relationship of **1**-TPU (A = neat TPU, B, C, D, E corresponds to the 5, 10, 15 and 20 wt % composite films of **1**-TPU).

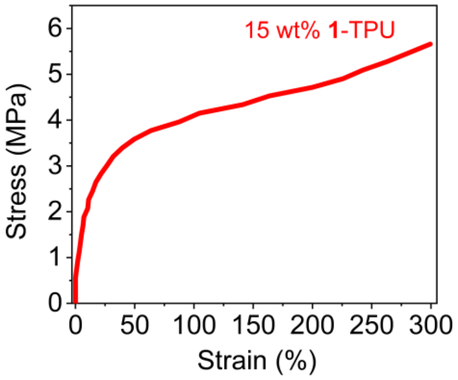

Figure 5A.33: Stress-strain curve relationship of selected 15 wt % of **1**-TPU.

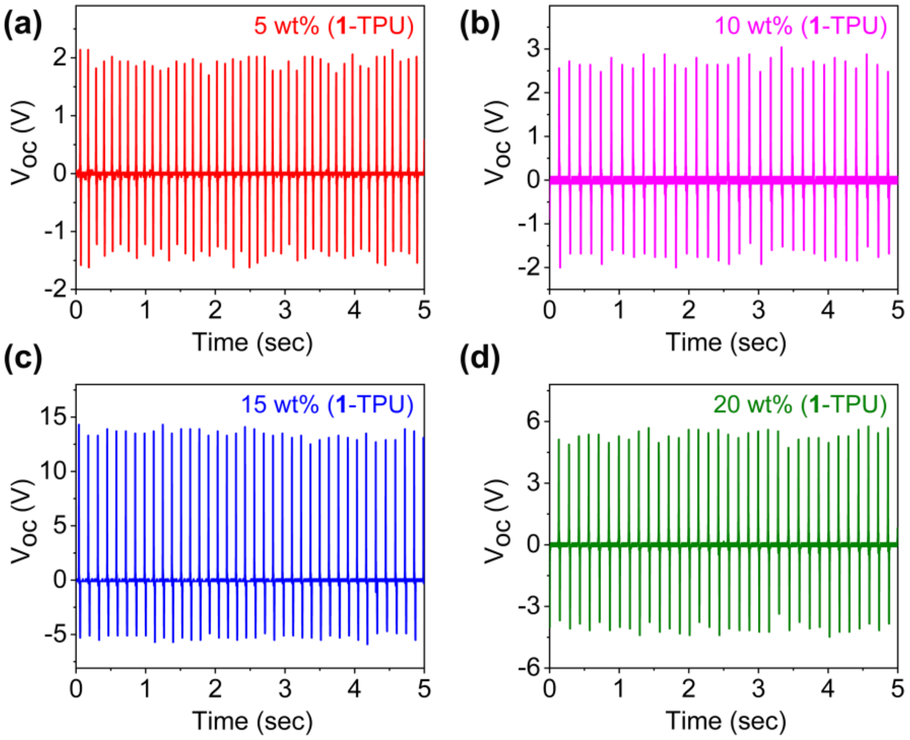

Figure 5A.34: Output voltage measurement of all the wt % **1**-TPU composite films.

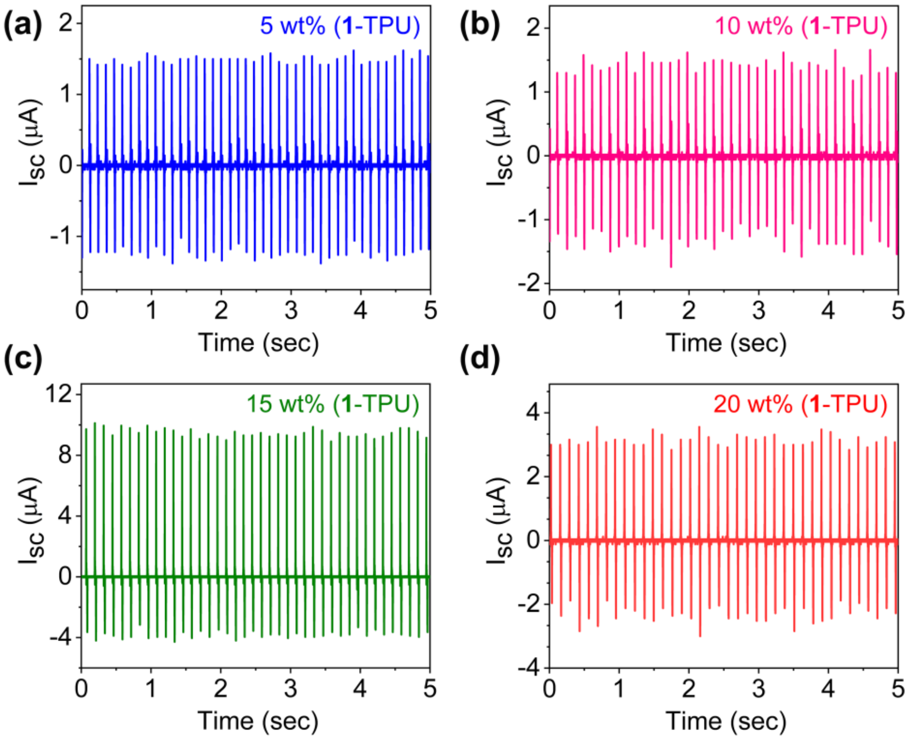

Figure 5A.35: Output current measurement of all the wt % **1**-TPU composite films.

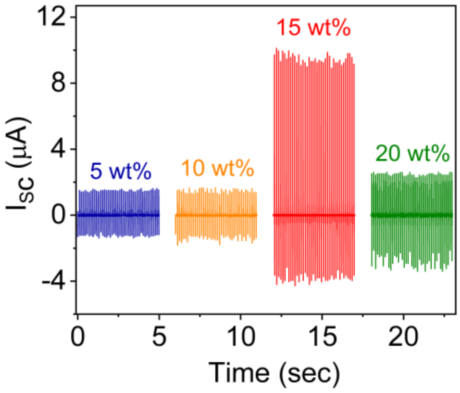

Figure 5A.36: The comparative output current performance of all the wt % **1**-TPU of composite films.

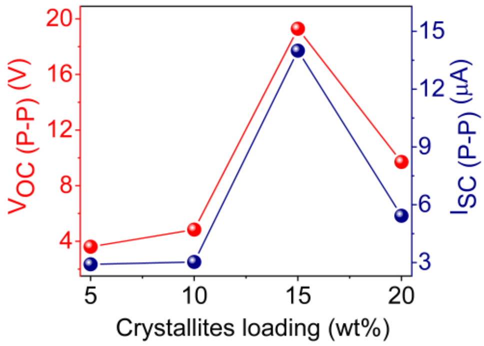

Figure 5A.37: The comparative output voltage and current data of all the wt % **1**-TPU of composite films.

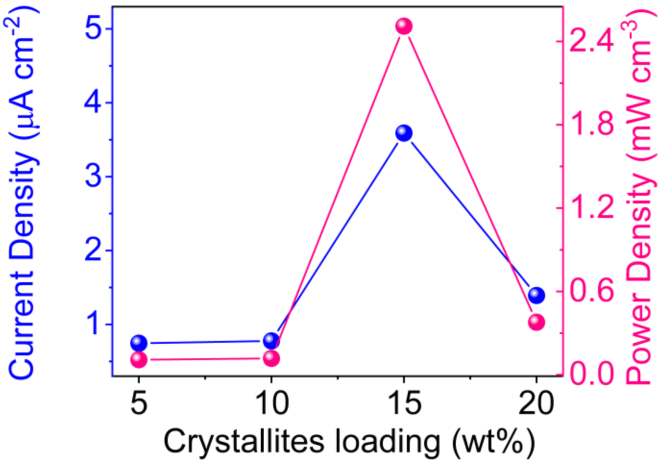

Figure 5A.38: The comparative output current and power densities of all the wt % **1**-TPU of composite films.

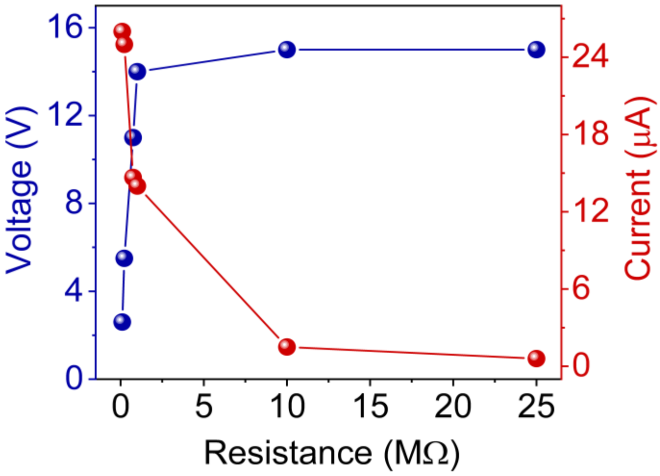

Figure 5A.39: The comparative output voltage and current data for the 15 wt % **1**-TPU composite device under various load resistances.

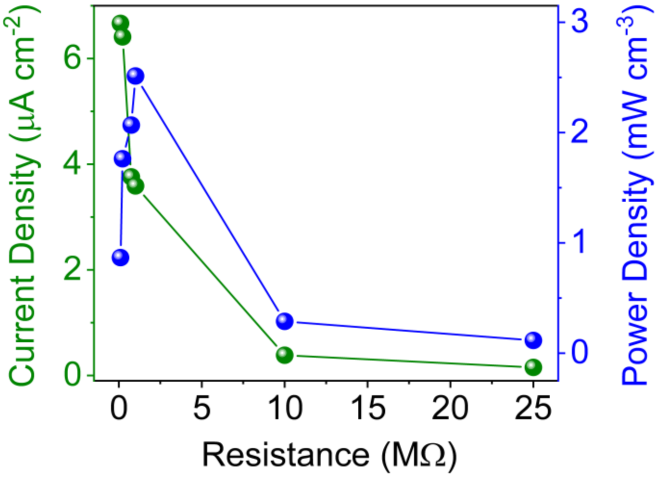

Figure 5A.40: The output current and power densities for the 15 wt % **1**-TPU composite device under various load resistances.

Table 5A.4. Output device performance of all the wt % of **1**-TPU composites films.

Composites (wt %)	**Output voltage (*VPP*)**	**Output current (*IPP*)**	**Power density (μW/cm^3)**	**Current density (μA/cm^2)**
5	3.61	2.91	0.1086	0.7462
10	4.84	3.03	0.1177	0.7769
15	19.29	14.00	2.5100	3.5900
20	9.71	5.43	0.3780	1.3923

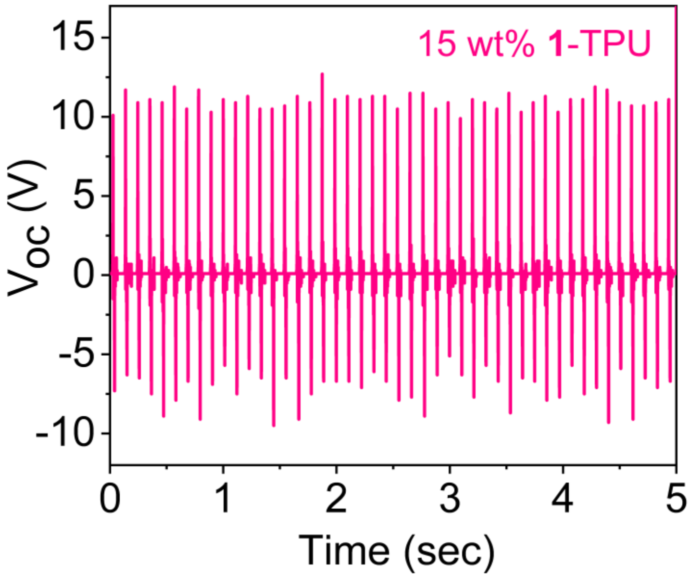

Figure 5A.41: Durability test (after eight months) for 15 wt % of **1**-TPU composite device.

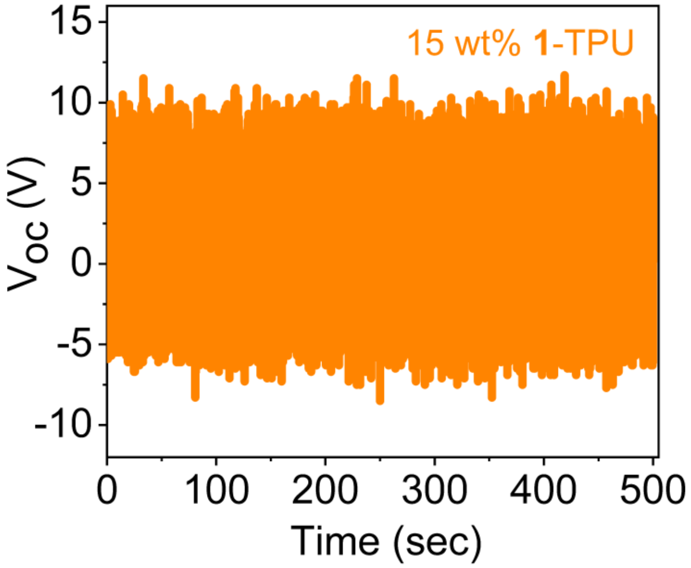

Figure 5A.42: Cyclic stability test for the 15 wt % of **1**-TPU composite device over a working period of 4000 cycles with a continuously applied force of 17 N and the frequency of 8 Hz.

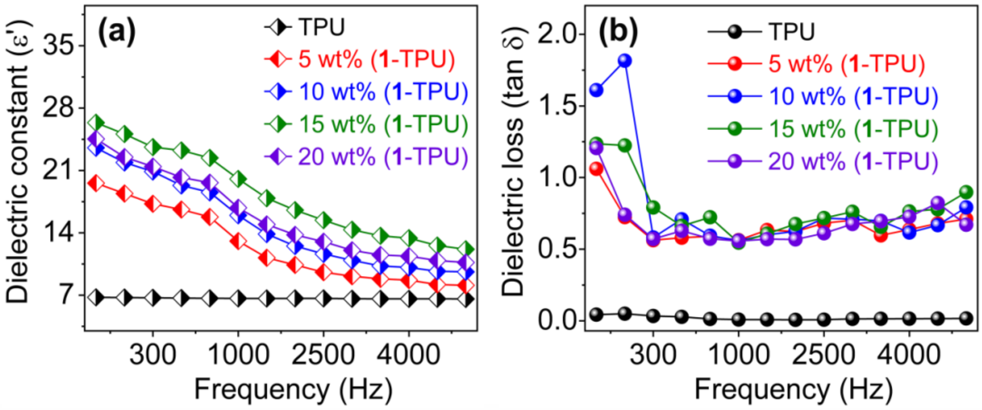

Figure 5A.43: Room temperature ε' and tan δ data for various wt % **1**-TPU composite films.

Table 5A.5. Output device performance of all the wt % of **1**-TPU composites films.

Materials Name	**Composites (wt %)**	**Area (mm^2)**	**Thickness (nm)**	**Dielectric constant (ε')**	**Dielectric loss (tan δ)**
Neat TPU	0	25.57	3.1 e^5	6.64	0.0087
1-TPU	5	29.31	3.20 e^5	13.07	0.5624
	10	34.77	3.90 e^5	15.97	0.5597
	15	24.5	3.90 e^5	20.05	0.5453
	20	29.95	4.0 e^5	16.81	0.5571

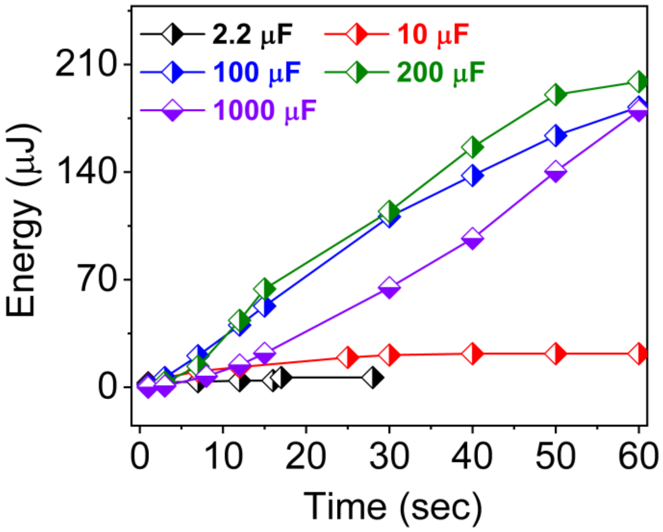

Figure 5A.44: The comparative capacitance dependent stored energies (E) of the capacitors using the 15 wt % **1**-TPU composite device.

****